# Cavity non destructive detection on an optical lattice clock

Grégoire Vallet

PSL UNIVERSITÉ PARIS

THÈSE DE DOCTORAT
DE L'UNIVERSITÉ PSL

Préparée à l'Observatoire de Paris

# Détection non destructive en cavité pour une horloge à réseau optique au strontium.


Soutenue par
**Grégoire Vallet**
Le 13 décembre 2018


École doctorale n°564
**Physique en Île-de-France**

Spécialité
**Physique (milieux dilués et optique)**

Composition du jury :

| | |
|---|---|
| **Caroline Champenois**<br>chargée de recherche CNRS, Aix-Marseille Université | *rapporteuse* |
| **Robin Kaiser**<br>directeur de recherche CNRS, Université Côte d'Azur | *rapporteur* |
| **Morgan Mitchell**<br>professeur | *examinateur* |
| **Jakob Reichel**<br>professeur, Sorbonne université | *examinateur* |
| **Sébastien Bize**<br>Chargé de recherche CNRS | *directeur de thèse* |
| **Jérôme Lodewyck**<br>Chargé de recherche CNRS | *invité* |

l'Observatoire de Paris | PSL

# Contents

# 1 Introduction

This thesis work was carried out within the context of the eventual re-definition of the S.I. second (see section 2.7.4) and can be described as being divided into three main fields of activity. The first one could be grasped under the "clock operation" formula and mainly refers to the participations to continental scale clock comparison campaigns (part III) as well as to TAI contribution and is directly aiming at realizing the requirements set by the roadmap given in [2] and reported above (section 2.7.4). The second field relates to the investigation and assessments of effects potentially mis-/under-estimated or even overlooked so far (part II) that could result in clock frequency shifts incompatible with our current accuracy estimation summed up in our uncertainty budget (part I, section 4.6). Last bu not least, the largest amount of the work carried out aimed at the realization of a non-destructive detection system allowing for the beating of the two current stability limitations of optical lattice clocks: the Dick effect (part IV, section 8.1) and the quantum projection noise (part IV, section 8.2). Because of corresponding to the innovative part of the project and having mobilized a major amount of the efforts spent during this PhD training period, this field gave its name to the thesis project.

This division is reflected in this thesis manuscript structure and in particular in the apparent disproportion between the corresponding parts. However, their respective volume does not scale as the amount of time and energy mobilized for their realization. This is inherent to any experimental work where overcoming an obstacle often demand an investment in time that can be hardly rendered in a dissertation.

In addition to these three fields, we gathered in part I some informations we found useful from an epistemological point of view regarding the choice of the characterization tools used in the frame of time and frequency metrology. Indeed, there is a large consensus nowadays about the standard tool box shared by most of the actors of the field world wide. However, we found relevant to question the reason of the historical convergence towards these particular set of tools which is vary rarely discussed within the community. Part I hosts as well some basics definitions required for the understanding of the whole work presented here.

## 1.1 Clock operation activities

In this field enters a wide range of tasks relating to the milestones of the S.I. second re-definition roadmap, centered around continental scale clocks comparison campaigns and contribution to TAI (part III). This includes a long list of localized modifications implemented on the clock setup such as setting up new laser sources, new routing of the different lights involved in the process and modifications of some sub-systems integrated into the full room-size experiment, all of them enabling new functionalities, possibilities and higher versatility of the whole clock system. We note that in spite of this improvements, operating the clock over durations of the order of a few days or weeks, as required during the comparison campaigns[1] or contribution to TAI[2], remains a challenge and our two clocks had to be human attended during days and nights during these periods.

## 1.2 Systematics investigation and assessment

Assessment of the systematics effects is in principle an unavoidable step in the preparation of clock comparisons and contribution to TAI and could be included *a priori* into the clock operations activities. In this manuscript, we single it out as a field in its own because of the unexpected development they induced. We focus on two particular such effects: hyperpolarizability and hot collisions shift (part II).

Regarding the hyperpolarizability (section 5), our choice to expose its theoretical background aims mainly at bringing the topic closer to what is usually accessible from a standard academic training as provided at the university and in particular in clarifying the reasons why such an effect is dealt with within the formalism of tensors. From a classical picture point of view, the development can be schematized in the following way. The polarization of a medium under the effect of an external electric field is expected to be describable, in its most general form, as a power expansion in the field amplitude vector components. The natural mathematical tool to address this description is the tensorial formalism. We then define general tensors and work out some simplifications typically based on particular symmetries

[1] Gathering enough data for a reliable statistical assessment the clock comparison typically requires running the clocks over a few weeks with at least 50% of operational *uptime*

[2] Contributing to TAI requires running the clock without any interruption over 5 days

of the considered medium. In the quantum picture, the tensorial structure emerges in a different way. It is not imposed *a priori* but emerges mathematically from the perturbative treatment of the atom-field interaction in its dipole approximation. Tracing this emergence has been the main motivation for the inclusion of a theoretical derivation of the polarizability and the hyperpolarizability in this manuscript.

For the hot collisions shift (section 6), we report the first measurement of the effect on a strontium optical lattice clock, justifying the presence of a dedicated chapter. Moreover, we propose a theoretical treatment of the phenomenon. This proposal aims at completing the few theoretical treatments published so far on this subject for the particular case of lattice clocks. As exposed in the dedicated section, our model gives a synthesis of the two models available in the literature, giving us some confidence in our approach.

## 1.3 Non-destructive detection

At the heart of the project lays the implementation of a non-destructive detection system of the atoms trapped in the lattice used for the clock interrogation (part IV). There are two reasons we want to set such a system.

First, in its classical non-destructivity operation (section 11), this detection projects each atom onto the clock ground or excited state and allows for the counting of the trapped atoms being in the clock ground states without heating them up sufficiently to be expelled out of the trap, whereas standards fluorescence detection systems such as that we used so far do. Hence, the atoms can be *recycled* for the next clock interrogation avoiding having to reload the lattice trap with new atoms (see section 4.4.3 for details about the clock operation), resulting in an increase of the duty cycle, itself leading to a reduction of the Dick effect (see section 8.1), currently limiting our clock stability. We report in this thesis on the realization of such a system (section 12.4) along with its characterization in terms of signal and noise analysis as well as a full mathematical derivation of the relevant quantities. It is in this context that we study the trap destruction mechanisms (section 9.2) and that we characterize two others detection systems at our disposal, allowing for a comparison between all of them (section 10).

Second, in its quantum non-destructivity regime (section 14), the system allows for the reading of the atoms states without projection, or at least with only a few projections occurring, allowing for the overcoming of the quantum projection noise (see section 8.2) which is expected to be the next stability limitation once the Dick effect is sufficiently reduced. We report on the design, setting and preliminary results of a detection system inspired from that with which we achieved the classical non-destructivity and expected to fulfill the requirements of the quantum non-destructivity. We as well indicate some prospects and investigation tracks that we think would be the next step for the implementation of this system in an efficient form.

# 2 Time scales and standards, a historical introduction

## 2.1 Twelve hours in the night

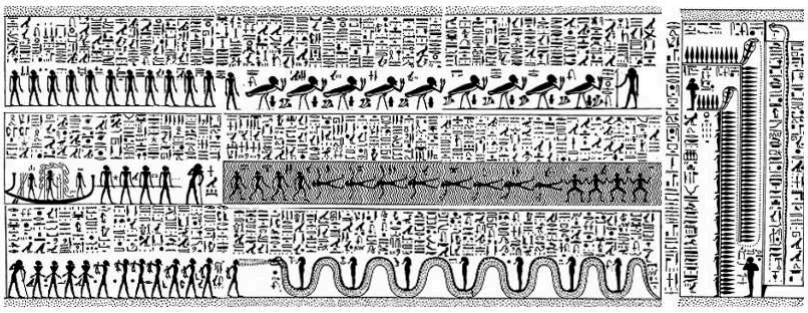

Figure 1: The 9$^{th}$ "hour" of the ancient Egyptians' *Book Of Gates*. For ancient Egyptians, death was as a night separating two lives. Emerging into the new life required passing through twelves gates, each of which symbolizing one of the twelves hours of the whole night. This was symbolically equivalent to the twelves hours the Sun, then considered a god, had to vanquish to resuscitate each morning.

"Before any creation, she was. When there was nothing, she was. When the chaos was king, she was. When the chaos became order, she was. [...] Condensed in the aethers, she is the light. Condensed in the matter, she is the heat. Condensed in the bodies, she is the motion". It is striking to realize how this statement would match the modern theory of universe History and one of our most fundamental physical concepts if one would rephrase it with "energy" instead of "she". To be more accurate, modern conceptions of universe make meaningless any reference to times before its birth, as well as an empty space-time decoupled from matter, meaning the first two sentences of the above quote are irrelevant for a modern representation. However, this unalterable presence suggests the idea of a conserved quantity immutably present to the world. The two next sentences about the chaos and its end when converted into order recall modern conceptions where the universe evolution through symmetry breakings goes from a homogeneous substance where all forms of energy are undifferentiated towards a more structured system. The different forms energy can endorse in the ordered phase are given with an impressive relevance in the second half of the quote where the light in the eathers recalls the electromagnetic radiation in vacuum, that is to say the form endorsed by energy when embodied into the void space, the heat within pieces of matter being actually conform to a thermodynamics picture and the energy stored in bodies as motion being nothing but the kinetic energy. We note that, obviously, there is nothing such as a concept of mass-energy equivalence principle or that of a space-time shaped by energy-mass distribution, markers of one of the XX$^{th}$ century great conceptual revolutions, nor of anything that would resemble the idea of quanta, witnesses of an other great conceptual revolution that took place within the same period. It is nevertheless surprising that moved by their own sens of poetry and their mythological representation of the world combined to their advanced mathematical skills, the ancient Egyptians, who wrote the *Book of the Dead* containing the *Book of the Gates* divided in twelve *Hours*, from where stems the quote, produced some pictures tending towards such conceptions. One can read, in the 9$^{th}$ Gate (or Hour) chapter "Duration, height, expanse: I have them in my becoming." where both the concepts of space-time and of its evolution are gathered. This idea of a space-time emerging out a primordial homogeneous system is even rendered in a picture of high poetic sensitivity at the 7$^{th}$ Gate stage as "I am one of the sparrowhawks whose eye, never dazzled, opens onto the four corners of the horizon and knows the depths of the primordial water." where the four corners could be seen as the undifferentiated four dimensions enclosing the universe and where the primordial water suggests the primordial universe. Even more astonishing is this combination of mythology, geometry, astronomy and poetic tastes found at the 9$^{th}$ Hour in "I traced the light pathway. I flew throughout the planetary spaces, the worlds convexity and the holly constellation of Sahu." where the light pathways and the worlds convexity sounds like a description of space-time curvature. Knowing that the glass produced by the ancient Egyptians was opaque, the flowing through the glass horizon could even be seen as an evocation of the possibility of a physical universe larger than the observable one. Finally, it is worth quoting the opening of the last Hour "I am a parcel among the parcels of the great incandescent soul." that gives a quantization taste to the driving soul of the universe evolution, its

total conserved energy.

It would of course be meaningless claiming that this excerpts might be the witnesses of an advanced scientific scaffolding erected by the ancient Egyptians that could compete with our current understanding of the physical laws of nature. How suggestive could be the pictures they provide, it is quite clear that the interpretations given above are driven by our current knowledge and not the opposite. Nevertheless, the development of scientific knowledge is a process with memory. This means that even in the case of conceptual revolutions, our knowledge at a given time is always built on that inherited from the past, remote or recent and thus always keeps trace of that previous representations, as a negative or a positive imprint. Some of the inherited representations and conceptions are so deeply entangled with the underlaying structure of that knowledge that it is almost impossible to get rid of them without threatening the stability of the whole establishment. Some of these mythological pre-scientific pictures are fed by our daily experience and thus are constantly reinforced and the efforts to provide in order not to be biased by them is most of the time unaffordable. As an example, our daily experience of the world reinforces the intuition that everything has a beginning, a period of development or expansion, followed by a phase of decline or contraction and, finally, and end. Most mythological systems enclose the universe between its creation and its final annihilation. It is interesting to note that as soon as our modern scientific representation of the world could break the mythological bolts, instead of moving freely to new representations, it adopted the same scheme, at least in the wide spread Big Bang - Big Crunch narrative. The previous example highlight what might be a conceptual lock rooted in some collective psychological edification mediated by the fact every body shares some common experiences of the world such as the rise and fall of the sun in the sky, the human life course from the birth till the death and many others. Other locks are based on more practical roots. During the First Republic that emerged from the French Revolution in the late XVIII$^{\text{th}}$ century, a decimal division of the day was adopted. Beyond the fact that equally dividing the perimeter of a circle by 12 is much easier than by 10, and that the graduation for a division by 10 does not make the four cardinal points appear on the quadrant, it seems the main reason why this switch was a failure is the unaffordable cost of the physical modifications to be carried out on the mechanism of each clock on the national territory.

But why did the History set the clocks on the rail of the 12 hours division of days and nights? It seems we inherited the duodecimal counting system from the Babylonians or possibly from the Sumerians, who used to count, as us, using their fingers. Does this means their biological package provided them with six fingers per hand instead of the today wide-spread five fingers hands? A more probable explanation is that they used the tip of their thumb, standing in opposition to the other four fingers of the same hand, making it hopping from a phalanx to an other. Having three phalanxes for each of the four fingers used to count, they naturally developed a duodecimal basis for numeration. We then understand why they spontaneously divided the day (understood as the connected interval of time over which the sun is above the horizon) and the night into twelve sub-intervals, the hours. The division of the day was based on the observation of the position of the sun in its course. Since the length of the day, as defined above, varies over the seasons, the length of the hours did as well. The shorter the days, the longer the nights. Hence the day's hours where equivalent to that of the night at the equinoxes only. Basic sundials were sufficient to provide this division, thanks to the sun orbit in the sky. But how could they keep their time over the night?

Figure 2: Ancient Egypt heliacal calendar. Each column contains the 12 stars (or group of stars) visible over the night as a function of the earth position on its orbit around the sun and corresponds to a period of 10 days (or one decanate). Every 10 days a new star is visible and another one disappear from the night sky.

As said earlier, the *Book of the Gates* is part of a larger corpus, the *Book of the Dead*. According to the believes of that time the Sun, then considered a god, was dying each night and resuscitated every morning. This resurrection was not granted each time and the Sun had to fight and vanquish, one

after the other, each of the twelves hours of the night. This struggle was reproducing symbolically what was believed to be the way for humans from life to death, considered a new life, separated from the former, as in the case of the Sun, by a night of twelve hours. To each hour of this "night" corresponded a gate at which each human had to pass a proof. The metrological interest of the Egyptian division of the night into twelve equivalent hours is that, in opposition to the Sumerians and Babylonians for which, having developed tools based on visible sun position in the sky, the night division was nothing but an impracticable abstraction, they found a way to realize it. They could achieve this observing the heliacal rise of stars. A star makes its heliacal rise when it pops up just above the horizon at dawn and directly vanishes in the strengthening sun light. The Egyptian year amounted to 360 days divided into 36 decanates of 10 days each. Each decanate was associated to a star[3] itself called the same way as the corresponding decanate. These 36 stars are aligned on the celestial archway within a strip such that each of them make a heliacal rise during the 10 days of the corresponding decanate, i.e. its rising happens approximately at the same place and time as the sun rise during this 10 days period. We then have 36 stars aligned in the sky rising one after the other at roughly regular time interval. Of course, their risings are visible during the night only. The number of total rising decanate stars during one night varies over the year but is always larger or equal to twelve. This means that, within each decanate, an observer can see roughly the same set of 12 stars rising at regular interval during the night. This risings are slowly shifted and occur earlier from night to night, till the point when the earliest rising star of the decanate occurs to early to be visible, i.e. occurs before sun set, and when a new star of the strip starts to have its rising happening sufficiently early to be visible at the very end of the night. This corresponds to entering into the next decanate. Therfore, the succesive risings of the decanate stars of the corresponding period of the year could be used as a twelve hours clock keeping the time over the night. They somehow found a way to keep track of the sun clock during periods where this clock was inaccessible. More than that, since the set of stars rising during the night changes over the year, this heliacal clock links the local time of the succession of the hours to that of the calendar. In other words, looking at the rising decanate stars, one can know what time it is at the scale of the daily earth spinning period as well as the date at the scale of the yearly orbiting period of the earth around the sun. This is, in a very simplified scheme, what time keepers, such a s astronomers or modern time and frequency metrologists, have been achieving over the past centuries. Astronomers had to build clocks, typically clepsydras, then pendula and more recently quartz oscillators, providing short time scales that had to be regularly synchronized to astronomical events in order to keep them on time with the walk of stars, i.e. not to diverge from the long scale useful timing provided by the cycle of the seasons. On the other hand, time and frequency metrologist regularly steer the frequency of the laser they use as a local oscillator after comparing it to the frequency of an atomic or ionic narrow transition.

## 2.2 Calendars, time units and time scales

At early stages of the technical development of humanity such as the periods referred to above, spreading roughly from -5000 to -1500 one can imagine three types of uses of clocks requiring different features depending on the time scale involved. Considering agricultural activities and farming, it was very important to be able to locate the current date within the seasons cycle with an accuracy of a few days. This kind of clocks, referenced to the cycle of the orbiting of the earth around the sun with an accuracy of a few percents, are referred to as calendars. Advanced calendars were already available at that early times, including a precisely managed adjustment of the number of days per year to account for the incommensurability of the earth spinning period, i.e. the duration of the days, to the orbiting period, i.e. the duration of a year. At the other side of the scale, regarding much shorter time intervals, mastering technical processes such as iron melting and crockery cooking required a timing reproducibility of the order of the second or at least the minute. Half way between this two scales lays the typical clocking requirement for organizing the *working* days of the slave mass as well as the political and cultual life. The success, at least in term of political power, of the ancient Egyptians over their close neighbors is probably partially due to their mastering of time from the short to the long scales. This might be the reason why sarchophagi of some of the most proeminent Pharaos of the upper Empire period display clear representations of both stellar clocks, such as the one presented above and providing very good calendars, beside clepsydras, also called water clocks, adressing timing at the scale of the second or minute.

There however is a deep difference between a calendar type clock and a clock providing a local timing at a scale very short compared to that of the earth orbiting period around the sun. Indeed, the only

[3] or group of stars

requirement for a clepsydra providing timing of the order of a few seconds, minutes or even hours, is to provide, each time the device is used, a time interval, that would not depart from the best possible duration necessary for the particular purpose for which it is used. Somehow the usage of such clocks is discrete, not continuous, meaning there is no requirement about the departure of the sum of all the successive timings it provides from any time interval reference. On the other hand this is not what is expected from a calendar which is supposed to provide a dating at the scale of the day while keeping in phase with the stars over decades and even centuries, i.e. accurate at the level of their unit when integrated over several thousands of units. In other words, a calendar should never miss a day, whereas a clepsydra might contract a second or a minute if used for to long.

This fundamental difference can be grasped saying calendars are used for labeling events on a time axis, whereas time units, or standards, are used to measure or provide calibrated durations with a given tolerance. The two concepts lived for a while separate lives, meaning that the time intervals one could obtain repeating the operation of a clock providing the time unit were not in well defined relationships with time intervals defined as separating events labeled on the calendar. In other words, there was no way to build the calendar just by agreeing about a starting date and piling up successive realizations of the time unit as provided by successive operation of the clock. Eventhough such a process would have been possible for a short duration of the order of a few time units, then the two scales, that given by the calendar and that given by the beginning of each successive units provided by the clock would diverge very fast and their relations after a while would be totally randomized. A time scale can be viewed as a synthesis of a calendar and a clock realizing a duration standard. It is a time labelling system obtained by successively adding to fixed origin the time units provided by a clock. Somehow, it is a calendar built not from the apparent motion of stars, but from a clock that never runs out of time with that motion. In other words, a calendar is a top-down device building sub-units from a long range master unit, typically a full year or even longer, while a time scale is a bottom→up designed device building long time super-units as a sum of fundamental units, such that this super-units always be in agreement with some external phyisical phenomenon of reference such as given positions of stars in the sky.

Things went on this way for a while, i.e. with calendars addressing long time scales while keeping in phase with astral phenomena and shorten time units addressed by clocks whose integrated cycles would strongly diverge from a clock to another. The two realms started to get entangled with the development of far off shore long range shipping, especially under the British empire impulse for ruling seas and oceans and establishing reliable see routes for worldwide trading.

## 2.3 Universal Time

Using clocks to master timing is based on the intuition of the reproducibility of the time interval provided by a clock, equal to itself when reiterated. Poincaré expressed this intuition writing "When we use a pendulum to measure time [...] we implicitly assume [...] that the durations of two identical phenomena are the same, or, [equivalently], that the same causes take the same time to produce the same effect". This invariance of time durations under translation along the time arrow is some times referred to as the uniformity of time. Inherited from the old Greeks, it has been believed for centuries, even by Copernicus, that the spinning of the earth was perfectly uniform and would thus provide a perfect clock in the meaning of Poincaré, i.e. the spinning would be in perfect adequacy with the uniformity of the time flow. The early definition of *True Solar Time* was based on this assumed uniformity of earth spinning. The length of the day was just defined as the time interval separating two passings of the sun through the plane defined by the local meridian[4]. It was from the ancients that, because of the spinning rotation axis of the earth is not normal to the plane containing its orbiting along the sun, the ecliptic plane, combined to the small ellipticity of its orbit expressed by Kepler's law of areas, this duration would vary over the year. But this variation were predictable and the corrections, of a maximal magnitude of 30 minutes, were known as the *equation of times* since long ago. The corrected then obtained is the *Mean Solar Time*. This effect, due simply to the geometry of the system, was not challenging the idea of a perfectly uniform spinning of the earth. This corrected time is called *Mean Solar Time*. The second was then defined as 1 s = 1/86 400 mean solar day. But why this requirement of a second commensurable to the length of the day? There are probably many different causes adding up together to converge to this requirement,

[4]The True Solar Time is defined as the angle between the half-plane of the local meridian and the half plane formed by the earth spinning axis and the center of the sun, with the conversion $15^\circ = 1$ hour, i.e. $360^\circ = 24$ hours

but it seems a determinant one was the fact that a clock beating synchronously with the days was a determinant factor for improvement in long range navigation techniques. Longitude was obtained using a sextant by measuring the angle between the local zenith and the direction of some distant stars. The ensemble of points corresponding to this given angle and chosen star is a circle at the surface of the globe. Pointing towards an other star gives a second circle, the right location corresponding to one of the two intersections with the first circle. A third pointing could even lift the remaining ambiguity. But this location is not well define since it does not distinguish between different phases of the earth spinning. The absolute position of the obtained point relative to some longitude origin on the earth surface depends on the timing difference between the ship longitude and the longitude origin, typically defined as the Greenwich meridian. The local timing was given by the Mean Solar Time as measured on the ship, but the timing at the origin meridian had to be provided on board by a clock, typically a pendulum. This clock had been synchronized with Greenwich solar mean time before starting its trip. But few days, weeks or even months later, it has to give on board the solar time of Greenwich. The ship clock was of course drifting away from the local Greenwich timing, and a big deal of efforts were made to minimize this drift, that would result in errors on the ship location.

This gives an illustration of the concept of *Universal Time*. Indeed, the time provided by the pendulum clock on board is, up to inevitable drifts and discrepancies due to technological limitations, equal to the mean solar time in Greenwich. One can imagine a very large set of such pendulum clocks, initially located in Greenwich and synchronized to its mean solar time and then dispatch all over the world that would reproduce the Greenwich mean solar time scale anywhere the are. This means the mean solar time of Greenwich (GMT) would be universally accessible locally anywhere on the globe. This is precisely the definition of *Universal Time* (UT): a time scale based on the earth spinning referenced to a given meridian. The idea is then that of a master clock, the mean solar time given by the earth spinning, in it self universal since the sun apparent motion is observable at any location on the earth, but referenced to a particular preferred meridian, that clocks dispatched over the world tries to produce locally. Because most of the maritime maps where drawn by the British Empire, with Greenwich as a reference for the compuutation of the longitude, it was agreed by most of the participants at an international conference that UT would be given by GMT shifted by 12 hours to account for the fact that the first hour of the day on the mean solar time scale coincides with having the sun at the zenith, whereas the UT is defined in such a way it is 12 o'clock when the sun passes through the reference meridian.

Note that this definition implicitly assumes it conceptually makes sens to consider that a global, universal time scale can be read directly on local clocks without any transformations. Such an assumption is actually reminiscent from the Newtonian conception of space-time where the simultaneity of two events is defined absolutely and does not depend on the frame from where the events are looked at.

## 2.4 Newtonian and post-Newtonian time scales

### 2.4.1 Coordinates systems in use

As will be seen in the next paragraphs, giving up the concept of an absolute time takes the reference frame and its coordinates systems to the foreground in the time scale building play. We then briefly introduce the three systems of coordinates preferably used by astronomers and spacial engineers, depending of the problem considered. The International Astronomical Union recommends the use of three coordinates systems: non-rotating heliocentric, non-rotating geocentric and rotating geocentric. The axis of the non-rotating frames are defined relatively to a frame determined by a set of nearly 600 quasars. They are of poor interests for our time scale building purposes and we will focus on the geocentric rotating system which is fixed relatively to the lithospheric mantel frame, itself based on the positions of about 200 sites spread at the surface of the earth. Note that this definition is adjusted in order to take into account variations in the relative positions of these sites due to tectonic activities of the mantel.

### 2.4.2 The Newtonian absolute time scale

Within the frame of Newtonian space-time conception, the time interval separating two events is absolute meaning it is intrinsic to this pair of events and does not depends on the particular referential frame of the observer. The simultaneity relationship between events is then absolute as well, two events being simultaneous when the absolute time interval separating them vanishes.It is then conceptually valid to imagine a set of clocks spread in space ticking simultaneously with a master clock, that of the GMT scale

for example. But, allowed by critical improvement of measurment instrumentation in the late XIX$^{\text{th}}$, careful measurements showed in the early XX$^{\text{th}}$ this conception failed to account for some observations, leading to the conceptual breach of the Special and later General Relativity. It is interesting that despite this discoveries date back to the early XX$^{\text{th}}$, relativistic effects did not reach the time metrology realm before 1980, up till when a Newtonian based definition of the UT scale was kept.

### 2.4.3 The Special Relativity time scale

Within the frame of Special Relativity, the time is no longer absolute and the only timing observable quantity experimentally accessible to an observer is the proper time of the clock he or she is attached to. A time scale is then defined as a coordinate $t$ shared by users, along with a set of rules to transform $t$ into the local proper time $\tau$ of each user an *vice versa*. In Special Relativity the concept of simultaneity is still valid but not absolute, in the meaning that the set of all simultaneous events depends on the reference frame from where the universe is looked at. Some particular frames, the inertial frames are such that it is possible to endow each of them with a time coordinate equal to the proper time of the clocks rigidly attached to it, i.e. such that $t = \tau$, the clocks being synchronized according to the Einstein synchronization convention. However, in the general case of a reference frame not necessarily inertial, the time scale has to be provided along with the transformation $t \longleftrightarrow \tau$ usually expressed in one of its differential or integral forms

$$\frac{d\tau}{dt} = 1 - h(t) \qquad \text{or} \qquad \Delta(t-\tau) = \int_{t_0}^{t} h(t')dt' \tag{1}$$

It turns out that the effect of the spinning is of the order $h(t) \lesssim 10^{-18}$ at distances $d \lesssim 3 \times 10^{18}$ m relative to the earth rotation axis.

### 2.4.4 General Relativity time scale

The possibility of having certain frames, the inertial ones, within which it is possible to define a time coordinate coinciding with the proper time of the clocks rigidly attached to it is due to the fact that the geometry of the SR space-time is flat. In other words, the local expression giving the invariant interval $ds$ as a function of the coordinates at a given location of the space-time

$$ds^2 = g_{\alpha\beta}(x^\mu)dx^\alpha dx^\beta \tag{2}$$

does actually not depend on the particular location $x^\mu$. This property is expressed saying the SR metric is flat and the formula

$$ds^2 = c^2dt^2 - \sum_i dx_i^2 \tag{3}$$

is valid over the whole space-time. In the frame of General Relativity, no such simplification holds and the more general formula 2 has to be considered. This means that the time coordinate to proper time transformation $t \longleftrightarrow \tau$ not only depends on the choice of coordinate system and frame but varies from point to point within a given system. The main difference with the Special Relativity case is that the metric given by 2 depends on the mass-energy distribution resulting in a dependence on the local gravitational potential and its gradient, including tide effects. The effect of the gravitational potential is of the order of $7 \times 10^{-10}$ at the geoid. The effect of the gradient of the gravitational field amounts to circa $10^{-16}$ per meter around the geoid. The tide effect induced by the sun and the moon is of the order of $10^{-17}$ at the surface of the earth but increases when going further away, reaching $10^{-15}$ at the distance $d \sim 36000$ km of geostationary satellites. This means the mismatch between the coordinate time $t$ and the proper time $\tau$ of a clock on the geoid is dominated by an effect amounting to $7 \times 10^{-10}$ resulting in a shift of 22 ms per year.

## 2.5 Coordinated universal times

### 2.5.1 International time scales in practice

In 1910 clocks signals realizing UT locally in Europe and in the U.S.A. are broadcast over the ocean and compared. While local estimation of their timing error are of the order of a few hundredths of a second, their comparison gives discrepancies up to one or two seconds. Meaning that a uniquely defined UT gives rise to contradictory realizations. In order to unify the UT realizations at the international scale,

the *Bureau international de l'heure* (BIH, time international office) is mandated to produce the so-called *definitive time* and to provide at the worldwide scale the best approximation of the UT. To do so the BIH collects the timing signals broadcast by several laboratories and institutions over the world, computes a weighted average out of them, and then send to each source its timing difference relative to this average. As will be seen later, this is still the way the current atomic standard based time scale is realized.

### 2.5.2 Universal time scales and atomic standards

In the first half of the XX$^{\text{th}}$ century most of the timing signals are provided by quartz oscillators. In 1949 is demonstrated the first oscillator referenced to an atomic transition [39] (see section 4.1 for atomic clocks working principles or [12]). A few years later they are used to interpolate and correct quartz oscillators, and the BIH starts the same year an atomic time scale, the *Integrated atomic time* (AT), a perfect example of the time scale definition given in section 2.2: a time labeling system obtained piling successive realizations of a time units from an agreed-upon origin. A way was found to benefit from the high uniformity of the atomic based AT scale while keeping the definition of UT as GMT-12h. The time unit provided by the atomic standards was not commensurate to the astronomical cycles defining UT so it was decided to realize UT based on AT but adding or subtracting now and then a fraction of a second, in order to keep this modified AT scale, called *Coordinated Universal Time* (UTC[5]) always within less than 0.05 s away from UT[6]. In 1965 the BIH officially defines UTC as

$$UTC - AT = y_U(AT - AT_0) + B \tag{4}$$

where $B$ is now and then discontinuously in order to keep $|UTC - UT| < 0.05$ s and where $y_U$ accounts for the fact that, as mentioned at the very end of sec 2.4.4, the gravitational potential due to the mass of the earth results in a 22 ms shift between local proper time and the time coordinate associated to the rotating geocentric system per year. $AT_0$ is just an agreed-upon origin from when AT is integrated.

## 2.6 International Atomic Time

In 1970 the BIH defines the *International Atomic Time* (TAI) scale, validated one year later at the 14$^{\text{th}}$ *Conférence Générale des Poids et Mesures*. This is nothing more than an official version of the previous AT scale accounting for the newly adopted definition of the second in the *International System* (S.I.) of units as based on a well defined atomic transition (see hereafter section 2.7.2). At this occasion UTC as well is redefined. It still given as in equation 4 but with TAI instead of AT and $y_U = 0$. The changings of $B$ are simplified as well and $B$ now has to be equal to an integer multiple of the S.I. second and is modified around once a year. The divergence relative to UT tolerance is as well changed to $|UTC - UT| < 0.9$ s. Note that while AT was thought of as, somehow, an atomic realization of UTC, TAI is conceived as realization of the *Terrestrial Time* (TT), defined as UTC minus the drift of 22 ms per year at the geoid due to the gravitational potential (see section 2.4).

### 2.6.1 Relativistic TAI

At their outset, the first atomic time standards hardly reached the level of $10^{-12}$ relative uncertainty, three orders of magnitude higher than what would be necessary to see the first relativistic corrections to the Newtonian space-time picture (see section 2.4, the 22 ms per year drift at the geoid having been absorbed in the definition of TT whose TAI is a realization). In the late 1970's, cesium standard improvements took their relative uncertainties to levels as low as a few $10^{-16}$. This means that frequency shifts due to height difference of the order of a few meters started to be detectable as well as tide effects at the scale of geostationary satellite communication. This required a new definition of TAI accounting for RG metric. With this new definition, TAI is then a time coordinate based on the S.I. atomic second obtained combining the proper times of the contributing clocks according to an agreed-upon metric. Again, as being a time coordinate, the TAI is given in S.I. units but a TAI second at a given point is not equal to the S.I. second realized as the proper time of a cock at that point, the relation between the two being precisely given by the agreed-upon metric, which depends on the particular point location, except on the geoid, where the TAI time coordinate coincides with the proper time (due to the fact that TAI is a realization of TT and not of UTC).

[5] should be CUT in English and TUC in French. A compromise was found as UTC

[6] Actually, the tolerance was 0.1 s from 1960 to 1963 and then moved to 0.05 S from 1963 to 1971

## 2.7 From a second to an other

### 2.7.1 The ephemeris second

Impulsed by the development of worldwide market and resulting need in accurate stable clocks for large range shipping, better and better clocks where available for the astronomers too, that could refine the time labelling, or dating, of their observation. They typically calibrated or tuned their clocks during the day comparing their timings with that given by the apparent motion of the sun, i.e. the mean solar time, and then let them run during the night and used them to label night observations. The day after, the clock were still running and a small discrepancy between their readings and the solar mean time, again accessible since the sun rise, was measurable and could be used to post-process the observation made during the night and correct their time labelling. But with the increased performance of the available clocks, fine instabilities in the earth spinning could no longer be ignored. The reasoning was then as follows. The absolute Newtonian time being perfectly uniform and being an element of the reality of the world, meaning it is a real thing and not just a commode abstraction for calculation, if the spinning is itself perfectly uniform , it is a realization of this absolute time scale. Therefore, any prediction based on the solution of Newtonian mechanics equations of motion using the mean solar time as time scale would provide the exact trajectories of celestial bodies. But in the second half of the XIX$^{\text{th}}$ century S. Newcomb discovered, studying carefully the ephemeris tables giving the relative position of earth, sun, and moon, discrepancies too large to be explained by computational errors. In 1929 Danjon proposed to correct the time used in the scale of the ephemeris by the amount that would make the observation matching the Newtonian mechanics based predictions. This allowed a redefinition of the second adopted later in 1960, which had till then be defined as 1/86 400 of a mean solar day. More precisely, the ephemeris second is defined as 1 s = 1/31 556 952.9747 of the 1900 tropical year[7].

### 2.7.2 The atomic second

As early as the late XIX$^{\text{th}}$ century Maxwell [6] voiced the idea that the wavelength and period of spectral lines of atoms or molecules could be used as standards for length and time. Less than one century later, the first atomic clock based on an ammonia absorption line around 24 GHz was demonstrated at the National Bureau of Standards in the U.S.. In 1955 the first atomic clock with an uncertainty better than the best quartz oscillators of the time was demonstrated in U.K. and directly started to contribute to the *integrated atomic time* (see section 2.5.2 above) held by the BIH. In 1967, less than two decades later, the best atomic clocks routinely achieved a relative accuracy of roughly $10^{-12}$, far better than any quartz oscillator could achieve. The second was then redefined as *the duration 9 192 631 770 periods of the radiation corresponding to the transition between the two hyperfine levels of the ground state of the cesium-133 atom.* This choice was made in such a way that the new second would correspond to the mean solar day based second averaged over the XVIII$^{\text{th}}$ and XIX$^{\text{th}}$ century. The TAI scale definition of 1970 by the BIH (see section 2.6) aims precisely at taking advantage of this more accurate and stable standard.

### 2.7.3 Discrepancy between the S.I. time unit and the unit of the time scale

It is interesting to note that from 1960 to 1967 the S.I. time unit is the ephemeris second and from 1967 on is the cesium-133 second, whereas the official time scale from 1960 to 1971 is the UT scale based on the mean solar day. Hence, the time scale broadcast by the BIH is given in mean solar day second and not in S.I. second. This discrepancy is resolved in 1971 when the BIH adopted the TAI as global time scale, i.e. a scale based on the S.I. second.

### 2.7.4 Towards a new definition

It was anticipated at the very begining of the XXI$^{\text{th}}$ century (in 2001, see [1]) that thanks to recent developments and improvements in the fields of microwave sources, laser sources, optical combs and high precision spectroscopy, other microwave and optical frequency standards would have soon reached the level of stability, accuracy, and uncertainty of the 1967 recognized Caesium standards. It was then decided to establish a list of *secondary representations of the second* (SRS), each of which realizing the S.I. second at at least the same level of stability and accuracy[8] while keeping the Caesium transition as

[7] A tropical year is defined as the time interval separating two passings of th sun at the vernal point. The vernal point being the intersection of the projection of the equator on the celestial sphere and the ecliptic plane

[8] the precise requirement actually is for the uncertainty to be not worse than one order of magnitude than the best Caesium standard at the date.

the unique official definition, the list being regularly updated in order to take new possible references into account, as it was the case with the $^{87}$Sr clock transition at 698 nm, on which is based the work carried out in the frame of this thesis, in 2005. It turned out a few years later that some SRS based on neutral atoms and ions optical transitions outperformed the Caesium standard in terms of both stability and accuracy, the projective uncertainties being evaluated thanks to the use of a continental scale fiber links network whose uncertainties have be shown to reach the $10^{-20}$ level, and are thus not limiting the estimation of the compared clocks uncertainties. Indeed, such efficient links combined to improvements of available frequency combs in the optical range allowed comparison between clocks based on different species and have led to the measurements of frequency ratios at the level of $10^{-18}$.

In order to harmonize and set a systematical procedure for the updating of the SRS list the *Consultative Comitee for Time and Frequency* (CCTF) established a set of rules each publication of a new estimate of a given transition frequency or of a frequency ratio has to fulfill to be taken into account and eventually added to the SRS list, such as being published in a peer-reviewed international scientific journals. Further, the uncertainty published along with the frequency value measurement is re-evaluated by the CCTF using a Baysian statistical approach account for all the informations relative to this transition available in earlier publications. When several published values are available, the value adopted is a weighted sum. The complete list of criteria and procedures is available in [2]. In principle, the evaluation of the absolute frequency of a candidate SRS transition should, by definition, rely on a direct comparison with a Caesium standard, i.e. should consist in a frequency ration measurement of the candidate transition frequency to that of the S.I. standard. However, as mentioned above, some optical-optical frequency ratio measurement outperform the uncertainties allowed by the limited uncertainty of the best Caesium standards. Such measurements, together with direct comparison to caesium standards resulting in an over-determined set of values for the considered transitions. Two schemes have been proposed to determined the best estimate of the corresponding frequencies taking advantage of this over-determination, one based on a nonlinear least method [3], the other on a close loop analysis in the frame of a graph theory approach [4]. Rules to calculate and estimate correlations in the measurements involved in the computation of the best estimate of frequency ratios by these two methods have been developed and are currently being reinforced to account for finer correlations effect due specifically to the use of fiber links network.

Right from its outset in 2001t, the SRS list had been establish in the perspective of a potential future redefinition of the S.I. second and for the realization of a better TAI scale. There is indeed a growing community that would benefit of the redefinition of the S.I. second based on an optical transition. As explained in section 2.5.1, the realization of a time scale relies on the contribution of several clocks dispatched at the surface of the globe, whose timing signals are averaged with a given weighting resulting in the time coordinate to be broadcast. Hence, outperforming the current Caesium standard is not sufficient to bring the redefinition of the S.I. second onto the table as a realistic project. Reproducibility of such performances as well as regular contributions to the TAI are unavoidable preliminaries to make such a redefinition a serious question. It is in this perspective the SYRTE realized the first contribution of a $^{97}$Sr clock to the TAI in 2016 as reported in [78], contribution to which I personally participated. In order to clarify the route towards this increasingly relevant redefinition of the S.I. second based on an optical transition the CCTF has devised a *roadmap* delineated by the five following milestones [2]:

1. at least three different optical clocks (either in different laboratories, or of different species) have demonstrated validated uncertainties of about two orders of magnitude better than the best Cs atomic clocks of the time.

2. at least three independent measurements of at least one optical clock from milestone 1. have been compared in different institutes with a relative frequency uncertainty $\Delta\nu/\nu < 5 \times 10^{-18}$ either by transportable clocks, advanced links, or frequency ratio closures.

3. three independent measurements of the optical frequency standards of milestone 1 with three independent Cs primary clocks have been performed, where the measurements are limited essentially by the uncertainty of these Cs fountain clocks with $\Delta\nu/\nu < 5 \times 10^{-16}$[9].

4. optical clocks (SRS) contribute regularly to TAI.

[9] $5 \times 10^{-16}$ being the relative uncertainty of the best Cs standards.

5. optical frequency ratios between a few (at least 5) other optical frequency standards have been performed; each ratio measured at least twice by independent laboratories and agreement was found to better than $\Delta\nu/\nu < 5 \times 10^{-18}$.

The work carried out in the frame of this thesis precisely aimed at stepping forward along this roadmap. It included studies of some systematics effects shifting the measured clock frequency from its ideal universal reference, i.e. the idealized clock transition frequency for a perfectly free atom, which understanding still needs to be clarified: the hyperpolarizability and the collision shift, that had been overlooked so far and for which we report the first measurement along with an attempt of theoretical derivation. A particular focus was made on the improving the stability of the clock by the implementation of a cavity-assisted non destructive detection of the atoms, allowing for the reduction of the current source of instability, the Dick effect, and paving the way the reduction on the next limitation, the quantum projection noise.

# Part I
# Clocks and their characterization

This first part is dedicated to the presentation of the main concepts used for the characterization of clocks (section 3) and provides the basics of atomic clocks in general as well as a presentation of the particular clock on which this thesis work has been carried out along with the operation details required for the understanding of the discussions of the following chapters (section 4).

## 3 Stability, accuracy and uncertainty

In this chapter we expose the basic tools used to characterized clocks and oscillators in general and that are used on a daily basis within the optical atomic clocks community. Section 3.1 clarifies the reason why we deal mainly with frequency in the context of atomic clocks while interested in time measurement. Very basics of the mathematical representation of oscillators, i.e. physical systems providing signals with a well defined central frequency, are given in section 3.2. Section 3.3 offers a historical perspective on the characterization of oscillators stability along with the main tool used for it: the Allan deviation. It also presents the two points of view that can be adopted: frequency-domain and time-domain description. The central concepts of accuracy and uncertainty are finally presented in sections 3.4 and 3.5.

### 3.1 Time or frequency ?

Following Poincaré's view of uniformity of time flow, building a clock would consist in finding a practical way of producing successive time units, i.e. time intervals, that, to a good level of approximation are *equal to each other*. In other words, one needs to setup and control a periodic phenomenon. In the context of this thesis, such time-periodic phenomena will be referred to as local oscillators (LO) and the corresponding measurable quantity as the LO signal. The elementary pattern of the LO signal that gets repeated over time is called an oscillation and its duration a period. A clock is then defined as a device able to count the number of oscillations of a LO signal that occurred since an agreed-upon origin. We can define two time scales over which the LO signal could be looked at, that we define using an intuitive example. If one wants to measure time durations of the order of the hour or the minute based on a solar clock[10], one needs to be able to follow the time flow at the scale of a fraction of the corresponding period. This is a very primitive vision of what could be seen as a phase measurement, i.e. the ability to follow the build up of the time unit interval itself, that is of one single LO signal oscillation, as can be done with a sundial for example by following the continuous trajectory depicted by the tip of the stick projected shadow on the reading plate. If, on the opposite, one wants to measure time lengths of the scale of the month or years, it is sufficient to count how many periods, i.e. days, have passed during this time length. Note that according to our definition given a few lines above, looking at time scale larger than the LO period only is conform to the use of a clock. However, using a clock is one thing, building it and keeping it on time an other, which may require getting involved in phase business. These two ways of looking at the LO signal, phase unfolding and periods counting, can be seen as being in a certain duality, that will be clarified a bit later. Technical advances achieved over the last centuries led to the possibility of engineering LO's and developing the ability to act on their time evolution at the scale of fraction of their period or to tune their periodicity. In other words, it became possible to drive their phase or their rate of phase unfolding over a large number of periods, i.e. their frequency.

Because the concept of frequency contains in itself the idea of several periods equal to each other repeated successively, it may seem advantageous to work in frequency domain instead of time domain. This is actually the case in the atomic clocks community. This means that even though our purpose is the production of sequences of time intervals of a well controlled duration, the quantity we monitor and control is the frequency of our LO. Beyond this practical reason, we see at least to other reasons to look at the things in frequency domain instead of directly in time. One is rooted in the mathematical link between the two quantities, phase and frequency, and is discussed in the next section. The second is deeper and more fundamental. Indeed, the concept of clock as providing successive time intervals of equal duration is closely linked to the idea of the uniformity of time flow. But from Hamiltonian mechanics, we know that translations in time, i.e. time evolutions of systems, are generated by the action of the

[10] i.e. based on the periodicity of the apparent motion on the sun in the sky

Hamiltonian operator, i.e. that corresponding to energy. In the quantum realm, the Schrödinger equation even directly links the rate at which the relative phases of sub-systems change over time. Henceforth, a way of producing a system whose dynamics mimics the uniformity of time flow, i.e. the uniformity of phase change rate, would be to keep its driving Hamiltonian operator constant, i.e. its energy constant. Plank's relation, stating, for some class of systems at least, the formal equivalence between frequency and energy, $E = h\nu$, might then be seen as a more fundamental expression of the relation between time intervals of equal duration, i.e. uniformity of time flow, and frequency. Hence, with Plank's relation, Schrödinger equation and Hamiltonian mechanics, it is not just because the period is mathematically the inverse of the frequency that dealing with the latter allows for a good time control of the former, but rather because a constant frequency implies a constant energy that at its turn implies a constant phase evolution rate, i.e. allows the corresponding system to mimic the uniformity of time flow.

## 3.2 Mathematical model of oscillator signals

### 3.2.1 Uniqueness of representations and Fourier frequencies

Let $s(t)$ be the fundamental physical quantity provided by our local oscillator (LO)[11], implying $s(t)$ is a real quantity. Usual mathematical representations of $s(t)$ for time and frequency analysis are of the form

$$s(t) = S(t)\sin(\Phi(t)) = \mathrm{Re}\left[e^{\gamma(t)+i\Phi(t)+\pi/2}\right] \tag{5}$$

where $S(t) > 0$, $\Phi(t)$ and $\gamma(t) = \ln(S(t))$ are real quantities. One would like to call $S$ the instantaneous amplitude of the signal and $\Phi(t)$ its instantaneous phase. However, it is clear from the second form that this representation is not unique, since it can be viewed as a one axis projection of a time dependent vector evolving in a two-dimension space. In other words, any variation of $s(t)$ might be accounted for by a change in $S(t)$ or in $\Phi(t)$[12]. As known from mathematicians, unique representation are the *chasse gardée* of vector space basis. Transporting a finite amount of energy, the integral of $|s(t)|^2$ over the whole time line is finite. Such functions actually form a vector space with a famous and useful basis, function of the form $e^{i\omega t}$. The unique decomposition of $s$ on this basis is given by its Fourier transform $F_s(\omega)$, a complex valued function, with $s(t) = \int F_s(\omega)e^{i\omega t}$. $F_s(\omega)$ being complex, one can write $F_s(\omega) = |F_s(\omega)|e^{i\phi_\omega}$, leading to $s(t) = \int |F_s(\omega)|e^{i(\Phi_\omega+\omega t)}$. $s$ then appears as a superposition of several amplitudes with phases of the form $\Phi_\omega(t) = \Phi_\omega + \omega t$, i.e. with $d\Phi_\omega(t)/dt = \omega$. There are two ideas to take away from the Fourier representation. First, one might define a frequency from the time derivative of an instantaneous phase. Hence, coming back to a representation of the form 5, one might define an instantaneous frequency of $s(t)$ as $2\pi\nu(t) = d\Phi(t)/dt$. Second, one should not get confused between the instantaneous frequency $2\pi\nu(t)$ such defined, which is uniquely determined by the choice of representation 5, and that appearing in the Fourier decomposition of $s(t)$, which are uniquely determined by $s(t)$ when given over the whole time line and which are not varying in time. To avoid confusions, the $\omega$ appearing in the Fourier decomposition are usually called Fourier frequencies, whereas that stemming from $\Phi$ are noted as $2\pi\nu$. The one we are interested in for the clock characterization is that related to an agreed-upon representation of the form 5.

Keeping in mind that we aim at building a clock, i.e. a device that provides with successive time intervals equal to each other by counting periods of an oscillator, we first note that the non-uniqueness of the representation 5 is in itself not a problem. Indeed, counting the number of periods of an oscillator might be simplistically seen as checking when the clock signal vanishes. Since $S(t) > 0$ the zeros of $s$ correspond to $\Phi(t) = n\pi$, $n$ an integer, which restricts the possible choices of $\Phi(t)$. It is possible to restrict further the choices of representations for $s$. Being roughly periodic, the Fourier frequencies of $s$ will be populated around a central value, say $\omega_s$. We then demand to the representations of $s$, i.e. to the coupled of real valued functions $(S, \Phi)$ to be such that the variations occurring over time scales larger than $T_s = 2\pi/\omega_s$ are encompassed in $S(t)$ while that occurring at shorter time scales to be endorsed by $\Phi(t)$. Further, for a given representation $(S, \Phi)$, a given time duration $T$ and a time origin $t_0$ we define $S_0$, $\delta(t)$, $\nu_0$ and $\nu(t)$ as

$$S_0 = \langle S(t)\rangle_T, \qquad \delta(t) = S(t) - S_0, \qquad 2\pi\nu(t) = \frac{d\Phi(t)}{dt}, \qquad 2\pi\nu_0 = \langle 2\pi\nu(t)\rangle_T, \qquad \varphi(t) = \Phi(t) - 2\pi\nu_0 t \tag{6}$$

[11] for a laser LO, fundamental means we consider the field amplitude and mot its intensity, even though it is the quantity directly accessible.

[12] note that the symmetry between variations in $S$ and $\Phi$ is not complete since variations due to changes in $\Phi$ are bound to $2|S|$ and that due to changes in $S$ can not result in sign flip of $s$

where $\langle x(t)\rangle_T$ represents the time average of the quantity $x$ over the time interval $[t_0, t_0+T]$[13], and demand the following conditions to be fulfilled

$$\left|\frac{\delta(t)}{S_0}\right| \ll 1 \ , \qquad \left|\frac{(d\varphi/dt)}{2\pi\nu_0}\right| \ll 1 \tag{7}$$

Note that in spite of these requirements, the functions $(S, \Phi)$ are still not uniquely determined by the time trace $s(t)$. In practice, the choice is implicitly made by the set of apartii used for the characterization and measurements of the LO signal, meaning that one never has a complete knowledge about the particular representation *imposed* by his/her aparatii. In other words, when one performs a phase noise or amplitude noise measurement, he/she get a measure for the statistics of $\varphi(t)$ and $\delta(t)$, which fixes the representation, in the sens that two different representation would be considered different only when the statistics of $\varphi(t)$ and $\delta(t)$ are distinct.[14]

### 3.3 Characterization of oscillators

Before describing the analytical tools that have been developed over the last century for the characterization of time-and-frequency sources, one should remember that the choice of a characterization toolbox has to be made according to the purpose to which the time-and-frequency device would be dedicated. The following quote, from E. J. Baghdady at the Short Term Frequency Stability IEEE-NASA Symposium in 1964 [5], clearly illustrates the importance of the question

> *The main problem that I see, which seems to dominate the whole issue [...] is the fact that people have not yet very clearly distinguished between two important aspects of what we are really talking about; namely (1) the RF spectrum of the signal we are looking at; and (2) the instantaneous frequency or phase fluctuations or instabilities of the signal. [...] In any application, we have to make a decision as to whether we are really interested in spectral purity, or instantaneous frequency, or phase instabilities. To just confuse the issue, and hop back and forth between these as if they were completely interchangeable, is a very bad mistake.*

The title of J. D. Hadad presentation at the same Symposium states the problem in clear words: "Basic Relations Between the Frequency Stability Specification and the Application". Regarding *timekeeping*, a characterization allowing for the estimation of the rate of time divergence between two independent clocks is of primary importance. This was the main consideration that motivated the D. W. Allan seminal work [8] where we could read

> *As atomic timekeeping has come of age, it has become increasingly important to identify quality in an atomic frequency standard. Some of the most important quality factors are directly related to the inherent noise of a quantum device and its associated electronics. For example, a proper measurement an classification of this inherent noise makes it possible to determine the probable rate of time divergence of two independent atomic time systems, as well as giving insight concerning the precision and accuracy obtainable from an atomic frequency standard.*

In this paper, D. W. Allan transfers frequency-domain characteristics to the time-domain and sets the idea of using the already well known *sample variance* statistics parameters for frequency stability analysis, in the perspective of timekeeping activities. The following quote from [9] gives some more clues about which type of characterization would be preferable

> *Since instabilities in oscillators are time variations of the quantities of interest (phase, frequency, fractional frequency), they may be characterized by the measure of the variations that occur over a specified time interval $\tau$ : this is the basis of the so-called time-domain characterization [...]. Since random phenomena are involved, the relevant measures are [...]*

[13] Note that such strict definitions are in general not applicable, in particular for $\nu$, since it demands the average to be finite, while a typical behavior like constant drift in $\nu(t)$ make the average not defined. See e.g. [7]

[14] In other mathematical words, one could define on the set of all representations $(S, \Phi)$ of $s$ a equivalent relationship $\sim$ defined as $(S, \Phi) \sim (S', \Phi')$ if and only if the corresponding measured statistics fulfill $stat(\delta(t)) = stat(\delta'(t))$, $stat(\varphi(t)) = stat(\varphi'(t))$, where $stat$ represents a set of measurable statistical quantities. Hence, the set of aparatii would fix the equivalence class of the measured representation.

*given in terms of statistical parameters. These values are usually plotted versus $\tau$ which may vary form say milliseconds to days, months or years.*

*Some important applications of frequency standards directly rely on the time-domain behavior of the output signal, e.g. timekeeping. In this case, a time-domain instability measure is really what is needed, rather than a frequency-domain one.*

### 3.3.1 Time-domain frequency stability characterization

We follow here the development given in [9]. Consider a given representation $(S, \Phi)$ of a clock LO signal and assume it is possible to choose it in such a way that $S(t) = S_0$ is constant. In order for the statistical tools to allow for comparison between LO of different frequencies, we define new variables. The instantaneous clock error is expressed as

$$x(t) = \frac{\varphi(t)}{2\pi\nu_0} \tag{8}$$

and has dimension time. The fractional frequency deviation is defined as

$$y(t) = \frac{\nu(t)}{\nu_0} - 1 = \frac{\Delta\nu(t)}{\nu_0} = \frac{(d\varphi(t)/dt)}{2\pi\nu_0 1} = \frac{dx(t)}{dt} \tag{9}$$

which is a dimensionless quantity. This is the quantity time and frequency metrologists use preferably. In the frame of atomic frequency standards activities, in order to make inter-laboratory comparison easier, the agreed-upon value for $\nu_0$, when the oscillator is referenced to the corresponding atomic transition, is that recommended by the BIPM (Bureau International des Poids et Mesures, see [2]).

**Measurable quantities**

Instantaneous quantities such as $\Phi(t)$, $\nu(t)$, $x(t)$ and $y(t)$, while of fundamental interest for theoretical elaboration, are not accessible by real measurements[15], which rather provide averages of such quantities. In the following we denote by $\overline{q}_k$ the instantaneous quantity $q(t)$ averaged over the time interval $[t_k, t_k+\tau]$, where the dependence on $\tau$ is kept implicit, i.e.

$$\overline{q}_k = \langle q(t) \rangle_{t_k,\tau} = \frac{1}{\tau} \int_{t_k}^{t_k+\tau} q(t)\ dt \tag{10}$$

**True variance, sample variance and Allan variance**

The discussion of this paragraph might seem too theoretical and abstract. However, it is at the heart of the decision by the atomic clock community to fix the definition of the characterization statistical parameters computable from the $\overline{y}_k$ and is then worth mentioning its main arguments.

The *true variance* is defined as $\sigma^2[\overline{y}_k] = \langle \overline{y}_k^2 \rangle - \langle \overline{y}_k \rangle^2$ where, assuming ergodicity of the variable $y$, the $\langle\ \rangle$ symbol denotes either a statistical average calculated over an infinite number of samples given at a given time $t_k$ or an infinite time average made out one sample $y(t)$. Involving an infinite number of samples or data points, the true variance is an idealization and therefore is not accessible to actual measurements. One then has to choose a definition that would mimic as good as possible the behavior of $\sigma^2[\overline{y}_k]$ but relying on a finite number of sample. This is achieved using *sample variances*.

The *sample variance* is defined from an ensemble of $N$ samples $\overline{y}_k$, $k = 1.., N$, each of which has been defined according to equation 10 with $t_{k+1} = t_k + T$, where $T$ denotes the measurement period. The general definition of a sample variance is

$$\sigma^2(N, T, \tau)_f = f(N) \sum_{i=1}^{N} \left( \overline{y}_i - \frac{1}{N} \sum_{j=1}^{N} \overline{y}_j \right)^2 \tag{11}$$

where the function $f$ typically scales as $1/N$ for large $N$. There are then three parameters to fix; $N$, $T$ and $f$. A first criteria for their choice was that of *bias*. An estimator[16] $\tilde{\chi}(N)$ of $\chi$ is said *unbiased* when its statistical *true* average, $\langle \tilde{\chi}(N) \rangle$, equals the true parameter $\chi$. In our case, this means

$$\langle \sigma^2(N, T, \tau)_f \rangle = \sigma^2[\overline{y}_k] \tag{12}$$

[15] Mainly because of measurement apartii finite bandwidth

[16] An estimator $\tilde{\chi}(N)$ of a *true* statistical parameter $\chi$ , i.e. based on an infinite number of available samples, is a parameter computed from a finite number $N$ of samples which asymptotically reaches $\chi$ for $N \to \infty$

It is not possible in general to build unbiased estimators independently on the statistical behavior of the variable $\overline{y}_k$. However, it is possible to choose $N$, $T$ and $f$ in such a way that $\sigma^2(N,T,\tau)_f$ is unbiased for white frequency noise, more precisely setting $N=2$ and restricting the possibilities for $f$. The final definition, proposed by the IEEE Subcommittee on Frequency Stability, was motivated mainly by the a criteria of convenience for computation as well as the possibility to link the chosen time-domain parameter to some previously well studied scaling characteristics of frequency-domain parameter such as the phase and frequency power spectral densities. Following this recommendation, the commonly agreed-upon definition is that corresponding to $N=2$, $T=\tau$ and $f(N)=1/(N-1)$ and is usually referred to as the Allan variance or zero dead-time two sample variance and will be hereafter denoted as $\sigma_y^2(\tau)$.

The Allan variance itself is a random variable meaning the characterization of the investigated LO is actually given by its statistical *true* average $\langle\sigma^2(N,T,\tau)_f\rangle$ which, again, involves an infinite number of samples and therefore is an idealized quantity. In practice, LO's are characterized using an estimator $\tilde{\sigma}_y^2(\tau)$ of $\sigma_y^2(\tau)$. For a series of $m$ samples, the widely used estimator is that given by

$$\tilde{\sigma}_y^2(\tau)=\frac{1}{2(m-1)}\sum_{i=1}^{m-1}\left(\overline{y}_{i+1}-\overline{y}_i\right)^2 \tag{13}$$

Since in practice we deal only with estimator, we use in the following the notation $\sigma_y^2(\tau)$ instead of $\tilde{\sigma}_y^2(\tau)$ for the Allan variance estimator.

**Clock error estimation from Allan variance**

As enhanced in the D. W. Allan quote 3.3, the choice of characterization tool should be motivated by the ability to *determine the probable rate of time divergence of two independent atomic time systems.* This might be achievable if one could estimate the probable error between the clock reading and the local proper time it is supposed to provide, namely $x(t)$. A natural way of predicting timing errors is to linearly extrapolate past errors. More precisely, the predicted error $\hat{x}(t_0+t)=$ at $t_0+t$ may be given as a function of the actual error at $t_0$ and that at $t_0-t'$ as

$$\hat{x}(t_0+t)=x(t_0)+t\frac{x(t_0)-x(t_0-t')}{t'} \tag{14}$$

Choosing $t=t'=\tau$, the statistical error made on the clock error prediction is given by

$$\sigma_{\hat{x}}^2(\tau)=\left\langle\left[x(t_0+\tau)-\hat{x}(t_0+\tau)\right]^2\right\rangle=\left\langle\left[x(t_0+\tau)-2x(t_0)+x(t_0-\tau)\right]^2\right\rangle \tag{15}$$

But from definitions 9 and 10 we have $\overline{y}_k=(x(t_k+\tau)-x(t_k))/\tau$. Hence, the Allan variance can be expressed as a function of the instantaneous clock errors as

$$\sigma_y^2(\tau)=\frac{1}{2(m-1)\tau^2}\sum_{i=1}^{m-1}\left[x(t_k+2\tau)-2x(t_k+\tau)+x(t_k)\right]^2 \tag{16}$$

Henceforth, $2\tau^2\sigma_y^2(\tau)$ is a natural estimator for $\sigma_{\hat{x}}^2(\tau)$.

### 3.3.2 Frequency-domain frequency stability characterization

Before the development of time-domain frequency stability characterization tool box, most of the scientific communities dealing with applications requiring frequency stability characterization, such as Radar detection, rocket tracking and driving, deep space communication *etc...*, had devloped tools matching their needs. Hence, a huge amount of theoretical as well as practical knowledge had been already developed for frequency-domain frequency stability investigation, most of which were based on the *power spectral density* (PSD) of the signal to be analyzed. We give here the very basics definitions and properties of PSD's.

The two side power spectral density $S_q^{(TS)}(f)$ of a quantity $q(t)$, where $f$ is the corresponding Fourier frequency[17], is defined as the Fourier transform of the autocorrelation function of $q(t)$, i.e. as

$$S_q^{(TS)}(f)=\frac{1}{\sqrt{2\pi}}\int_{-\infty}^{\infty}e^{-2i\pi ft'}\langle q(t)q(t-t')\rangle dt' \tag{17}$$

[17] We use on purpose a different notation, i.e. $f$ instead of $\nu$ to avoid confusion between the instantaneous frequency $\nu(t)$ and Fourier frequencies $f$, see 3.2.1 or [9].

which is defined for both positive and negative frequencies. Note that, involving integrals over infinite spectrum and averages over the whole time line (or equivalently, assuming ergodicity of $q(t)$, over an infinite number of samples), this is an idealized definition out of experimental reach. In practice, we prefer using the one side PSD which is defined as twice the two side PSD, restricted to positive frequencies, i.e. $S_q(f > 0) = 2S_q^{(TS)}(f)$. The PSD of $\varphi$, $\Delta\nu$, $y$ and $x$ are related according to

$$S_y(f) = \frac{1}{\nu_0^2} S_{\Delta\nu}(f) = \left(\frac{f}{\nu_0}\right)^2 S_\varphi(f) = 4\pi^2 f^2 S_x(f) \tag{18}$$

From many experiments carried out in many laboratories on many types of oscillators, it turned out that the fractional frequency PSD can be most of the time modeled by

$$S_y(f) = \sum_{\alpha=-2}^{2} h_\alpha f^\alpha \tag{19}$$

for $f$ lower than a sharp cutoff frequency which depends on the particular system under study, rapidly dropping to zero above this cutoff. Each value of $\alpha$ corresponds to a particular type of noise. Random walks scale as $f^{-2}$, flicker noise as $f^{-1}$ and white noise as $f^0$ (higher power noises in $\alpha = 1$, 2 do not have particular names).

### 3.3.3 From frequency-domain to time-domain

It can be shown (see [10]) that the Allan variance $\sigma_y^2(\tau)$ can be obtained from $S_y(f)$ as

$$\sigma_y^2(\tau) = \int_0^\infty S_y(f) \frac{2\sin^4(\pi f\tau)}{(\pi f\tau)^2}\, df \tag{20}$$

The interesting point is that this relation implies that the power lows of $S_y(f)$ as expressed in 19 get imprinted onto the behavior of the Allan variance. Indeed, it can be shown (see [7] and [9]) that for a PSD scaling as $S_y(f) = h_\alpha f^\alpha$ for $f$ lower than the corresponding cutoff $h_\alpha$, the Allan variance scales as

$$\langle \sigma_u^2(\tau) \rangle \propto |\tau|^\mu \tag{21}$$

where $\mu = -\alpha + 1$ for $-2\alpha < 1$ and $\mu = -2$ for $\alpha = 2$. In particular, it can be shown that for pure frequency white noise the Allan variance is given by

$$\sigma_y^2(\tau) = \frac{S_y(f)}{2\tau} \tag{22}$$

## 3.4 Concept of accuracy

In section 3.2 we defined the instantaneous fractional frequency deviation $y(t)$ of an oscillator represented by the couple of time dependent functions $(S, \Phi)$ as

$$y(t) = 1 - \frac{\nu(t)}{\nu_0} \tag{23}$$

where $\nu_0$ was defined as the average of a duration $T$ of the instantaneous frequency $\nu(t)$. In the particular frame of time and frequency metrology, $\nu_0$ is used as a frequency standard. Because of the high level of precision to which atomic clock frequencies are measured, $y(t) \approx 10^{-16}$ for microwave standard, $10^{18}$ for state-of-the-art optical standards, it was decided in 1967 to base the definition of the S.I. time unit, the second, on this type of atom based oscillators. Hence, the game was no longer to simply realize an oscillator with $y(t)$ as defined above using $\nu_0$ reaching extremely low values in a stable manner, i.e. extremely high precision, but doing the same thing using $\nu^o$ instead of $\nu_0$, where $\nu^o$ is a frequency that does not depend on the particular oscillator realized (whereas $\nu_0$ since it is defined as the average of the frequency realized by the oscillator over a certain duration), but is the idealized frequency of the corresponding atomic transition chosen as a standard, in the idealized case of a perfectly free atom. This is caught in the concept of accuracy. The question, for time and frequency metrologists, is no longer just

*"how does $\nu(t)$ fluctuates around its average?"*

but further includes

*"how far does $\nu(t)$ stands, in average, from the idealized reference $\nu^o$ ?"*

Of course the second question can only be answered within the limits set by the answer to the first one, i.e. the difference between the realized frequency $\nu(t)$ and the idealized frequency $\nu^o$ can not be known with a higher precision than the resolution allowed by the statistics of the fluctuations of $\nu(t)$ around its average $\nu_0$. More precisely, the accuracy in fractional frequency units (i.e. $y(t)$ defined with $\nu^o$ instead of $\nu_0$), after a measure of duration $\tau$ can not be known with a precision better than $\sigma_y(\tau)$. The problem then is

*"which value should we choose for $\nu^o$ ?"*

Indeed, the frequency standards are defined with common languages statement such as

*"$\nu^o$ is the frequency corresponding to the $X \longrightarrow Y$ transition of a perfectly free atom of species $A$ "*

which does not help to give any value for $\nu^o$. In practice, the value of $\nu^o$ is fixed by the CPIM which recommend, for each transition of the approved standards (see [2]) a value given in S.I. Hz. This is both a solution and a problem. A solution because it gives a concrete number to use for $\nu^o$, a problem because, as being given in Hz, this value can not be given with a higher degree of precision than that allowed by the best realization of the S.I. Hz, i.e. $10^{-16}$ of the S.I. second. But we precisely aim at building clocks with a higher degree of precision to define a *better* S.I. second, i.e. with fractional uncertainty below $10^{-16}$ ($5 \times 10^{-18}$ at least according to the re-definition road map [2]). The only solution is to rely on direct frequency comparison, usually handled as frequency ratio. Indeed, there is no limitation on the degree of precision to which a ratio $\nu_1/\nu_2$ can be measured. As discussed in section 7.1.1, it is even possible to measure ratios of frequencies based on different atomic species with fractional uncertainty lower than $10^{-16}$ by measuring not $\nu_1/\nu_2$, that would depart from unity in the general case, but the quantity

$$\frac{\nu_1/\nu_1^o}{\nu_2/\nu_2^o} \approx 1 + y_2(t) - y_1(t) \tag{24}$$

which is always close to unity, even for frequencies based on different atomic species (see section 7.1.1).

## 3.5 Uncertainty

Their are many effects that possibly pull the actual measured clock transition $\nu_m$ away from its idealized value $\nu^o$. The first task consist in listing this effects, usually called *systematics*. Once a list is set, one has to estimate the size of each effect, $\Delta\nu_i$, i.e. by how each of them contribute to shifting $\nu_m$ from $\nu^o$

$$\nu_m = \nu^o + \sum_i \Delta\nu_i \tag{25}$$

This is done combining theoretical models and experimental measurements. Further more, one can not content himself with an estimate of each of these systematics but has to characterize how *good* they are. Indeed, once the $\Delta\nu_i$ are estimated, the measured frequency is corrected, leading to

$$\nu_m - \sum_i \Delta\nu_i = \nu^o \tag{26}$$

But of course this equality is not perfect. Each systematics is estimated with an uncertainty $\sigma_{\Delta\nu,i}$, giving the more realistic relation

$$\left| \left( \nu_m - \sum_i \Delta\nu_i \right) - \nu^o \right| \lesssim \sqrt{\sum_i \sigma^2_{\Delta\nu,i}} \tag{27}$$

This is usually summed up in the so-called *uncertainty budget* giving the list of the systematics along with their respective uncertainty, usually given in relative frequency. In other words, each systematics give rise to a shift estimated as $\Delta\nu$ and the uncertainty appearing in the budget is nothing but the *error bars* for this estimate $\sigma_{\Delta\nu}$.

Note however that the list of systematics might not be exhaustive. If the terms ignore are small compared to the dominating $\sigma_{\Delta\nu,i}$, this does not affect relation 27. But if some systematics of significant amplitude, labeled $j \in J$, are missed, then 27 holds but with $\nu^o + \sum_j \Delta\nu_j$ instead of $\nu^o$ and $\sum_{i\in I} \sigma^2_{\Delta\nu,i} + \sum_{j\in J} \sigma^2_{\Delta\nu,j}$ instead of $\sum_{i\in I} \sigma^2_{\Delta\nu,i}$, where non of the $\sigma_{\Delta\nu,j}$ are estimated. In other words, $\nu^o$ might be missed by far at the scale of the estimated systematics uncertainties $\sigma_{\Delta\nu,i}$. This was indeed the case for the static charges and the background systematics, that were added to the list in 2012 and 2018 respectively (see sections 4.6.7 and 4.6.6).

# 4 The SYRTE's strontium optical lattice clocks.

The aim of this chapter is to present the optical lattice clock on which this thesis work has been carried out. At first, the very basics of atomic clocks, i.e. the fact that atomic transitions can be used as frequency references, are briefly exposed in section 4.1. Then the choice of both the species (which element in the periodic table) and the nature (ionic or neutral) of the atomic reference is discussed in section 4.2. After that, the optical lattice clocks architecture we have at the SYRTE laboratory is depicted in section 4.3. After these general preliminaries, section 4.4 provides a presentation of the "SrB" strontium clock on which the works reported in this thesis were carried out, giving the details required for a good understanding of the manuscript. Finally, section 4.5 gives an overview of the state-of-the-art optical clocks performances and where are our clocks positioned within this landscape. It also provides our full uncertainty budget for 2018 and brief discussions about each of its contribution (section 4.6).

## 4.1 Basics of atomic clocks

As outlined earlier, a clock is a device used to measure the time separation between two events, (i.e. the amount of time elapsed between them) and that accounts for the apparent uniformity of time flow (i.e. the reproducibility of phenomena durations). As a result of a centuries long conceptual and technical development, efficient clocks achieving this two functions are based on periodical phenomena. One then counts how many periods of this phenomena elapse between the two considered events, allowing for the assignment of a measure to their time separation. A clock must then be able to achieve two tasks: producing a periodical phenomena (the clock signal) and regulating the periodicity of this phenomena in order to keep it uniform, i.e. invariant under translation towards past and future. This last task requires having a stable reference to which one could compare the periodicity of the clock signal. At the early stage of the clocking history periodical phenomena have been found directly in nature (most of them based on the Earth spinning), on which humans had no control. Later on, technical advances allowed for an "engineering" of the systems producing the clock signal, making our ability to regulate their periodicity stronger and stronger.

The realization of a clock as defined above then requires four main ingredients (see figure 3) : i) a periodical signal, ii) a periodicity reference, iii) a way of comparing the periodicity of the clock signal to that of the reference and iv) a way of steering the periodicity of the clock signal to make it match that of the reference.

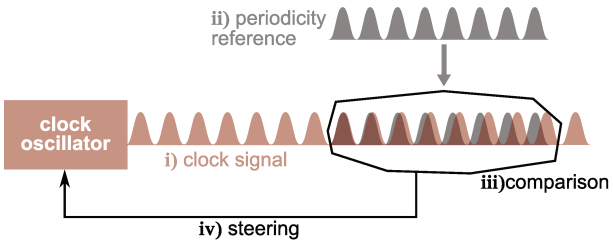


Figure 3: The four basic ingredients of a clock: i) a periodical phenomenon or clock signal (provided by the clock oscillator), ii) a periodicity reference, iii) a way of comparing the periodicity of the clock signal to that of the reference and iv) a way of steering the clock signal periodicity to make it match that of the reference.

In the case of atomic clocks, the clock periodical signal i) consist in an electromagnetic radiation, in the microwave or the optical domain (see figure 4). The periodicity reference ii) is provided by the frequency corresponding to the energy difference between two well chosen configurations of the electronic cloud surrounding the nucleus of an atom (in an ionic or neutral form). The comparison iii) between the periodicity of the clock signal and that of the reference is achieved based on the dependency of the strength of the coupling between the two well chosen electronic configurations induced by the electromagnetic radiation used as the clock signal on the frequency of this radiation. The steering iv) of the radiation periodicity, or frequency, is achieved through the available technologies depending on the electromagnetic radiation frequency range (e.g. digital synthesis for microwave radiations and electro-optic or acousto-optic techniques for optical radiations)

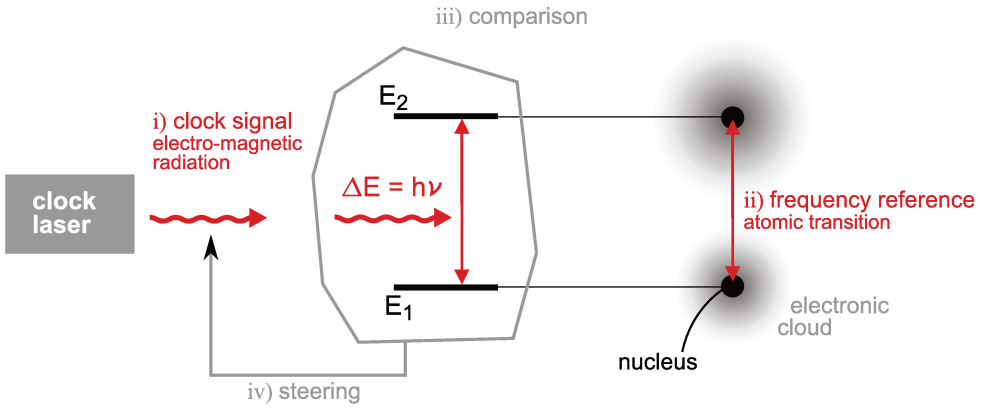


Figure 4: Schematic of an optical clock system. The clock signal i), an electromagnetic radiation in the optical domain, is generated by a clock laser. The frequency reference $\nu$ ii) is defined by the energy separation $\Delta E$ between the two clock states (i.e; two different well chosen electronic configurations) as $\Delta E = h\nu$ ($h$ the Plank's constant). The comparison iii) between the radiation frequency and the reference is carried out via spectroscopy the reading out of which is used as a signal for the steering iv) of the frequency of the radiation provided by the clock laser (see figure 10 for details).

## 4.2 Why a strontium clock?

Stabilizing the frequency of the oscillator to the atomic transition requires extracting a signal $S$ via atomic spectroscopy (see figure 10) that depends on the clock oscillator frequency $\nu_{\text{osc}}$. During one clock cycle (see section 4.4) the fractional frequency error $\delta y$ resulting from fluctuations $\delta S$ in $S$ can be expressed as (see e.g. [12])

$$\delta y = \frac{\delta S}{S_0 Q \kappa} \tag{28}$$

where $S_0$ is the value of the spectroscopy signal when the oscillator frequency matches that of the reference (i.e. when $\nu_{\text{osc}} = \nu$), $\kappa$ is a numerical constant close to unity that depends on the spectroscopy profile shape and $Q = \nu/\Delta\nu$ ($\Delta\nu$ the width of the spectroscopy profile) is the quality factor of the transition. The resulting Allan deviation (see section 3.3), in the case of white noise dominated fluctuations $\delta S$, reads

$$\sigma_y(\tau) = \frac{\delta S}{S_0} \frac{\sqrt{d}}{Q\kappa} \sqrt{\frac{T_c}{\tau}} \tag{29}$$

where $T_c$ is the clock cycle duration (see section 4.4) and $d$ the duty cycle, i.e. the ratio $T_m/T_c$ where $T_m$ is the duration of the spectroscopy stage within the cycle. This consideration pushes for a choice of atomic species providing high-Q transitions, i.e. which are high in frequency and as narrow as possible. State-of-the-art cesium microwave fountainsn such as that used for the realization of the S.I. second, typically achieve $Q \approx 10^{10}$ [11]. On the other hand, alkali-earth atoms, both in their neutral or ionic forms, display forbidden transition in the optical domain with width down to the sub mHz region with quality factors as high as $Q \approx 10^{15}$ [12] offering unprecedented performance perspectives. The total instability of the clock is a combination of various contributions, most of which of the form given by equation 29[18]. Most of them stem from technical noises and can *a priori* be mitigated to arbitrary small levels. However, one of them results from a more fundamental phenomenon, the quantum projection noise, and can not be reduced arbitrarily by technical improvements (see section 8.2). In this particular case the instability contribution expressed in equation 29 scales as (see equation 240)

$$\frac{\delta S}{S_0} \propto \frac{1}{\sqrt{N}} \tag{30}$$

with $N$ the number of atoms, which highlights the importance of operating with a number of atoms as large as possible[19]. Furthermore, an important criteria for the choice of the atomic species used is the

[18] Some contribution are different in nature, such as the Dick effect (section 8.1), and thus have another form.

[19] Note however that arbitrary high numbers of atoms can not be reached because of increasing the atomic density, which has detrimental effects on the clock accuracy (see section 4.6).

sensitivity of their clock transitions to the environment (electric and magnetic fields, gravity...). On top of these metrological criteria, practical implementation issues have to be taken into consideration, the main point being how easy is the manipulation (trapping, cooling and state preparation) of the atoms or ions used.

Summing up, good metrological performances require the use of species (neutral or ionic) with high-$Q$ clock transition, the possibility of operating with a high number $N$ of atoms and a clock transition as less as possible sensitive to the environment. On the other hand, a trade-off between these features and the possibility of easily manipulate the atoms has to be reached for the final choice of the atomic species used.

#### 4.2.1 High-$Q$ transitions

The high-$Q$ criteria motivated the search for narrow optical transitions. Such transitions could be $E_1$ intercombination lines in group II atoms or group III and IIIA (i.e. group XIII) ions. It could as well be electric quadrupolar or octopolar transitions as found for example in group I atoms or group II ions.

#### 4.2.2 High number of atoms probed

Ionic clocks, in spite of their very good accuracies (see table 3), suffer from their very low number of probed atoms, most of them being single-ion clocks, i.e. operated with $N = 1$, making the quantum projection noise contribution, scaling as $N^{-1/2}$, a serious limitation and disadvantage compared with their neutral atoms counterparts. However, trapping neutral atoms for clocks has been achieved so far in optical lattices, requiring powerful lasers at well defined wavelengths (the so called magic wavelength [58], see section 5.0.1). The late availability of such laser sources explains, partially, the reason why ion clocks have led the optical clocks ballet over the 2000 - 2010 decade in spite of having their stability limited by the quantum projection noise because of probing a single ion. Now that this technological limitation has been unlocked, confinement of neutral atoms is achieved on a daily basis in many atom physics laboratories throughout the world allowing for a recoilless, Doppler-free[20] spectroscopy (see section 5.0.1). In optical lattice clocks, dipole forces trapping atoms in a coherent standing wave enable the simultaneous interrogation of a large number of atoms ranging from a few hundreds to hundreds of thousands, giving a significant advantage to the neutral atoms optical clocks over their ionic counterparts in terms of stability (see [12] and section 8.2). This has been a key criterion for the choice made at SYRTE to work with neutral atoms instead of ions.

However, trapping the atoms in an optical lattice presents some serious drawbacks due to the light shift the trapping light induces on the atomic energy levels. This is described in details in section 5. In short, the parade found is to choose $J = 0 \rightarrow J = 0$ forbidden transitions to reference the clock, since this allows for a cancellation (to the first order in lattice trap intensity) of the vector and tensor components of the lattice light shift. The scalar component is cancelled setting the lattice at the magic wavelength (see [13] and section 5). Such transitions are found in group II atoms only, which further restricted our choice.

#### 4.2.3 Group II atoms and their singlet-triplet structure

Group II atoms, because of having only two electrons on their outer shell, have a level scheme based on a singlet-triplet structure, as that depicted in figures 5 and 9. The ground state is a $^1S_0$ state whereas the P states are split into a singlet $^1P_1$ and a triplet of meta-stable states $^3P_{0,1,2}$. The singlet-to-singlet $^1S_0 \rightarrow {}^1P_1$ cycling transition is suitable for a first stage trapping and cooling whereas the singlet-to-triplet *spin forbidden* narrow transitions offer both low temperature Doppler cooling ($^1S_0 \rightarrow {}^3P_1$ transition) as well as the *doubly forbidden*[21] $^1S_0 \rightarrow {}^3P_0$ transition, perfectly suited for a clock transition (see figure 9).

#### 4.2.4 Boson or fermion ?

The absence of nucleus spin for the bosonic isotopes of alkali-earth atoms make them easier to manipulate. However, this absence of nuclear spin let the $^1S_0 \rightarrow {}^3P_0$ clock transition impossible to excite with a single photon and requires enabling the clock states coupling via the adding of a *dc photon* [19], i.e. a constant

[20] to the first order

[21] Spin forbidden: $\Delta S = 0$ and $J = 0 \rightarrow J = 0$

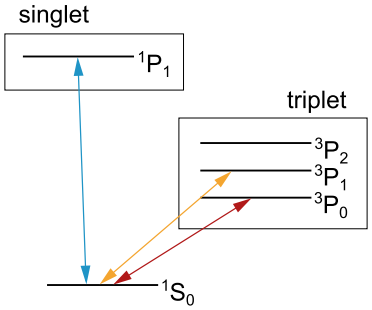


Figure 5: Group II singlet-triplet levels structure. The $^1S_0 \rightarrow {}^1P_1$ cycling transition (blue arrow) provides a first cooling and trapping stage. The spin forbidden $^1S_0 \rightarrow {}^3P_1$ transition allows narrow cooling and the doubly forbidden (spin forbidden and $J = 0 \rightarrow J = 0$) $^1S_0 \rightarrow {}^3P_0$ provides a high-$Q$ clock transition.

magnetic field mimicking a nuclear spin. The control of such field required for the operation of bosonic clocks at the state-of-the-art level has only very recently be achieved (see for example [15, 16, 17, 18]) but was out of reach at the time the optical clocks projects were initiated at SYRTE. On the opposite, the nuclear spin of the fermionic isotopes induces a mixing between singlet and triplet states of the P levels making the clock transition weakly allowed [20]. Moreover, bosonic statistics allows for a by far higher rate of cold collisions between atoms trapped at the same lattice site compared to the fermionic case, inducing significant shifts (this issue has been addressed by trapping the atoms in a 3D lattice to reduce the local density and therefore the collisions rate, as reported in [15]). This are the two reasons (no mixing enabling the clokc transition and cold collisions) why all the optical lattice clocks developed at SYRTE are based on fermionic isotopes ($^{87}$Sr [21] and $^{199}$Hg [22]).

#### 4.2.5 Why strontium ?

As noted at the beginning of the section, high-$Q$ clock transitions are required to maximize the clock performances. Quality factors of fermionic isotopes of the most commonly used atoms are gathered in table 1.

| species | $^{87}$Sr | $^{171}$Yb | $^{199}$Hg |
|---|---|---|---|
| $Q$ ($\times 10^{15}$) | 430 | 54 | 12 |

Table 1: Natural linewidth limited quality factor $Q$ of neutral fermionic atoms explored for optical clock applications [12]

In terms of $Q$ factor, $^{87}$Sr is the most attractive species and this is one of the reasons two $^{87}$Sr clocks are developed at SYRTE. On the other hand, the nuclear spin of $^{87}$Sr is 9/2, resulting in an electronic levels structure more complex than that of $^{171}$Yb and $^{199}$Hg both having a 1/2 nuclear spin, making the manipulation of the atoms a bit more involving.
Another criterion is the width $\Delta_{\mathrm{nc}}$ of the $^1\mathrm{S}_0 \rightarrow {}^3\mathrm{P}_1$ narrow cooling transition (or intercombination line), which determines the lowest temperature achievable with Doppler cooling. They are reported in table 2 below. This creteria as well pushed for working with $^{87}$Sr.

| species | $^{87}$Sr | $^{171}$Yb | $^{199}$Hg |
|---|---|---|---|
| $\Delta_{\mathrm{nc}}$ | 7.5 kHz | 180 kHz | 1.3 MHz |

Table 2: Width of the intercombination line used for the cooling of the atoms trapped in the lattice for the mostly used species in neutral optical clocks.

Regarding the availability of laser sources required for the atom state manipulation (trapping, cooling, state preparation and clock interrogation), they all fall in the visible and near infrared region for $^{87}$Sr and $^{171}$Yb whereas most are in the UV region for $^{199}$Hg, making the latter by far more demanding in terms of lasers engineering.

However, due to their static polarizabilities, $^{87}$Sr and $^{171}$Yb are by one order of magnitude more sensitive than $^{199}$Hg to the black body radiation due the non vanishing temperature of the atoms close environment [12], which is an effect hard to control and estimate. Indeed, the black body radiation shift is the largest contribution to the uncertainty budget of $^{87}$Sr and $^{171}$Yb clocks operated at room temperature, making it difficult to enter the $10^{-18}$ accuracy region (see section 4.6). This was the main motivation for the starting of the $^{199}$Hg optical clock project at SYRTE (along with a higher sensitivity to potential variations of the fine structure constant [23]) in addition to the strontium clock project.

## 4.3 SYRTE clocks architecture

As a state institution, SYRTE[22] sees a large part of its activities devoted to the french national time scale generation and dissemination. These "service" tasks are achieved using four commercial cesium beam clocks along with four commercial hydrogen masers referenced to a cryogenic sapphire oscillator itself compared to one of the three fountains operated at SYRTE (a standard cesium fountain, a transportable one and a dual rubidium-cesium fountain [24]).

On a more *exploratory* side, development of optical lattice clocks is carried out at SYRTE. More precisely, as motivated in the previous section, SYRTE hosts two strontium [21] and one mercury [22] optical lattice clocks. The clock laser of each being beating with an optical frequency comb referenced to the cryogenic sapphire oscillator (see figure 6). This allows for both the reading of the absolute clock lasers frequencies as well as connecting the clocks to the external world, as required for the comparisons reported in part III. The architecture of these optical lattice clocks is detailed in the following paragraph.

On top of all these clock systems, compact size CPT (Coherent Population Trapping) [27] and iodine [25] clocks are developped at SYRTE.

### 4.3.1 SYRTE optical lattice clocks

An optical lattice clock is made of a few key ingredients (see figure 6): the clock laser (which is the clock local oscillator whose periods are piled up one after the other for the generation of the time scale), the ultra stable cavity that serves as a prestabilization stage for the clock laser (which is required to achieve a Fourier limited spectroscopy of the sub Hertz wide clock transition), the lattice trap (an in vaccum electro-magnetic standing wave) where the atoms used as a frequency reference are stored, a detection system, allowing for the reading out of the atoms states after the spectroscopy stage, and a clock frequency steering element allowing for the adjustment of the clock laser frequency according to the spectroscopy outcome.

At SYRTE the two strontium clocks, SrB and Sr2, lay in the same room and share the same clock laser and ultra stable cavity, a Fabry-Perrot cavity of high finesse $\mathcal{F} \gtrsim 5 \times 10^5$ (for further details see [106]). More precisely, the 698 nm clock light is generated by an extended cavity laser diode prestabilized on a first Fabry-Perrot cavity and located in another room. It is then sent through a fiber to the strontium clocks room where it injects a slave laser [28]. It is then dispatched through phase noise compensated fibers [29] to the two clocks and the ultra stable cavity (located in the same room) as well as to the optical frequency comb (located in a third room). Each clock has its own clock frequency steering achieved by an acousto-optic modulator driven by a direct digital synthesizer referenced to a signal stemming from the cryogenic sapphire oscillator. This allows for a knowledge of the frequency difference between the clock light sent to the optical frequency comb and the clock light seen by the atoms at level below $10^{-18}$. Both strontium clocks have a one dimension vertical lattice. The atoms trapped in Sr2 lay 1262 mm above that of SrB corresponding to a redshift fractional frequency difference of $2.86 \times 10^{-17}$ taken into account for the clocks comparisons. Further details can be found in section 4.4.

The mercury optical lattice clock and its clock laser source as well as its ultra stable cavity stand in their own room. It is built on a similar architecture as the strontium clock and its clock laser is beaten with the same optical frequency comb to which it is linked by a phase noise compensated fiber (see [26] for details).

[22] The SYRTE laboratory (SYstèmes de Référence Temps-Espace) is the LNE (Laboratoire Nationale de métrologie et d'Essais) departement devoted to time and frequency standards. It is host at the Observatoire de Paris-Meudon in Paris.

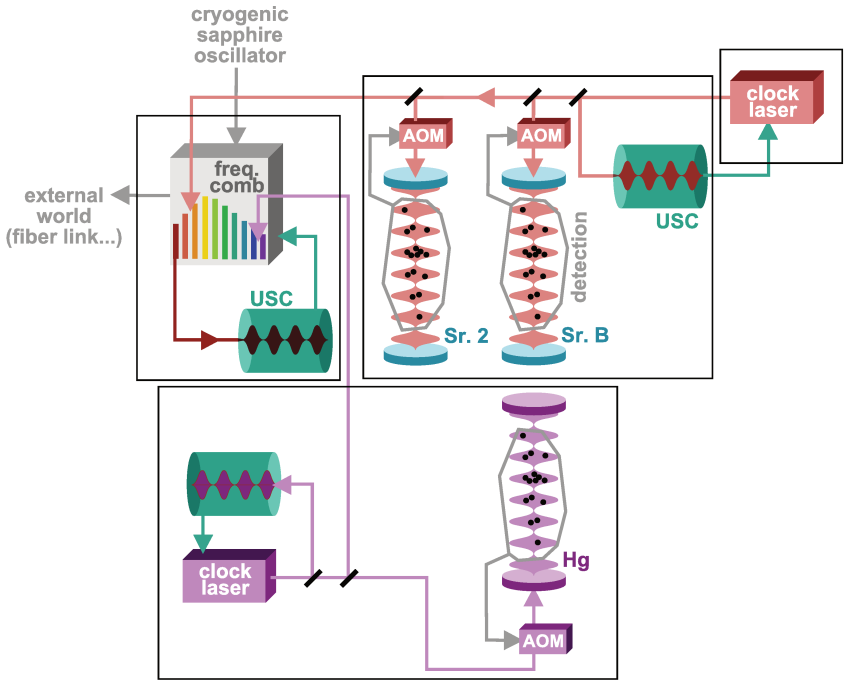


Figure 6: The three optical lattice clocks developed at the SYRTE laboratory at the Observatoire de Paris (two based on strontium, one on mercury). Each clocks requires a few fundamental ingredients to work: a clock laser, a ultra stable cavity (USC) used as a first prestabilization stage, an optical lattice, the atoms trapped in this lattice and used as a frequency reference and finally a clock laser frequency adjustment mechanism (this steering function is operated by an acousto-optic modulator for our three clocks). The two strontium clocks lay in the same room (black boxes) and share the same clock laser and USC. The reading out of the absolute frequency of the clock laser referenced to the USC is performed by an optical frequency comb which repetition rate is referenced to a cryogenic sapphire oscillator. The comb is also used as a *gate* to the external world.

The comb itself is referenced to its own ultra stable cavity. It allows for the reading of the absolute frequencies of the strontium and mercury clock lasers in S.I. Hertz at a level of stability ($\sigma_y \sim 10^{-14}$ at 1 s) and accuracy ($10^{-16}$) limited by the cesium fountains operated at SYRTE (as required by the second redefinition roadmap [2], point 3.). It further allows for the direct measurement of frequency ratios between the SYRTE optical lattice clocks as well as between SYRTE clocks and remote clocks connected with each others through the continental scale optical fiber links network (presented in section III) beyond the limits set by the fountains (as required by the second redefinition roadmap [2], points 2. and 5.).

## 4.4 SrB clock setup and operation

In this paragraph is presented the setup and operation of the SrB optical lattice clock, that on which was carried out this PhD work.

### 4.4.1 The vacuum system

The SrB vacuum system is depicted in figure 7. It is composed of an oven containing a solid strontium sample heated up to roughly 500 °C providing a strontium jet containing all natural isotopes in proportions given by their natural abundances. Two ion pumps are connected at the oven output. The hot strontium atoms then fly through a cube endowed with three viewports and a bellow holding an in-vacuum metallic flag tilted by the action of a stepper motor, allowing for the blockade of the strontium flux stemming from the oven during the interrogation stage. This was implemented in order to minimize the trap atoms loss rate due to collisions with hot strontium atoms. However, it did not result in any significant reduction of the loss rate and the clock is currently operated without using it. It could as well

have led to some changes in the frequency shifts due to the black-body radiation stemming from the oven (that are partially blocked by the metallic flag) or to hot collisions with strontium emanating from the oven, but such effects have not been detected. After comes a Zeeman slower, $\sim$ 40 cm long, surrounded by a cylindrical three-layers magnetic shield.

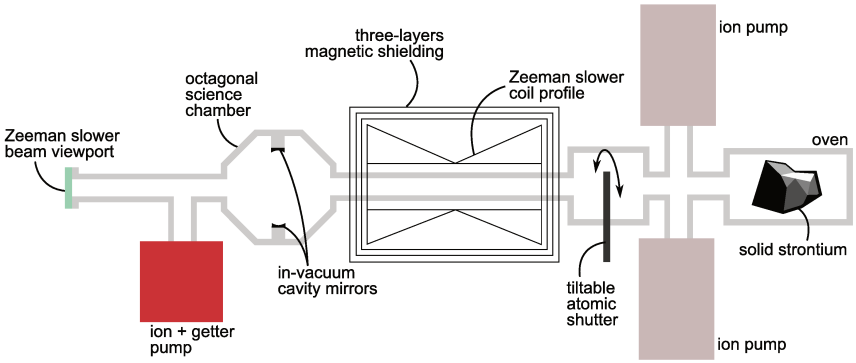


Figure 7: Schematic view of the SrB clock vacuum system.

The atoms then reach the octagonal science chamber (see figures 7 and 8). It consists in a prism with octagonal bases of diameter $\sim$ 10 cm parallel to each other and separated by around 4 cm. Four of the surrounding faces are endowed with small viewports ($\sim$ 2.5 cm diameter) used for two of the magneto-optical trap beams paths. The bases are endowed with large ($\sim$ 7 cm diameter) viewports providing access for the remaining magneto-optical trap beam as well as the fluorescence detection light, the transverse cooling light and the optical pumping light (see section 4.4.2). A particularity of our design is that two opposite surrounding faces (that on the vertical axis) are endowed with bellows the tip of each holding a mirror forming the in-vacuum cavity used for the lattice trap buildup and the non-destructive detection probe (see section 11). Finally, the two remaining surrounding faces host flanges connecting the science chamber to the Zeeman slower on one side, to a pipe ended by a viewport on the other side for the Zeeman slower light access. This pipe is connected to a third ion pump containing a getter pump.

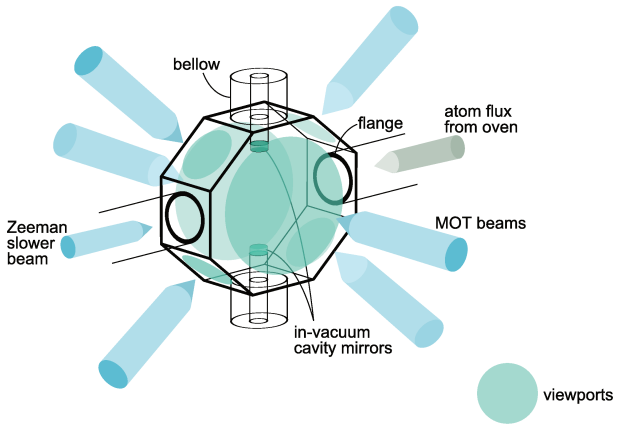


Figure 8: **The octagonal chamber**. It consists in an octagonal prism with six viewports used for all the optical access (the MOT beams are represented on the schematic). The top and bottom entries are plugged with two bellows (bendable vacuum-compatible cylinders) on which the two in-vacuum cavity mirrors are fixed. This 4 cm long cavity is resonant at both the 813 nm lattice light and the 461 nm detection light (see figures 9).

### 4.4.2 The lasers system

The $^{87}$Sr atoms trapping and preparation require a bunch of lasers with frequencies and linewidths reported, along with their functions, on the energy levels chart of figure 9.

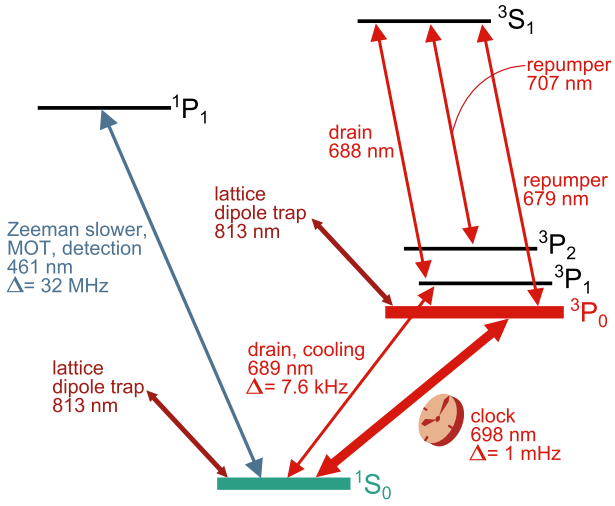


Figure 9: $^{87}$**Sr** energy chart.

The 461 nm light used for the Zeeman slower, the magneto-optical trap (MOT) and the detection stems from a 922 nm extended cavity laser diode which light is doubled in a bow tie cavity hosting a non-linear crystal[23]. It is tuned to the $^1S_0 \rightarrow {}^1P_1$ transition via a saturation absorption spectroscopy performed in a dedicated vacuum system[24]. It is then dispatched to the Zeeman slower, MOT and detection paths, each endowed with acousto-optic modulators for independent tuning optimization.

The lattice dipole trap light at 813 nm stems from a M-squared solid state laser pumped by a Coherent Verdi laser at 532 nm. Typical power of 1.5 W at 813 nm is obtained for a 15 W pump. It is then dispatched to the two strontium clocks. Its frequency is tuned to the so-called magic wave length for which the light shift induced on both the clock ground and excited states is the same to first order in lattice intensity [13], the tuning relying on regular light shift measurements [31]. To avoid drift of its frequency, it is referenced to a transfer cavity[25] whose length is referenced to the $^1S_0 \rightarrow {}^1P_3$ transition at 689 nm, measured in the same spectroscopic chamber as that for the 461 nm light (see above).

The 689 nm light used for the drain (see section 4.4.3, Trap loading stage paragraph) and the cooling stems from an extended cavity laser diode referenced to a prestabilization cavity in order to achieve the narrow width of 7.6 kHz required to resolve the natural width of the $^3P_1$, to which it is referenced by spectroscopy, which is required for the cooling to be efficient. It is also required to achieve sub-Doppler cooling operated in the cooling stage in the lattice transverse plane.

The 688 nm light stems from an extended cavity laser diode and is referenced to the $^3P_1 \rightarrow {}^3S_1$ transition by spectroscopy in the same dedicated chamber as for the 461 nm and 689 nm lights. Since this spectroscopy requires the atoms to first be pumped to the $^3P_1$ metastable state, we proceed as follows. The spectroscopy system is endowed with its own oven, providing a hot strontium atoms jet. The atoms first pass through the 689 nm beam (perpendicular to the atoms jet) which pumps some of them to the $^3P_1$ state. They then pass through the 688 nm beam, parallel to the 689 nm beam but translated by $\sim$ 1 cm along the atoms jet. The fluorescence corresponding to the $^3P_1 \rightarrow {}^3S_1$ is then collected by a avalanche photodetector providing with the signal used to lock both the 688 nm and the 689 nm lights.

The 698 nm light used to drive the $^1S_0 \rightarrow {}^3P_0$ clock transition is obtained from an extended cavity laser diode first prestabilized on a Fabry-Perrot cavity laying in an other room. Its light is then sent to the strontium clocks room through a phase noise compensated fiber where it is injected into a slave providing with light dispatched to both strontium clocks as well as to a high finesse ($\mathcal{F} \sim 5 \times 10^5$) ultra stable cavity used to obtained the sub-Hertz width required to address the clock transition. The lock to this ultra stable cavity is done with a PDH technique [30].

[23] The 922 nm source is shared by our two strontium clocks but each has its own doubling cavity.
[24] Shared by the two strontium clocks.
[25] A bichromatic cavity used to reference the frequency of a laser directly to that of an other one.

The 707 nm and 679 nm repumpers light stem from extended cavity laser diodes which cavities lengths and driving currents are scanned in order for their frequencies to be scanned over several GHz.

### 4.4.3 The clock sequence

The normal clock operation consists in the successive repetition of a sequence as that described in the following of typical duration of the order of the second. A sequence is itself a succession of *stages*: lattice trap loading stage, cooling stage, state preparation stage, clock interrogation stage and finally detection stage.

**Trap loading stage**
During this stage, except at its very end, the Zeeman, MOT (461 nm, see figure 8 for the beams geometry) and drain (689 nm + 688 nm, colinear to the lattice) lights are on as well as the lattice trap. Some of the atoms slowed down by the Zeeman slower are captured by the MOT which has a diameter of roughly 1 mm, a temperature of about 3 mK and contains around $10^6$ $^{87}$Sr atoms. The drain constantly takes some of these atoms into the $^3S_1$ state from where they naturally decay to the two metastable states $^3P_0$ and $^3P_2$, where they are insensitive to the 461 nm light. If they are cold enough, they are kept in the lattice dipole trap at 813 nm. At the very end of this stage the Zeeman, MOT and drain lights are turned off and the repumpers are turned on while the lattice is kept on. The repumpers resend the remaining atoms to the $^3S_1$ state from where they decay back to the ground state $^1S_0$. The loading stage lasts typically between 250 and 600 ms. At the end of this stage the typical number of atoms trapped in the lattice is about $5\times10^3$.

**Cooling stage**
During this stage the 689 nm and the lattice lights only are on. The lattice intensity is linearly ramped down to the desired level while a side band cooling is performed in the lattice longitudinal direction and a sub-Doppler cooling is achieved in its transverse direction. At the end of this $\sim$ 100 ms stage, for a 50 Er[26] trap depth and 2000 - 5000 atoms initially trapped in the lattice we are left with 500 - 1000 atoms at 1 - 10 $\mu$K.

**State preparation stage**
The atoms are then optically pumped into one of the extreme Zeeman sublevels $m_F = \pm 9/2$ of the $^1S_0$ clock ground state. For these states to be well defined, a magnetic field perpendicular to the lattice longitudinal direction is produced by a pair of anti-Helmotz coils and provide the quantization axis. Then, a $\sigma^{\pm}$ polarized 689 nm light is swept over a few MHz to pump the trapped atoms into one of the Zeeman extreme sublevels. This stage lasts a few tens of ms.

**Clock interrogation stage**
During the clock interrogation the lattice and the clock lights only are on. The clock light is colinear to the longitudinal direction of the trap and is linearly polarized along the quantization magnetic field which magnitude is set in order to reach the desired splitting between the $m_F$ sublevels. For nominal operation of our strontium clocks the magnetic field magnitude is of the order of 100 $\mu$G resulting in a difference between the $m_F = -9/2 \rightarrow m_F = -9/2$ and the $m_F = +9/2 \rightarrow m_F = +9/2$ clock transitions of the order of the kHz. This separation has to be large enough for each Zeeman sublevel transition to be resolved and for the line pulling to be minimized but small enough for the quadratic Zeeman shift to remain compatible with metrology applications (see section 4.6). The interrogation is operated in a Rabi $\pi-$pusle configuration meaning that the clock laser power and the clock interrogation duration are set in such a way that for a vanishing detuning the Rabi pulse transfers the atoms from the clock ground state to the cock excited state (in practice, sequences with different detuning and starting from different $m_F$ are carried out successively as described in paragraph 4.4.4 hereafter).

**Detection stage**
The clock interrogation Rabi pulse transfers the atoms from the clock ground state $|g\rangle$ into the normalized superposition

$$\alpha\,|g\rangle + \beta\,|e\rangle$$

[26] Recoil energy. Throughout tis thesis, when not specified, Er is computed with the lattice wavelenght $\lambda_{813}$, i.e. 1 Er $= \frac{\hbar^2 k^2}{2m}$ with $k = 2\pi/\lambda_{813}$.

where $|e\rangle$ stands for the clock excited state[27] and where $\alpha$ and $\beta$ depend on the clock detuning from the probed transition. The useful information for the clock frequency steering is the transition probability $|\alpha|^2$ which can be readout by operating a projective measurement of the atoms state. This can be achieved in (at least) two ways: fluorescence detection (see section 10 for details) and phase detection (see section 11). Both methods use the 461 nm transition.

### 4.4.4 Clock lock

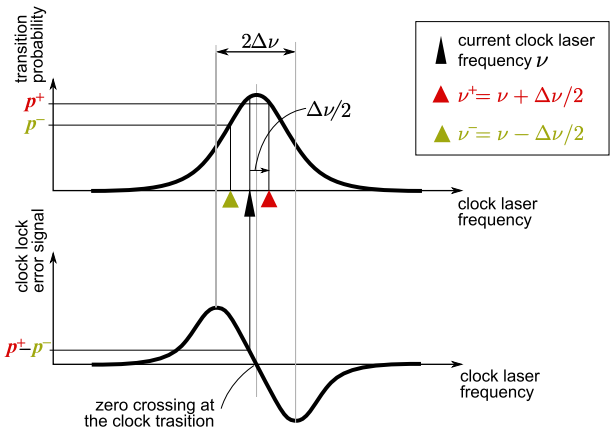


Figure 10: Locking the clock. **Top**: Sketch of the line profile, i.e. the $^1S_0 \rightarrow {}^3P_0$ transition probability as a function of the clock laser frequency for a given Zeeman sublevel ($m_F = \pm 9/2$) and a given power. For each Zeeman sublevel the transition probability is successively measured around the corresponding current frequency (i.e. that obtained after the last steering) $\nu$ (black elongated triangle). More precisely at $\nu^+ = \nu(t) + \Delta\nu/2$ (red triangle) and $\nu^- = \nu(t) - \Delta\nu/2$ (green triangle) where $\Delta\nu$ is the transition half width at half maximum. **Bottom**: The difference of the corresponding measured transition probabilities $p^+$ and $p^-$ is then used as an error signal. Indeed, the quantity $p^+ - p^-$ is positive for $\nu$ lower than the clock transition frequency, negative for $\nu$ higher and has its zero crossing at the transition. Locking the clock then consists in the iteration of this process, alternating between the two extreme Zeeman sublevels.

The effective width of the clock transition depends on the clock power sent to the atoms, or, equivalently for a Rabi $\pi-$pulse, on the Rabi pulse duration $T$ as

$$\Delta\nu = \frac{0.8}{T}$$

when the width $\Delta\nu$ is expressed in Hz and the duration $T$ in s. Our strontium clocks are nominally operated with $T = 200$ ms , corresponding to a transition width $\Delta\nu = 4$ Hz. To lock one of the clock transitions ($m_F = \pm 9/2$) we probe alternatively the transition with a detuning $\Delta = \pm\Delta\nu/2$ and then compute the difference of two successive transition probability measurement (see figure 10). This results in a signal crossing zero at the clock transition frequency, anti-symmetric around this zero crossing and linear within a range $\sim \Delta\nu$ (see figure 10)

## 4.5 Clock performances

In 1955, 6 years after the demonstration of the first atomic clock based on an absorption line of Ammonia at NBS (National Bureau of Standards, U.S., now NIST) [39], L. Essen and J.V.L. Parry built at NPL (National Physical Laboratory) the first atomic clock surpassing in accuracy the best quartz oscillators available at that time [40]. Their clock was based on a microwave hyperfine transition of the $^{133}$Cs ground state and reached a fractional accuracy at the level of a few $10^{-10}$ (whereas quartz where limited to the low $10^{-8}$). Over the following half century the accuracy of the beset atomic microwave clocks has

[27] A more complete notation should make clear which Zeeman sublevel transition $m_F \rightarrow m_F$ is considered, but it is useless here for the understanding of the working principle of the clock.

improved by one order of magnitude per decade, finally reaching in the 2010's what seems to be their ultimate accuracy limit at the low $10^{-16}$ level (see figure 11) and stability $\sigma_y \gtrsim 2 \times 10^{-14}$ at 1s [41]. The history of the optical transition based atomic clocks started later in the 1980's. At that time optical clocks laid behind their microwave counterparts by more than 2 orders of magnitude in terms of accuracy but soon showed a high rate of improvement of around two orders of magnitude per decade. For this reason it was expected at the end of the XX$^{\text{th}}$ century that optical standards would have soon outperformed the $^{133}$Cs fountains introduced in the 1990's and used for the realization of the S.I. second throughout the world so far. The CIPM then published a list of secondary representations of the second included one new microwave standards and eight optical standards "*in order to investigate their suitability for a future redefinition of the SI second and to utilize them in the realization of TAI with the prospect of improved time scales*" [2]. The cross over occurred around 2010 (see figure 11).

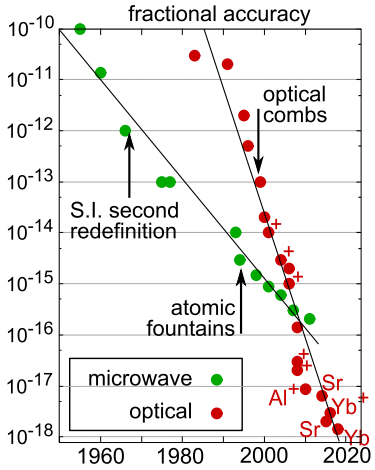


Figure 11: Accuracy of atomic standards since the realization of the first atomic clock surpassing quartz-based devices in 1955 [40]. **Green dots**: standards based on microwave transitions. It follows roughly the rule "one order of magnitude gained per decade". In 2010 it reached what seems to be its ultimate limit $\approx 10 \times 10^{-16}$. **Red dots**: the history of standards based on optical transitions started in the early 1980's. The gains are of 2 order of magnitude per decade. The cross over occurred just before 2010. The first decade of the XXI$^{\text{th}}$ century was led by the ion clocks (labelled with a +). The neutral atom clocks caught up just before 2015.

### 4.5.1 State-of-the-art: accuracy

The uncertainty budget is the figure of merit used for characterizing clocks accuracy (see section 3.5). Here we briefly give the state-of-the-art uncertainties reached by optical clocks. Until very recently the highest accuracies were achieved by optical ion clocks (see figure 11, from 2000 to 2010). Some of their most relevant published accuracies are displayed in table 3.

| species (publ. year) | $^{27}Al^+$ (2010) | $^{88}Sr^+$ (2014) | $^{40}Ca^+$ (2016) | $^{171}Yb^+$ (2016) |
|---|---|---|---|---|
| fract. accuracy | $8.6 \times 10^{-18}$ [42] | $4 \times 10^{-17}$ [33] | $3.2 \times 10^{-17}$ [34] | $3 \times 10^{-18}$ [35] |

Table 3: Ion clocks accuracy sate-of-the-art. This table displays some of the most significant optical ion clocks accuracies published over the past years.

However, neutral atom clocks bridged the gap in the past few years. Their most recent significant published accuracies are given in table 4.

However, uncertainties estimations are not immune to omissions and/or undetected biases (e.g. see 4.6.7) and therefore require to be checked via direct clocks comparisons (see section 7.2). Only a few of the values presented in tables 3 and 4, i.e. at the $10^{-18}$ level, have been confirmed so far such as the neutral ytterbium clocks of the NIST [32] and the ionic ytterbium clocks of the PTB [43]. On our side,

| species (publ. year) | $^{87}$Sr (2014) | $^{87}$Sr (2015) | $^{174}$Yb (2018) |
|---|---|---|---|
| fract. accuracy | $6.4 \times 10^{-18}$ [36] | $2 \times 10^{-18}$ [37] | $1.4 \times 10^{-18}$ [38] |

Table 4: Neutral atom lattice clocks accuracy state-of-the-art. This table displays some of the most significant optical lattice neutral atom clocks accuracies published over the past years.

the $1.7 \times 10^{-17}$ uncertainty of our two strontium clocks (see figure 12) has been confirmed at the level of a few $10^{-17}$ (e.g. $1.5 \times 10^{-17}$ for SYRTESr2 - PTBSr, see section 7.2.2).

### 4.5.2 State-of-the-art: stability

Regarding the stability, ion clocks suffer from the low number of ions probed at each clock cycle and their best stabilities are limited by the quantum projection noise scaling as $1/\sqrt{N}$ ($N$ the total number of ions or atoms probed per cycle see section 8.2), whereas that of neutral atoms based optical clocks are Dick limited (the transfer of high frequency noise of the clock laser frequency to low frequencies due to sampling, see 8.1). The best stabilities for ion and netral atoms clocks are reported in tables 5 and 6 respectively. Since the Allan deviation $\sigma_y(\tau)$ integrates as white noise for optical clocks (this is because the instability main contributions are detection noise, Dick effect and quantum projection noise see section 8.3) only the value at 1 s is reported.

| species (publ. year) | $Al^+$ (2010) | $^{171}Yb^+$ (2016) |
|---|---|---|
| $\sigma_y(1s)$ | $2.8 \times 10^{-15}$ [42] | $5 \times 10^{-15}$ [35] |

Table 5: Ion clocks stability (at 1 s) in fractional frequency unit.

| species (publ. year) | $^{87}$Sr (2014) | $^{87}$Sr (2015) | Yb (2017) | $^{87}$Sr (2017) |
|---|---|---|---|---|
| $\sigma_y(1s)$ | $1.5 \times 10^{-15}$ [36] | $1.6 \times 10^{-16}$ [44] | $6 \times 10^{-17}$ [45] | $3.1 \times 10^{-17}$ [46] |

Table 6: Neutral atoms clocks stability (at 1 s) in fractional frequency unit. The impressive two lasts values (at the $10^{-17}$ level) were obtained using particular clock operation configurations. The result reported in [45] was obtained implementing a "zero-deatime" sequence in which two different atoms ensembles are probed alternatively in order for the clock laser to be constantly reference to the atomic transition. That reported in [46] was based on 3D lattice geometry.

Our two strontium optical lattice clocks have a Dick limited stability of $7.4 \times 10^{-16}$ at 1 s (see figure 38). To gain on this side, several approaches can be explored as discussed in part IV.

## 4.6 SYRTE strontium clocks uncertainty budget

| Effect | Uncertainty in $10^{-18}$ |
|---|---|
| Black-body radiation shift | 12 |
| Quadratic Zeeman shift | 5 |
| Lattice light-shift | 3 |
| Lattice spectrum | 1 |
| Density shift | 8 |
| Line pulling | 6 |
| Background collisions | 4 |
| Static charges | 1,5 |
| **Total** | 17 x $10^{-18}$ |

Figure 12: Uncertainty budget of our two $^{87}$Sr clocks.

At SYRTE we have two strontium optical lattice clocks, SrB[28] and Sr2. Their shared 2018 budget[29] is

[28] A first clock was built, named Sr1 and a bit later a second one Sr2. Afterward Sr1 was stopped, and a third generation clock was built on its *skeleton*. Because of this combination of first and third generation, the resulting clock was labeled SrB, B being a 1 and a 3 put beside each other.

[29] *Stricto sensu* each clock has its own uncertainty budget, but their are so close in our case that we can pack them in a

depicted in Figure 12. In this section we introduce briefly the systematics considered for our budget.

### 4.6.1 Black-body radiation shift

As discussed in details in section 5, the response of the atoms to any oscillating electric field, even far detuned from any electronic transition, induces a shift of the electronic energy levels, and of the two clock state in particular. Being at non zero temperature, the environment surrounding the atoms radiates electromagnetic fields (in the tens of THz domain at room temperature) thus inducing a shift of the clock levels and therefore of the clock transition. The spectrum of this radiation is described by the Black-body radiation theory, hence giving its name to the corresponding systematics. The estimation of this effect relies on both a modelization of the phenomenon and an estimate of the field radiated by the environment. The theory predicts a frequency shift $\delta\nu$ expressed as

$$\delta\nu = \delta_{\text{stat}} \left(\frac{T}{T_0}\right)^4 + \delta_{\text{dyn}} \left(\frac{T}{T_0}\right)^6 + \mathcal{O}(T^8) \tag{31}$$

where $T$ is the effective temperature seen by the atoms, $T_0 = 300$ K and $\delta_{\text{stat}}$ and $\delta_{\text{dyn}}$ are coefficient related to the static and dynamic first order polarizabilities. In our case, the uncertainty on the estimation does not stem from these coefficient estimation but is dominated by that on the effective temperature $T$ seen by the atoms [78, 47]. Due to the complex shape of the vacuum structure and the multiplicity of materials it involves, estimating the emissivity of the whole environment is a difficult task. Our strategy consists in measuring the temperature spread over the vacuum chamber and workout a design that minimizes this spread. For the measurement, six pt100 sensors are glued in small holes dug at the outer surface of the vacuum chamber (see Figure 13).

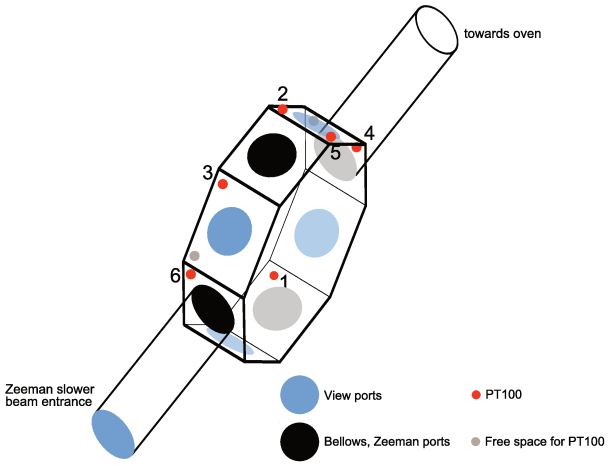


Figure 13: Location of the pt100 temperature sensors on the vacuum chamber of SrB.

Note that the temperature as to be known in terms of S.I. units. We then use one LNE-calibrated[30] sensors along with others whose temperature measurements differ from the calibrated one by less than 0.2 K (see Figure 14).
The main sources of radiations are suspected to be the MOT coils that stands very close to the chamber and the oven providing the strontium flux necessary for the experiment. The effect of the coils could be estimated from a differential measurement varying their temperature, changing the cooling power of the coils cooling system, running the other clock, Sr2, as a reference. An attempt for the measurement of the oven effect was done using an in-vacuum mechanical shutter placed between the oven and the main chamber. This shutter was initially meant for shutting the atomic flux during the trap stage of the clock sequence that was suspected of reducing the atoms lifetime in the trap because of the collisions they induce (see 6). However, it is as well probably shutting partially the way radiations emitted by the oven reach the trap region. We then carried out a differential measurement alternating clock cycle with and without the shutter activated. The resulting shift between the two configuration was compatible to

single table.
[30] LNE: Laboratoire Nationale de métrologie et d'Essais

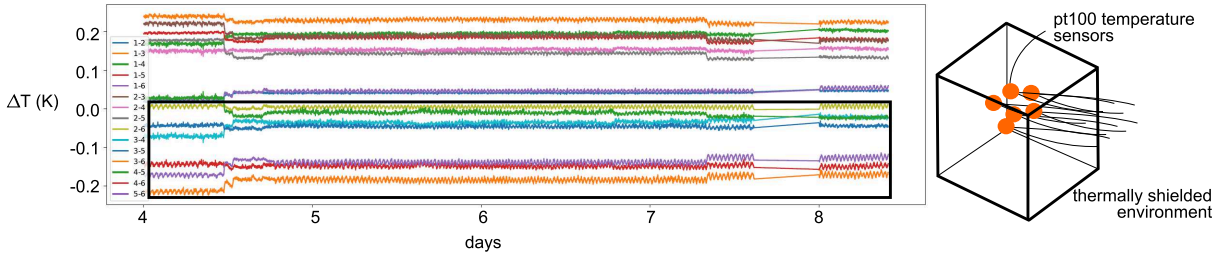


Figure 14: Calibration of the six pt100 temperature sensors to be glued on the vacuum chamber. The six sensors where packed together very close to each other in a temperature shielded environment. After days of thermalization we can assume the probe the same temperature. The reading difference can then be taken as a relative calibration between the sensors. However, one of them was calibrated by the LNE laboratory and can thus be used as an absolute reference. All the traces corresponding to the difference to that LNE-calibrated sensor are enclosed in the rectangle, meaning they over less than 0.2 K.

$0 \pm 1 \times 10^{-17}$ in fractional frequency unit.

In terms of uncertainty, as reported in [78], the black-body radiation estimation is dominated by the uncertainty on the temperature distribution around the atoms and amounts to $12 \times 10^{-18}$. It is the largest contribution to the budget. To enter the $10^{-18}$ region, other approaches are required (see for example [48, 49]).

### 4.6.2 Quadratic Zeeman shift

As explained in 5.1.2, the first order Zeeman shift can be canceled by alternating clock sequences probing the $m_{F=-9/2} \longrightarrow m_{F=-9/2}$ transition of the $1^{\mathrm{S}}_0 \longrightarrow {}^3\mathrm{P}_0$ clock transition and that probing the $m_{F=+9/2} \longrightarrow m_{F=+9/2}$ transition and making their difference $\overline{\nu} = (\nu_{m_F=-9/2} - \nu_{m_F=+9/2})/2$. However, in opposition to the first order Zeeman that is the same for both $m_F$ transition but with opposite signs, the second order Zeeman has same sign for both and is not canceled out. Its estimation in achieved carring out differential measurements varying the applied bias magnetic field splitting the Zeeman component. The resulting measured frequencies are then fitted with a parabola, the uncertainty on the quadratic coefficient giving the contribution to the uncertainty budget. Note that because we do not perform any direct measurement of the magnetic field, the quadratic part is considered as a function of the measured Zeeman shift, which is obtained as $\Delta\nu_Z = (\nu_{m_F=-9/2} + \nu_{m_F=+9/2})/2$.

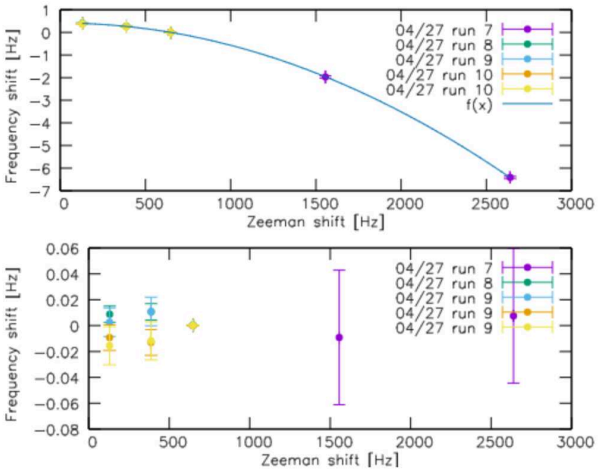


Figure 15: Estimation of the quadratic Zeeman shift (top) and of its uncertainty (bottom). The bottom graph represents the error made on the quadratic coefficient of the parabola fitting the data presented in the top graph.

#### 4.6.3 Lattice shifts

As for the black-body radiation shift, the response of the atoms to the lattice field is given by its poralizabilities. Here we use a plural form, polarizabilities instead of poralizability, to enhance the fact that in the effect is apprehended by decomposing it into several components, each of them being addressed independently. This is possible thanks to their particular structure and as well thanks to there relative magnitudes. This is discussed in section 5. The polarization of the atoms by the lattice light results in energy levels light-shifts, and therefore in a clock frequency shift, at least in the general case where the clock ground and excited states energies are not shifted by the amount.

Note that, depending on the light source used, the spectrum can present a non negligible amount of energy even far from the central frequency. This effect is similar to that of the black-body radiation. It as been studied in details in [78].

#### 4.6.4 Density shift

Our two strontium clocks are based on the $^{87}$Sr fermionic isotope. Hence, in the *naive* view of undistinguishable particles, s-wave collisions are forbidden by Pauli exclusion principle and p-wave collisions only are allowed, which are expected to be strongly suppressed at low temperatures (typical temperatures are of a few $\mu$K in our lattice trap) [50]. However, due to excitation inhomogeneity, the undistinguishability of the fermionic atoms is lost and s-wave collisions can occur [51] (see [78]). Before our 2018 comparison campaign (see section 7.2), we measured the effect by varying the number of atoms per site. This was achieved including a repumper pulse during the loading of the MOT to lattice at different timings. During this stage, the drain lasers send the atoms from the ground $^1$S$_0$ state to the $^3$S$_1$ from where they naturally decay to the two metastable states $^3$P$_2$ and $^3$P$_0$. These atoms do not see the MOT light anymore and are, if sufficiently cold, trapped by the lattice. The repumpers take them the other way back to the ground state. They then go through absorption-emission cycles of MOT light, which kick them out the trap (see section 9.2). Hence, varying the timing at which the repumper pulse is sent results in a variation the number of atoms left in the trap. We did not observe any effect above $10^{-17}$ in fractional frequency unit.

#### 4.6.5 Line pulling

Line pulling consists in slight changes of the clock resonance profile for a given $m_F \longrightarrow m_F$ transition contaminated by the proximity of the other $m_{F'}$ transitions. It then typically occurs in the case of imperfect spin polarization leaving population in $m_{F'}$ states aside from the one probed. It can result as well from clock laser ellipticity allowing for non-zeros $\Delta m_F$ transitions to occur or even from clock transition sidebands that result from tunneling between lattice sites [37]. The effect can be mitigated increasing the frequency separation of the different $m_F$ sublevels by increasing the bias magnetic field. However, this results in an increase on the uncertainty on the quadratic Zeeman shift as seen in the second plot of Figure 15 where it is apparent that the error bars on the quadratic coefficient uncertainty increase swiftly with the Zeeman shift, i.e. with the magnetic field amplitude. A compromise has then to be reached between this two effects, leading to the values presented in the budget table of Figure 12.

#### 4.6.6 Background collisions

This is a new line in our budget since the effect was overlooked till our measurement reported in section 6, which where inspired by investigations carried out at the NIST (National Institute of Standards and Technology, U.S.A.). The effect was considered till then as being at least one order of magnitude lower than what we measured. This therefore required an re-assessment of the corresponding uncertainty.

#### 4.6.7 Static charges

Some unexpected shift was revealed thanks to a direct clocks comparison at SYRTE in 2012 [82]. At that time the common budget for the two clocks was in the $10^{-16}$ region. A direct comparison of the two clocks was then expected to result in difference in fractional frequency of that order. However, the comparison revealed a discrepancy at the level of $10^{-13}$, by far incompatible to the claim of the budget. A careful investigation then showed this was due to the presence of charges stuck at the dielectric surfaces surrounding the atoms, resulting in a strong static polarization of the atoms, i.e. in a strong DC Stark shift. This is a typical case showing the importance of clock comparison for the validation of the budget

as well as the difficulty of operating at a metrological level requiring reproducibility in space and time. The solution found to remove these charges was to shine UV light on the surrounding of the atoms fort a few hours (see [82]), which is till now an unavoidable step in the preparation of the clocks each time their are involved in a metrological measurement, as international comparison campaign as those we report in section 7.2.

In the following part we focus on the study of two particular systematics: the hyperpolarizability leading to shift in the second order in trap field intensity and the shift induced by collisions with hot atoms of the residual background gas.

# Part II
# Study of two frequency shift sources: hyperpolarizability and hot collisions

This part is dedicated to two particular systematic effects that have been investigated during this thesis in some details. The first one, explored in section 5, is the hyperpolarizability which corresponds to the second non vanishing term appearing in the perturbation expansion of the effect of the trapping light on the atomic levels in the dipole approximation for the atom-field interaction. The reason we explore this effect is the poor consistency between the experimental estimations published so far and the discrepancy between these measurements and the theoretical prediction. Section 6 describes our investigation in the effect of hot collisions between trapped atoms and back ground gas particles on the clock transition. This is motivated by the fact such effect had been so far estimated extrapolating the model used for microwave clocks to the optical domain, which turned to lead to a serious underestimation of the effect. We propose our own model along with the first measurement of the effect on an optical strontium lattice clock.

## 5 Hyperpolarizability

In this section, we start with reminding the reasons we confine the neutral atoms in a lattice trap and the draw backs resulting from such trapping, namely lattice induced clock transition shifts. We then discuss briefly what are the low orders corrections one may think about, including geometric terms appearing when going beyond the dipolar (or long wavelength) approximation such as magnetic dipole and electric quadrupole, as well as non linear terms in the electric polarization of the atom. We give their hierarchy in order to sort out the relevant terms, resulting in keeping the dipolar terms only. A brief reminder about the classical treatment of non linear polarization then suggests an expected tensorial form for the these effects, which will indeed result from the Wigner-Ekart theorem in the classical treatment. We set (see appendix B) the frame of Floquet time dependent perturbation theory which is particularly well suited to the case of time-periodic Hamiltonians. We first derive the shift due to the linear dipole interaction with the fields, in the following referred to as the polarizability, also known as the first order AC Stark shift. It has been extensively explored in the frame of Cs primary standards and concepts developed there already have been successfully applied to first order lattice intensity shifts in optical lattice clocks and we content ourselves with a brief report on our last experimental estimates. The final part is dedicated to the study of the next non vanishing term in the perturbation series, the so-called hyperpolarizability, and includes a short discussion about its physical interpretation as well as our recent attempts to measure the effect.

### 5.0.1 Why a lattice trap?

Time and frequency standards based on atomic transitions probed by electromagnetic radiations demand a careful treatment of the effects due to motional degrees of freedom of the atoms. These effects stem from: i) the relative motion of the probed atoms with respect to the radiation source and ii) the transfer of the momentum of the absorbed photon to the atom. Considering a free atom of mass $m$ with momentum $\mathbf{p}$ in the laboratory frame, its momentum just after absorbing a photon with wave vector $\mathbf{k}$ will be $\mathbf{p}+\hbar\mathbf{k}$ , resulting in a kinetic energy gain

$$\Delta E_{\mathrm{K}} = \frac{(\mathbf{p}+\mathbf{k})^2}{2m} - \frac{p^2}{2m} = \frac{\hbar^2 k^2}{2m} + \frac{\hbar \mathbf{p}\cdot\mathbf{k}}{m} \tag{32}$$

while its internal energy will have changed by an amount $\Delta E_{\mathrm{int}} = \hbar\omega_0$ equal to the energy difference between the two atomic states coupled by the radiation. This means that the total amount of energy $\hbar\omega$ ($\omega$ the angular frequency of the photon in the laboratory frame) transferred from the field to the atom amounts to

$$\hbar\omega = \hbar\omega_0 + \frac{\hbar^2 k^2}{2m} + \frac{\hbar \mathbf{p}\cdot\mathbf{k}}{m} \tag{33}$$

The first term corresponds to the frequency we would like to use as a reference, the second shifts this reference by the recoil energy stemming from the transfer of momentum from the photon to the atom, and the third one, also known as the first order Doppler shift [12], depends on the atom initial momentum $\mathbf{p}$, resulting in broadening and distorting the line profile according to the atoms momenta distribution.

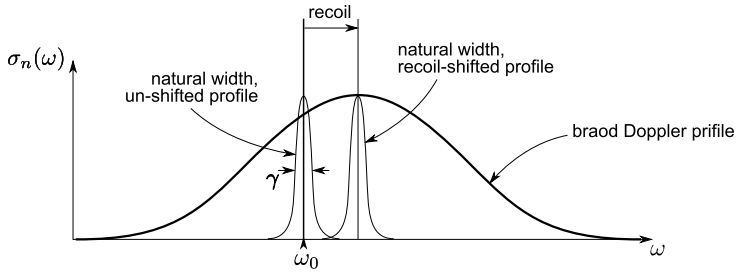


Figure 16: Schematic representation of free atoms absorption cross section $\sigma_n$ as a function of the light frequency $\omega$. The un-shifted profile of natural width $\gamma$ corresponds to the first term $\hbar\omega_0$ of equation 33. It is then shifted by the recoil energy $\hbar^2k^2/2m$ (second term of equation 33) and 1$^{\text{st}}$-order Doppler broadened by the third term $\hbar\mathbf{p}\cdot\mathbf{k}/m$ to which contribute all possible atoms centers of mass momenta $\mathbf{p}$ weighted by their thermal distribution. These three contributions add up to the recoil-shifted Doppler-broadened absorption profile (thick line).

Since the very first stage of atomic frequency standards development, this Doppler broadening and distortion of the atomic lines have been one of the main concerns and many efforts have been done to attempt subduing its detrimental effects on the clocks performances. For optical standards based on cold trapped ions or neutral atoms, the cancellation of both the recoil and Doppler shifts relies on the realization of the Lamb-Dicke regime [135] which is obtained confining the atoms to regions with spacial extension shorter than the wavelength of the clock light. In this regime, the atoms behave as those trapped in a solid state crystalline matrix, resulting in the transfer of the absorbed photon momentum to the whole structure [139]. Hence, the corresponding recoil energy shift appearing in equation 33 is rescalled by the ratio $m/M$ where $M$ is the mass of the whole system[31] and is then negligible compared to all the transition spectrum features and can be dropped out, enabling *recoilless* spectroscopy [137, 138, 139].

Regarding the first-order Doppler shift, its cancellation arises from the quantization of the motional degrees of freedom of the trapped atoms due their confinement. To simplify the discussion, let us reduce the problem to the confinement in the longitudinal direction of the trap only. In the case of a harmonic trap profile (which is a good approximation in the case of sufficiently cold atoms in a lattice), the motion of each atom center of mass can be described as a quantum harmonic oscillator, i.e. by means of Fock states $|n\rangle$, $n = 0, 1, ...$ The global state of the atom, i.e. encompassing both internal and external degrees of freedom, can then be written as a combination of direct product states of the form $|x\rangle \otimes |n\rangle \equiv |x, n\rangle$ where $x = g$ for internal ground state, $e$ for excited state. A photon to be absorbed then needs to couple $|g, n\rangle$ to $|e, m\rangle$. The absorption spectrum is determined by the absorption cross sections $\sigma_n(\omega)$ corresponding to a photon absortpion by an atom in initial state $|g, n\rangle$, which is proportional to [137]

$$\sum_m \left| \frac{(1/2)\gamma \langle m| e^{-ikx} |n\rangle}{\omega_0 - \omega + (m-n)\Omega - (1/2)i\gamma} \right|^2 \tag{34}$$

where $k$ is the radiation wave number in the laboratory frame, $x$ the location of the absorbing atom, $\gamma$ the natural width of the $|g\rangle \rightarrow |e\rangle$ transition and $\Omega$ the frequency of oscillation of the atoms in the longitudinal direction of the trap. This expression let the sideband structure of the absorption spectrum clearly appear in the case $\gamma \ll \Omega$. Indeed, in such case, the cross section is significant only for $|\omega - (\omega_0 + (m-n)\Omega)| \lesssim \gamma/2$. On top of that, the broad profile of the spectrum is determined by the $\left|\langle m| e^{-ikx} |n\rangle\right|$ which turns out to match the Doppler broadened profile corresponding to the average temperature of the trapped atoms centered at $\omega_0 + (\hbar k^2)/2m$ [137] i.e. shifted from the recoilless transition frequency $\omega_0$ by a recoil (see figure 17 for a schematic representation). In the case of neutral atoms trapped in a 1D lattice, the trap depth is set to sufficiently high values (usually expressed in recoil energy $\hbar^2k^2/2m$, $k$ the clock radiation wave number and $m$ the atom mass) for the carrier ($n = 0$) to dominate the spectrum, resulting in reducing the line pulling effect. Moreover, the dynamics in the lattice transverse plane and the coupling between the longitudinal and transverse motional degrees of freedom of the atoms induce a distortion of the absorption sidebands [106]. Fitting the carrier plus first-order

[31] the lattice cavity structure in the case of neutral atoms optical lattice clocks as that considered within the frame of this thesis.

sidebands spectrum provides the trap depth as well as the temperatures in both lattice longitudinal and transverse direction (see figure 17).
However, first order Doppler effects cancellation resorting on lattice trapping present a serious drawback: lattice induced light shifts.

For low trap depths no larger than a few dozens of energy recoils and for a targeted accuracy of a few $10^{-17}$ in relative frequency, a good understanding of shifts of first order in trap depth, i.e. scaling as $\mathcal{E}_0^2 \propto U_0$, is sufficient. Indeed, it has been shown that one can find a lattice wavelength, the so-called magic wavelength $\lambda_m$, such that the first order lattice induced shift is the same for both clock ground and excited states, resulting in a vanishing shift for the clock transition. The first order shifts in trap depth are referred to as polarizabilities and are discussed in section 5.1.

Nevertheless, improvements in both systematics control and estimation enabling considering target accuracies in the $10^{-18}$ range as well as the achievement of high trap depths of the order of a few thousands of $E_r$ with current setups demands a better understanding of the lattice induced shifts and require investigating higher order dipolar shifts corrections (see section 5.2) and may even demand scrutinizing geometrical corrections such as magnetic dipole and electric quadrupole terms. This is discussed in section 5.0.2.

### 5.0.2 Perturbations induced by the trap

The lattice trap used to obtain the Lamb-Dicke regime results, in our case, from an intra cavity linearly polarized electromagnetic standing wave whose electric field amplitude along the longitudinal axis of the lattice reads

$$E(x,t) = E\cos(kx)\cos(\omega t) \tag{35}$$

$k$ the corresponding wave number, $x$ the longitudinal coordinate with its origin at a field anti-node. Based on the long wavelength approximation amounting to considering the lattice field wavelength to be much larger than the atomic radius, which is typically the case for optical wavelength and ground state atoms, and which is equivalent to $|k\delta x| \ll \pi$, $\delta x$ the size of the atomic wave function, one usually consider the lattice-atoms interaction to be driven by the dipolar interaction Hamiltonian $\hat{H}_{\text{Dip}} = -\hat{\mathbf{d}} \cdot \mathbf{E}$, where $\hat{\mathbf{d}}$ stands for the atomic dipole induced by the field $\mathbf{E}$. Such an interaction affects both the internal and the external degrees of freedom (DOF) of the atoms. Internally it results in light shift of the electronic transitions depending on the field amplitude and frequency at the atom location, while the external effect results in a force acting on the atom center of mass proportional to the field amplitude gradient and depends on the field frequency as well. In the dipolar approximation the electronic cloud explore a region around the center of mass location over which the field amplitude is constant. The internal and external DOF then decouples which is rendered in the resulting potential expression

$$V(x,\omega) = \hat{V}_{E_1}(\omega)\cos(k\hat{x}) \tag{36}$$

where the variable $\hat{x}$ is the center of mass position operator and thus acts within the external DOF space whereas $\hat{V}_{E_1}(\omega)$ acts on the internal atomic DOF. For well localized trapped atoms confined at anti-nodes of the standing wave, the electronic wave function explores regions where $\cos(kx) \simeq 1$ to a good approximation. The linear part of the induced dipole is proportional to the field amplitude meaning that $\hat{V}_{E_1}(\omega)$ is at least quadratic in $E$, or equivalently linear in lattice field intensity $U_0 = |E|^2$. The resulting potential can then be expressed as

$$U^{(1)}(\omega) = -\alpha^{E_1}(\omega)E^2 = -\alpha^{E_1}(\omega)U_0 \tag{37}$$

where the exponent (1) stands for the fact we kept the first order term in field intensity $U_0$ only in the dipolar interaction, and $\alpha^{E_1}$ is the polarisability operator investigated in section 5.1. As mentioned at the end of section 5.0.1, the effects of $U^{(1)}$ in terms of clock shifts are well understood and characterized but recent advances in accuracy improvement of optical clocks rose the necessity of a better understanding of higher order contributions of the atom-lattice interaction potential. Furthermore, even before moving to higher terms in field amplitude, following the approach of [56], we may wonder whether higher order geometric corrections should be taken into account, considering for example magnetic dipole and electric quadrupole interactions, accounting for the fact that the field amplitude is actually not constant over the extant of the electronic cloud, leading to a lattice-atom interaction of the form (see [56],[57] and [58])

$$V(\omega,x) = \hat{V}_{E_1}(\omega)\cos(kx) + \left(\hat{V}_{M_1}(\omega) + \hat{V}_{E_2}(\omega)\right)\sin(kx) \tag{38}$$

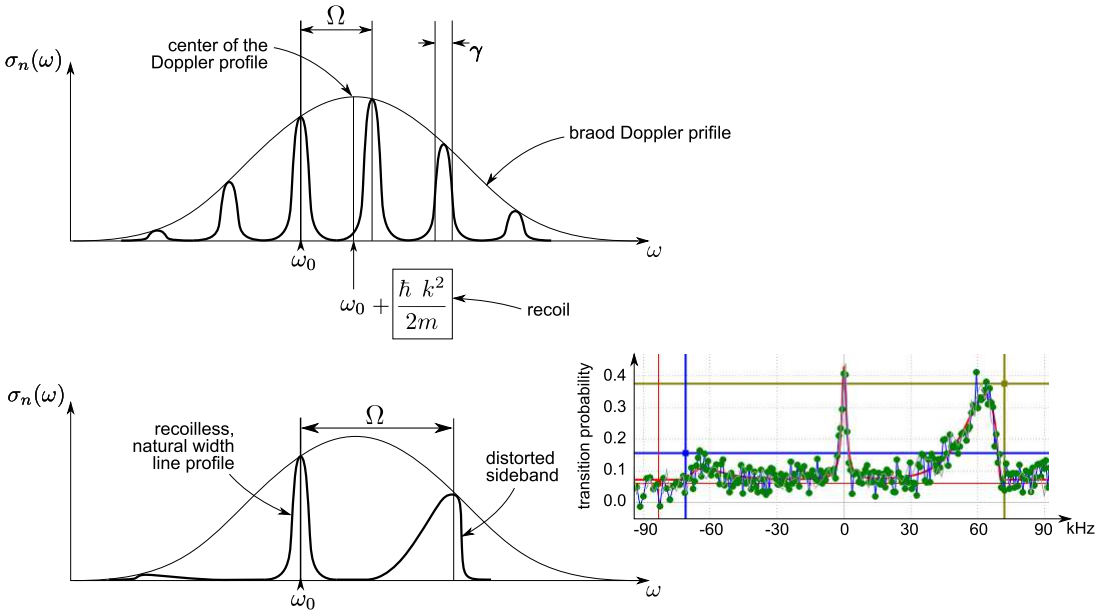


Figure 17: Schematic representation of the recoilless normalized absorption cross section of spatially confined atoms.
**Top**: When the atoms are confined in a trap (e.g. as are neutral atoms or ions in optical clocks) they behave like absorbers bound in a crystalline matrix. Because of the confinement the motional degrees of freedom of the atoms (or ions) are quantized and they spatially oscillate at a frequency $\Omega$ determined by the trap depth. This results in a multiple sidebands structure at frequencies $\omega_0 + n\Omega$ and width the natural width $\gamma$ of the internal atomic $|g\rangle \rightarrow |e\rangle$ transition. The over all envelop of the spectrum is determined by the Doppler profile shifted by one recoil energy $\hbar^2 k^2/2m$ ($\hbar k^2/2m$ in frequency units). Moreover the momenta transferred from the absorbed photons to the atoms are absorbed by the whole mechanical structure hosting the trap (cavity mirrors and their holding system e.g. in the case of neutral atoms trapped in an optical cavity hosted lattice) with a macroscopic mass. The recoil energy associated to this mass is by far negligible compared with all the spectrum features of the absorption line meaning that the corresponding shift can be neglected. Hence the carrier resonance ($n = 0$) occurs at the un-shifted frequency $\omega_0$.
**Bottom**: In practice, for neutral atoms optical lattice clock, the trap depth is such that the sidebands separation is sufficiently large for the carrier to dominate the spectrum (resulting in a reduced line pulling, i.e. shift and line shape distortion induced by neighboring sidebands). The first order sidebands are nevertheless still visible but their shape is distorted due to the dynamics occurring in the lattice transverse plane where the confinement is much weaker than in the longitudinal direction. The frequency separation between carrier and first-order sidebands gives the trap depth, the ratio between the intensity of the sideband at $\omega_0 + \Omega$ (blue sideband) and that of the sideband at $\omega_0 - \Omega$ (red sideband) gives the longitudinal temperature. Finally, a fit of the distortion of the blue and red sidebands gives the transverse temperature [106]. On the bottom right are displayed experimental data. The graph shows the transition probability (unitless, proportional to the absorption cross section) as a function of the detuning to carrier frequency (in kHz). The green points are the measured data, the solid red line is the fit (other color bars are cursors use to set the initial fitting parameters). In this particular case, the trap depth was found to be 100 energy recoil, the longitudinal temperature 1.7 $\mu$K and the transverse temperature 6.5 $\mu$K.

where it is visible the magnetic dipolar and electric quadrupolar terms are in quadrature with the electric dipolar interaction. With this geometrically remodeled potential $U^{(1)}$ is corrected to (see [57], [58])

$$U^{(1)}(\omega, x) \simeq -\left[\alpha^{E_1}(\omega) - \{\alpha^{M_1}(\omega) + \alpha^{E_2}(\omega)\}k^2x^2\right] E^2 \tag{39}$$

It is *a priori* not clear whether the added geometric terms would dominate over the next correction in power of electric field amplitude to the dipole-field interaction. As will be shown in section B.2, the next non vanishing term in the dipole interaction potential is in $E^4$, i.e. in $U_0^2$. This correction is usually referred to as the hyperpolarizability, and is depicted by the hyperpolarizability tensorial operator $\beta(\omega)$. Adding this term to equation 39 leads to

$$U(\omega, x) \simeq -\left[\alpha^{E_1}(\omega) - \{\alpha^{M_1}(\omega) + \alpha^{E_2}(\omega)\}k^2x^2\right] E^2 - \beta(\omega)E^4 \tag{40}$$

Though the terms hierarchy of 40 still remains to be fully clarified, we estimated, based on experimental measurements, that the contribution of the magnetic dipolar and electric quadrupolar interaction to the clock frequency shift is of the order of $10^{-7}$ lower than that of the electric dipolar around the magic wavelength and is thus suspected to be small enough to be neglected within our uncertainty limitation. Indeed, we estimated a lattice induced relative uncertainty around $3\times10^{-18}$ whereas our current stability gives a limited resolution of roughly $10^{-17}$. In the following, we focus our study on the electric dipolar terms only, meaning we consider a lattice potential of the form

$$U(x) \simeq -\alpha(\omega)E^2 - \beta(\omega)E^4 \tag{41}$$

where $\alpha \equiv \alpha^{E_1}$.

As depicted in section 5.0.3 below, a classical description of the polarizability (linear and non-linear) suggests a tensorial form for the $\alpha$ and $\beta$ operators. Afterwards, in section B.2, the basics of Floquet perturbation theory are set, giving a powerful frame for the treatment and computation of these operators which broad lines are given in section 5.1 and 5.1.1 for the polarizability and in section 5.2.1 for the hyperpolarizability.

### 5.0.3 Classical polarizability and irreducible tensor decomposition

The aim of this paragraph is to introduce the notion of tensors and their irreducible decompositions which is the standard language for light shifts formalism and computation.

The response of a dielectric media, e.g. an ensemble of neutral atoms, to an external electric field $\mathbf{E}$ consist in its polarization $\mathbf{P}$, i.e. the production of an electric field that last as far as the external field is applied. Classically, it can be expended in multiple variables power series of the external field components as

$$\mathbf{P} = \sum_k \mathbf{P}^{(k)} = \sum_k \overline{\alpha}_k \overline{\mathbf{E}^k} \tag{42}$$

where each $\mathbf{P}^{(k)}$ is a three components vector, $\overline{\alpha}_k = [\alpha^k_{i_1,\dots,i_{k+1}}]_{i_j=1,\dots,3}$ a rank k+1 tensor[32], $\overline{\mathbf{E}^k} = [E^k_{i_1,\dots,i_k}]_{i_j=1,\dots,3}$ a rank k tensor, with

$$E^k_{i_1,\dots,i_k} = \prod_{j=1,\dots,k} E_{i_j} \tag{43}$$

where $\overline{\mathbf{E}^0} = \mathcal{I}$ the identity operator. Each $\mathbf{P}^{(k)}$ is rank-1 tensor, or a vector, whose components are given by

$$\mathbf{P}^{(k)}_i = \sum_{i_2,\dots,i_{k+1}} \alpha^k_{i,i_2,\dots,i_{k+1}} E_{i_2} \times \dots \times E_{i_{k+1}} \tag{44}$$

Note that the $0^{th}$ order term $\mathbf{P}^{(0)}$ corresponds to an intrinsic dipole, since it does not depends on the application of an external electric field.

[32] give requirement for a set of $d^k$ components to be a rank k tensor of dimension d

The interaction energy $\mathcal{E} = -\mathbf{P}.\mathbf{E}$ then reads

$$\mathcal{E} = \sum_k \mathcal{E}_k = -\sum_k \mathbf{P}^{(k)}.\mathbf{E} \tag{45}$$

with

$$-\mathcal{E}_k = \mathbf{P}^{(k)}.\mathbf{E} = \sum_{i_1,\ldots,i_{k+1}} \alpha^k_{i_1,\ldots,i_{k+1}} E_{i_1} \times \ldots \times E_{i_{k+1}} \tag{46}$$

which scales as $|\mathbf{E}|^{k+1}$. As explained in appendix A, each of the rank k tensors $\overline{\alpha}_{k-1}$ can be decomposed as a sum of k+1 irreducible tensors of ranks $i = 0, ..., k$. The rank $i = 0$ irreducible component is referred to as the scalar irreducible component, that of rank $i = 1$ as to the vector irreducible component. Higher rank components are simply referred to as higher rank tensor components. This decomposition plays a key role for the computation of the quantum polarizabilities.

When moving to the semi-classical picture where the internal atomic degrees of freedom are quantized but the field still classical, the electronic wave functions symmetries force components with even indices $\mathcal{E}_{k=2p}$ to vanish, at least in the case of non degenerate energy levels. Hence, the two first terms contributing to the energy shift given by 42 are

$$\mathcal{E}_1 = \sum_{i,j} \alpha^1_{ij} E_i E_j, \quad \mathcal{E}_3 = \sum_{i,j,k,l} \alpha^3_{ijkl} E_i E_j E_k E_l \tag{47}$$

which scale as $|\mathbf{E}|^2$ and $|\mathbf{E}|^4$ respectively. $\mathcal{E}_1$ corresponds to the polarizability while $\mathcal{E}_3$ is referred to as the hyperpolarizabillity. When the field of interest is that of an oscillating light beam, these two terms contribute to the total light shift experienced by the trapped atoms. While the effect of the linear polarizabilty $\mathcal{E}_1$, also known as first order AC Stark shift[33], has been extensively explored and is well understood and estimated (for both Alkali [53],[54],[55] and Alkaline earth [56],[57],[58],[59],[60],[61],[62] atoms), a proper estimation and understanding of the hyperpolarizability reamains to be achieved. Our contribution to this scope is discussed in section 5.2.

## 5.1 Quantum polarizability

In the classical case, the tensorial structure of the polarizability is *imposed* a priori (equation 44), the reason being that it is the most general form to express a dependence on the components of the polarizing electric field $\mathbf{E}$ to all possible order (in the dipole approximation). In other words, any polynomial of order $k$ in the variables $E_{j=1,2,3}$ (such as the polarization components of order $k$: $\mathbf{P}^{(k)}_i$) can be expressed in a tensorial form as in equation 44. Once this general structure has been *imposed*, the symmetries of the system are used to reduce the number of free parameters, i.e. the number of independent tensor coefficients $\alpha^k_{i_1,..,i_{k+1}}$, for a given order $k$ (see for example [52]). In the quantum case, on the other hand, the tensorial structure of the poloarizabiltiy emerges *naturally* from the perturbative treatment, as exposed in section 5.1.1. Indeed, the perturbative treatment results in expressions containing products of scalar products which can be expressed in a tensorial form (see equation 55).

In the context of AC Stark shifts, Floquet perturbation theory is is particularly well suited since it was developed to deal with time-periodic perturbations, such as that due to radiation fields oscillations. Its basics and useful results are exposed in appendix B.

In the frame of quantum treatment of atomic polarizabilities, there is an ambiguity on the vocabulary that needs here to be lifted. While the term *polarizability* usually refers to the general phenomenon of a medium response to an external field to all orders, it is restricted in this frame to the first non vanishing term in the Floquet pertubative treatment of the atomic response to an electromagnetic radiation obtained after operating the approximations exposed previously in section 5.0.2 on the resulting potential. The polarizability then corresponds to the second order correction term $\mathcal{E}^{(2)}_{nq}$ obtained in appendix B (equation 602). It is a combination of terms of the form (see appendix B)

$$\langle\langle nq|V|n'q'\rangle\rangle\langle\langle n'q'|V|nq\rangle\rangle \tag{48}$$

[33] first order in field intensity, i.e. second order in field amplitude

Dropping out the vanishing combinations we are left with the expression

$$\mathcal{E}^{(0)}_{nq} = \sum_{n' \neq n} \left( \frac{\langle n| V_+ |n'\rangle \langle n'| V_- |n\rangle}{E_{n'} - E_n - \hbar\omega} + \frac{\langle n| V_- |n'\rangle \langle n'| V_+ |n\rangle}{E_{n'} - E_n + \hbar\omega} \right) \tag{49}$$

where we used the relation $\mathcal{E}^{(0)}_{nq} = E_n + q\hbar\omega$ to rewrite $\mathcal{E}^{(0)}_{n'q\pm1} - \mathcal{E}^{(0)}_{nq}$ into $E_{n'} - E_n \pm \hbar\omega$. We did not simplify terms of the form $\langle n| V_\pm |n'\rangle \langle n'| V_\mp |n\rangle$ into $|\langle n| V_\pm |n'\rangle|^2$ because the extended form facilitates the physical interpretation of the polarizability corrections as well as the possibility of expressing it as the expectation value of the the operator $\hat{V}^{EE}$, i.e. $\mathcal{E}^{(0)}_{nq} = \langle n| \hat{V}^{EE} |n\rangle$, where $\hat{V}^{EE}$ is defined as

$$\hat{V}^{EE} = \sum_{n' \neq n} \left( \frac{V_+ |n'\rangle \langle n'| V_-}{E_{n'} - E_n - \hbar\omega} + \frac{V_- |n'\rangle \langle n'| V_+}{E_{n'} - E_n + \hbar\omega} \right) \tag{50}$$

the computation of which is addressed in section 5.1.1. For a specific state $|n\rangle$, this energy shift can be expressed the same way as $\mathcal{E}^{(0)}_{nq} = \langle n| \hat{V}^{EE}_{|n\rangle} |n\rangle$ where

$$\hat{V}^{EE}_{|n\rangle} = \sum_{n'} \left[ \Big( |n\rangle \langle n| V_+ |n'\rangle \langle n'| \Big) \Big( |n'\rangle \langle n'| V_- |n\rangle \langle n| \Big) \frac{1}{E_{n'} - E_n - \hbar\omega} \right] \tag{51}$$

$$+ \sum_{n'} \left[ \Big( |n\rangle \langle n| V_- |n'\rangle \langle n'| \Big) \Big( |n'\rangle \langle n'| V_+ |n\rangle \langle n| \Big) \frac{1}{E_{n'} - E_n + \hbar\omega} \right] \tag{52}$$

Each of the operators $|f\rangle \langle f| V_\pm |i\rangle \langle i|$ can be physically interpreted as corresponding to the process of starting in state $|i\rangle$ and ending up in state $|f\rangle$ through the emission or the absorption of a photon with optical frequency $\omega$, depending on the subscript sign of $V_\pm$ (more precisely, $V_-$ corresponds to the absorption of a photon, $V_+$ to an emission). Hence $\hat{V}^{EE}_{|n\rangle}$ is a weighted combination of operators corresponding to all possible 2-photons processes such as that depicted in Fig. 18, with the only constraint being that the loop should start and end in state $|n\rangle$.

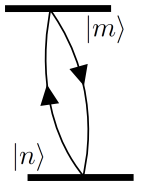


$|n\rangle \to |m\rangle \to |n\rangle$

Figure 18: 2-photons transition cycles involved in the polarizability effect

The fact that the lattice light is out of resonance for all the possible single photon transitions involved in the polarizability effect plays here an important role. Indeed, were one of the $|n\rangle \longleftrightarrow |n'\rangle$ transition resonant, the denominator $E_{n'} - E_n - \hbar\omega$ would have been very small and the rotating wave approximation would have ruled out all the other terms. Here, the non resonance condition implies that no terms can be overlooked in the expression 51, even those appearing in the second summation, even though they correspond to process where a photon is first emitted before a second one is absorbed ($V_+$ appears before $V_-$). This means that in spite its full validity in terms of states explored during the 2-photons process underlying the polarizabilty effect, Fig. 18 might be misleading in term of chronology since it seems to imply that the photon is first absorbed and then, in a second time, re-emitted. However, the non resonant feature of the process implies the system can start with a photon emission, the absorption occurring after. This is better rendered with the diagrammatic representations of Fig. 19.

### 5.1.1 Tensor decomposition of the polarizability

As suggested from a full classical approach, we expect the polarizability, understood as the second order perturbation in electric field amplitude, to take a tensorial form, more precisely to be encompassed in a rank-2 3-dimensional tensor. This tensorial form naturally results from the expression of the polarizability operator given in equation 49. We follow the development done in [53].

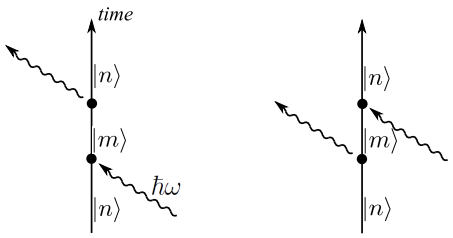


Figure 19: diagrammatic representation of the two types of 2-photons processes involved in the polarizability effect. On the left: classically allowed process, corresponding to operators of the form $|n\rangle\langle n|V_+|m\rangle\langle m|V_-|n\rangle\langle n|$. On the right, process usually ruled out by the rotating wave approximation (at least when $E_m > E_n$), corresponding to operators of the form $|n\rangle\langle n|V_-|m\rangle\langle m|V_+|n\rangle\langle n|$

At a given longitudinal position $x$ in the lattice where the electric field amplitude reads $E \equiv E(x)$, from the lattice potential expression as given by 611, equation 50 can be recast as

$$\hat{V}^{EE} = |E|^2 \left[ (\boldsymbol{\varepsilon}^* \cdot \mathbf{d})(\boldsymbol{\varepsilon} \cdot \mathcal{R}_- \mathbf{d}) + (\boldsymbol{\varepsilon}^* \cdot \mathbf{d})(\boldsymbol{\varepsilon} \cdot \mathcal{R}_+ \mathbf{d}) \right] \tag{53}$$

where the operators $\mathcal{R}_\pm$ are given by

$$\mathcal{R}\pm = \sum_{\alpha' j' m' \neq \alpha j m} \frac{|\alpha' j' m'\rangle\langle \alpha' j' m'|}{E_{\alpha' j' m'} - E_{\alpha,j,m} \pm \hbar\omega} \tag{54}$$

It can be shown that (see [53] for references), for commuting vector operators,

$$(\mathbf{A}\cdot\mathbf{B})(\mathbf{A}'\cdot\mathbf{B}') = \sum_{k=0,1,2} (-1)^k \{\mathbf{A}\otimes\mathbf{A}'\}^{(k)} \cdot \{\mathbf{B}\otimes\mathbf{B}'\}^{(k)} \tag{55}$$

Hence, $\hat{V}^{EE}$ takes the form

$$\hat{V}^{EE} = |E|^2 \sum_{k=0,1,2} (-1)^k \{\boldsymbol{\varepsilon}^*\otimes\boldsymbol{\varepsilon}\}^{(k)} \cdot \left[ \{\mathbf{d}\otimes\mathcal{R}_-\mathbf{d}\}^{(k)} + (-1)^k \{\mathbf{d}\otimes\mathcal{R}_+\mathbf{d}\}^{(k)} \right] \tag{56}$$

The scalar product between the resulting tensors is obtained from expression 581, leading to

$$\hat{V}^{EE} = |E|^2 \sum_{k=0,1,2} (-1)^k \sum_{q=-k,..,k} (-1)^{-q} \{\boldsymbol{\varepsilon}^*\otimes\boldsymbol{\varepsilon}\}^{(k)}_q \left[ \{\mathbf{d}\otimes\mathcal{R}_-\mathbf{d}\}^{(k)}_{-q} + (-1)^k \{\mathbf{d}\otimes\mathcal{R}_+\mathbf{d}\}^{(k)}_{-q} \right] \tag{57}$$

where the irreducible components $\{\boldsymbol{\varepsilon}^*\otimes\boldsymbol{\varepsilon}\}^{(k)}_q$ (see appendix A) can be easily obtained from 581 expressing the unit polarization vector $\boldsymbol{\varepsilon}$ in the spherical basis given in 579 (see [53] and appendix A). The tough part of the job consists in computing the irreducible components of $\{\mathbf{d}\otimes\mathcal{R}_\pm\mathbf{d}\}^{(k)}$. This achieved using the Wigner-Eckart theorem (appendix A). Remembering that the energy shift of the atomic state $|ajm\rangle$ is given by $\langle ajm|\hat{V}^{EE}|ajm\rangle$ we then need to compute the matrix elements of the terms between square brackets in equation 57 which, using 581, are given by

$$\langle ajm| \{\mathbf{d}\otimes\mathcal{R}_\pm\mathbf{d}\}^{(k)}_{-q} |ajm\rangle = \sum_{q_1,q_2=-1,0,1} C^{k,-q}_{1q_1,1q_2} \sum_{a'j'm'} \frac{\langle ajm|\, d_{q_1}\, |a'j'm'\rangle\langle a'j'm'|\, d_{q_2}\, |ajm\rangle}{E_{a'j'm'} - E_{a,j,m} \pm \hbar\omega} \tag{58}$$

where the summation over the $\{a'j'm'\}$ excludes the indices corresponding to the state whose energy correction we want to compute, $|ajm\rangle$. The computation is taken a step further applying the Wigner-Eckart theorem the factors at the numerator of the *r.h.s.* of equation 58, i.e.

$$\langle ajm|\, d_{q_1}\, |a'j'm'\rangle = C^{j'm'}_{jm,1q_1} \frac{\langle aj\|\mathbf{d}\|a'j'\rangle}{\sqrt{2j'+1}} \tag{59}$$

Finally, from equation 57, the energy shift $\Delta E_{ajm} = \langle ajm|\hat{V}^{EE}|ajm\rangle$ can be expressed as a sum of three component, corresponding to each value of index $k$ appearing in the the summation 57 and therefore can be written as

$$\Delta E_{ajm} = h\left(k^s_{ajm} + k^v_{ajm} + k^t_{ajm}\right) U_0 \tag{60}$$

where $U_0 = |E|^2$ at the position of a lattice node and where $k^s_{ajm}$ stands for scalar (k=0), $k^v_{ajm}$ the vectorial (k=1) and $k^t_{ajm}$ the tensorial (k=2) polarizabilities, in frequency shift per recoil energy, and are given by

$$k^r_{ajm} = \frac{1}{h} \sum_{-r \leq q \leq r} (-1)^{q+r} \{\boldsymbol{\varepsilon}^* \otimes \boldsymbol{\varepsilon}\}^{(r)}_q \alpha^r_{ajm} \tag{61}$$

$$\alpha^r_{ajm} = \sum_{-1 \leq q_1, q_2 \leq 1} \sum_{a'j'm'} C^{r,-q}_{1q_1,1q_2} C^{j'm'}_{jm,1q_1} C^{jm}_{j'm',1q_2} \frac{|\langle aj \| \mathbf{d} \| a'j' \rangle|^2}{\sqrt{(2j+1)(2j'+1)}} (R_- + (-1)^r R+) \tag{62}$$

$$R_\pm = \frac{1}{E_{a'j'm'} - E_{a,j,m} \pm \hbar\omega} \tag{63}$$

where $r = s$, $v$ and $t$ and has to be replaced by respectively 0,1 and 2 when appearing as indices or exponents in the *r.h.s.* of 61. The frequency shift $\Delta\nu$ of the transition $|ajm\rangle \to |a'j'm'\rangle$ is obtained from 60 as $h\Delta\nu = \Delta E_{a'j'm'} - E_{ajm}$ and reads

$$\Delta\nu = \left(\Delta k^s + \Delta k^v + \Delta k^t\right) U_0 \tag{64}$$

where $\Delta k^r = k^r_{a'j'm'} - k^r_{ajm}$.

### 5.1.2 Polarizability in presence of magnetic field

The expression of the lattice light shift derived above was obtained considering the total Hamiltonian was the summation of the free atom Hamiltonian plus the dipole interaction. But in actual operation of the clock, we set a constant magnetic field during the clock interrogation and address one of the Zeeman sub-levels at a time. We do so to cancel the first order Zeeman shift that would result from any uncontrolled residual magnetic field. The ground $^1S_0$ and excited $^3P_0$ states of the clock transitions each contain 10 Zeeman sub-levels corresponding to the possible values for total angular momentum projection on any quantization axis $m_F = -9/2, .., +9/2$. This sub-levels are degenerate in absence of magnetic field. Canceling or shielding the environmental magnetic field (that typically stems from bulky metallic objects set around the vacuum chamber, from electrical devices running in the laboratory room or even from the nearby underground railways lines activity) is practically impossible and we are always left with a residual DC magnetic field $\delta\mathbf{B}$ inducing a frequency shift dependent on the considered $m_F$ sub-level given, to the first order in field amplitude, by $\Delta\nu_{m_F} = -(\mu_B \delta_g/h) m_F \delta B$ ($\mu_B$ the Bohr magneton, $\delta_g$ the differential Landé factor $\delta B = \|\delta\mathbf{B}\|$). Typical residual fields are not strong enough to resolve the $m_F \to m'_F$[34] transition. We then add a bias field $\mathbf{B}$, typically of the order of a few 10 $\mu$T to clearly resolve the Zeeman splitting of the transition, i.e. to have $\left|\Delta\nu_{m_F} - \Delta\nu_{m_{F'}}\right| \gg \Delta\nu_S$ where $\Delta\nu_S$ is our spectroscopy resolution, of the order of a few Hertz. We then probe successively the $m_F = -9/2 \to m'_F = -9/2$ and the $m_F+ = 9/2 \to m'_F = +9/2$ occurring respectively at $\nu_{m_F=\pm 9/2} = \nu_0 \pm (9/2)(\mu_B \delta_g/h)\|\mathbf{B} + \delta\mathbf{B}\|$ where $\nu_0$ is the transition frequency in absence of magnetic field. The average of two successive clock interrogations then gives

$$\overline{\nu} = \frac{\nu_{m_F=9/2} + \nu_{m_F=-9/2}}{2} = \nu_0 \tag{65}$$

allowing for the cancellation of the first order Zeeman shift. Hence the actual Hamiltonian must account for the interaction with the bias magnetic field $\mathbf{B}$. Then good quantum numbers for the unperturbed states used for the Floquet correction calculations are no longer $j$ and $m$ but $F$ and $m_F$. This bias field imposes a quantization axis in the direction given by the unitary vector $\boldsymbol{\varepsilon}_B = \mathbf{B}/\|\mathbf{B}\|$[35]. In absence of magnetic field, the unperturbed Hamiltonian was isotropic, this spherical symmetry being broken by the direction of the lattice field polarization. This means the problem was invariant under angular change of the polarization direction. On the other hand, when the bias magnetic field is set, the unperturbed Hamiltonian it-self is not invariant under rotations . Hence, the relative configuration between the bias field and the lattice polarization has to be taken into account and the problem is no longer invariant under changes of the lattice polarization orientation. When this effect is taken into account, equation 64 has to be slightly modified adding geometrical factors and the transition frequency shift is given by (see [54], [59] and [60])

$$\Delta\nu = \left(\Delta k^s + \Delta k^v m_F \xi \vec{\varepsilon_k} \cdot \vec{\varepsilon_B} + \Delta k^t \gamma\right) U_0 \tag{66}$$

[34] $m_F$ being the being the sub-level of the ground involved in the transition probed, $m'_F$ being that of the excited state

[35] The actual direction should take into account the residual field $\delta\mathbf{B}$ i.e. be defined as $\boldsymbol{\varepsilon}_B = (\mathbf{B} + \delta\mathbf{B})/\|\mathbf{B} + \delta\mathbf{B}\|$, but the $\|B\| \gg \|\delta\mathbf{B}\|$ this is negligible

where $\xi\vec{\varepsilon_k} = i\vec{\varepsilon}^* \wedge \vec{\varepsilon}^*$ is the ellipticity of the lattice polarization and

$$\gamma = (3|\vec{\varepsilon}^* \cdot \vec{\varepsilon_B}|^2 - 1)[3m_F^2 - F(F+1)] \tag{67}$$

### 5.1.3 Polarizability measurements

We now would like to give a hint about how the three contributions to the lattice shift, scalar, vectorial and tensorial, could be measured and characterized experimentally. One of the main feature of the lattice shift decomposition as expressed by 66 from which we can take advantage is the particular dependency of each term on $m_F$. The scalar term does not depend on it while the vector term scale as $m_F$ and the tensor term as $m_F^2$. In term of parity, this gives

$$\Delta\nu^s_{-m_F} = \Delta\nu^s_{+m_F} \qquad \Delta\nu^v_{-m_F} = -\Delta\nu^v_{+m_F} \qquad \Delta\nu^t_{-m_F} = \Delta\nu^t_{+m_F} \tag{68}$$

where $\Delta\nu^X$ is equal to $\Delta k^X$ times the corresponding geometrical factor appearing in 66 times the trap depth $U_0$. Thus, measuring successively $\Delta\nu_{\pm_F}$ and subtracting two successive measurements would allow for a measurement of the $m_F$ depency only

$$\frac{\Delta\nu_{+m_F} - \Delta\nu_{-m_F}}{2} = \Delta\nu^v_{+m_F} \tag{69}$$

But one should not forget that the Zeeman shift, at least to first order in bias field amplitude, scales as $m_F$ as well and it should be incorporated to equation 66. This is done the following way.

The fact the vector shift $\Delta k^v m_F \xi \vec{\varepsilon_k} \cdot \vec{\varepsilon_B}$ involved in equation 66 is proportional to $m_F$ suggests it might be possible viewing it formally as a Zeeman shift induced by a fictitious magnetic field. Indeed, accounting for the Zeeman effect induced by the bias field it-self, the total $m_F$ dependent shift can be obtained considering an effective magnetic field (see [60])

$$\vec{b}_{\text{eff}} = \frac{hk^v i(\vec{\varepsilon}^* \wedge \vec{\varepsilon}^*)U_0}{\mu_B g} + \mathbf{B} \tag{70}$$

The $m_F$ dependent component $\Delta\nu_Z$ of $\Delta\nu$, i.e. that encompassing both the bias field induced Zeeman shift as well as the vector shift as appearing in 66 can then be expressed as $\Delta\nu_Z = -(\mu_B g m_F/h)|\vec{b}_{\text{eff}}|$ which can be expanded to the second order in trap depth $U_0$ as, with $\theta$ the angle between the lattice wave vector and the bias field,

$$\Delta\nu_Z \simeq m_F \left( \frac{\mu_B g}{h} B + k^v \xi \cos\theta U_0 + \sin^2\theta \frac{h}{\mu_B g} \frac{(k^v\xi)^2}{B} U_0^2 \right) \tag{71}$$

which is experimentally accessible via differential measurement on the various parameters $U_0$, $\xi$ and $\theta$ (as described in section 5.1.4 but not necessarily making the difference between opposite Zeeman sublevels.).[36] Extrapolating to $U_0 = 0$ gives the first order Zeeman shift $m_F(\mu_B g/h)B$ while repeating the experiment with various angles $\theta$ provides the vector shift coefficient

$$|\Delta k^v| = 0.22 \pm 0.05 \text{ Hz/E}_R \tag{72}$$

with its uncertainty limited by the knowledge of the polarization state $\vec{\varepsilon}$ in the lattice cavity.

In the normal clock operation protocol, it is the quantity $\overline{\nu}$ as defined by equation 65 that is measured. From equation 66 and because of the parities of its different components (see 68) , it reads

$$\Delta\nu = \left(\Delta k^s + \gamma \Delta k^t\right) U_0 \tag{73}$$

The tensor shift coefficient $k^t$ is obtained repeating this measurements for various values of $\gamma$. Note that all the measurements carried out led to results in good agreement with expected theoretically computed values. The scalar shift can theoretically be canceled operating the lattice at the magic wavelength. In practice, when running the clock, we tune the lattice wavelength in such way that the $\Delta\nu$ cancels to the first order in $U_0$. This is achieved experimentally via a the differential measurement sequence, which a protocol widely used to track systematics effects and as such is interested to describe, at least in its principles.

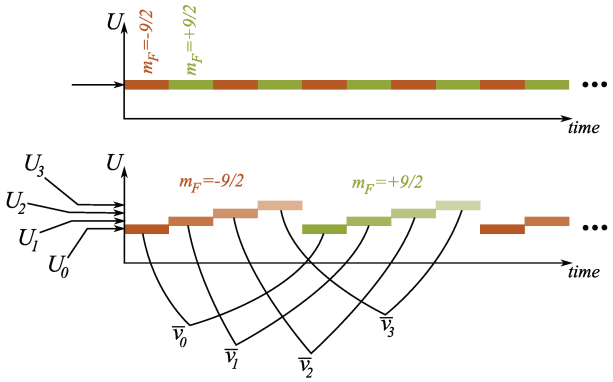


Figure 20: Schematic of differential measurements. The first graph represents a normal clock operation sequence where alternated cycles of $m_{F=-9/2} \rightarrow m_{F=-9/2}$ (brown rectangles) and $m_{F=+9/2} \rightarrow m_{F=+9/2}$ follow each others, with a trap depth $U$ kept constant. The second graph represents a trap depth differential measurement between 4 different trap depths, $U_0$, $U_1$, $U_2$ and $U_3$. The 4 trap depths are measured on one Zeeman sublevel in a raw, and afterward on the other. Then, the difference between two successive measure at the same trap depth but opposite Zeeman sublevels is made, giving $\overline{\nu}_i = (\nu_{i+4} - \nu_i)/2$. Note that, for example, when investigating the terms appearing in 71, we do the same but without alternating the Zeeman sublevels and explore other parameters such as the lattice polarization ellipticity $\xi$ or its angle to the quantization axis $\theta$.

### 5.1.4 Differential measurement and magic wavelength

A normal operation of the clock consists in alternated measurements of the $m_F = \pm 9/2 \longrightarrow m'_F = \pm 9/2$ Zeeman transitions. Considering a clock run consisting in $N$ successive measurements labeled by $n = 1, ..., N$, this means that, for example, the measurement corresponding to even $n$ probe the $m_F = -9/2 \longrightarrow m'_F = -9/2$ whereas the odd $n$ correspond to $m_F = +9/2 \longrightarrow m'_F = +9/2$. This is a differential measurement in $m_F$ for $m_F = \pm 9/2$, allowing to compare how the clock frequency depends on $m_F$. This protocol can be used varying an other parameter instead of $m_F$ and exploring more than two values. In the case we are interested in, we keep all parameters fixed except the lattice depth $U$ and explore typically four values. But we still want to have the vectorial and Zeeman shifts canceled and consequently run a trap depth differential measurement in the following way (see Figure 20): for 4 values of trap depth explored $U_{j=0,..,3}$, the differential measurement consists in the succession of a sequence of 8 measurements each characterized by a particular couple of parameters $(m_{F,i}, U_i)_{i=0,..,7}$ where $m_{F,i=0,..,3} = -9/2$, $m_{F,i=4,..,7} = +9/2$, $U_{i+4} = U_i$, $k = 0, .., 3$. The frequency outcome of each of the measurements of such a sequence are denoted $\nu_{i=0,..,7}$. The Zeeman-free[37] frequency $\overline{\nu}_{j=0,..,3}$ corresponding to each trap depth $U_{j=0,..,3}$ is then obtained as $\overline{\nu}_j = (\nu_{j+4} - \nu_j)/2$. The total number $N$ of such 8-measurements sequences gives the statistical resolution on each value $\nu(U_{j=0,..,3}) = \langle \overline{\nu}_j \rangle_N$, i.e. defined as the average of all the $\overline{\nu}_j$ obtained for a given $j$. The set $\nu(U_j)$ is then fitted by a parabola with $U_j$ as variable. The second order coefficient of the fit is the one given by our best estimate of the hyperpolarizanility (see section 5.2). If the slope of the fit does not vanish, the lattice must be changed. This process is iterated till obtaining a vanishing slope, corresponding to $\Delta\nu = 0$. When this is achieved the lattice is said to be at *the magic wavelength*. Note that there is actually *a* magic wavelength for each particular configuration of lattice polarization. A magic wavelength is then a lattice wavelength such that all first order shifts in $U_0$ that are not canceled by alternated measurement of the extreme Zeeman sublevels are compatible with zero.

[36] Note that $\Delta\nu_Z$ is the difference between the energy shift of each clock level, rescaled by the Plank constant $h$ and thus should account for the fact the Landé factors of these levels are different. However, each of these factor is of the order of unity whereas their difference is of the order of $10^{-4}$. We can thus consider the two Landé factors as equal, leading to 71.

[37] Here Zeeman-free means that the dependency in $m_F$ is canceled. It should then be called (Zeeman/vector shift)-free frequency.

## 5.2 Hyperpolarizability

Relative uncertainty budgets of state-of-the-art optical clocks have reached close to the $10^{-18}$ level (see section 4.5.1), meaning that the "magic" condition $(\Delta k^s + \gamma \Delta k^t) = 0$ is realized within the bounds set by

$$\frac{|(\Delta k^s + \gamma \Delta k^t)| U_0}{\nu_0} \lesssim 10^{-18} \tag{74}$$

Including second order terms in trap depth $U_0$ (see 5.0.2) we then have that the ratio between the measured clock transition frequency $\nu_M$ and the target absolutely unperturbed one $\nu_0$ is approximately

$$\frac{\nu_M}{\nu_0} \sim \frac{\nu_0 + \left[\Delta\nu' + (\Delta k^s + \gamma \Delta k^t) U_0\right] + bU_0^2}{\nu_0} = 1 + \varepsilon^{(1)} + bU_0^2 \tag{75}$$

where $\Delta\nu'$ encompasses shifts stemming from other sources than the lattice and $b$ is the hyperpolarizability differential shift coefficient. Even though $\Delta\nu'$ might be non vanishing, it is known at the level of $10^{-18}$ in relative uncertainty. Henceforth, pushing further the estimation of $\nu_M/\nu_0$ requires estimating $bU_0^2/\nu_0$ at the $10^{-18}$ level.

We proceed the same as in the polarizability investigation and start from the $4^{\text{th}}$ order energy correction $\mathcal{E}^{(4)}_{nq}$ provided by the Floquet theory and given in equation 602. Because $\langle\langle nq|V|nq\rangle\rangle = 0$, the three first terms appearing in the expression of $\mathcal{E}^{(4)}_{nq}$ vanish. The forth term is a weighted sum of coefficients of the form

$$\langle\langle nq|V|n'q'\rangle\rangle\langle\langle n'q'|V|n''q''\rangle\rangle\langle\langle n''q''|V|n'''q'''\rangle\rangle\langle\langle n'''q'''|V|nq\rangle\rangle \tag{76}$$

Dropping out the vanishing terms, it reduces to

$$\sum_{n',n'',n'''} \frac{\langle n|V_+|n'\rangle\langle n'|V_+|n''\rangle\langle n''|V_-|n'''\rangle\langle n'''|V_-|n\rangle}{(E_{n'}-E_n-\hbar\omega)(E_{n''}-E_n-2\hbar\omega)(E_{n'''}-E_n-\hbar\omega)} \tag{77}$$

$$+\sum_{n',n'',n'''} \frac{\langle n|V_+|n'\rangle\langle n'|V_-|n''\rangle\langle n''|V_+|n'''\rangle\langle n'''|V_-|n\rangle}{(E_{n'}-E_n-\hbar\omega)(E_{n''}-E_n)(E_{n'''}-E_n-\hbar\omega)} \tag{78}$$

$$+\sum_{n',n'',n'''} \frac{\langle n|V_-|n'\rangle\langle n'|V_+|n''\rangle\langle n''|V_+|n'''\rangle\langle n'''|V_-|n\rangle}{(E_{n'}-E_n+\hbar\omega)(E_{n''}-E_n)(E_{n'''}-E_n-\hbar\omega)} \tag{79}$$

$$+\sum_{n',n'',n'''} \frac{\langle n|V_-|n'\rangle\langle n'|V_-|n''\rangle\langle n''|V_+|n'''\rangle\langle n'''|V_+|n\rangle}{(E_{n'}-E_n+\hbar\omega)(E_{n''}-E_n+2\hbar\omega)(E_{n'''}-E_n+\hbar\omega)} \tag{80}$$

$$+\sum_{n',n'',n'''} \frac{\langle n|V_-|n'\rangle\langle n'|V_+|n''\rangle\langle n''|V_-|n'''\rangle\langle n'''|V_+|n\rangle}{(E_{n'}-E_n+\hbar\omega)(E_{n''}-E_n)(E_{n'''}-E_n+\hbar\omega)} \tag{81}$$

$$+\sum_{n',n'',n'''} \frac{\langle n|V_+|n'\rangle\langle n'|V_-|n''\rangle\langle n''|V_-|n'''\rangle\langle n'''|V_+|n\rangle}{(E_{n'}-E_n-\hbar\omega)(E_{n''}-E_n)(E_{n'''}-E_n+\hbar\omega)} \tag{82}$$

$$\tag{83}$$

The fifth term is a weighted sum of coefficients of the form

$$\langle\langle nq|V|n'q'\rangle\rangle\langle\langle n'q'|V|nq\rangle\rangle\langle\langle nq|V|n''q''\rangle\rangle\langle\langle n''q''|V|nq\rangle\rangle \tag{84}$$

which leads, keeping the non vanishing combinations only

$$\sum_{n',n''} \frac{\langle n|V_+|n'\rangle\langle n'|V_-|n\rangle\langle n|V_+|n''\rangle\langle n''|V_-|n\rangle}{(E_{n'}-E_n-\hbar\omega)^2(E_{n''}-E_n-\hbar\omega)} \tag{85}$$

$$+\sum_{n',n''} \frac{\langle n|V_+|n'\rangle\langle n'|V_-|n\rangle\langle n|V_-|n''\rangle\langle n''|V_+|n\rangle}{(E_{n'}-E_n-\hbar\omega)^2(E_{n''}-E_n+\hbar\omega)} \tag{86}$$

$$+\sum_{n',n''} \frac{\langle n|V_-|n'\rangle\langle n'|V_+|n\rangle\langle n|V_-|n''\rangle\langle n''|V_+|n\rangle}{(E_{n'}-E_n+\hbar\omega)^2(E_{n''}-E_n+\hbar\omega)} \tag{87}$$

$$+\sum_{n',n''} \frac{\langle n|V_-|n'\rangle\langle n'|V_+|n\rangle\langle n|V_+|n''\rangle\langle n''|V_-|n\rangle}{(E_{n'}-E_n+\hbar\omega)^2(E_{n''}-E_n-\hbar\omega)} \tag{88}$$

Here again we did not simplify terms of the form $\langle n| V_{\pm} |n'\rangle \langle n'| V_{\mp} |n\rangle$ into $|\langle n| V_{\pm} |n'\rangle|^2$ for the ease of the physical interpretation of the hyperpolarizability corrections as well as the possibility of expressing it as a first order correction induced by a perturbation encapsulated in the *hyperpolarizability operator*, as done in the case of the polarizability analysis. Indeed, from the computations above, $\mathcal{E}^{(4)}_{nq}$ is a combination of terms of the form

$$\langle n| V_{\varepsilon_{n,q}} |q\rangle \langle q| V_{\varepsilon_{q,p}} |p\rangle \langle p| V_{\varepsilon_{p,m}} |m\rangle \langle m| V_{\varepsilon_{m,n}} |n\rangle = \langle n| \hat{\mathbf{Q}} |n\rangle \tag{89}$$

where $\varepsilon_{k,l} = \pm$, the operator $\hat{\mathbf{Q}}$ being given by

$$\hat{\mathbf{Q}} = \hat{\mathbf{Q}}_{nq} \times \hat{\mathbf{Q}}_{qp} \times \hat{\mathbf{Q}}_{pm} \times \hat{\mathbf{Q}}_{mn} \tag{90}$$

with

$$\hat{\mathbf{Q}}_{qp} = |q\rangle \langle q| V_{\varepsilon_{q,p}} |p\rangle \langle p| \tag{91}$$

which is the operator corresponding to starting in state $|p\rangle$, ending up in state in state $|q\rangle$ while absorbing or emitting a photon depending on whether $V_{\varepsilon_{q,p}} = V_+$ or $V_-$. Hence, the hyperpolarizability shift can be viewed as a first standard time independent first order correction where the perturbation is a weighted sum over all possible 4-photons transitions starting and ending in state $|n\rangle$. The algebra derived above means that, because some of the dipole operator symmetries, the only 4-photons transitions allowed by the system must assume one of the two following forms (see Fig. 21)

$$|n\rangle \to |m\rangle \to |p\rangle \to |q\rangle \to |n\rangle \tag{92}$$

with $n$, $m$, $p$ and $q$ all different one from each other, or

$$|n\rangle \to |m\rangle \to |n\rangle \to |p\rangle \to |n\rangle \tag{93}$$

which loops by the starting state $|n\rangle$ at the middle of the cycle.

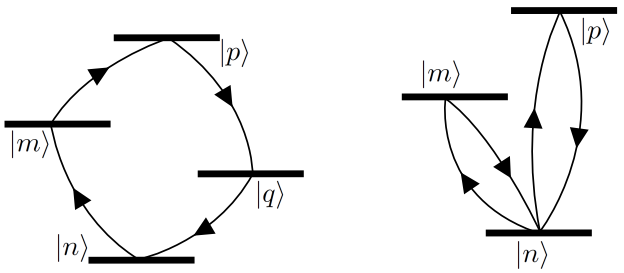


Figure 21: The two different types of 4-photons transition involved in the hyperpolarizability effect.

Note that even though Fig. 21 is valid in terms of transition involved in the 4-photons process, it is chronologically misleading, as was the case for the polarizability case, since it seems to consider only classically allowed cycles for which the total number of photons absorbed at a given time $t$ is always higher than that of the emitted ones.

### 5.2.1 Tensor decomposition of the hyperpolarizability

For the polarizability, the tensorial structure of the energy correction emerged from the products stemmed from equation 55. Each term of 77 has the form

$$\sum_{n',n'',n'''} \frac{\langle n| V_{\varepsilon_1} |n'\rangle \langle n'| V_{\varepsilon_2} |n''\rangle \langle n''| V_{\varepsilon_3} |n'''\rangle \langle n'''| V_{\varepsilon_4} |n\rangle}{(E_{n'} - E_n + u_1\hbar\omega)(E_{n''} - E_n + u_2\hbar\omega)(E_{n'''} - E_n + u_3\hbar\omega)} \tag{94}$$

where $\varepsilon_i = \pm$ and $u_j = \pm 1, \pm 2$ according to 77 and where $n$ stands for a complete set of quantum numbers $ajm$. Following the same treatment as for the polarizability, each of these terms can be expressed as an

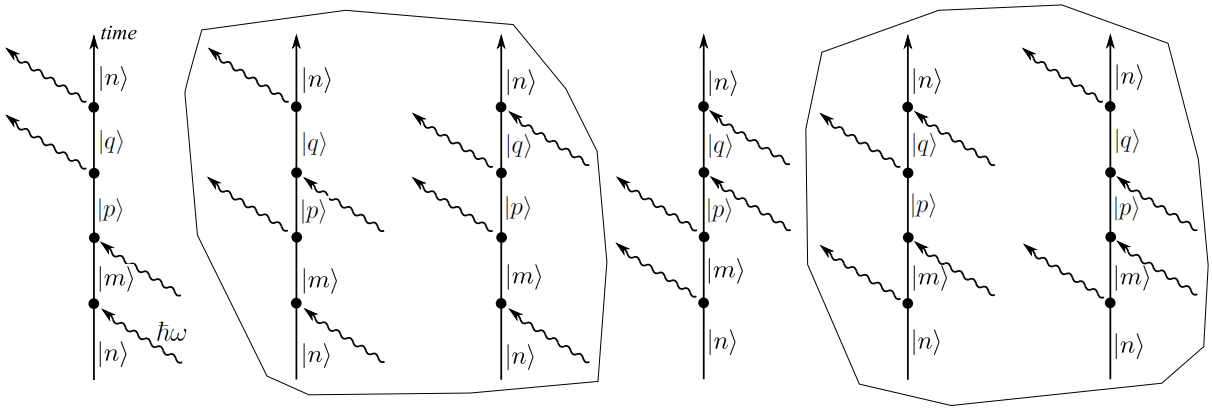


Figure 22: Diagrammatic representations of the 6 types of 4-photons processes involved in the hyperpolarizability effect. Only four of these processes are involved in the second 4-photon cycle type (that looping back by the $|n\rangle$ state) and are encircled in the picture (where one should replace $|p\rangle$ with $|n\rangle$).

expectation value $\langle n|\,\hat{A}^{\Lambda}\,|n\rangle$ where $\Lambda = {}^{\varepsilon_1,\varepsilon_2,\varepsilon_3,\varepsilon_4}_{u_1,u_2,u_3}$ stands for the set of exponents and subscript appearing in 77 and with

$$\hat{A}^{\Lambda} = |E|^4 \left\{ (\boldsymbol{\varepsilon}_{\varepsilon_1} \cdot \mathbf{d}) \, (\boldsymbol{\varepsilon}_{\varepsilon_2} \cdot \mathcal{R}_{u_1}\mathbf{d}) \, (\boldsymbol{\varepsilon}_{\varepsilon_3} \cdot \mathcal{R}_{u_2}\mathbf{d}) \, (\boldsymbol{\varepsilon}_{\varepsilon_4} \cdot \mathcal{R}_{u_3}\mathbf{d}) \right\} \tag{95}$$

where $\boldsymbol{\varepsilon}_+ = \boldsymbol{\varepsilon}$, $\boldsymbol{\varepsilon}_- = \boldsymbol{\varepsilon}^*$ and where

$$\mathcal{R}_{u_j} = \sum_{m \neq n} \frac{|m\rangle \langle m|}{E_m - E_n + u_j \hbar\omega} \tag{96}$$

Similarly, each term of 85 has the form $\langle n|\,\hat{B}^{M}\,|n\rangle$ with

$$\hat{B}^{M} = |E|^4 \left\{ (\boldsymbol{\varepsilon}_{\varepsilon_1} \cdot \mathbf{d}) \, (\boldsymbol{\varepsilon}_{\varepsilon_2} \cdot \mathcal{P}_{u_1}\mathbf{d}) \, (\boldsymbol{\varepsilon}_{\varepsilon_3} \cdot |n\rangle \langle n|\,\mathbf{d}) \, (\boldsymbol{\varepsilon}_{\varepsilon_4} \cdot \mathcal{Q}_{u_2}\mathbf{d}) \right\} \tag{97}$$

where this time $u_j = \pm$

$$\mathcal{P}_{\pm} = \sum_{m \neq n} \frac{|m\rangle \langle m|}{(E_m - E_n \pm \hbar\omega)^2} \qquad\qquad \mathcal{Q}_{\pm} = \sum_{m \neq n} \frac{|m\rangle \langle m|}{E_m - E_n \pm \hbar\omega} \tag{98}$$

and $M = {}^{\varepsilon_1,\varepsilon_2,\varepsilon_3,\varepsilon_4}_{u_1,u_2}$ stands for the set of exponents and subscripts appearing in 85. $\hat{A}^{\Lambda}$ and $\hat{B}^{M}$ can be considered as counterparts of 53 from where, combined to formula 55, emerged the explicit tensorial structure of the polarizability. Note that the operator $\sum_{\Lambda} \hat{A}^{\Lambda}$ corresponds to the first type of 4-photons transitions involved in the hyperpolarizability phenomena consisting in 4-cycles (on the left on Figure. 21) whereas $\sum_{M} \hat{B}^{M}$ corresponds to the second type, that consisting in 2 successive 2-cycles (on the right in Figure. 21) The frequency shift for a given level $|n\rangle \equiv |ajm\rangle$ is therefore given by

$$\Delta E_n = \sum_{\Lambda} \langle n|\,\hat{A}^{\Lambda}\,|n\rangle + \sum_{M} \langle n|\,\hat{B}^{M}\,|n\rangle \tag{99}$$

where the sums extend to all possible sets of exponents and indices $\Lambda = {}^{\varepsilon_1,\varepsilon_2,\varepsilon_3,\varepsilon_4}_{u_1,u_2,u_3}$ and $M = {}^{\varepsilon_1,\varepsilon_2,\varepsilon_3,\varepsilon_4}_{u_1,u_2}$ appearing in 77 and 85. Similar algebraic techniques as that used in the case of the polarizability leads to the possibility to express $\Delta E_{ajm}$ in a similar fashion as 60 but involving tensor components up to rank 4. We skip the mathematical derivation and provide directly the corresponding expression as found in [63] (with slightly different notations though)

$$\Delta E_{ajm} = h \left( \sum_{k=0,..,4} \ell^{(k)}_{ajm} \right) U_0^2 \tag{100}$$

where each irreducible component $\ell^{(k)}_{ajm}$ reads

$$\ell^{(k)} = \frac{1}{h} \sum_{q,r=0}^{2} \left[ \{\boldsymbol{\varepsilon}^* \otimes \boldsymbol{\varepsilon}^*\}^{(2)}_q \otimes \{\boldsymbol{\varepsilon} \otimes \boldsymbol{\varepsilon}\}^{(2)}_r \right]^{(4)}_k \beta^{1(k)}_{ajm} + \left[ \{\boldsymbol{\varepsilon} \otimes \boldsymbol{\varepsilon}^*\}^{(2)}_q \otimes \{\boldsymbol{\varepsilon} \otimes \boldsymbol{\varepsilon}^*\}^{(2)}_r \right]^{(4)}_k \beta^{2(k)}_{ajm} \tag{101}$$

The fact there are two terms comes from the fact that the set of possible sets of indices $\{\varepsilon_1, \varepsilon_2, \varepsilon_3, \varepsilon_4\}$ can feature types of symmetries. Those with $\varepsilon_1 = \varepsilon_2 = -\varepsilon_3 = -\varepsilon_4$, corresponding to the first term in the summation of equation 101, and those with $\varepsilon_1 = -\varepsilon_2 = \varepsilon_3 = -\varepsilon_4$, corresponding to the second term (as it can be guessed from the complex conjugation $^*$ position within the tensorial factors). We do not give here the general form of the $\beta_{ajm}^{1,2(k)}$ but just note that each of them is a sum of two terms, one stemming from the 4-cycle operator $\sum_\Lambda \hat{A}^\Lambda$, the other from the double 2-cycle operator $\sum_M \hat{B}^M$.

### 5.2.2 Hyperpolarizability measurement

When the Zeeman splitting bias field **B** is taken into account (see section 5.1.2 and 5.1.3), neglecting the hyperfine structure, i.e. considering $F = J = 0$ for the $^1S_0$ and the $^3P_0$ clock sates, and restricting our-selves to the case of a lattice linear polarization, it can be shown that the clock transition hyperpolarizability shift reads

$$\Delta\nu = \frac{1}{9} Y_{101} + \frac{\left(3|\boldsymbol{\varepsilon} \cdot \mathbf{e}_Z|^2 - 1\right)^2}{90} Y_{121} \tag{102}$$

with the $Y$ coefficients defined in [56] and [63]. This theoretical prediction is represented on Figure 24 in purple. To measure the effect, we run the clock successively with different angles $\theta$ between the lattice polarization and the quantization axes defined by the applied magnetic field, with our second clock Sr2 as a reference. However, we know from equation 67 that the first order tensor part of the lattice shift depends on $\theta$. Hence, for each angle probed, we need to readjust the lattice wavelength in order to keep the magic *condition*, i.e. having all differential first order lattice shifts[38] (scalar, vector and tensor) canceling each other. Hence, for each angle probed, we run a differential trap depth measurement as described in section 5.1.4. Fitting the obtained data gives us the slope at zero trap depth of the first order lattice shift. We then correct the lattice frequency to have this slope vanishing. We iterate the process till having effectively a zero slope.

The measurements carried out in the frame of this thesis have been obtained tuning the angle between the lattice linear polarization and the quantization axis by rotating the lattice polarization, keeping the orientation of the quantization fixed. This was done adding a half-waveplate and polarization cube at the chamber input, as sketched on the left-side drawing of figure 23.
All the measurements carried out at SYRTE before 2017 are reported on the left-side plot of picture 24 along with the theoretical prediction of [56]. The right-side plot displays our last measurement of 2017. The order of magnitude as well as the sign of the effect measured is compatible with that of the prediction of [56] but the particular behavior in term of lattice polarization-to-quantization axis angle is not. Further investigation of the effect requires a better control of the liattice light polarization and of its angle with the quantization axis. We expect such a level of control to be out of reach with the current implementation based on the addition of half-waveplate and a polarazing beam splitter on the lattice lmight path to the chamber. We think however it could be achieved keeping the lattice polarization fixed while controlling the quantization axis orientation instead (see figure 23). For nominal operation of the clock the angle between the quantization axis and the polarization ,linear, of the lattice is set to zero. The value used to correct the hyperpolarizability effect (see section 4.6) during the June 2017 reported hereafter in section 7.2 is the one reported on Figure 24, the corresponding error bars being that used for the uncertainty appearing in the budget presented earlier.

[38] i.e. the difference between these effects on the ground and excited clock state

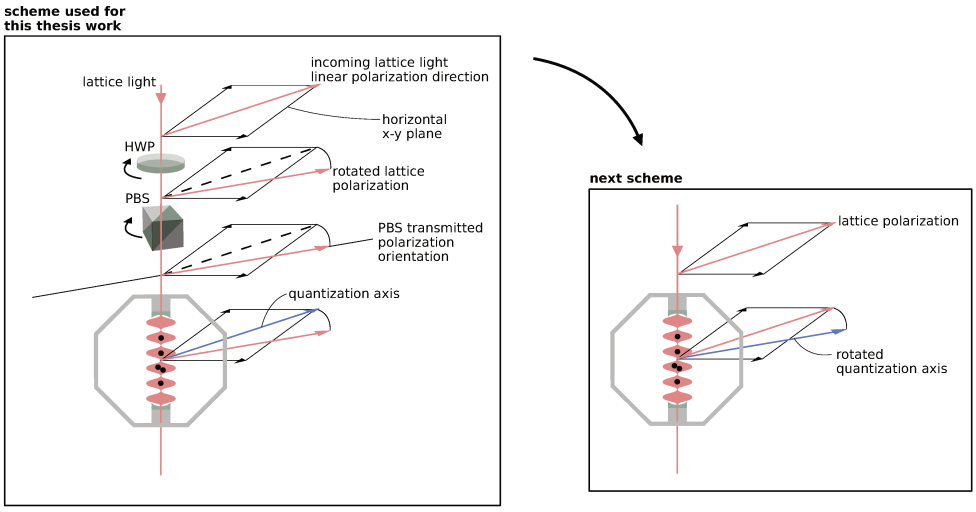


Figure 23: Schemes used for the hyperpolarizability measurement. **Left**: The polarization of the incoming lattice light is linear (pink arrow in the top x-y horizontal x-y plane), colinear with the quantization axis (blue arrow in the bottom x-y plane representation). The half-waveplate (HWP) and polarizing beams splitter (PBS) are are added on purpose for the hypepolarizability measurement. The orientation of the PBS defines the angle between the lattice linear polarization and quantization axis while the HWP orientation is set in order to maximize the lattice light transmission through the PBS. The results obtained with this scheme are presented on the right-side plot of figure 24. This scheme however proved being difficult to implement because of the lack of sufficiently accurate control of the optics alignment and orientation. **Right**: in order to improve the precision of our measurement we came up with a new idea consisting in rotating the quantization axis instead of the lattice polarization, as depicted. This could not be implemented so far because of software-hardware driving issues is expected to be feasible soon after modification carried out currently on the experiment operating system.

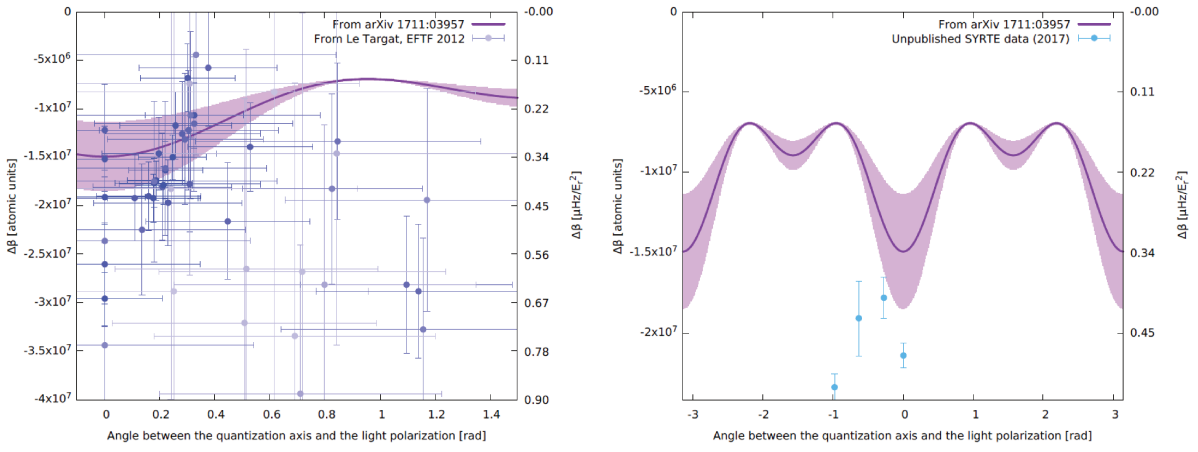


Figure 24: Hyperpolarizability measurements (in atomic units) as a function of the angle between the linear polarization of the lattice and the quantization axis defined by the magnetic field. The purple line is the theoretical computations provided in [56] along with the calculation error bars. All the measurement done before 2017 are represented on the left-side plot. Our measurement are presented on the right-side plot.

# 6 Hot collisions shift

After a brief introduction to the problem (section 6.1) I expose the way the phenomena has been dealt with so far in the atomic clock community and motivate our decision to go further in the investigation (section 6.2). Useful classical preliminaries are given in section 6.3 and the basics of the quantum scattering theory required for our treatment, in particular the definition of the partial wave phase shifts and the expression for the collision cross section, are given in section 6.4. I expose the model I developed in section 6.5. This model relates the partial wave phase shifts to the clock transition shift resulting from the collisions with the background gas. In section 6.6 I give the standard semi-classical treatment of the scattering problem enabling an estimation of the partial wave phase shifts and the resulting expression for the collisions cross section as a function of the $C_6$ coefficients. The atoms loss rate is derived in section 6.7 followed by an investigation of the relation between loss rate and clock transition shift cross section in section 6.8. Finally, our measurements are discussed in section 6.9.

## 6.1 Neutral atoms interaction potential

Since the $19^{th}$ century physicists and chemists were aware molecules and atoms, even though neutral, attract each other on very short range, as they could infer from observation of capillarity and deviation from the perfect gas laws. In 1873 Van der Waals proposed in his thesis [65, 66] a modified form for the gas law

$$\left(P + \frac{a}{2}\right)(V - b) = RT \tag{103}$$

where $P$, $V$, $R$ and $T$ are the gas pressure, occupied volume, perfect gas constant and temperature respectively. The coefficient $b$ account for the fact that each particle have access to a smaller volume than the total volume $V$ because of the presence of the other particles, while $a$ is associated to two-body attractive interaction between the particles. In the case of polar molecules, i.e. both with permanent polarizations, it was understood since the 1920's that the attraction was due to permanent dipole-dipole interaction, the so-called Van der Waals direction force. At the same period, it was as well understood that if one only of the two particles has a permanent dipole, the corresponding field would give rise to an induced dipole in the other particle, again resulting in dipole-dipole interaction, the so-called induction Van der Waals force. In the case of neutral atoms with vanishing permanent dipoles, the origin of this attractive force was first explained by London in 1930 in the frame of quantum perturbation theory. He showed the only requirement for the emergence of such interaction was that both atoms be polarizable and provided the formula

$$V_L = -\frac{2}{3}\frac{1}{r^6}\sum_{k,l}\frac{|\langle 0|\, d_A\, |k\rangle|^2\, |\langle 0|\, d_B\, |l\rangle|^2}{\hbar\,(\omega_{0,k} + \omega_{0,l})} = -\frac{c_6}{r^6} \tag{104}$$

where the summation runs over possible electronic states $|k(l)\rangle$ and $|l\rangle$ of atom A (B), $\omega_{0,k} = E_k - E_0$ and $d_{A(B)}$ is the transition dipole moment operator of atom A (B). Because of the role played in this process by polarizability, and its fundamental link to dispersive behavior of light when interacting with matter, this third type of Van der Waals force is referred to as dispersion force. It is important to note that, on top of being a $4^{\text{th}}$ order perturbation approximation, an other assumption has been down for obtaining eq. 104: infinite electro-magnetic field propagation celerity. This is the reason why the London form of Van der Waals potential is labeled as non-retarded. A retarded version of eq. 104 has been derived by Casimir and Polder, leading to a change in power law. Indeed, the Casimir-Polder potential fall as $r^{-7}$ instead of the standard $r^{-6}$. However, it was shown that over short range it reduces to the London formula. In the following all the results are worked out with eq. 104.

Note that while on the long range the potential is dominated by the London term $V_L$, the interaction at short distance is ruled by a strong repulsive potential

$$V_{sh} = \frac{c_{12}}{r^{12}} \tag{105}$$

accounting for the impossibility for the electron clouds of the two colliding atom and molecule to penetrate themselves. The actual value for $c_{12}$ can in general hardly be derived theoretically and is given most of the time an empiric value. Moreover, it has been shown in [73] that the scattering dynamics is non affected by the choice for $c_{12}$ over a very large range of values (spanning more than four orders of magnitude). As discussed in the classical preliminaries below (section 6.3), only the collisions not resulting in the

expulsion of the collided strontium atoms contribute to the clock frequency shift. It turns out that such collisions occurs for impact parameters such that $V_{sh} \ll V_L$. In the following we thus neglect the short range component of the potential and consider

$$V(r) \approx V_L = -\frac{c_6}{r^6} \tag{106}$$

As mentioned earlier, when an atom undergoes a collision, it experiences the Van der Waals (or London) potential due to the vicinity of the other atom or molecule. There are mainly two possible outcomes to such an event: the momentum transfered to the trapped atom can be sufficient to kick it out of the lattice, or, if its not the case, both its clock ground and excited states will be shifted due to the interaction potential $V(r)$, having a detrimental effect on the clock accuracy (except in the case where the shift on both ground and excited state are the same). In what follows we explore how to estimate both the rate of atom expulsion off the trap and the shift induced by the collisions to ground and excited state, in the case of hot collisions with vacuum back ground atoms and molecules.

## 6.2 Hot collisions treatment so far

### 6.2.1 Background gas collisions in micro wave clocks

Microwave standards based on cold atoms such as cesium and rubidium fountains have since their first realizations motivated investigations of the effect of collisions on both the theoretical and the experimental sides. Until recently, such estimations were based on shifts measurements made with cesium or rubidium vapor mixed with buffer gases at room temperature [72]. This gave an upper bound by far overestimating the effect as showed in [69]. This is due to the fact that, in opposition to what happens for an atomic vapor, most of the collisions between a background gas particle and a trapped cooled atom result in the atom being expelled from the trap and therefore not being detected. Hence, the corresponding frequency shift does not contribute to the measure. However, in spite of the improvements provided by [69], background gas collisions remain one of the largest contribution to the state-of-the-art cesium fountains [74] with, for example, uncertainties ranking up to $1.0 \times 10^{-16}$ out of a total budget of $3.3 \times 10^{-16}$ [75].

### 6.2.2 Background gas collisions in optical lattice clocks

Until very recently, estimations of the background gas collisions shift in optical lattice clocks were based on the same model as for the cold atoms microwave clocks exposed in [69] (see above). Based on this approach, a correction of $1.5 \times 10^{-18}$ as well as an uncertainty of $1.5 \times 10^{-18}$ out of a $5.2 \times 10^{-17}$ budget were reported in 2014 in [36], and a correction of $0.0 \times 10^{-18}$ for an uncertainty lower than $6 \times 10^{-19}$ out of a budget of $2.1 \times 10^{-18}$ was claimed in 2015 in [37]. In 2016 we published a budget of $4.1 \times 10^{-17}$ with a background gas collisions contribution estimated at $8 \times 10^{-18}$ [21].

This approach was challenged by the direct measurement of the effect reported in [38]. In this study, the authors report a linear dependency of the clock fractional frequency shift on the loss rate (the inverse of the atomic lifetime in the lattice trap) for an ytterbium optical lattice clock amounting to $1.62 \times 10^{-17}$ per $s^{-1}$ (with an uncertainty of $3 \times 10^{-19}$). For the typical trap lifetimes achieved in state-of-the-art optical lattice clocks of the order of a few seconds, this corresponds to a correction of a few $10^{-18}$ and can therefore not be overlooked for targeted fractional accuracies at the $10^{-18}$ level.

The question then arose about the magnitude of the effect in strontium based optical lattice clocks. This is the reason why we decided to measure the effect, using a technique similar to that reported in [38] and described hereafter.

## 6.3 Classical preliminaries

As far as we are concerned, the main contribution to collisional shifts is that of collisions between hot, i.e. with high kinetic energy, background particles (typically $H_2$ molecules, He atoms...) with the trapped Sr atoms. In the following we thus consider collisions between two particles of mass of *a priori* same order of magnitude, one considered at rest in the lab frame, corresponding to the Sr lattice trapped atoms, the other from a very low density gas with Maxwell-Boltzmann room temperature velocity distribution. For a given pair of such particle the parameters and variables associated to the trapped one are labeled with the subscript $t$, and those for the background one with the subscript $b$. Moving to the center-of-mass

(COM) frame representation of the particle pair results in a redefinition of the problem in terms of a new particle pair. We then define the center of mass particle position as

$$\mathbf{R} = \frac{m_t \mathbf{r}_t + m_b \mathbf{r}_b}{m_t + m_b} \tag{107}$$

and its mass as

$$M = m_t + m_b$$

and the fictitious particle position as

$$\mathbf{r} = \mathbf{r}_b - \mathbf{r}_t$$

with reduced mass

$$\mu = \frac{m_t m_b}{m_t + m_b}$$

With these definitions, the lab frame particles position and velocity vectors read

$$\mathbf{r}_{t,b} = \mathbf{R} \pm \frac{\mu}{m_{t,b}} \mathbf{r} \qquad \text{and} \qquad \mathbf{v}_{t,b} = \mathbf{V} \pm \frac{\mu}{m_{t,b}} \mathbf{v} \tag{108}$$

where $\mathbf{v} = \mathbf{v}_b - \mathbf{v}_t$. Therefore, labeling the variables far before the collision with subscript $_{-\infty}$ and those far after with $_{+\infty}$, and remembering the assumption that the trapped atom is initially at rest in the lab frame, we get

$$\mathbf{v}_{t,+\infty} = \frac{\mu}{m_t} \left( \mathbf{v}_{+\infty} - \mathbf{v}_{-\infty} \right)$$

and thus, the final kinetic energy of the trapped particle reads

$$E^K_{t,+\infty} = \frac{1}{2} \frac{\mu^2}{m_t} \| \mathbf{v}_{+\infty} - \mathbf{v}_{-\infty} \|^2 \tag{109}$$

The center of mass particle dynamics variables are not affected by the collision, and thus its kinetic energy is left unchanged by the collision. Therefore, the two-body system being closed, the conservation of the total energy implies that, far after the collision, when the potential energy $V(|\mathbf{r}|)$ that scales as $r^{-6}$ at large range (see section 6.1) vanishes, the final kinetic energy of the fictitious particle is the same as that it had far before. Thus $\|\mathbf{v}_{+\infty}\| = \|\mathbf{v}_{-\infty}\|$, and the change in velocity of the fictitious particle can be seen as a rotation along a well chosen axis of angle $\alpha$, and $\|\mathbf{v}_{+\infty} - \mathbf{v}_{-\infty}\|^2 = 2v^2(1 - \cos\alpha)$, where $v = \|\mathbf{v}_{\pm\infty}\|$, leading to

$$E^K_{t,+\infty} = \frac{\mu^2 v^2}{m_t} (1 - \cos\alpha) \tag{110}$$

If this final kinetic energy is higher than the trap potential $U$, the collided atom is kicked off the trap. We can thus define a maximal value for the deflection angle, $\alpha_m$, above which $E^K_{t,+\infty} > U$, i.e. above witch the atom escapes the trap

$$\alpha_m = \arccos\left(1 - \frac{U m_t}{\mu^2 v^2}\right)$$

In the impulse regime, the amount of momentum transfered to the trapped atom is very low compared with that of the incoming background particle and $\mathbf{v}_{+\infty} \sim \mathbf{v}_{-\infty}$ meaning that $\alpha \ll 1$. Note that in this regime $\alpha_m$ might be out of reach. Indeed, for small $\alpha$ we have

$$E^K_{t,+\infty} \sim \frac{\mu^2 v^2}{m_t} \frac{\alpha^2}{2}$$

or

$$\alpha_m \sim \frac{2 m_t U}{\mu^2 v^2}$$

witch might not be small, depending on the ratio between the trap depth and the incoming particle momentum. More precisely, $\alpha_m$ is reachable in the impulse regime only when

$$U \ll \frac{\mu^2 v^2}{m_t} = \frac{\mu}{m_t + m_b} \left( \frac{1}{2} m_b v^2 \right) \sim \frac{\mu}{m_t + m_b} k_B T$$

For trapped Sr and $H_2$ or He background gas at room temperature, this requires that $U/k_B \ll 10$ K. This condition is practically verified for optical lattice clocks.

## 6.4 Quantum scattering theory in brief

Including the time independent collision potential into the time independent Schrödinger equation leads to the so-called Lipmann-Schwinger scattering equation

$$\left[\hat{T}_1 + \hat{T}_2 + V - E\right]\psi_E(\mathbf{r}_1, \mathbf{r}_2) = 0 \tag{111}$$

where $\hat{T}_{1,2}$ stands for the kinetic energy operator $-\frac{\hbar^2\nabla^2_{1,2}}{2m_{1,2}}$ of colliding particle 1 and 2 of respective masses $m_1$ and $m_2$, $V \equiv V_L(|\mathbf{r}_1 - \mathbf{r}_2|)$, $E$ one of the Hamiltonian eigenvalues and $\psi_E(\mathbf{r}_1, \mathbf{r}_2)$ the corresponding two-body wave function.

### 6.4.1 Center of mass frame Lipmann-Schwinger equation

The first step in solving the Lipmann-Schwinger eq. 111 is to rewrite it in the center of mass frame. In this new set of coordinates the two body Hamiltonian then reads

$$\hat{H}_{CM}(\mathbf{R}) + \hat{H}_F(\mathbf{r}) \tag{112}$$

where $\hat{H}_{CM}(\mathbf{R}) = -\frac{\hbar^2\nabla^2_{\mathbf{R}}}{2M}$ is the center of mass Hamiltonian and $\hat{H}_F(\mathbf{r}) = -\frac{\hbar^2\nabla^2_{\mathbf{r}}}{2\mu} + V_L(|\mathbf{r}|)$ is the fictitious particle Hamiltonian that encompasses all the collision interactions. Because $[\hat{H}_{CM}(\mathbf{R}), \hat{H}_F(\mathbf{r})] = 0$, the eigen-wave functions can be factorized into $\psi(\mathbf{R}, \mathbf{r})_{E_{CM}+E_F} = \psi(\mathbf{R})_{E_{CM}}\psi(\mathbf{r})_{E_F}$

$$\hat{H}_{CM}(\mathbf{R})\,\psi(\mathbf{R})_{E_{CM}} = E_{CM}\psi(\mathbf{R})_{E_{CM}} \quad , \quad \hat{H}_F(\mathbf{r})\,\psi(\mathbf{r})_{E_F} = E_F\psi(\mathbf{r})_{E_F} \tag{113}$$

This means we can drop out all what regards the center of mass dynamics and focus on the fictitious particle only and eventually recombined the two at the end of the computation. We then simplify the notations dropping off the $F$ subscripts since in what follows all the computation are carried out for the fictitious particle. We are then left with the fictitious particle Lipmann-Schwinger equation

$$\left[\hat{T} + V_L(r) - E\right]\psi_E(\mathbf{r}) = 0 \tag{114}$$

### 6.4.2 Asymptotic behavior

We then split the wave function into two parts, one corresponding to the incoming wave $\psi_{in}$ plus an other standing for the scattered wave $\psi_{SC}$. We assume for the incoming wave a momentum eigenfunction i.e. a plane wave

$$\psi_{in}(\mathbf{r}) = \frac{e^{i\mathbf{k}\cdot\mathbf{r}}}{(2\pi)^{3/2}}$$

For the scattered wave we assume, because of the fast decay of the scattering potential, an asymptotic spherical wave (for a rigorous proof, see [*http* : *//web.mst.edu/ parris/QuantumTwo/Class_Notes/Scattering.pdf*])

$$\psi_{SC}(r = |\mathbf{r}| \longrightarrow \infty) = \frac{f(k,\theta,\phi)}{(2\pi)^{3/2}}\frac{e^{ikr}}{r} \tag{115}$$

modulated by the scattering amplitude $f(k, \theta, \psi)$ that contains all the physical informations about what happened during the collision in terms of momentum transfer from the incoming particle to the collided one.

### 6.4.3 Differential scattering cross section

We now introduce one of the main concepts in scattering theory, the differential scattering cross section. In order to grasp its physical meaning, we first consider it in a classical scattering picture. Imagine a a beam of incident particles impinging onto a target. Each incoming particle is then scattered into a certain direction of space according to its relative motion with respect to the target. Considering a sphere of radius r centered at the target, one can consider the flux of scattered particles through an elementary portion of the sphere defined by the two angles $\theta$ and $\phi$ and having a given momentum $k$, i.e. the number of scattered particles passing through this elementary surface per unit time, that we denote with $S_{SC}(k, \theta, \phi)r^2$ where the $r^2$ accounts for the fact that the flux depends only on the angular coordinates,

at least asymptotically, i.e. for large r. This flux depends linearly on the flux of incoming particles, all assumed with the same momentum $k'$, per unit elementary area normal to the beam direction, denoted as $S_{in}$. The differential scattering cross section is then defined as

$$\frac{d\sigma}{d\Omega}(k,\theta,\phi) = \frac{S_{SC}(k,\theta,\Omega)r^2}{S_{in}} \tag{116}$$

For a quantum description of scattering, no such thing as the flux of particles is defined, since the classical picture assume a point wise localization of each particle, whereas the quantum view is based on the spatial distribution described by the wave function. However, it is possible to build the analog to the classical flux , or particle current, the so called probability current $j_\psi$ for a particle of mass $\mu$ described by the evolving wave function $\psi$ as

$$j_\psi = \frac{-i\hbar}{\mu}\left(\psi^*\nabla\psi + \psi\nabla\psi^*\right) \tag{117}$$

It can be shown that in the limit of localized wave function, the probability current is equivalent to the classical current. We then replace $S_{in}$ and $S_{SC}$ by the corresponding probability currents

$$S_{in} \longrightarrow j_{\psi_{in}} \propto \frac{k}{\mu} \tag{118}$$

$$S_{SC}(k,\theta,\phi) \longrightarrow j_{\psi_{SC}} \propto \frac{k}{\mu r^2}|f(k,\theta,\phi)|^2 + \mathcal{O}\left(\frac{1}{r^3}\right) \tag{119}$$

leading to

$$\frac{d\sigma}{d\Omega}(k,\theta,\phi) = \frac{j_{\psi_{SC}}r^2}{j_{\psi_{in}}} = |f(k,\theta,\phi)|^2 \tag{120}$$

Note that, due the particular symmetries of the problem, and choosing the $z$-axis as the incoming

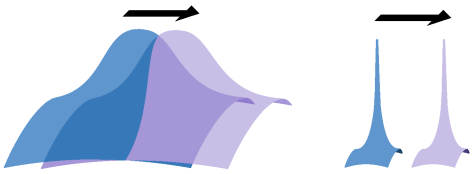

Figure 25: Equivalence between quantum probability current and classical particle current

beam propagation axis, $[\hat{H}, \hat{\mathbf{L}}_z] = 0$. This means that the $\phi$ dependency can be dropped out and that any decomposition onto the spherical harmonics will involve only those with $m_l = 0$, i.e. the $\mathcal{Y}_{l,0}(\theta) \equiv \mathcal{Y}_{l,0}(\theta,\phi) \propto P_l(\cos\theta)$, $P_l$ the Legendre polynomial of order $l$.

### 6.4.4 Partial wave expansion

We now perform partial wave expansions of the involved functions, i.e. decompose them on the $\{\mathcal{Y}_{l,m=0}\}_{l\in\mathbf{N}}$ basis, or equivalently, since only the spherical harmonics with $m = 0$ are involved, onto the Legendre polynomial basis. The general form for the wave function is

$$\psi(\mathbf{r}) = \psi_{in}(\mathbf{r}) + \psi_{SC}(\mathbf{r}) = \sum_{l\in\mathbf{N}} c_l \frac{u_l(r)}{r} P_l(\cos\theta) \tag{121}$$

where the angular part satisfies the angular part of the Lipmann-Schwinger equation. Regarding the radial part enclosed in the $u_l(r)$, it has to satisfy the standard unidimensional Shrödinger equation

$$\frac{d^2u_l(r)}{dr^2} - \left(\frac{l(l+1)}{r^2} + \frac{2\mu}{\hbar}V_L(r) - k^2\right)u_l(r) = 0 \tag{122}$$

The incoming wave function reads, using the Bessel functions $J_l$

$$\psi_{in}(\mathbf{r}) = \frac{r^{i\mathbf{k}\cdot\mathbf{r}}}{(2\pi)^{3/2}} = \sum_{l\in\mathbf{N}}(2l+1)i^l J_l(kr)P_l(\cos\theta) \tag{123}$$

Since we are investigating the asymptotic behavior of the wave function, we replace the Bessel functions by their asymptotic expressions

$$\lim_{r\to\infty} J_l(kr) = \frac{1}{kr}\frac{(-i)^l e^{ikr} - i^l e^{-ikr}}{2i} \tag{124}$$

giving

$$\psi_{in}(\mathbf{r}) = \sum_{l\in\mathbf{N}} (2l+1) P_l(\cos\theta) \frac{(-1)^{l+1} e^{-ikr} + e^{ikr}}{2ikr} \tag{125}$$

Furthermore, $f(k,\theta) \equiv f(k,\theta,\phi)$ as well can be given a partial wave expansion of the general form

$$f(k,\theta) = \sum_{l\in\mathbf{N}} (2l+1) f_l(k) P_l(\cos\theta) \tag{126}$$

Then, inserting eq. 126 into the asymptotic expression of $\psi_{SC}$ given in eq. 115 and summing with the asymptotic partial wave expansion of $\psi_{in}$ given by eq. 125, we get for the total wave

$$\psi(\mathbf{r}) = \sum_{l\in\mathbf{N}} (2l+1) P_l(\cos\theta) \frac{(-1)^{l+1} e^{-ikr} + S_l(k) e^{ikr}}{2ikr} \tag{127}$$

with $S_l(k) = 1 - 2ikf_l(k)$. The $\frac{e^{ikr}}{r}$ term corresponds to a spherical wave outgoing from the origin, thus corresponding to a leak of probability current out of the origin, whereas the $\frac{e^{-ikr}}{r}$ term corresponds to a spherical wave incoming, or collapsing onto, the origin and thus relates to a loss of probability current into the origin (see Fig. 26). The probability current to be conserve then requires their respective factors to have same moduli, i.e. $|S_l(k)| = 1$.

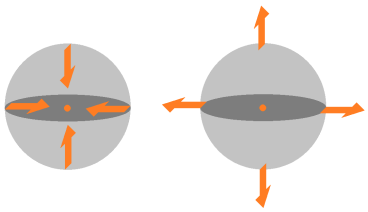

Figure 26: Spherical waves collapsing onto the space origin (left), leaking out from the origin (right).

Hence $S_l(k) = e^{i2\delta_l}$ for some real phase $\delta_l$. Since these terms appear in front of the spherical wave moving away from the origin $\frac{e^{+ikr}}{r}$, we interpret these phases $2\delta_l(k)$ as the phase shift induced by the scattering process to the angular momentum component $l$ of the scattered wave with initial momentum $k$.
Inserting

$$f_l(k) = \frac{1 - S_l(k)}{2ik} = e^{i\delta_l}\frac{\sin(\delta_l)}{k}$$

into the partial wave decomposition of $f_l(k)$ given by eq. 126 we get

$$f(k,\theta) = \sum_{l\in\mathbf{N}} (2l+1) P_l(\cos\theta) e^{i\delta_l}\frac{\sin(\delta_l)}{k} \tag{128}$$

from where

$$|f(k,\theta)|^2 = \sum_{l,m\in\mathbf{N}} (2m+1)(2l+1) P_m(\cos\theta) P_l(\cos\theta)\frac{\sin(\delta_l)\sin(\delta_m)}{k^2} \tag{129}$$

Legendre polynomials form a orthogonal basis satisfying the relation

$$\int_{-\pi/2}^{\pi/2} P_m(\cos\theta) P_l(\cos\theta)\sin\theta d\theta = \delta_{l,m}\frac{2}{2l+1}$$

and therefore

$$\sigma(k) = \int_\Omega \frac{d\sigma}{d\Omega}(k,\theta) d\Omega = \frac{4\pi}{k^2}\sum_{l\in\mathbf{N}} (2l+1)\sin^2(\delta_l) \tag{130}$$

Computing $\sigma(k)$ requires knowing the partial wave phase shifts $\delta_l$, which are estimated in the next paragraph, based on the quasi-classical regime approach.

## 6.5 Frequency shift cross section

There is no well established theoretical formulation for the collision induced shift and one may find in literature contradictory results. We present here our own treatment which provides somehow a synthesis of the two main theories available currently, that of K. Gibble [69], the other from A. C. Vutha *et al.* [68]. It turned out indeed that our calculations predict an effect consisting in the summation of the K. Gibble prediction and that of A. C. Vutha. Our approach is inspired by the work of L. Diosi [67] in which a quantum master equation for particles in gas (i.e. a quantum equation for the Brownian motion) is derived and that of A. C. Vutha, in particular in the critical step where some density matrix elements are interpreted as the transition frequency shift (see 6.5.2) we want to characterize.

### 6.5.1 Master equation

In our treatment we consider a density matrix representation of the three-partite joint physical system depicting the trapped particle internal degree of freedom (DOF) along with its external DOF and that of the background hot particle. Assuming an initial separable state, i.e. that there are no quantum correlations between these DOF's, one may right the initial joint state as $\rho_i \equiv \rho_i^{I+M+E} = \rho_i^I \otimes \rho_i^M \otimes \rho_i^E \equiv \rho_i^I \rho_i^M \rho_i^E$ where $\rho^I$ depicts the internal DOF of the trapped strontium atom, $\rho^M$ its external motional DOF and $\rho^E$ that of the environment, i.e. the back ground gas particle colliding with the trapped atom. The idea here is to let the joint state evolve to its post scattering final state $\rho_f^{I+M+E}$. This evolution is unitary and is driven by the scattering operator $S$ according to

$$\rho_f = S\rho_i S^\dagger \ , \qquad\qquad S^\dagger S = \mathbf{1} \tag{131}$$

where the time evolution due to the atom-light interaction is already included $\rho^I$.

As a first step, we content our selves with investigating the transition frequency shift without considering atom losses that would be kicked out from the trap under the effect of the collisions. Hence, we are interested with the internal DOF only, meaning that the final state of interest is defined as the partial trace of $\rho_f$ over both the baground particle motion DOF and that of the trapped atom as well

$$\rho_f^I = \mathrm{Tr}_M\Big(\mathrm{Tr}_E\left(\rho_f\right)\Big) = \mathrm{Tr}_M\Big(\mathrm{Tr}_E\left(S\rho_i S^\dagger\right)\Big) \tag{132}$$

The scattering operator can be expressed using the transition operator $T$ as $S = 1 - iT$ where $T$ is given by

$$T = \frac{1}{2\pi\mu}\int d\mathbf{p}_i d\mathbf{k}_i d\mathbf{k}_f \hat{f}\left(\mathbf{k}_i^*, \mathbf{k}_f^*\right)\delta E_{i,f}\left|\mathbf{p}_i - \mathbf{k}_{fi}, \mathbf{k}_f\right\rangle\left\langle\mathbf{p}_i, \mathbf{k}_i\right| \tag{133}$$

where $\mathbf{p}$ refers to the trapped atom momentum, $\mathbf{k}$ to that of the incoming background particle, the subscripts $i$ and $f$ referring to the initial and final states and where the star $^*$ indicates the corresponding variables have to be considered in the COM frame (see section 6.3), whereas it refers to the lab frame otherwise. The fact we consider only elastic collisions is encompassed in the $\delta E_{i,f} = \delta\left(E(\mathbf{k}_f^*) - E(\mathbf{k}_i^*)\right)$, i.e. in the requirement that the kinetic energy of the ficitious particle in the COM frame be conserved. $\mathbf{k_{fi}} = \mathbf{k_f} - \mathbf{k_i}$ is the momentum change undergone by the incoming particle in the lab frame. The hat on $\hat{F}$ enhances the fact that it is an operator acting on the internal DOF's of the atom. Its general form would be

$$\hat{f}(\mathbf{k}_1, \mathbf{k}_2) = f_e(\mathbf{k}_1, \mathbf{k}_2)\left|e\right\rangle\left\langle e\right| + f_{eg}(\mathbf{k}_1, \mathbf{k}_2)\left|e\right\rangle\left\langle g\right| + f_{ge}(\mathbf{k}_1, \mathbf{k}_2)\left|g\right\rangle\left\langle e\right| + f_g(\mathbf{k}_1, \mathbf{k}_2)\left|g\right\rangle\left\langle g\right| \tag{134}$$

In our case we assume the collisions can not couple the clock ground and excited states, meaning that $f_{eg} = f_{ge} = 0$ and

$$\hat{f}(\mathbf{k}_1, \mathbf{k}_2) = f_e(\mathbf{k}_1, \mathbf{k}_2)\left|e\right\rangle\left\langle e\right| + f_g(\mathbf{k}_1, \mathbf{k}_2)\left|g\right\rangle\left\langle g\right| \tag{135}$$

Therefore $T$ actually acts on all DOF of the joint state. Replacing $S$ with $1 - iT$ in eq. 132 leads to

$$\rho_f = S\rho_i S^\dagger = \rho_i + \frac{i}{2}\left[T^\dagger + T,\ \rho_i\right] + T\rho_i T^\dagger - \frac{1}{2}\left\{T^\dagger T,\ \rho_i\right\} \tag{136}$$

from where we will obtain, tracing out both the atomic and background particle motional DOF, our master equation for the atomic internal DOF

$$\frac{d\rho^I}{dt} \simeq \frac{\Delta\rho^I}{\Delta t} = \frac{\rho_f^I - \rho_i^I}{\Delta t} \tag{137}$$

In the following paragraphs we detail the calculation of each of the contribution to the *right hand side* (r.h.s.) of equation 136 as well as their trace over both the trapped particle motional DOF and the incoming motional DOF.

**Computation of the $T\rho_i T^\dagger$ term** .

From equation 133 we have

$$T\rho_i T^\dagger = \frac{1}{(2\pi\mu)^2}\int d\mathbf{p}_i d\mathbf{k}_i \mathbf{k}_f \int d\mathbf{p}'_i \mathbf{k}'_i d\mathbf{k}'_f \ \delta E_{i,f}\delta E'_{i,f} \tag{138}$$

$$\times \hat{f}\left(\mathbf{k}_i^*, \mathbf{k}_f^*\right) \hat{A} \hat{f}^\dagger\left(\mathbf{k}_i^*, \mathbf{k}_f^*\right) \tag{139}$$

where $\hat{A} = |\mathbf{p}_i - \mathbf{k}_{fi}, \mathbf{k}_f\rangle \langle \mathbf{p}_i, \mathbf{k}_i| \rho_i |\mathbf{p}'_i, \mathbf{k}'_i\rangle \langle \mathbf{p}'_i - \mathbf{k}'_{fi}, \mathbf{k}'_f|$.

For the sake of simplicity we assume the trapped atom is at rest in the lab frame and the incoming particle is in a momentum eigenstate $\mathbf{k}_0$. We then have $\rho_i = \rho_i^I \otimes |0, \mathbf{k}_0\rangle \langle 0, \mathbf{k}_0|$. In this condition eq. 138 becomes

$$T\rho_i T^\dagger = \frac{1}{(2\pi\mu)^2}\int d\mathbf{k}_f d\mathbf{k}'_f \ \delta E_{i,f}\delta E'_{i,f} \times \hat{f}\left(\mathbf{k}_i^*, \mathbf{k}_f^*\right) \rho_i^I \hat{f}^\dagger\left(\mathbf{k}_i^*, \mathbf{k}_f^*\right) \otimes |\mathbf{k}_0 - \mathbf{k}_f, \mathbf{k}_f\rangle \langle \mathbf{k}_0 - \mathbf{k}'_f, \mathbf{k}'_f| \tag{140}$$

Note that because of the spherical symmetry of the Lennard-Jones scattering potential, the scattering amplitude does actually depend only on the modulus of the difference $\mathbf{k}_k^* - \mathbf{k}_i^*$ and its expression in the equation above can be replaced by $\hat{f}\left(\left|\mathbf{k}_f^* - \mathbf{k}_i^*\right|\right)$. The scattering amplitudes and the energy conservation terms are expressed in the COM frame because their forms are simpler in this case. But the integrals are written in the lab frame. The integration domain in the lab frame variables space imposed by the energy conservation term has a non-trivial shape. Indeed, the $\delta E_{i,f}$ Dirac distribution implies $\mathbf{k}_k^* = \mathbf{k}_i^*$ which in lab coordinates translates into

$$k_0^2\left(\frac{m_b^2 - m_t^2}{M^2}\right) + k_f^2 - \frac{2m_b}{M}\mathbf{k}_0 \cdot \mathbf{k}_f = 0 \tag{141}$$

which defines an 2D hyper-surface embedded in the global 3D momentum space of the background gas particle over which should be carried out the above integrals. However, in the case of a trapped particle much heavier than the background gas ones[39], i.e. in the case where $m_t \gg m_b$, we have $m_t/M \sim 1$, $m_b/M \ll 1$, the lab's frame can be considered to coincide with the COM's, i.e. $\mathbf{k}_{i,f}^* = \mathbf{k}_{i,f}$ and equation 141 simplifies to

$$k_f \simeq k_0 \tag{142}$$

This means the quantity $\left|\mathbf{k}_f^* - \mathbf{k}_i^*\right|$ depends only on the angular configuration between $\mathbf{k}_0$ and $\mathbf{k}_f$, and the scattering amplitudes can be expressed as $\hat{f}(k_0, \theta)$ with $\theta = \mathbf{k}_0 \cdot \mathbf{k}_f/(k_0 k_f)$, the same occurring for the primed variables. The double integral 140 then reduces to two shell integrals, i.e.

$$\int d\mathbf{k}_f d\mathbf{k}'_f \longrightarrow \int k\ dk\ d\Omega\ k'\ dk'\ d\Omega' \delta\left(\frac{|k_0|^2 - |k_f|^2}{2\mu}\right)\delta\left(\frac{|k_0|^2 - \left|k'_f\right|^2}{2\mu}\right) \longrightarrow (2\pi\mu)^2 k_0^2 \int d\Omega d\Omega' \tag{143}$$

from where we obtain

$$T\rho_i T^\dagger = k_0^2 \int d\Omega d\Omega' \times \hat{f}(k_0, \theta) \rho_i^I \hat{f}^\dagger(k_0, \theta') \otimes |\mathbf{k}_0 - \mathbf{k}_f, \mathbf{k}_f\rangle \langle \mathbf{k}_0 - \mathbf{k}'_f, \mathbf{k}'_f| \tag{144}$$

Tracing over the back ground gas particle momentum DOF forces $\mathbf{k}_k = \mathbf{k}'_k$ killing out the integral over, say, $\Omega'$ while tracing over the trapped particle DOF gives the trivial equality $\mathbf{k}_k = \mathbf{k}_k$ and therefore

$$\mathrm{Tr}_S\left(\mathrm{Tr}_E\left(T\rho_i T^\dagger\right)\right) = k_0^2 \int d\Omega \times \hat{f}(k_0, \theta) \rho_i^I \hat{f}^\dagger(k_0, \theta') \tag{145}$$

[39]The trapped Strontium atoms have a mass of 87 a.m.u.,w which is nearly two orders of magnitude higher than the mass of the main residual gas particles suspected to collide with the trapped strontium, believed to be mainly di-hydrogen molecules

Finally, assuming an initial atomic internal state $\rho_i^I = \rho_{gg}\left|g\right\rangle\left\langle g\right| + \rho_{eg}\left|e\right\rangle\left\langle g\right| + \rho_{ge}\left|g\right\rangle\left\langle e\right| + \rho_{ee}\left|e\right\rangle\left\langle e\right|$ equation 145 reads

$$\begin{aligned}\mathrm{Tr}_S\left(\mathrm{Tr}_E\left(T\rho_i T^\dagger\right)\right) &= k_0^2\int d\Omega \hat{f}\left(k_0^*,\Omega\right)\rho_i^I\hat{f}^\dagger\left(k_0^*,\Omega\right) &(146)\\ &= k_0^2\int d\Omega\Big[\left|f_g\left(k_0^*,\Omega\right)\right|^2\rho_{gg}\left|g\right\rangle\left\langle g\right| + \left|f_e\left(k_0^*,\Omega\right)\right|^2\rho_{ee}\left|e\right\rangle\left\langle e\right| &(147)\\ &\qquad + f_e\left(k_0^*,\Omega\right)f_g^*\left(k_0^*,\Omega\right)\left|e\right\rangle\left\langle g\right| + h.c.\Big] &(148)\end{aligned}$$

**Computation of the $\left\{T^\dagger T,\rho\right\}$ term**

$$\begin{aligned}T^\dagger T\rho_i &= \frac{1}{(2\pi\mu)^2}\int d\mathbf{p}_i d\mathbf{k}_i\mathbf{k}_f\int d\mathbf{p}_i'\mathbf{k}_i' d\mathbf{k}_f'\ \delta E_{i,f}\delta E_{i,f}' &(149)\\ &\quad\times\hat{f}^\dagger\left(\mathbf{k}_i^*,\mathbf{k}_f^*\right)\hat{f}\left(\mathbf{k}_i'^*,\mathbf{k}_f'^*\right)\hat{B} &(150)\end{aligned}$$

with

$$\begin{aligned}\hat{B} &= \left|\mathbf{p}_i-\mathbf{k}_{fi},\mathbf{k}_f\right\rangle\left\langle\mathbf{p}_i,\mathbf{k}_i|\mathbf{p}_i',\mathbf{k}_i'\right\rangle\left\langle\mathbf{p}_i'-\mathbf{k}_{fi}',\mathbf{k}_f'|\rho_i\right.\\ &= \rho_i^I\otimes\left|\mathbf{p}_i-\mathbf{k}_{fi},\mathbf{k}_f\right\rangle\left\langle 0,\mathbf{k}_0\right|\times\delta(\mathbf{p}_i-\mathbf{p}_i')\ \delta(\mathbf{k}_i-\mathbf{k}_i')\ \delta(\mathbf{p}_i'-\mathbf{k}_f'+\mathbf{k}_i')\ \delta(\mathbf{k}_f'-\mathbf{k}_0)\end{aligned}$$

Therefore

$$\begin{aligned}T^\dagger T\rho_i &= \frac{1}{(2\pi\mu)^2}\int d\mathbf{p}_i d\mathbf{k}_i\mathbf{k}_f\ \delta E_{i,f}\delta E_{i,f}'\\ &\quad\times\hat{f}^\dagger\left(\mathbf{k}_i^*,\mathbf{k}_f^*\right)\hat{f}\left(\mathbf{k}_i'^*,\mathbf{k}_f'^*\right)\rho_i^I\otimes\left|\mathbf{p}_i-\mathbf{k}_{fi},\mathbf{k}_f\right\rangle\left\langle 0,\mathbf{k}_0\right|\end{aligned}$$

from where we get, tracing out both the atom and the incoming particle motion DOF

$$\mathrm{Tr}_S\Big(\mathrm{Tr}_E\left(T^\dagger T\rho_i\right)\Big) = \frac{1}{(2\pi\mu)^2}\int d\mathbf{k}_i\ \delta E_{i,f}\delta E_{i,f}'\ \hat{f}^\dagger\left(\mathbf{k}_i^*,\mathbf{k}_f^*\right)\hat{f}\left(\mathbf{k}_i'^*,\mathbf{k}_f'^*\right)\rho_i^I$$

where we should keep in mind that the two tracings imply $\mathbf{k}_f=\mathbf{k}_0$ and $\mathbf{p}_i=\mathbf{k}_f-\mathbf{k}_i=\mathbf{k}_0-\mathbf{k}_i$. Analyzing carefully how the COM variables relate to that of the lab frame, we have

$$\begin{aligned}\mathbf{k}_i^* &= \frac{-m_b}{M}\mathbf{p}_i+\frac{m_t}{M}\mathbf{k}_i = \frac{-m_b}{M}\mathbf{k}_0+\mathbf{k}_i\\ \mathbf{k}_f^* &= \frac{-m_b}{M}\mathbf{k}_i+\mathbf{k}_0\end{aligned}$$

Henceforth the condition set by the factor $\delta E_{i,f}$ and $\delta E_{i,f}'$ in the integrand, which requires $|\mathbf{k}_i^*| = \left|\mathbf{k}_f^*\right|$ and $|\mathbf{k}_i'^*| = \left|\mathbf{k}_f'^*\right|$ forces simultaneously the equality $|\mathbf{k}_i^*| = k_0$. In other words, the volume integral above is, again, a shell integral. Using the same symmetry argument as in the previous paragraph, we end up with

$$\begin{aligned}\mathrm{Tr}_S\Big(\mathrm{Tr}_E\left(T^\dagger T\rho_i\right)\Big) &= k_0^2\int d\Omega\left(\left|f_g(k_0,\theta)\right|^2\left|g\right\rangle\left\langle g\right| + \left|f_e(k_0,\theta)\right|^2\left|e\right\rangle\left\langle e\right|\right)\rho_i^I\\ &= k_0^2\int d\Omega\Big(\left|f_g(k_0,\theta)\right|^2\left(\rho_{gg}\left|g\right\rangle\left\langle g\right| + \rho_{ge}\left|g\right\rangle\left\langle e\right|\right)\\ &\qquad + \left|f_e(k_0,\theta)\right|^2\left(\rho_{eg}\left|e\right\rangle\left\langle g\right| + \rho_{ee}\left|e\right\rangle\left\langle e\right|\right)\Big)\end{aligned}$$

where we used

$$\begin{aligned}\hat{f}^\dagger\hat{f} &= \left(f_g^*\left|g\right\rangle\left\langle g\right| + f_e^*\left|e\right\rangle\left\langle e\right|\right)\left(f_g\left|g\right\rangle\left\langle g\right| + f_e\left|e\right\rangle\left\langle e\right|\right)\\ &= \left|f_g\right|^2\left|g\right\rangle\left\langle g\right| + \left|f_e\right|^2\left|e\right\rangle\left\langle e\right|\end{aligned}$$

To complete the computation of the anti-commutator, we notice that $\rho\hat{T}^\dagger T = \left(\hat{T}^\dagger T\rho\right)^\dagger$ and therefore

$$\begin{aligned}\mathrm{Tr}_S\Big(\mathrm{Tr}_E\left(\rho_i T^\dagger T\right)\Big) &= \mathrm{Tr}_S\Big(\mathrm{Tr}_E\left(T^\dagger T\rho_i\right)\Big)^\dagger \\ &= k_0^2\int d\Omega\Big(|f_g(k_0,\theta)|^2\big(\rho_{gg}\,|g\rangle\langle g| + \rho_{eg}\,|e\rangle\langle g|\big) \\ &\qquad + |f_e(k_0,\theta)|^2\big(\rho_{ge}\,|g\rangle\langle e| + \rho_{ee}\,|e\rangle\langle e|\big)\Big)\end{aligned}$$

which is almost the same but with $\rho_{ge}\,|g\rangle\langle e|$ and $\rho_{eg}\,|e\rangle\langle g|$ interchanged.

**Computation of the $\left[T+T^\dagger,\rho\right]$ term**

$$T\rho_i = \frac{1}{2\pi\mu}\int d\mathbf{p}_i d\mathbf{k}_i d\mathbf{k}_f \hat{f}(\mathbf{k}_i^*,\mathbf{k}_f^*)\ \delta E_{if}\ \hat{C}$$

with $\hat{C} = |\mathbf{p}_i-\mathbf{k}_{fi},\mathbf{k}_f\rangle\langle\mathbf{p}_i,\mathbf{k}_i|\,\rho_i = \rho_i^I\otimes|\mathbf{p}_i-\mathbf{k}_{fi},\mathbf{k}_f\rangle\langle 0,\mathbf{k}_0|\ \ \delta(\mathbf{p}_i)\delta(\mathbf{k}_0-\mathbf{k}_i)$ leading to

$$T\rho_i = \frac{1}{2\pi\mu}\int d\mathbf{k}_f \hat{f}(\mathbf{k}_i^*,\mathbf{k}_f^*)\ \delta E_{if}\ \rho_i^I\otimes|\mathbf{k}_0-\mathbf{k}_f,\mathbf{k}_f\rangle\langle 0,\mathbf{k}_0|$$

Tracing over the motional DOF of both colliding particles enforces $\mathbf{k}_f=\mathbf{k}_0$ and since we already have form the computation of $\hat{C}$ that $\mathbf{p}_i=0$ and $\mathbf{k}_i=\mathbf{k}_0$, we have in the COM frame $\mathbf{k}_i^*=\mathbf{k}_f^*=(m_t/M)\mathbf{k}_0\simeq\mathbf{k}_0$ in the case $m_t\gg m_b$, which leads to

$$\mathrm{Tr}_S\Big(\mathrm{Tr}_E\big(T\rho_i\big)\Big) = k_0 f_g\big(k_0,0\big)\Big(\rho_{gg}\,|g\rangle\langle g| + \rho_{ge}\,|g\rangle\langle e|\Big) + k_0 f_e\big(k_0,0\big)\Big(\rho_{ee}\,|e\rangle\langle e| + \rho_{eg}\,|e\rangle\langle g|\Big)$$

Proceeding in a similar fashion gives

$$\mathrm{Tr}_S\Big(\mathrm{Tr}_E\big(T^\dagger\rho_i\big)\Big) = k_0 f_g^*\big(k_0,0\big)\Big(\rho_{gg}\,|g\rangle\langle g| + \rho_{ge}\,|g\rangle\langle e|\Big) + k_0 f_e^*\big(k_0,0\big)\Big(\rho_{ee}\,|e\rangle\langle e| + \rho_{eg}\,|e\rangle\langle g|\Big)$$

and, since $(\rho T)^\dagger = T^\dagger\rho$ and $\left(\rho T^\dagger\right)^\dagger = T\rho$, we have

$$\begin{aligned}\mathrm{Tr}_S\Big(\mathrm{Tr}_E\big(\rho_i T^\dagger\big)\Big) &= \mathrm{Tr}_S\Big(\mathrm{Tr}_E\big(T\rho_i\big)\Big)^\dagger \\ &= k_0 f_g^*\big(k_0,0\big)\Big(\rho_{gg}\,|g\rangle\langle g| + \rho_{eg}\,|e\rangle\langle g|\Big) + k_0 f_e^*\big(k_0,0\big)\Big(\rho_{ee}\,|e\rangle\langle e| + \rho_{ge}\,|g\rangle\langle e|\Big) \\ \mathrm{Tr}_S\Big(\mathrm{Tr}_E\big(\rho_i T\big)\Big) &= \mathrm{Tr}_S\Big(\mathrm{Tr}_E\big(T^\dagger\rho_i\big)\Big)^\dagger \\ &= k_0 f_g\big(k_0,0\big)\Big(\rho_{gg}\,|g\rangle\langle g| + \rho_{eg}\,|e\rangle\langle g|\Big) + k_0 f_e\big(k_0,0\big)\Big(\rho_{ee}\,|e\rangle\langle e| + \rho_{ge}\,|g\rangle\langle e|\Big)\end{aligned}$$

**Master equation** .

Gathering all this results in eq. 136 we get

$$\begin{aligned}\Delta\rho_I &= \rho_f^I - \rho_i^I \\ &= \rho_{ge}\,|g\rangle\langle e|\left(k_0^2\int d\Omega f_e^*(k_0,\theta)f_g(k_0,\theta) - \frac{k_0^2}{2}\sigma_e - \frac{k_0^2}{2}\sigma_g + ik_0\mathrm{Re}\left(f_g(k_0,0)-f_e(k_0,0)\right)\right) \\ &+ \rho_{eg}\,|e\rangle\langle g|\left(k_0^2\int d\Omega f_g^*(k_0,\theta)f_e(k_0,\theta) - \frac{k_0^2}{2}\sigma_e - \frac{k_0^2}{2}\sigma_g + ik_0\mathrm{Re}\left(f_e(k_0,0)-f_g(k_0,0)\right)\right)\end{aligned}$$

### 6.5.2 Interpretation in term of frequency shift

Separating the real part form the imaginary one in the expression above, we end up with

$$\dot{\rho}_{ge} \propto \rho_{ge} \left( R_{ge} + i I_{ge} \right)$$

where

$$R_{ge} = k_0^2 \int d\Omega \ \mathrm{Re}\big(f_e^*(k_0,\theta) f_g(k_0,\theta)\big) - \frac{k_0^2}{2}\sigma_e - \frac{k_0^2}{2}\sigma_g$$
$$I_{ge} = k_0^2 \int d\Omega \ \mathrm{Im}\big(f_e^*(k_0,\theta) f_g(k_0,\theta)\big) + k_0 \mathrm{Re}\left(f_g(k_0,0) - f_e(k_0,0)\right)$$

We then remember, following [68], that in the case of standard Rabi flopping, the evolution equation for the density matrix off-diagonal terms is

$$\dot{\rho}_{ge} = i\left(\frac{\Omega}{2}\left(\rho_{gg} - \rho_{ee}\right) - \Delta\rho_{ge}\right)$$

where $\Omega$ is the Rabi frequency and $\Delta$ the detuning between the light field frequency and the two-level transition frequency. Adding the scattering evolution terms to that given by the Rabi evolution then leads to

$$\dot{\rho}_{ge} = i\frac{\Omega}{2}\left(\rho_{gg} - \rho_{ee}\right) + i\left(I_{ge} - \Delta\right)\rho_{ge} + R_{ge}\rho_{ge} \tag{151}$$

where we see that $I_{ge}$ plays formally the same role as the detuning $\Delta$ and can thus be interpreted as shifting the atomic transition. The term in $R_{ge}$, having a real factor, is a de-coherence term, meaning its effect is to take the initial internal pure state of the ensemble of trapped atoms towards an evolved mixed state, eventually ending in a pure statistical mix of states projected on the ground or excited clock state. Using the partial expansion given by eq. 126 for the scattering amplitudes $f_{e,g}$ we have

$$\int d\Omega \ f_e^*(k_0,\theta) f_g(k_0,\theta) = \frac{1}{k_0^2}\sum_{l,m}(2l+1)(2m+1)e^{i(\delta_{g,l}-\delta_{e,m})}\sin(\delta_{g,l})\sin(\delta_{e,m})\int d\Omega P_l(\cos\theta)P_m(\cos\theta) \tag{152}$$

$$= \frac{4\pi}{k_0^2}\sum_l (2l+1)e^{i(\delta_{g,l}-\delta_{e,l})}\sin\left(\delta_{g,l}\right)\sin\left(\delta_{e,l}\right) \tag{153}$$

and

$$f_g(k_0,0) - f_e(k_0,0) = \frac{1}{k_0}\sum_l (2l+1)P_l(\cos(0))\left(e^{i\delta_{g,l}}\sin(\delta_{g,l}) - e^{i\delta_{e,l}}\sin(\delta_{e,l})\right) \tag{154}$$

and we can express $I_{ge}$ as

$$I_{ge} = 4\pi\sum_l (2l+1)\sin\left(\delta_{g,l}-\delta_{e,l}\right)\sin\left(\delta_{g,l}\right)\sin\left(\delta_{e,l}\right) + \frac{1}{2}\sum_l (2l+1)\left(\sin\left(2\delta_{g,l}\right) - \sin\left(2\delta_{e,l}\right)\right) \tag{155}$$

where we used $P_l(1) = 1$. Since $\int d\Omega \ f_e^*(k_0,\theta) f_g(k_0,\theta)$ is formally equivalent to definition of the total scattering cross section $\int d\Omega \ |f^*(k_0,\theta)|^2 = \sigma$, we refer to $I_{ge}$ and $R_{ge}$ as the frequency shift cross section and the de-coherence cross section respectively. Note that our result is nothing but the summation of the two different shift cross sections proposed by A. Vutha in [68] and K. Gibble in [69]. For this reason the first term is denoted as $\sigma_{\nu,V}$ and the second one $\sigma_{\nu,G}$, i.e.

$$I_{ge} = \sigma_{\nu,V} + \sigma_{\nu,G} \tag{156}$$
$$\sigma_{\nu,V} = 4\pi\sum_l (2l+1)\sin\left(\delta_{g,l}-\delta_{e,l}\right)\sin\left(\delta_{g,l}\right)\sin\left(\delta_{e,l}\right) \tag{157}$$
$$\sigma_{\nu,G} = \frac{1}{2}\sum_l (2l+1)\left(\sin\left(2\delta_{g,l}\right) - \sin\left(2\delta_{e,l}\right)\right) \tag{158}$$

Note that the first r.h.s. term, stemming from an integration over the whole solid angle has a counterintuitive behavior since it predicts that if the partial scattering phase shifts $\delta_l$ vanish for one of the atomic

internal state the total frequency shift vanishes as well, whereas we expect the frequency shift to occur even when one only of the internal state is affected by the scattering. On the other hand, the second r.h.s. term is just the difference of each level shift considered independently. But note that this second term does not stem from an integration over the whole solid angle but only from scattering events where the incoming particle is not deflected at all, i.e. corresponds to the *forward* scattering, as argued by K. Gibble.

## 6.6 Quasi-classical regime

The next step consists in finding a way to estimate the partial wave phase shifts $\delta_l$ appearing in the collisional frequency shift cross section as expressed in the previous section. Equation 121 compared with equation 127 gives

$$c_l \frac{u_l(r)}{r} = (2l+1)\frac{(-1)^{l+1}e^{-ikr} + S_l(k)e^{ikr}}{2ikr} = (2l+1)\frac{(-1)^{l+1}e^{-ikr} + e^{2i\delta_l}e^{ikr}}{2ikr} \tag{159}$$

which gives a relation between $\delta_l$ and $u_l(r)$, where $u_l(r)$ is solution of the radial part of the Lipmann-Schwinger eq. 122. We follow here the development of [70] to estimate the solutions of eq. 122 for large values of $l$, which are expected to dominate summation in the expressions of the different cross sections. This is done in the framer of the quasi-classical regime.

### 6.6.1 Quasi-classical momentum and wave functions

In the classical-regime, the formalism is still that of the quantum mechanics but some fundamentally quantum features are dropped out such as the non-commutativity of position and momentum operators, in the sens that we allow ourselves to consider expressions such as $p(r)$, which could not make any sens with $[\hat{r}, \hat{p}] \neq 0$. In other words, we still consider the possibility of delocalized wave functions but with Heisenberg uncertainty principle released for position and momentum. For this picture to have any meaning requires of course some constraint on the potential driving the dynamics, as briefly explored hereafter.

Let us start with writing $u_l(r)$, solution of eq. 122, as

$$u_l(r) = e^{i\sigma(r)/\hbar} \tag{160}$$

where all the complexity of this wave function is contained in the function $\sigma$ that we expand as a power series of $\hbar$ as

$$\sigma(r) = \sum_k \sigma_k(r) \left(\frac{\hbar}{i}\right)^k \tag{161}$$

We then have (see. [70]) to the $0^{th}$ order in $\hbar$

$$\sigma_0(r) = \pm \int_{r_0}^{r} p(r')dr' \qquad\qquad p(r) = \sqrt{2m\left(E - U(r)\right)} \tag{162}$$

this expression for $p$ being the classical one, i.e. $p^2/2m = mv^2/2 = E - U = E^K$ the kinetic energy. Note that such an approximation to be valid demands $\hbar\left|\partial_r^2\sigma / \left(\partial_r\sigma\right)^2\right| \ll 1$ where $\partial_r \equiv d/dr$ or equivalently $\partial_r(\hbar/\partial_r\sigma) \ll 1$. Assuming $\sigma \sim \sigma_0$ gives $\partial_r\sigma \sim p(r)$ and therefore the condition above reads

$$\partial_r\lambda(r)/2\pi \ll 1 \tag{163}$$

with $\lambda(r) = 2\pi/p(r)$ is the quasi-classical de Broglie wavelength, i.e. given using the classical expression for $p$ in $p = \hbar k = \hbar 2\pi/\lambda$. This is the main assumption one has to make to validate the quasi-classical formulation. However, the wave function is constant over the space and can not be normalized. Including the first order term of the power series of $\sigma$ will modulate its amplitude and is, as seen hereafter, consistent with what would expect from a classical description of the system. Indeed, the first order term reads (see [70])

$$\sigma_1(r) = -\frac{1}{2}\log\left(p(r)\right) \tag{164}$$

leading to

$$u_{l,\pm}(r) = \frac{1}{\sqrt{p}} e^{(\pm i/\hbar)\int p(r)dr} \quad , \qquad\qquad u_l(r) = C_+ u_{l,+}(r) + C_- u_{l,-}(r) \tag{165}$$

The connection to the classical case is as follows. From a quantum point of view the probability of finding a particle in state $\psi_\pm$ in a given small interval around the position $r$ over a time duration $t$ scales as $|\psi(r)_\pm|^2 = 1/p(r)$. Classically, the faster the particle, the lower the time it spends in the spatial interval, i.e. the probability scales as $1/v \propto 1/p$. Hence, with this definition of the quasi-classical wave function the particle behavior mimics in some aspects that of a classical one.

### 6.6.2 Quasi-classical phase shift

For large values of $l$ the corresponding partial waves can be considered Quasi-classical and can be expressed as

$$u_{l,\pm}(r) = \frac{e^{(\pm i/\hbar)p(r)}}{\sqrt{p(r)}} \quad , \qquad p(r) = \int_{r_0}^{r} \sqrt{k^2 - \frac{l(l+1)}{r'^2} - \frac{2\mu}{\hbar} V_L(r')}\, dr' \tag{166}$$

Remembering that $r_0$ is the smallest value of the radial variable $r$ such that the radical under the square root in the integrand of the $p$ is positive and that $V_L$ scales as $r^{-6}$ at large range, the larger $l$ the larger $r_0$ as well and the lower the ratio of the London potential to the centrifugal one

$$\lim_{l\to\infty} \frac{2\mu V_L(r)/\hbar}{l(l+1)/r^2} = 0 \qquad\qquad \text{for } r > r_0(l) \tag{167}$$

and therefore

$$\sqrt{k^2 - \frac{l(l+1)}{r'^2} - \frac{2\mu}{\hbar} V_L(r')} \sim \sqrt{k^2 - \frac{l(l+1)}{r'^2}} - \frac{\frac{2\mu}{\hbar} V_L(r')}{\sqrt{k^2 - \frac{l(l+1)}{r'^2}}} \tag{168}$$

We now consider that the phase shift $\delta_l$ of the partial wave $\psi_l$ due to scattering is equal to the above scattered partial wave phase to which we subtract the non scattered QC partial wave phase $p^0$ obtained for a vanishing scattering potential $V_L = 0$ and consider all of this in the asymptotic limit $r \longrightarrow \infty$, i.e.

$$\delta_l = \frac{\pm i}{\hbar} \left(p(r) - p^0(r)\right) \sim \frac{\mp i}{\hbar} \int_{r_0(l)}^{\infty} \frac{\frac{2\mu}{\hbar} V_L(r')}{\sqrt{k^2 - \frac{l(l+1)}{r'^2}}}\, dr' \tag{169}$$

For specific potentials $V(r) = -C_n r^{-n}$ this gives

$$\delta_l \simeq \frac{\sqrt{\pi}\,\Gamma((n-1)/2)}{2\,\Gamma(n/2)} \frac{\mu C_n k^{n-2}}{\hbar^2 l^{n-1}} \tag{170}$$

and in the particular case of the London potential, i.e. for $n = 6$

$$\delta_l \simeq \frac{3\pi\mu C_6 k^4}{16\hbar^2 l^5} \tag{171}$$

Injecting this expression for $\delta_l$ in equation (130) yields an expression for the total cross-section in the quasi-classical regime for the $1/r^n$ potential:

$$\sigma(k) = \xi_n \left(\frac{\mu C_n}{\hbar^2 k}\right)^{\frac{2}{n-1}} \tag{172}$$

where $\xi_n$ is a numerical constant, with $\xi_6 \simeq 8.0$. Integrating over the Maxwell-Boltzmann distribution yields:

$$\langle \sigma(\mu v_0/\hbar) \rangle_{\mathrm{MB}} = \frac{2\xi_n\,\Gamma((3n-5)/(2n-2))}{\sqrt{\pi}} \left(\frac{C_n}{\hbar v^*}\right)^{\frac{2}{n-1}} \tag{173}$$

and

$$\langle v_0\ \sigma(\mu v_0/\hbar) \rangle_{\mathrm{MB}} = \frac{2\xi_n\,\Gamma((2n-3)/(n-1))}{\sqrt{\pi}} v^* \left(\frac{C_n}{\hbar v^*}\right)^{\frac{2}{n-1}} \tag{174}$$

For $n = 6$, this reduces to:

$$\langle \sigma(\mu v_0/\hbar) \rangle_{\mathrm{MB}} = 8.1 \left(\frac{C_6}{\hbar v^*}\right)^{\frac{2}{5}} = 8.1 \left(\frac{2k_B T}{m_b}\right)^{-\frac{1}{5}} \left(\frac{C_6}{\hbar}\right)^{\frac{2}{5}}, \tag{175}$$

and

$$\langle v_0\ \sigma(\mu v_0/\hbar)\rangle_{\mathrm{MB}} = 8.4\, v^* \left(\frac{C_6}{\hbar v^*}\right)^{\frac{2}{5}} = 8.4 \left(\frac{2k_B T}{m_b}\right)^{\frac{3}{10}} \left(\frac{C_6}{\hbar}\right)^{\frac{2}{5}}. \tag{176}$$

It can be shown that the approximate quantum expression 174 for the loss rate is valid as long as it is smaller than the classical loss rate. This is satisfied for

$$U_0 \lesssim \frac{\hbar^2}{m_t \sigma} \tag{177}$$

where $\sigma$ is the maximal quantum cross-section given by equation (173).

## 6.7 Losses

### 6.7.1 Losses for an incoming flux of background gas particles

This paragraph gives some hints about should be done in order to include particle losses in the model we derived in section 6.5.

Note that our master equation was derived starting from the unitary two-body state evolution $\rho_f = S\rho_i S^\dagger$, which, as being unitary, does not address atom losses, i.e. the fact that if the momentum transferred from the incoming particle to the trapped atom is to large it kicks it out from the trap. At the very beginning of this chapter we defined classically the maximal deflection angle $\alpha_{x,m}$, $x = g, e$ (ground and excited clock states) for the fictitious particle over which the trapped atom is expelled off the trap, giving a loss cross section

$$\sigma_{x,\mathrm{loss}}(k) = 2\pi \int_{\alpha_{x,m}}^{\pi} \frac{d\sigma_x(k,\theta)}{d\Omega} \sin\theta d\theta \quad , \quad x = e, g \tag{178}$$

This means that for a flux of incoming particles with momentum $\mathbf{k}$, i.e. a speed $v = \hbar k/\mu$, and density $n = 1/(\sigma_{x,\mathrm{loss}} v\tau)$ it takes a tim $\tau$ for a trapped atom in internal state $|x\rangle$ to be expelled out from the trap, i.e. for the fictitious particle momentum be deflected by an angle larger than $\alpha_{x,m}$. In other words, the loss rate is of one atom per duration $\tau(v,n) = 1/(nv\sigma_{x,\mathrm{loss}})$, i.e. $\gamma_x(v,n) = nv\sigma_{x,\mathrm{loss}}$. For a given speed distribution $\mathrm{D}(v)$ for the incoming background gas particles the loss rate is just given by the average of $\gamma_x(v,n)$ over this distribution

$$\gamma_x = n\langle\gamma_x(v,n)\rangle_{\mathrm{D}} = n\langle v\ \sigma_{x,\mathrm{loss}}(\mu v/\hbar)\rangle_{\mathrm{D}} \tag{179}$$

To incorporate this in our model we introduce populations decay rate in the master equation. We add the terms $-\gamma_g\rho_{gg}$ and $-\gamma_e\rho_{ee}$ to the time evolution equations of $\gamma_{gg}$ and $\gamma_{ee}$ respectively, leading to

$$\begin{aligned}\dot{\rho}_{gg} &= -i\frac{\Omega}{2}(\rho_{eg} - \rho_{ge}) - \gamma_g\rho_{gg} \\ \dot{\rho}_{ee} &= +i\frac{\Omega}{2}(\rho_{eg} - \rho_{ge}) - \gamma_e\rho_{ee}\end{aligned}$$

Therefore, the total loss rate depends on the population balance, i.e. difference $\rho_{gg} - \rho_{ee} = 2\rho_{gg} - 1$ according to

$$\frac{dN}{dt} = \frac{d(N(\rho_{gg} + \rho_{ee}))}{dt} = -N(\gamma_g\rho_{gg} + \gamma_e\rho_{ee}) = -N(\rho_{gg}(\gamma_g - \gamma_e) + \gamma_e) = -\gamma N$$

### 6.7.2 Losses for a Maxwell-Boltzmann distribution

In the case of a trap sufficiently low such that the maximal deflection angle $\alpha_m$ is almost 0, we can consider as good approximation that the loss cross section equals the total cross section, i.e. $\sigma_{x,m} \simeq \sigma_x$. In order to compute the loss rates in the case of a Maxwell-Boltzmann distribution for the speed of the background gas particles, we convert the discrete sum in the expression of $\sigma_x(k)$ into an integral, leading

to

$$\sigma(k) = \frac{4\pi}{k^2}\sum_l (2l+1)\sin^2\delta_l \tag{180}$$

$$= \frac{4\pi}{k^2}\sum_l (2l+1)\sin^2\frac{\sqrt{\pi}\,\Gamma(5/2)}{2\,\Gamma(3)}\frac{\mu C_6 k^4}{\hbar^2 l^5} \tag{181}$$

$$\simeq \frac{4\pi}{k^2}\int 2l\sin^2\frac{\sqrt{\pi}\,\Gamma(5/2)}{2\,\Gamma(3)}\frac{\mu C_6 k^4}{\hbar^2 l^5}dl \tag{182}$$

$$= \xi_6\frac{1}{k^2}\left(\frac{\mu C_6 k^4}{\hbar^2}\right)^{\frac{2}{5}} = \xi_6\left(\frac{\mu C_6}{\hbar^2 k}\right)^{\frac{2}{5}} \tag{183}$$

By a numerical calculation of the actual sum, we find that $\xi_6 \simeq 8.0$ and for the average over the Maxwell-Boltzmann distribution

$$\gamma_x = n\langle v\ \sigma_{x,\mathrm{loss}}(\mu v/\hbar)\rangle_{\mathrm{MB}} = 8.4\left(\frac{2k_BT}{m_b}\right)^{3/10}\left(\frac{C_{x,6}}{\hbar}\right)^{2/5} \tag{184}$$

## 6.8 Shift and losses

Since the ejected atoms are not detected they do not contribute to the frequency shift we must restrain the integrals over $\theta$ in expression of the general form $\int d\Omega f_x^{(*)} f_y^{(*)}$ to $\theta \in [0, \alpha_m]$. Hence, the orthogonality relationship between the Legendre polynomials can no longer be used to compute $\int d\Omega f_e^*(k_0^*,\theta) f_g(k_0^*,\theta)$. However, for low trap depth, the maximal angles $\alpha_{x,m}$, $x = e, g$ is very low, meaning that this integral is ran over small values of $\theta \in [0, \alpha_m \ll \pi]$. Hence $P_l(\cos(\theta \ll \pi)) \sim 1$ can be considered constant over the integration domain and, in the case $\alpha_{g,m} \sim \alpha_{e,m} \sim \alpha_m$

$$\sigma_{\nu,\mathrm{V}} = \int_{0<\theta<\alpha_m} d\Omega f_e^*(k_0^*,\theta) f_g(k_0^*,\theta) \sim \frac{4\pi\alpha_m}{k_0^{*2}}\sum_{l,m}(2l+1)(2m+1)e^{i(\delta_{g,l}-\delta_{e,m})}\sin(\delta_{g,l})\sin(\delta_{e,m}) \tag{185}$$

Note that for $\alpha_{g,m} \neq \alpha_{e,m}$ the above formula is not valid. Indeed, it stems from an integral of the form

$$\int d\mathbf{p}_i d\mathbf{k}_i d\mathbf{k}_f \int d\mathbf{p}_i' d\mathbf{k}_i' d\mathbf{k}_f'\ \ f_g(\mathbf{k}_i^*, \mathbf{k}_f^*) f_e^*(\mathbf{k}_i'^*, \mathbf{k}_f'^*)\hat{Q}$$

which no longer simplifies to 185 when the domains of integration for the primed variables are not the same as for the un-primed ones. However, in the case the Boltzmann distribution of momenta for incoming particle varies slowly over regions where $\arccos\left(\mathbf{k}_i^* \cdot \mathbf{k}_f^*/k_i^* k_f^*\right)$ is of the order of the difference $\alpha_{e,m} - \alpha_{g,m}$, we expect eq. 185 to be a good approximation and in the limit $\alpha_m \ll 1$, the second r.h.s. of 155 term dominates the expression of $I_{ge}$ which then reduces to the expression given in [69] for frequency collisional shift, i.e.

$$\sigma_\nu \sim \sigma_{\nu,\mathrm{G}} = \mathrm{Re}\left(f_g\left(k_0^*, 0\right) - f_e\left(k_0^*, 0\right)\right) = \frac{\pi}{2k_0^*}\sum_l (2l+1)\left(\sin 2\delta_{g,l} - \sin 2\delta_{e,l}\right) \tag{186}$$

Using the same trick of converting the discrete sum into an integral as for the calculation of the total cross section leads to

$$\sigma_{\nu,\mathrm{G}} \simeq \zeta_6\left(\frac{\mu C_6}{\hbar^2 k}\right)^{2/5} \tag{187}$$

with numerical calculations giving $\zeta_6 \simeq 1.45$ . Averaged value over the Maxwell-Boltzmann distribution could be obtained in a similar fashion as well. Comparing expression 183 for the loss cross section and expression 187 for the frequency shift cross section, one sees that both scale the same way with the $C_6$ coefficient and the incoming momentum $k$. We then expect the frequency shift to be proportional to the loss rate, i.e. inversely proportional to the atoms lifetime in the trap. We report on the first measurement of this effect on a strontium optical clock in section 6.9.

### 6.8.1 Shift and losses, other approach

This paragraph just gives hints about what could be tried to explore and investigate the effect of the high difference in the $C_6$ coefficients of the ground and the excited clock state.

Because of the factor $2l+1$ in the summation giving $\delta_\omega$, the dominant terms are those corresponding to large values of $l$. Since $\delta_l \sim 3\times10^5\ [m^5]\ l^{-5}$, the dominant terms of this summation are such that (for say $l>20$) $\delta_l \ll 1$ and the shift can be approximated as

$$\delta_\Omega \sim \sum_l \frac{2l+1}{k_0^*} 2\left(\delta_{g,l}-\delta_{e,l}\right) \propto \sum_l \frac{2l+1}{k_0^*}\frac{2}{l^5}\Delta_{C_6} \tag{188}$$

where $\Delta_{C_6} = C_{g,6} - C_{e,6}$. Regarding the total cross section this leads to

$$\sigma_g - \sigma_e \sim \frac{4\pi}{k_0^*}\sum_l (2l+1)\left(\delta_{g,l}^2-\delta_{e,l}^2\right) \propto \sigma_e \sim \frac{4\pi}{k_0^*}\sum_l (2l+1)\frac{1}{l^5}\left(2\overline{C}_6\Delta_{C_6}-\Delta_{C_6}^2\right) \tag{189}$$

where $\overline{C}_6 = (C_{g,6}+C_{e,6})/2$ is the averaged $C_6$ coefficient of the two atomic internal states. Hence, in the case $\Delta_{C_6} \ll \overline{C}_6$, the frequency shift is proportional to the difference between the total scattering cross sections of the two clock states.

## 6.9 Hot collisions shifts measurement

### 6.9.1 Hot collision shift model

Let us first consider the case where only one type of particles are present in the residual background gas of the vacuum chamber, i.e. associated with particular coefficients $c_6$ and $c_12$. As exposed in the previous section, the clock frequency shift $\delta\nu$ induced by hot collisions this particles is expected to scale linearly with the partial pressure $P$ of this gas. Moreover, $P$ is expected to scale linearly with the loss rate $\gamma$, i.e. the rate at which atoms are expelled from the trap due to hot collisions, which can be expressed as the inverse of the life time $\tau$ of the atoms in the trap. Thus, we expect a behavior of the form

$$\delta\nu = \alpha\frac{1}{\tau} \tag{190}$$

If we now consider to possibility of having several types of particles in the residual background gas, labeled by the index $_i$, each of them would contribute to the shift proportionally to the corresponding residual pressures $P_i$, i.e. proportionally to the inverse of the *partial loss rate* $1/\tau_i$, leading to

$$\delta\nu = \sum_i \delta\nu_i = \sum_i \alpha_i\frac{1}{\tau_i} \tag{191}$$

However, we do not have experimentally access to each $\tau_i$ individually but only to an *effective lifetime* $\tau_e$ defined as

$$\frac{1}{\tau_e} = \sum_i \frac{1}{\tau_i} \tag{192}$$

resulting from the intuitive fact that the loss rates add up, i.e. $\gamma_e = \sum_i \gamma_i$. In our first attempt to measure the effect of this collisions on the clock frequency, as described in section 6.9.3, we let vary some partial pressures $P_i$ but in an uncontrolled manner. Hence, some of the $P_i$ do probably not vary, and others vary but probably not in the same proportion. In practice, we tune one parameter, say $x$ on which depends each of the partial pressure $p_i \equiv P_i(x)$ and therefore the partial lifetimes $\tau_i \equiv \tau_i(x)$ and measure $\delta\nu(x)$ and $\tau_e(x)$. We can then *eliminate* $x$ from the relation and plot $\delta\nu(\tau_e)$ while varying $x$. In section 6.9.3 we work out a simplified relation to address the question.

### 6.9.2 Atoms lifetime in the trap

Atoms lifetime in the trap plays a central role form the measurement of the clock frequency shift induced by hot collisions. It is clear as well from the previous section that the longer the lifetime, the lower the clock frequency shift. Moreover, we enhance in section 8.4 how having a long atom lifetime in the trap is crucial for an effective reduction of the clock frequency instability induced by Dick effect via the implementation of a non destructive detection system. Hence, in 2017, even before being aware of the

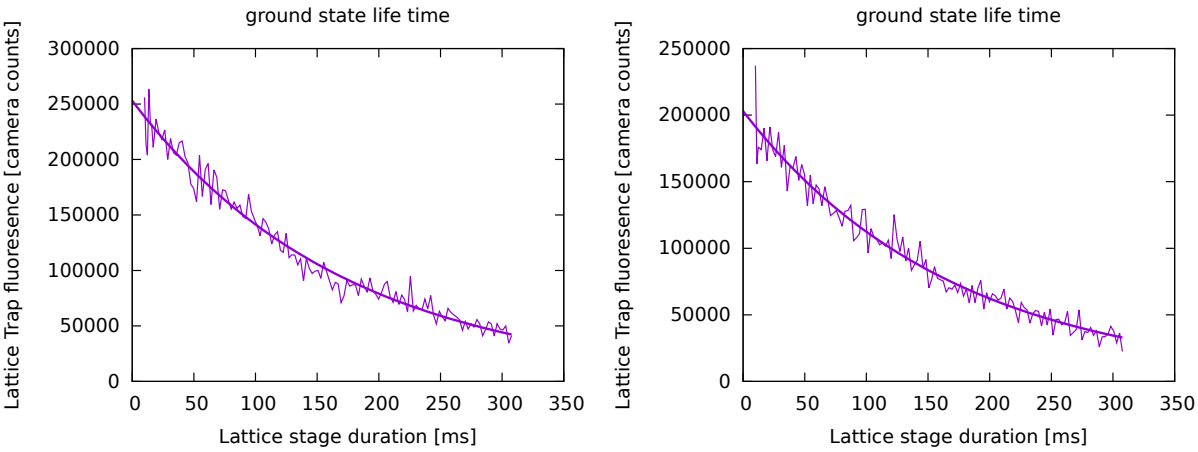


Figure 27: Decay of the number of atoms trapped in the lattice trap before summer 2017 on our SrB strontium. The number of atoms is given in number of camera counts ($\sim$ 240 counts per atom) as a function of the lattice trap stage duration. Typical lifetime were about 150 - 200 ms. This has to be compared with the almost 10 s of lifetime in our other clock Sr2.

significant amplitude of the collisions induced shift, we put a lot of efforts to extend the atom lifetime. Before summer 2017, the lifetime on the SrB clock[40] was about 170 ms (169 ms on the measurement displayed in figure 27, left side plot), which is almost 50 times lower than on our other clock, Sr2, for which the lifetime is close to 10 s. One of the main differences between our two clocks is that the atomic beam stemming from the oven is aligned to the position of the trap in SrB, but not in Sr2 for which an all-optical deflection scheme has been implemented. Our first guess was then that the lifetime in the trap was limited by the collisions with hot strontium atoms from the oven beam. We then decided to set an atomic beam mechanical shutter consisting in an in vacuum metallic flag fixed on a bellow[41] activated from a stepper motor located outside the vacuum system. This resulted in no significant increase of the lifetime (172 ms on the measurement displayed on Figure 27, right plot).

Overlooking the time evolution pattern of the lifetime as appearing on Figure 28 (right plot), the averaged lifetime over the covered period amounts to 566 ms (with a standard deviation of $\pm$ 106 ms), which is a three fold improvement compared to the situation before the chamber change.

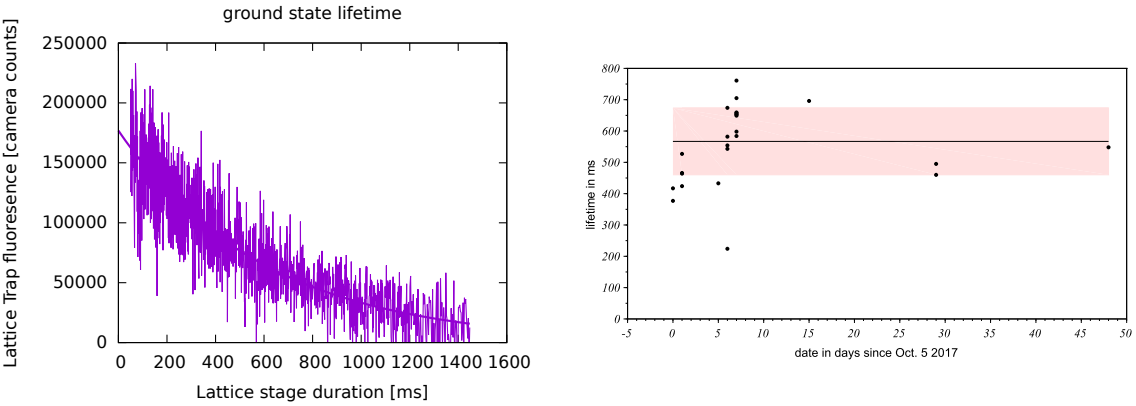


Figure 28: Lifetime measurements after we change the vacuum chamber. The lifetime improved a bit, reaching typical values between 400 and 600 ms. However, this has not been very stable over time. On the right-side is plot the evolution of the lifetime over time over a period streching from 2017 Oct. 5 till Nov. 17.

[40] that on which the work of this thesis has been carried out
[41] a vacuum compatible soring

We then suspected there was a leak allowing for gas exchange with the outside of the chamber. After unfruitful leakage tests, we conclude the lifetime was limited by a *virtual leak*, i.e. by some gas trapped somewhere in the chamber being released at very low rate into the chamber. In summer 2017 we then change the vacuum chamber, which is an heavy operation that last a bit more than one month. Few weeks after the chamber change, we measured regularly the lifetime whose evolution over a bit less than two months is represented on Figure 28 (right side). The behavior over such time scale is however not well defined: we observe a clear increase over the 5 first days over the whole measurement period, but this increase then mitigates over the 40 following days, even though more data would be necessary to obtain a reliable statistics. We nevertheless note that the spread of the data taken on a same day suggests other sources of lifetime instabilities, which could stem from lattice amplitude and/or frequency instabilities.

### 6.9.3 Hot collisions shift measurement

Probing effects of collisions with hot background atoms or molecules requires deteriorating or further improving the vacuum environment of the atoms. Pushing further the level of vacuum in the chamber has been held in focus in our attempt to extend the atoms lifetime in the trap which we believe is limited by hot collisions with chamber background molecules and is hardly achievable without radical interventions on the setup and might even be impossible without renewing our chamber design. We are thus left with the only option of artificially degrade the vacuum within the chamber. However, this has to be compatible with keeping a sufficiently high number of atoms trapped in the lattice to be available for the clock interrogation. On our setup the vacuum in achieved by a set of three ion pumps plus a chemical getter disposed as in Figure 29 We take advantage of the proximity of the getter to the trapping region

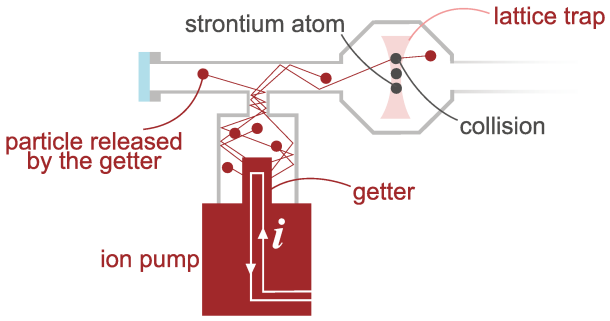


Figure 29: Schematic of the part the setup involved in the background pressure variation procedure. The vacuum system is represented in gray. The high vacuum level is maintained in the chamber thanks to three ion pumps. Two of them are located at the oven output (not showed here) and one the Zeeman tube (horizontal tube on the schematic) and is endowed with a getter (typically a tube with a chemical absorber). When we run a constant current $i$ within the getter, it releases some of the particles it had absorbed. In our case, we expect most of the particles to be released to be di-hydrogen molecules (this is what is specified by the manufacturer). Some of this particles reach the lattice trap region and collide with trapped strontium atoms. Each time we change the current, we monitor the lifetime of the atoms in the trap until reaching a steady state. Then we run the clock with Sr2 as a reference.

and use it as a source of hot molecules. To do so, we run a low current through the getter and monitor both the chamber ion pump (located just under the getter, thus close to the trapping region) as well as the atoms lifetime in the trap, which can be considered an actual measurement of the chamber averaged partial pressures. For each probed current level, after stabilization of the atoms lifetime in the trap, we measure the SrB transition frequency with Sr2 as a reference. We observe a linear behavior of the shift as a function of the inverse $\gamma$ of the lifetime $\tau$, see Figure 30.

Considering only di-hydrogen molecules are released from the getter amounts to keep all the $\tau_i$ in 192 constant expect the one corresponding to the di-hydrogen gas. We then expect a behavior for the effective lifetime as a function of the current run through the getter

$$\frac{1}{\tau(i)} = \frac{1}{\tau_0} + \frac{1}{\tau_{H_2}(i)}, \qquad \frac{1}{\tau_0} = \sum_{j \neq H_2} \frac{1}{\tau_j} \text{ being constant} \tag{193}$$

and in terms of clock frequency shift

$$\delta\nu(i) = \delta\nu_0 + \alpha_{H_2}\frac{1}{\tau_{H_2}(i)} = \delta\nu_0' + \alpha_{H_2}\frac{1}{\tau(i)}, \qquad \delta\nu_0' = \delta\nu_0 - \alpha_{H_2}\frac{1}{\tau_0} \tag{194}$$

or equivalently

$$\delta\nu(i) = \delta\nu_0' + \alpha_{H_2}\gamma_e(i) \tag{195}$$

We then expect a linear behavior of the shift as a function of the total decay rate $\gamma_e(i)$ for a given current $i$ running through the getter. Our data are compatible with such a behavior (see Figure. 30) from where we get for the relative frequency

$$\frac{\delta\nu(\gamma)}{\nu_0} = (-3.0 \pm 0.3) \times 10^{-17}\gamma \tag{196}$$

Note that the uncertainty on this value includes an evaluation of the stability of Sr2 over the whole experiment. On the graph reported Figure 30, we choose the vertical axis in such a way that the data extrapolate linearly to a zero shift, whereas it should go to $\delta_0'/\nu_0$ instead, but since we have no way of knowing where this lay on the vertical axis, we focus on the assumed di-hydrogen-only induced shift. However, assuming that this is the dominant collision shift contribution at nominal pressure for which $\gamma \approx 1.5\ \mathrm{s}^{-1}$, this means our clock relative frequency has to be corrected by roughly $+4.5 \times 10^{-17}$. When this correction was done *a posteriori* on the comparison campaign of spring 2018, better agreements with the other strontium clocks of the network were obtained, meaning probably that the applied correction was done in the right direction, which means that the collision shift contribution from the other species is probably somewhere above the zero[42] of the di-hydrogen fit extrapolation.

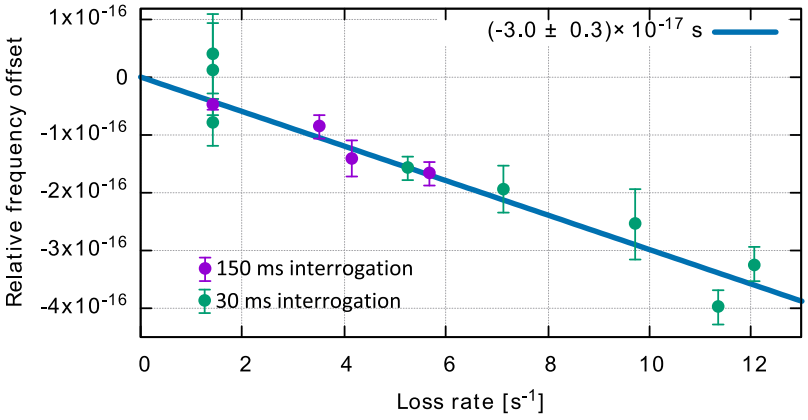


Figure 30: Fractional frequency shift as a function of the loss rate $\gamma$. As described in the text, we could tune the lifetime time of the atoms in the lattice trap by running a steady current in the getter (see Figure 29). For each lifetime $\tau$, i.e. loss rate $\gamma$, we measured the clock frequency difference between SrB (where the lifetime is changed) and Sr2, whose parameters are kept fix over the whole experiment. For loss rates above 6 per second, we had to run the clock with a short interrogation time of 30 ms, in order to still a sufficiently high number of atoms at the end of each cycle. For lower loss rates, we could carry out the measurement with a 150 ms interrogation. The measured shift behavior is compatible with the linear behavior predicted by our simple model.

Note that this is the first ever measurement of the hot collision shift on a strontium optical lattice clock.

## 6.10 Probing hot collisions shifts: qualitative approach

A better control of collisional effects would require a deeper knowledge of the phenomenon, which may be provided, at this early stage of the investigation at least, by a rough classical billiard balls model. Such

[42] or below but by less than $2.25 \times 10^{-17}$, otherwise the correction would probably have not taken the clock frequency closer to the others.

models have been developed in the passed, and we rely in the following on the one exposed by [71]. We hope as well that further investigations in the direction of the quantum model we developed in section 6 could provide better estimation of the effect and allow for a more quantitative approach.

From specifications of our getter, provided by the manufacturer, we know that the gas it releases when some current run through it is di-hydrogen. Thus, using the billiard balls model of [71] or that developed in 6 in order to estimate the collisional effects on the clock transition frequency would require knowing the $c_6$ and $c_12$ coefficients for Sr-$H_2$ collisions. Unfortunately, these coefficients have never been computed so far. However, they are known for Sr-He collisions. Setting up an experiment involving Sr-He was much more involving than that for probing the Sr-$H_2$ collisions since there is no way to introduce helium from within the chamber using the getter. We thus had to set an artificial helium leak into the chamber. This was achieve connecting a highly controlled low flux van just after the oven providing the strontium atoms jet, through which was injected helium from a standard laboratory helium can. However, the model predicts comparable shifts for both ground and excited clock states, meaning that no shift should be observed, within the error bars due the model simplification at least. Because of experimental complications, it was possible to measure the shift for only one non vanishing steady state helium flux to be compared with the case when the van is closed, still using Sr2 as a reference. However, drawing conclusion from these measurements would ask more efforts for the analysis of the data and is out of the frame of this thesis work.

# Part III
# Continental scale clock comparison

## 7 International clock comparison

As highlighted in section 2.7.4, a redefinition of the second requires a set of reliable clocks dispatched around the world proving reproducibility of uncertainty and accuracy. The milestones number 2., 3. and 5. of the recommendations established in [2] clearly state the importance of clock frequency ratios measurement between different clocks based on the same as well as on different species and require agreements better than $5 \times 10^{-18}$ in fractional frequency unit. These three points set the requirements in terms of clock technology reliability advancement. On the other hand, milestone 4. demands regular contributions of candidate clocks to TAI (Atomic International Time), which is more connected to the time dissemination aspect of the *timekeeping* activity. Aiming at participating to this coming redefinition of the second, we dedicate a lot of efforts in contributing to the realization of the recommended milestones.

Regarding milestone 4., we reported the world first strontium contribution to TAI in 2017 (see [78].) and do it an a regular bases since then (around $2 \times 5$ days twice a year). In this section the discussion focuses on our recent contribution to milestone 2., 3. and 5..

### 7.1 Fiber links comparisons

It is stipulated in [2] that frequency comparison for a given candidate could be performed either by transportable clocks, advanced links, or frequency ratio closures. As a member of the European Refimev+ fiber link network (see [79]), we have access to a continental scale fiber links network dedicated to research and in particular to time and frequency standard dissemination as well as optical clock frequency comparisons (see [81]). This link connects us to the NPL laboratory in the UK and to the PTB laboratory in Germany and soon to the INRIM institute in Italy. For a detailed topology of the network see [80]. The link itself reaches a relative frequency stability of $4 \times 10^{-16}$ at 1 s integration time and $5 \times 10^{-20}$ at 60 000 s integration time. Because of its stability at 1 s being close to that of the state-of-the-art clocks compared on the link network, i.e. at the mid $10^{-16}$ level, one could expect it to limit the stability of the frequency comparison. But because its stability $\sigma_{\text{link}}(\tau)$ averages down faster than in $\tau^{-1/2}$ whereas clocks oscillator stability does, it is actually not the case. The NPL is endowed with an Ytterbium ion ($^{171}Yb^{+}$) clock [87, 89], Strontium ion ($^{88}Sr^{+}$) clock [88] as well as a neutral Strontium ($^{87}Sr$) clock [90]. At the PTB are found three neutral Strontium clocks: two based on the fermion isotope ($^{87}Sr$), one stationary [44], the other transportable [91], the third one based on the bosonic isotope ($^{88}Sr$) [92] as well as an Ytterbium ion ($^{171}Yb^{+}$) clock [35]. The LNE-SYRTE institute in Paris, where the present thesis work was carried out, has two neutral Strontium ($^{87}Sr$) [93] clocks along with a neutral Mercury ($^{199}Hg$) clock [22]. All these clocks can be connected to the Refimev+ fiber links, allowing for the comparison of five ($^{87}Sr$) clocks dispatched in three different locations distant from each other by around thousand kilometers, as well as frequency ratio measurements of several optical standards, as reported in section 7.2. Then, this fiber link network allows us to directly address milestones 2. and 5. as recommended in [2]. Note that such fibered comparison have been carried out as well in Japan [95, 96, 97] and in the U.S..

#### 7.1.1 Working principle

In this section we give the very basics of optical frequency measurement based on optical frequency combs and how this technique is used for remote comparison of clocks via fiber links.

**Combs and optical frequency measurements**

Currently, primary representations of the second are based on atomic transition in the microwave range at frequency around 10 GHz (9.19263177 GHz exactly for the Cesium standards, on which is based the S.I. definition of the second). The phase of such signals is measurable by commercially available electronics aparatii making their frequency counting easily achievable. On the other hand, phase of optical signals, with frequencies of hundreds of THz are inaccessible directly. The basic idea of optical frequency counting is to link experimentally the frequency to be measured to another laying in a part of a directly measurable spectrum, typically radio frequencies or microwaves. Till the very end of the XX$^{\text{th}}$ century

this was achieved with cumbersome techniques involving room size experiments dedicated to harmonics generation of measurable frequencies till reaching close to the optical frequency to be measured (see for example [83]). In 1999 T. Hänsch had the idea to use an optical comb to link the optical frequency directly to a microwave reference (see [84]). The basics of this method is exposed hereafter.

In the frequency space, a comb is a bunch of modes of frequencies $\nu_n$, $n = 0, 1, ..$ a positive integer such that two consecutive modes are separated by a constant frequency distance $\nu_r$, with a global offset given by $\nu_0$, i.e. $\nu_n = \nu_0 + n\nu_r$ (see figure 31). The main features of combs used for optical frequency metrology is that $\nu_r$ is in the radio frequency or microwave domain whereas the brightest modes $\nu_n$ are in the optical domain. The comb is operated in such a way that $\nu_r$ is referenced to a stable oscillator whereas $\nu_0$ is let free but measured. Then, the frequency $\Delta$ of the beatnote between the clock laser and the closets comb mode $\nu_n$ is measured. Finally, the number $n$ of the adjacent mode $\nu_n$ is determined[43] and the optical frequency $\nu$ of the clock laser is obtained as[44] (see [106] for more details)

$$\nu = \nu_0 + n\nu_r + \Delta \tag{197}$$

When this technique is used for absolute frequency measurement, the quantity $\nu_r$ is expressed in S.I. unit, i.e. in Hz. This unit is realized by a radio-frequency source, typically a Hydrogen maser, itself referenced to a Cesium clock standard (on which is based the definition of the second, and thus that of the Hf). Therefore, no absolute frequency measurement can reach frequency fractional uncertainty lower than that of the radio-frequency source. Moreover, the stability of $\nu_r$ is crucial because of the scalling factor $n \sim 10^6$ for optical frequency $\nu$ (see [86]).

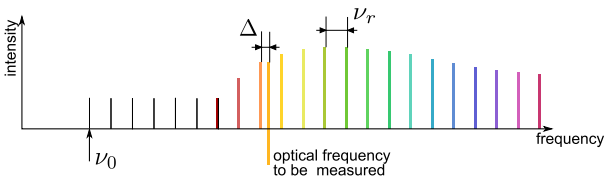


Figure 31: Schematic representation of an optical frequency comb spectrum. It is composed of several lines at optical frequencies equal to multiples of the repetition rate $\nu_r$ plus an offset $\nu_0$ both well known and eventually locked to an external reference. The optical frequency to be measured is beaten with the comb lines. The beatnote is filtered within a band of width smaller than $\nu_r/2$, keeping only the component corresponding to the beatnote (frequency $\Delta$) with the closest comb line (frequency $\nu_0 + n\nu_r$). The measured frequency then reads $\nu = \nu_0 + n\nu_r \pm \Delta$.

Somehow, the absolute frequency measurement of an optical frequency as done according to 197 can be seen as a measure of the ratio of this optical frequency to that of the Cesium frequency standard oscillator, the fractional frequency stability being limited by that imposed by the Cesium standard. In the next paragraph we show how a method developed by H. R. Telle at the beginning of the XXI$^{st}$ century [85, 86] allows for the direct measurement of the frequency ratio of two optical frequencies limited by the fractional stability of the less stable source. When comparing two optical oscillators both with fractional stability better than the cesium standards, the ratio is known with a lower uncertainty than if deduced from two separated measurements relying on 197.

**Combs and optical frequency comparison**

In this paragraph we discuss two possible approaches for comparing clocks oscillators frequency: making *1)* their difference or *2)* their ratio. The first approach relies on equation 197 and is thus limited to the cesium referenced radio-frequency source stability used to measure and/or stabilize $\nu_0$ and $\nu_r$, which is not the case for the second one, reason why it is universally applied when employing fiber links.
Consider two clocks $CL_1$ and $CL_2$ in different locations, each with its own comb, and assume the spectrum of each comb is broad enough to cover a spectral region including the clock laser frequency of its associated clock $\nu_i$, $i = 1, 2$, as well as a *communication frequency* $\nu_{\text{com}}$ that is used for the transportation

[43] this is typically do relying on wave meters

[44] A more general formula would let the beatnote sign undetermined, i.e. $\nu = \nu_0 + n\nu_r \pm \Delta$, which can be deduced via a dedicated protocol.

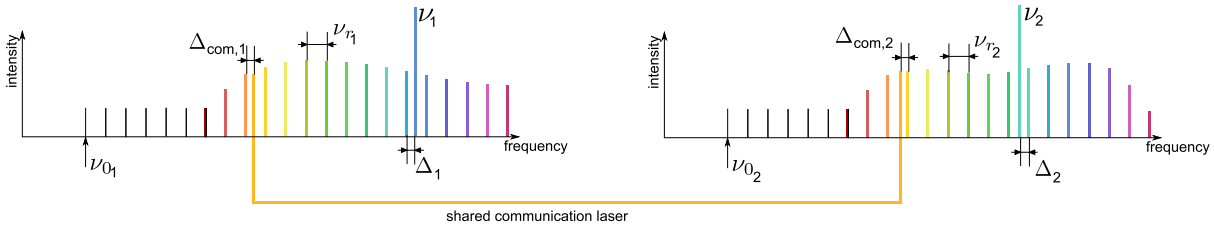


Figure 32: Comparing two optical clocks remotely using combs. Two combs (index 1 and 2) are linked via a communication laser at frequency $\nu_{\text{com}}$. The clock 1 (2) as well as the communication laser are measured by the comb 1 (2). This allows for the measurement of the frequency ratio or difference between the clock 1 (2) and the communication laser. The ratio of these ratios or the difference of these differences gives the ratio or the difference between the two clocks.

of the clock information from one location to the other [45]. The two clock frequencies may differ if the clocks are not based on the same atomic species. In a first step we consider the *communication frequency* to be that of a shared communication laser of infinite stability, measured at the two ends of the link. We will then briefly discuss how the link stabilization is achieved and finally give a picture conform to the one we use for our continental scale comparisons for which a communication laser is injected from each location into half of the link, the frequency ratio of these two lasers being measured at a dedicated station half way between the link ends.

*1) Frequency differences*

As described in the previous paragraph each of the clocks frequency can be obtained as

$$\nu_i = \nu_{0i} + n_i \nu_{ri} + \Delta_i \tag{198}$$

where the index $i = 1, 2$ indicates which of the two locations is considered (see figure 32). The same occurs for the shared $\nu_{\text{com}}$ in the two locations

$$\nu_{\text{com}} = \nu_{0i} + m_i \nu_{ri} + \Delta_{\text{com,i}} \tag{199}$$

where the characteristic parameters $\nu_{0i}$ and $\nu_{ri}$ of the two combs differ. For each clock and comb setup, equation 198 and 199 can be combined to give

$$\nu_i = \nu_{\text{com}} + (n_i - m_i)\nu_{ri} + \Delta_{beat,i} \tag{200}$$

where $\Delta_{\text{beat,i}} = \Delta_i - \Delta_{\text{com,i}}$ where the quantities $n_i$, $m_i$, $\nu_{ri}$ and $\Delta_{\text{beat,i}}$ are measured and thus known. We then end up with

$$\nu_2 - \nu_1 = (n_2 - m_2)\nu_{r2} - (n_1 - m_1)\nu_{r1} + \Delta_{\text{beat},2} - \Delta_{\text{beat},1} \tag{201}$$

which, as explained in the previous paragraph is basically limited by the measurement of $\nu_{ri}$. When the instability of the link is taken into account, the phase noise on the communication laser induced by link (temperature fluctuation, acoustic noise, see section 7.1.3) needs to be compensated. This compensation however can not be perfect (section 7.1.3), resulting in fluctuations in the communication laser frequency between the two ends of the link. This can be accounted for by including a $\Delta\nu_{\text{com}}$ term to equation 201, leading to

$$\nu_2 - \nu_1 = \Delta\nu_{\text{com}} + (n_2 - m_2)\nu_{r2} - (n_1 - m_1)\nu_{r1} + \Delta_{\text{beat},2} - \Delta_{\text{beat},1} \tag{202}$$

However, recent advances in fiber link technologies developed by REFIMEV+ collaborators enabled fractional frequency uncertainty of the link to reach below $10^{-19}$, and is thus not a limitation.

[45] The reason the measure is achieved using the transfer of a carrier at $\nu_{\text{com}}$ along the fiber link and not at $\nu_i$ directly is the length of the links that stretch in our case over more than thousand kilometers. Thanks to recent telecommunication technologies development, transfer of optical signals over such long distances is achievable but only in the wavelength window used for commercial telecommunications which lays around $\simeq 1.5$ $\mu$m. Hence, propagating the clock laser carrier along the link would be impossible whereas is can be done for $\nu_{\text{com}} \simeq 1.5$ $\mu$m.

*2) Frequency ratio*

As mentioned earlier, fluctuations of the comb parameter $\nu_r$ are intractable below the fractional stability and uncertainty imposed by the reference used to measure it ($10^{-16}$), making the *frequency difference* technique irrelevant for state-of-the-art clocks comparison ($10^{-18}$). To overcome this problem H. R. Telle invented a clever way to drastically reduce the contamination of the fractional frequencies measured by the fluctuations of the comb (i.e. the limited stability of the reference used to determine $\nu_r$), based on the so-called *elastic tape picture* [85]. Exposing its working principle would require a full development (see [85, 86]) and we content ourselves with giving the main result of this so-called *transfer* technique.

Let us focus on the ratio measurement at one location, thus dropping the index$i = 1, 2$ for the moment. Instead of measuring $\nu_{\mathrm{CL}} - \nu_{\mathrm{com}}$, we measure a quantity that relates to $\nu_{\mathrm{CL}}/\nu_{\mathrm{com}}$. The beatnotes $\nu_{\mathrm{beat}}$ between the clock laser and the closest comb mode and that $\nu_{\mathrm{beat,com}}$ between the communication laser and the closets comb mode are measured, as well as the offset comb frequency $\nu_0$. Telle then finds a smart way to obtain, via analog and digital beatnote, the frequencies

$$\nu_A = \nu_0 + \Delta \tag{203}$$

$$\nu_B = (\nu_0 + \Delta_{\mathrm{com}})\frac{n}{m} \tag{204}$$

where $n$ and $m$ are defined in 198 and 199. We then note that, from 198 and 199

$$\nu_0 + \Delta = \nu_{\mathrm{cl}} - n\nu_r \tag{205}$$

the same being valid for the communication laser as well. Hence

$$\nu_A - \nu_B = (\nu_0 + \Delta) - (\nu_0 + \Delta_{\mathrm{com}})\frac{n}{m} = (\nu_{\mathrm{cl}} - n\nu_r) - (\nu_{\mathrm{com}} - m\nu_r)\frac{n}{m} = \nu_{\mathrm{cl}} - \nu_{\mathrm{com}}\frac{n}{m} \tag{206}$$

Mixing down $\nu_A$ and $\nu_B$ leads to

$$\nu_C = \nu_A - \nu_B = \nu_{\mathrm{cl}} - \nu_{\mathrm{com}}\frac{n}{m} \tag{207}$$

Because it involves a digital generation of $\nu_B$ (for which the ratio $n/m$ is approached to typically $(1/2)^{48}$ with currently available commercial devices) $\nu_C$ is some times referred to as a *virtual* beat [94]. Quoting H. R. Telle in [86]

> *We* [synthetized] *one radio frequency signal containing all necessary information from the external optics signal. This radio frequency is independent of* [$\nu_0$] *and* [$\nu_r$] *and is thus immune against noise contribution from the* [comb].

From 197 any optical frequency ratio ratio $\nu_1/\nu_2$ can be expressed as

$$\frac{\nu_1}{\nu_2} = \frac{\nu_0 + n_1\nu_r + \Delta_1}{\nu_0 + n_2\nu_r + \Delta_2} \tag{208}$$

with $\Delta_i$ the corresponding beatnotes to closets comb mode, and where $\nu_0$ and $\nu_r$ are idealized as infinitely stable and known quantities[46]. Hence

$$\frac{\nu_1}{\nu_2} \approx \frac{n_1}{n_2}\frac{1+\varepsilon_1}{1+\varepsilon_2} \approx \frac{n_1}{n_2}(1+\varepsilon_1)(1-\varepsilon_2) \approx \frac{n_1}{n_2}(1+\varepsilon) \tag{209}$$

where

$$\varepsilon_i = \frac{\nu_0 + \Delta_i}{n_i\nu_r} \tag{210}$$

and $\varepsilon = \varepsilon_1 - \varepsilon_2$. Therefore

$$\nu_1 - \nu_2\frac{n_1}{n_2} \approx \nu_2\varepsilon \tag{211}$$

which is of the order of a radio-frequnecy multiplied by the reatio of an optical frequency and is thus still in the radio-frequency domain. Hence $\nu_C$ is a measure of the small departure between the ratio $\nu_{\mathrm{CL}}/\nu_{\mathrm{com}}$ to be measured and the rational $n/m$. It is in this sens that $\nu_C$ provides a measurement of the frequency ratio $\nu_{\mathrm{CL}}/\nu_{\mathrm{com}}$.

However, recent improvement in the stabilization of $\nu_r$ allows for the direct use of equation 208 to determine optical frequency ratios with better resolution than $10^{-16}$ in fractional frequency unit.

[46] this is purely a theoretical view since the actual knowledge on these quantities is limited by the standard defining the Hz itself.

### 7.1.2 Measuring frequency ratio from experimentally accessible quantities

As mentioned in section 3.3.1, the quantity that we use to characterize each clock is $y(t) = (\nu(t)/\nu^o) - 1$, $\nu^o$ being the recommended value for the corresponding transition frequency. More precisely, comparisons consist in measuring

$$\Delta y_{1,2} = y_1(t) - y_2(t) \tag{212}$$

where the index $1, 2$ labels each of the two clocks compared.Typically, the recommended values are known to better than $10^{-16}$ in fractional frequency units (via direct comb based absolute frequency measurement), i.e. $\nu_i(t) - \nu_0 \lesssim \nu_0 \times 10^{-16}$ and therefore

$$\frac{\nu_1/\nu_1^o}{\nu_2/\nu_2^o} \approx 1 \tag{213}$$

More precisely

$$\frac{\nu_1(t)}{\nu_2(t)} = \frac{\nu_1^0(1+y_1(t))}{\nu_2^0(1+y_2(t))} \simeq \frac{\nu_1^0}{\nu_2^0}\,(1+y_1(t))\,(1-y_2(t)) \simeq \frac{\nu_1^0}{\nu_2^0}\,(1+\Delta y_{1,2}(t)) \tag{214}$$

In practice, except when the two clocks to be compared stands at proximity of the same comb, equation 208 can not be directly used. The actual structure of the link linking a pair of clocks at the continental scale is as follows. Each institute is endowed with its clock (frequency $\nu_i$) and comb. A communication laser is sent from each institute (frequencies $\nu_{c,i}$). The two communication lasers meet in a dedicated station (located in Strasbourg for the PTB-SYRTE link, in Villetaneuse for the NPL-SYRTE link). In each institute is measured the ratio $\nu_i/\nu_{c,i}$ between its clock and the communication it sends to the link. The beatnote $\Delta_c = \nu_{c,2} - \nu_{c,1}$ between the two communication laser is measured in the dedicated station.

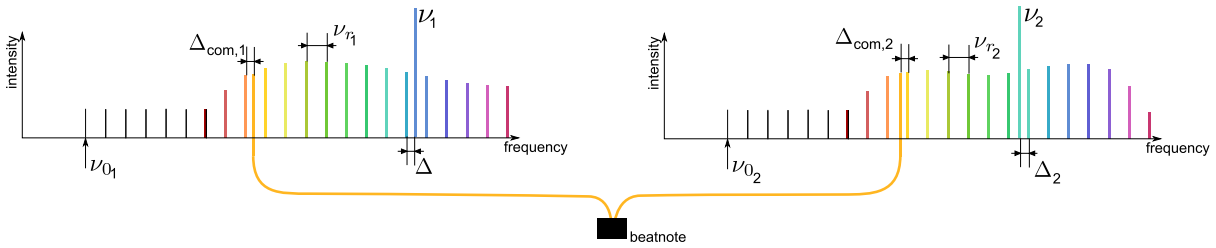


Figure 33: Realistic structure of an optical link used for remote optical clocks comparison. Each of the two laboratories taking part to the comparison hosts its own optical clock (frequency $\nu_i$, $i = 1, 2$), its own optical frequency comb (with offset $\nu_{0_i}$ and repetition rate $\nu_{r_i}$) and its own *communication* laser (frequency $\nu_{\text{com,i}}$). The communication lasers are then sent through the link from each laboratory towards a station located between the two laboratories (black box on figure) where their beatnote is measured. Locally, i.e. in each laboratory, the comb allows or the measurement of the frequency ratio between the clock laser and the communication laser, whereas the beatnote measured at the station provides a measurement of the frequency ratio between the two communication lasers. These three ratios can be combined to obtain the frequency ratio of the two clock lasers to be compared (see equation 215).

Then the ratio of the ratios is obtained as

$$\frac{\nu_1/\nu_1^o}{\nu_2/\nu_2^o} = \left(\frac{\nu_1/\nu_1^o}{\nu_{c1}/\nu_{c1}^o}\right)\left(\frac{\nu_{c1}/\nu_{c1}^o}{\nu_{c2}/\nu_{c2}^o}\right)\left(\frac{\nu_{c2}/\nu_{c2}^o}{\nu_2/\nu_2^o}\right) \tag{215}$$

where the quantities $\nu_1^o$, $\nu_2^o$ are the values provided by the CPIM for the corresponding transitions and $\nu_{c1}^o$, $\nu_{c1}^o$ are measured at each institute. The first and third factors are determined at each institute using relation 214. The central factor is obtained the following way

$$\left(\frac{\nu_{c1}/\nu_{c1}^o}{\nu_{c2}/\nu_{c2}^o}\right) = \frac{\nu_{c2}^o}{\nu_{c1}^o} \times \frac{\nu_{c2}+\Delta_c}{\nu_{c2}} = \frac{\nu_{c2}^o}{\nu_{c1}^o}\left(1+\frac{\Delta_c}{\nu_{c2}}\right) \approx \frac{\nu_{c2}^o}{\nu_{c1}^o}\left(1+\frac{\Delta_c}{\nu_{c2}^o}\right) \tag{216}$$

Where the error made using $\nu_{c2}^o$ instead of $\nu_{c2}$ is of the order of $10^{-21}$. When combined with equations 214 and 215, this leads to

$$\frac{\nu_1/\nu_1^o}{\nu_2/\nu_2^o} \approx \frac{\nu_{c1}^0}{\nu_1^0}(1+y_{c1}-y_1)\frac{\nu_{c2}^0}{\nu_{c1}^0}(1+y_{c2}-y_{c1})\frac{\nu_2^0}{\nu_{c2}^0}(1+y_2-y_{c2}) \tag{217}$$

$$\approx \frac{\nu_{c1}^0}{\nu_1^0}\frac{\nu_{c2}^0}{\nu_{c1}^0}\frac{\nu_2^0}{\nu_{c2}^0}(1+y_{c1}-y_1+y_{c2}-y_{c1}+y_2-y_{c2}) \tag{218}$$

$$= \frac{\nu_2^0}{\nu_1^0}(1+y_2-y_1) \tag{219}$$

This is the reason why the quantity presented in the measurement is $y_j - y_i$ (see section 7.2).

### 7.1.3 link stabilization

As mentioned earlier, optical clock frequency ratio comparison can be achieved with a shared communication laser injected into the link at one end and received at the other end, while its frequency ratio to the two clocks is simultaneously measured at the two locations using the combs via the *transfer* technique, i.e. measuring $\nu_C$ as defined in 207 in both laboratories (see for example [94, 97]). The idea is then to consider the following simple equation

$$\frac{\nu_1}{\nu_2} = \frac{\nu_1}{\nu_c}\frac{\nu_c}{\nu_2} \tag{220}$$

which implicitly assumes that the frequency of the shared communication laser is the same in both laboratories. As discussed before, this is in general not the case. More precisely, the link physical properties fluctuate over time inducing phase noise on the traveling laser light. Typical noise due to the fiber transport itself are thermal fluctuation, mechanics ans acoustic noise (see e.g. [98, 99]). If not treated properly this noise translate into an increase frequency instability of the communication laser oscillator, therefore degrading the stability and uncertainty of the ratio measurement. Hence the problem can be stated in the following way [100]

> *The purpose of an optical link is to reproduce the frequency of an ultra-stable signal seeded at the input end of the fibre with the best fidelity at the output end.*

For the link stability to match the metrology requirement imposed by the stability of the clocks to be compared, the noise induced by the link then needs to be measured and compensated. The current techniques rely on the Doppler cancellation scheme [29]. In this scheme, the light injected at the input end of the fiber is reflected at the output end back to the fiber. The phase difference between the back reflected light and that coming directly from the source is measure in a Michelson interferometer. The measured phase difference is used to feedback an acousto-optic modulator place at the fiber input end in order to compensated for the phase difference due to the noise accumulated over the round trip in the fiber [98, 99, 100]. It is crucial for this scheme to work that the phase noise acquire along the forward and the backward paths are the same. However, as soon as the length of the link goes beyond a few hundreds of kilometers, the delay along the fiber is such that the forward noise differs from the backward one. More over, this delay reduces as well the bandwidth of the compensation feedback loop [100]. To overcome this problem the concept of cascaded link was proposed and implemented [102, 100, 81]. In the cascaded scheme the total link is divided into shorter spans. Two successive spans are connected by a repeater laser station enabling for the implementation of a Doppler cancellation system on each span. The propagation delay scales linearly with the length of the fiber to compensate. Hence, dividing a link into $N$ span is expected to improve the link stability by a factor $\sqrt{N}$ [81].

### 7.1.4 Connection of links

When it comes to continental size links a single cascaded link joining two laboratories distant by more than thousand kilometers is hardly achievable. For example, for the Paris-Braunschweig link, the main reason the link is plit into two part is the fact that different technologies are used on the two national territories (see for example [101]). In Germany the link is based on so-called *dark fibers* entirely dedicated to ultra-stable optical frequency transfer, whereas in France is has been implemented on *dark channels*, i.e. cohabiting with internet data traffic (see [100, 98]). This latter approach offers to possibility to widely disseminate time and frequency at a metrological level all over the national territory, based on the commercial internet fiber network backbone which covers a large part of the territory. However, note that this to be achieved requires some small modification of the standard internet repeater stations.

Indeed, to be of metrological interest the link noise must be compensated via Doppler cancellation. This requires propagation along the fiber in the two direction, and thus requires the implementation of optical bidirectional amplifiers, whereas the usual telecommunication amplifier are unidirectional. We note however that in the prospect of building a time and frequency dissemination network as broad as possible to fulfill both forecast academic and industrial needs, the possibility of using two unidirectional fibers for the transfer has been studied. Nevertheless, this scheme proved long term fractional frequency stabilities in the high $10^{-17}$, to be compared with the $10^{-20}$ for single bidirectional fiber links [99].

## 7.2 Continental scale comparisons

### 7.2.1 June 2017 comparison campaign

In june 2017 many of the clocks in SYRTE, PTB and NPL participated to a continental scale fiber link clock comparison campaign (see Figure 34). As explained in section 7.1.2, to compare clocks based on different species, instead of measuring the clock frequency ratio $\nu_1/\nu_2$ we measure the ratio of the ratio of each clock measured frequency to its value recommended by the CPIM (see [2]), i.e.

$$\frac{\nu_1/\nu_1^o}{\nu_2/\nu_2^o} = \frac{1-y_1}{1-y_2} \approx 1 + y_2 - y_1 \tag{221}$$

Since these values are expected to be very close to unity the quantity usually reported is $y_2 - y_1$, which is typically of the order of $10^{-16} - 10^{-17}$ for state-of-the-art optical clocks. The data collected during a bit more than one month are presented in the lower-half matrix depicted in Figure 34. The intersection of column "clock $i$" with the raw "clock $j$" displays the plot of the Allan deviation $\sigma_{ij}(\tau)$ (see section 3.3.1) of the quantity $y_i - y_j$. Such matrix representation usually includes the average $\langle y_i - y_j \rangle$[47] for each clock pair in the corresponding plot box. However, because such comparisons involve several collaborating laboratories and because the results are still to be published, we omitted them here and content ourselves with the quantity $\sigma_{ij}(\tau)$ only.
A first thing to note is that giving a value at a $10^{-17}$ level of precision for the $y_i - y_j$ makes sens only if the statistical resolution of the corresponding measured quantity, characterized by its Allan deviation $\sigma_{ij}(\tau)$ where $\tau$ is the duration of the comparison, reaches such low level. The statistical resolution is given by the last points of the Allan deviation (the very last point is usually dropped out because of too large error bars). The statistical resolution can be seen as the error bars on the quantities $y_i - y_j$. If one does take the values $y_i - y_j$ without taking care of this aspect, the algebraic closure is not fulfilled, i.e.

$$\theta_{ijk} = (y_i - y_j) - (y_i - y_k) - (y_k - y_j) \neq 0 \tag{222}$$

In practice, we however note that in practice we always have[48] $\theta_{ijk} \lesssim \sup\{\sigma_{ij}(\tau), \sigma_{ik}(\tau), \sigma_{jk}(\tau)\}$, meaning the closure is satisfied within the statistical resolution of the measurement. To illustrate this, let us consider three plausible values $y_A - y_B = 6.0$, $y_B - y_C = 3.6$ and $y_C - y_A = 9.3$ in units of $10^{-17}$ for three clocks labelled A, B and C among those taking part to the campaign. We get $\theta = -6.9 - 3.6 + 9.3 = -1.2$ in units of $10^{-17}$ and $\sup\{\sigma(\tau)\} \approx 1$ in units of $10^{-17}$. We discuss this in more details in the next section (section 7.2.2).

We mentioned that the presented SYRTE strontium clocks measurements have been post-processed in order to correct some effects that were not understood at the moment of the campaign. Indeed, at the beginning of the campaign, our two clocks where shifted by almost $10^{-15}$ in fractional frequency unit. It took us about one week to realize the problem was related to the relative sequence timing of the two clocks. Once this was understood, we needed a few more days to find the source of the problem. It turned out that some ground-loop problem involving the mechanical shutters of one of our clocks, Sr2, was resulting in deterministic fluctuations of the error signal used for the lock of the clock laser to its ultra-stable cavity, as schematically depicted in Figure 35. The clock laser frequency excursions due to shutter activity amounted to about 2 Hz over around hundred milliseconds. The two clocks cycles being not commensurate in general, the interrogation stages of SrB where probing different section of the clock laser fluctuation pattern. Knowing the sensitivity function of each clock, we could estimate the shift induced by these fluctuations and check our understanding by operating the two clock sequences at the

[47] The $\langle\ \rangle$ symbolizes here an estimated statistical average derived from the available data, and the idealized average obtained from an infinite data set.

[48] this is the case for all comparisons presented here, but can not be displayed here on the actual data because they have not been published yet.

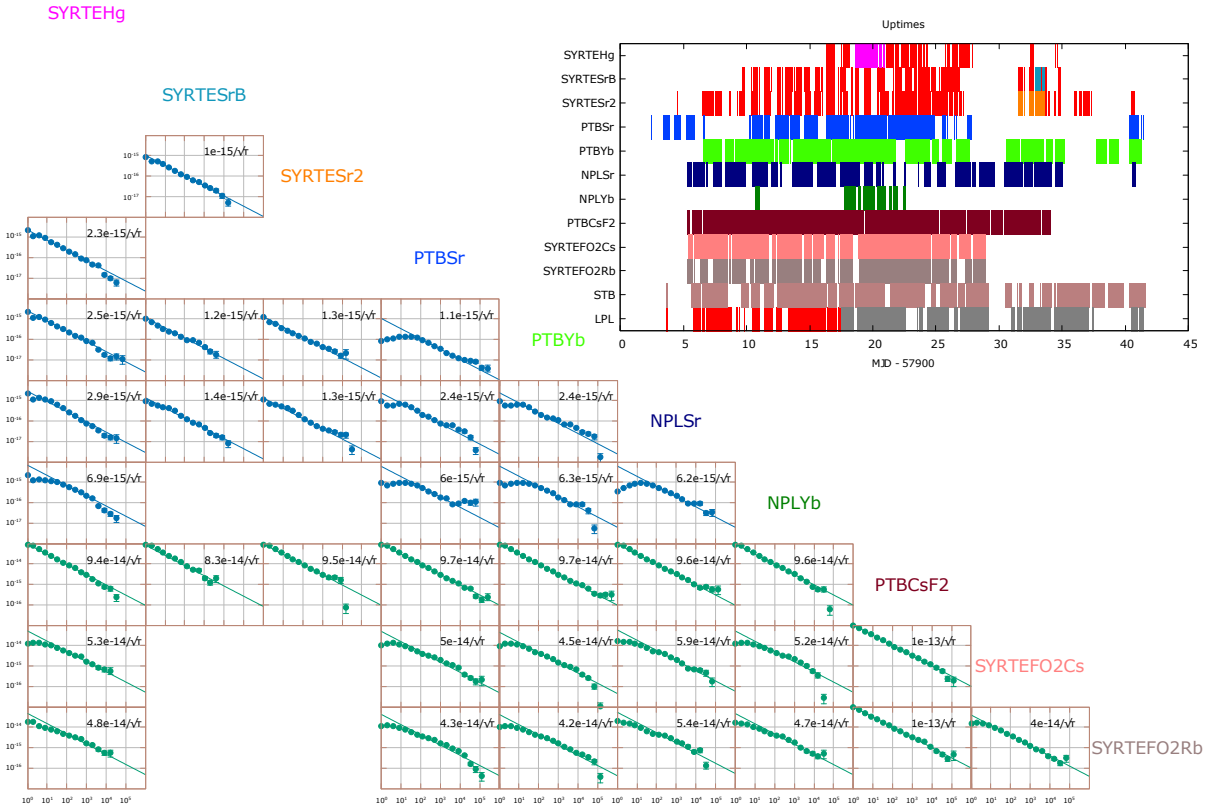


Figure 34: Lower-half clocks-pairs comparison matrix of the June 2017 campaign. Each line and each column are assigned a given clock of the set of clocks taking part to the comparison. The plot at line $i$ and column $j$ represents the fractional Allan deviation $\sigma_{ij}(\tau)$ of the quantity $y_i - y_j$ (which is used as a measure of the ratio $(\nu_j/\nu_j^o)/(\nu_i/\nu_i^o)$, see equation 219) as a function of $\tau$. On the top right corner of each plot is given the coefficient of the log-scale linear fit of $\sigma_{ij}(\tau)$ in unit of $\tau^{-1/2}$ ($\tau$ in second). The top right uptimes graph represents the time intervals over which each clock was running, as well as the that corresponding to the two beatnote stations located at Villetaneuse (LPL) and Strasbourg (STB). The red colored intervals correspond to data not considered for the comparison for technical reasons.

same rate, i.e. with equal durations, but changing their relative delay (see Figure 35). Once the effect was well understood, it was possible to post-process the measurements inn order to correct the effect (this was possible since all parameters of each sequence, in particular their durations, used are saved in one of the experiment programs).
An important thing to notice here is that the typical fractional ratios uncertainties are higher than the claimed uncertainty budgets (see 4.6). This highlights the importance of comparisons campaigns involving uncorrelated clocks located at different places, designed, built and operated by different teams (see section 4.6 and in particular the paragraph about the charges and [82]). In other words, it makes no sens, when aiming at metrological applications such as timekeeping and S.I. second realization, to go on digging in the $10^{-18}$ of fractional uncertainty while the comparisons hardly go to the low $10^{-17}$.

We insists as well on the fact that having these complex systems operated over a period of a bit more than one month remains very challenging. This can be seen in the top-right graph of Figure 34 which represents the *uptime* of each unit (a unit being a clock or a link station) involved in the comparison, i.e. the periods during which a given unit is operational. We notice that the densest uptimes were achieved by the cesium and rubidium fountains, reaching almost 100%, which proves there reliability, while our optical clocks hardly achieved more than 50%. We mention that till 2017 human attendance was unavoidable over night and day for the system to be kept running over such long period, with a few incidents occurring per hour, typically a laser loosing its stabilization reference or a program managing

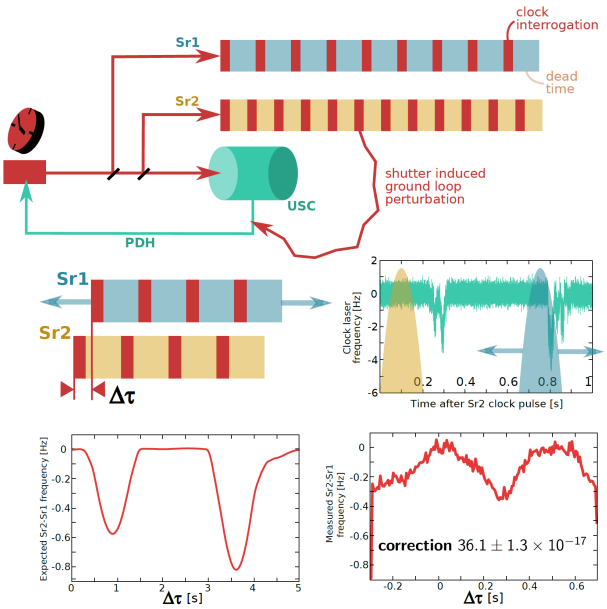


Figure 35: **The shutter ground-loop problem**. On top of the picture is a schematic of the clocks system. The clock laser is dispatched to the two clocks while a third part is sent to the ultra-stable cavity. The stabilization is achieved via a standard Pound-Drever-Hall (PDH) feedback. The blue (yellow) rectangles represent the dead time of Sr2 (SrB) clock cycles, whereas the red ones stand for the interrogations. Because of having different cycles duration, the timing between the two clocks interrogations evolves over time. The activation of the shutters of Sr2 induces a perturbation on the PDH error signal, resulting in variation in the laser frequency, as seen on the clock frequency plot (middle-right). SrB then samples this perturbed pattern at varying times, resulting in a frequency shift between the two clocks (the effect is not averaged out by the fact that SrB samples the pattern at random timing because the perturbation has non vanishing average). In order to investigate the effect we set an equal cycle durations for the two clocks and scan the delay $\Delta\tau$ between the two (middle-left figure). The bottom-left plot represent the simulated frequency shift as a function of $\Delta\tau$ obtained making the product of the sensitivity function of SrB with the frequency profile of the laser for a given delay (sliding the sensitivity function along the time axis as in the middle-right plot). The bottom-right plot shows the frequency difference measured as a function of $\Delta\tau$. The simulation reproduces well the effect.

a particular task crashing. A lot of effort have been devoted to minimize the need in human attendance and in the 2018 spring campaign, incidents requiring human interventions were much more sparse.

### 7.2.2 Early 2018 comparison campaign

The reason the recommended road map as given in [2] insists on inter-laboratory frequency comparisons is that auto-evaluations of the uncertainties is never exhaustive and one could easily miss systematics effects that reveal themselves only when comparing clocks running in uncorrelated environments. Such systematics can stem from phenomena not taken into account *a priori*, i.e. that escapes the range of phenomena the experimentalists could think about when setting up the list of possible sources of inaccuracy, such as the DC Stark shift induced by charges trapped on dielectric surfaces placed under vacuum close to the atomic sample as reported in [82]. It can as well stem from phenomena taken into into account but mis- or under-estimated as it is the case for the hyperpolarizability discussed in section 5 for which our measurements display a behavior qualitatively in disagreement with the theoretical predictions and higher by a factor almost 2 (see as well [56]). An other systematics effect by far underestimated so far for $^{87}$Sr clocks was the hot collisions shifts (see section 6) for which the available models predict values far below what we report in section 6.

Aiming at fulfilling the requirements of the milestones of the road map proposed in [2] for the re-definition of the S.I. second, we are eager to regularly compare our clocks to asses the reproducibility in time of their results and to check whether our constant efforts lead to effective reductions of their frequency differences. We then took part to an other comparison campaign that took place in March-April 2018 involved once more the NPL, PTB and LNE-SYRTE institutes and most of the clocks available there took part to the comparison. As mentioned in the previous section, running such complex, room-size experiments over days is an involving task and not all the clocks could work at the expected level of performance over the dedicated period. In this section we briefly presents the data corresponding to those which could be run for sufficiently long intervals and with sufficiently large overlaps with other clocks for the statistics to be workable. These are the two $^{87}$Sr of LNE-SYRTE, the $^{87}$Sr of the NPL and the stationary $^{87}$Sr and $^{171}$Yb$^{+}$ of the PTB. As for the 2017 campaign, the results are provided in Figure 36 under the form of clock-pair Allan deviations plots matrix. We display as well the uptimes rows for each clock as well as those of the French fiber links stations in Strasbourg (STB) and Villetaneuse (LPL). For this particular campaign, we can clearly distinguish three periods, or slots, such that the clocks of the different institutes are running together and such that out of these slots no clocks are operated. We then give three different matrices, one per slot, as seen on Figure 36.

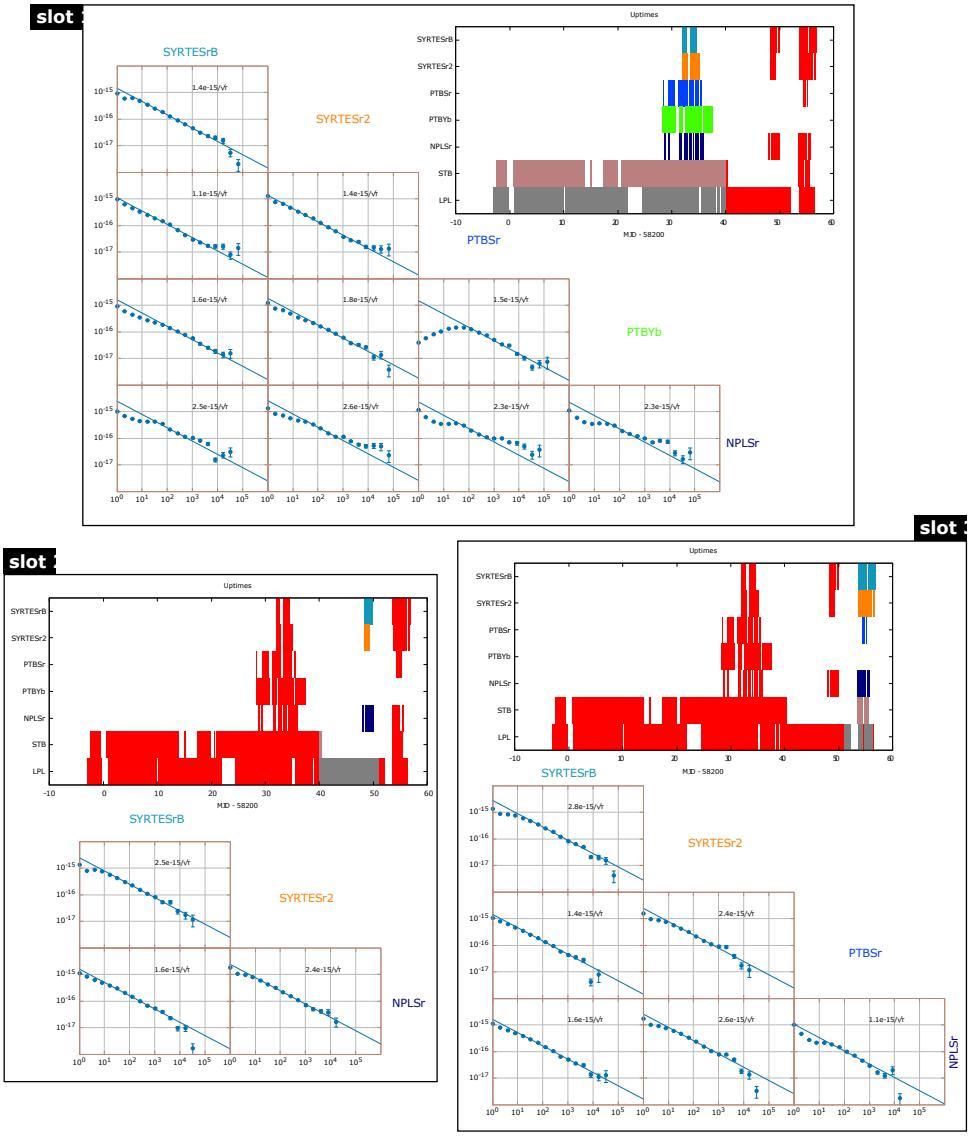


Figure 36: Lower-half clocks-pairs matrices of the early 2018 comparison campaign (see figure 34).

As mentioned in the previous section, the algebraic closure condition $\theta = 0$ is satisfied only within the

sup of the error bars of the measurements considered (see 222) given by the lasts points of the Allan deviation of each comparison. This makes the results of the comparisons hard to visualize and we propose here a way to cope with this difficulty. The problem can be stated in the following way. Far a given slot, i.e. a given time interval over which the uptimes of a set a clocks as well as their overlaps are sufficient, the "distance" between the clocks, i.e. the quantities $y_j - y_i$, differ according to which clock is chosen as a reference. This can be seen on the *a)* part of Figure 37 where each graph represents the distance between four hypotetical clocks for a given reference clock, for the three slots. The top graph has clock A as reference, the middle one clock B and the bottom one clock C The color code for this Figure light-blue: clock A, blue: clock B and green:clock C red for clock D (available only during the first and third slots). We denote by $x_{ij}$ the quantity $y_j - y_i$ when the clock labeled $i$ is taken as a reference. The difficulty for data visualization is that the relative distances between clocks, for a given slot, depend on the reference chosen, i.e. $x_{ij} - x_{kj} \neq x_{i\ell}x_{k\ell}$. Part *b)* of Figure 37 displays the three different sets of relative distances for the first slot. The question is: is there a smart way of adjusting the offset between these sets, i.e. their relative positioning, in order to have a distance estimate independent on the choice for a reference clock? Inspired by the proposal made in [3] for the determination of the best estimate of a clock frequency from an over-determinate set of data based on a least square method, we choose the relative positioning that minimizes the spread of each clock position to an arbitrary zero[49], that we choose to be that of the first set of distances, in this particular case that with clock A as a reference. Mathematically, this amounts to considering for each clock labeled by $i = 1, .., 4$, the set

$$X_i(a, b) = \{x_{i,1}, a + x_{i,2}, b + x_{i,3}\} \tag{223}$$

and to find the parameters $(a, b)$ that minimizes the quantity

$$\sigma^2(a, b) = \sum_{i=1,..,4} \sigma^2_{X_i(a,b)} \tag{224}$$

where $\sigma_{X_i(a,b)}$ is the standard deviation of the set $X_i(a, b)$. This provides a particular couple of parameters $(a_o, b_o)$. Finally, the value $x_i$ assigned to each clock is the average of the set $X_i(a_o, b_o)$, with error bars given by $\sigma_{X_i(a_o,b_o)}$. This is represented on part *c)* of Figure 37.

We then end up for each slot and each clock $i$ with a distance $x_i$ to an arbitrary zero, as represented on Figure 37 part *c)*. The next problem to solve would be the relative positioning of this arbitrary zero from slot to slot. In Figure 37 we made this choice in such a way that $x_{\mathrm{B}}$ is zero for each slot. At this stage, this is totally arbitrary. Indeed, this would suggest that the clock B could be considered a reference, i.e. that its frequency would be very stable, at the $10^{-17}$ level, from slot to slot. This means however that it would be possible to choose as reference the clock for which the stability proves to be the best. A hint about how to asses and potentially hierarchize the stability of a single clock is given in the next paragraph. The interesting information that one gets from graph 37 is the evolution of relative positioning between the clocks from slot to slot.

### 7.2.3 Stability of a single clock

The stability of an oscillator is always measured comparing it to a reference. The resulting stability is limited by the worse stability between that of the reference and the oscillator investigated. This is visible on the left-side plot of Figure 38. The blue and yellow triangles correspond to the direct measure of the stability of each of the two $^{87}$Sr clocks we have at SYRTE against the ultra-stable cavity to which is referenced the shared clock laser (see figure 6). But this oscillator, i.e. the clock laser referenced to the ultra-stable is less stable than that consisting in this stabilized laser referenced to the atomic clock transition. Hence the resulting measured stability is limited by the stability of the clock laser referenced to the ultra-stable cavity. However, these measurements can be used to measure each clock against the other. Each of them have a stability far better than the stabilized laser, resulting in the stability behavior represented by the red trace on the same plot. However, this stability measurement is limited by the worse of the two clocks, and the only thing that can be said is that at least one of the two clocks has a stability better than that obtained by a factor $\sqrt{2}$[50], but there is no way to now more about each single clock stability, unless resorting on a third clock. When a third clock is available, the two-by-two stability

[49] we care on the relative distances only

[50] i.e. such that $\sigma_i(\tau) \leq (1/\sqrt{2})\sigma_{ij}$

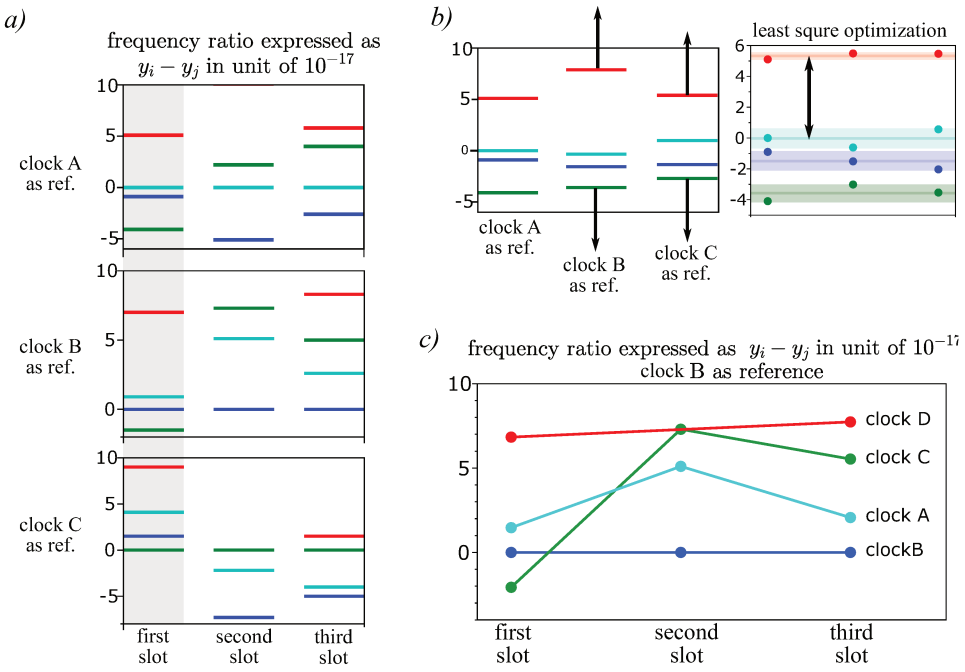


Figure 37: *a)* Each plot represents the values of the frequency ratios of the three comparison slots displayed in Figure 36 but with a different clock taken as a reference (color code in subplot *c)*). The ordering is conserved from reference to an other but not the differences $y_j - y_i$. *b)* The first graph represents the differences $y_j - y_i$ (in $10^{-17}$ of fractional frequency unit) for the first slot as a function of the chosen reference. The offset between the set of differences corresponding to a given reference are *a priori* arbitrary, meaning there is no *a priori* natural choice for this relative offset (black arrows). The second graph on the right shows the offset as determined by our least square optimization method (see equation 224). *c)* This graph gives a reference-invariant representation of the differences $y_j - y_i$ for each slot. However, the offset from slot-to-slot is arbitrary. The same least-square technique could be used but with a weighting to be carefully determined as a function of the reliability of the clocks, which is not done here.

measurements can be combined in such a way that the contribution of only a single clock is kept. This is the so-called three-cornered hat method (see for example [103]). More precisely, the stability $\sigma_i(\tau)$ of a single clock labeled $i$ is obtained from the two-by-two stabilities $\sigma_{ij}(\tau)$ and $\sigma_{ik}(\tau)$ measured with all possible pairs of clocks $(i,j)$, $(i,k)$ and $(j,k)$ as[51]

$$\sigma_i^2(\tau) = \frac{1}{2}\left(\sigma_{ij}^2(\tau) + \sigma_{ik}^2(\tau) - \sigma_{jk}^2(\tau)\right) \tag{225}$$

This method might be used to determined the stability hierarchy required for the relative positioning of the arbitrary zero from the slot to slot (see previous paragraph). As mentioned a bit earlier in the text, we know at least one of our two clocks is such that $\sigma_i(\tau) \leq (1/\sqrt{2})\sigma_{ij}$. The comparison campaign allowed for the use of the three-cornered hat method and it turned out that each of our two clocks had a stability of precisely $(1/\sqrt{2})\sigma_{ij}$ (see right-side plots of Figure 38).

[51] Note that this method to be valid requires the two-by-two stabilities to be of the same order of magnitude: it is not possible to asses the stability of a very good stable oscillator measuring against two independent bad oscillators.

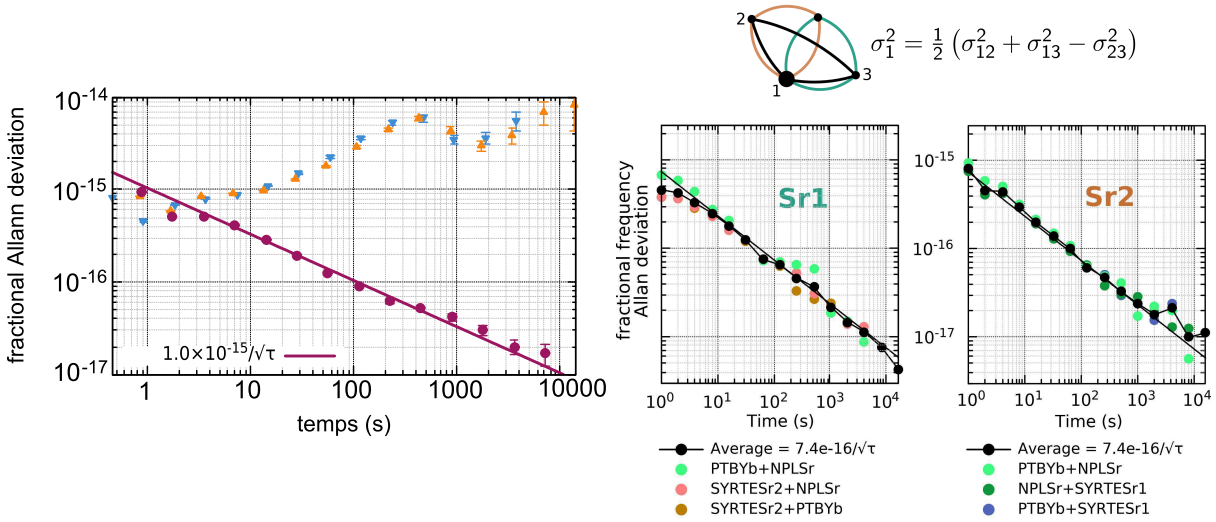


Figure 38: The Allan deviation (left plot) of each clock measured against the ultra-stable cavity are displayed in blue and yellow and are clearly not averaging down as $\tau$ is increased (this is due to the fact that the ultra-stable cavity has a good short term stability of $\approx 5\times10^{-16}$ at 1 s but drifts by typically a few mHz per second). However, this data can be used to measure the stability of each clock against the other, eliminating the cavity, leading to the red trace, averaging down as $1/\sqrt{\tau}$ as expected for white noise (see equation 22). The stability at 1 s reads $1 \times 10^{-15}$ meaning at least on of the two clocks has a stability lower than $(1/\sqrt{2})10^{-15} \approx 7.4 \times 10^{-16}$ at 1 s. On the top-right is a schematic view of the three-cornered hat method used to determine the stability of a single clock based on a network of three clocks. Below are shown the stabilities obtained this way for each of our two clocks (the bottom color legend provides the list of clocks pairs used to obtain a clocks triplet for the three-cornered-hat method implementation: for each of our two clocks, we have three pairs that can be combined to it to form such triplets). It turned out that each of them has a stability of $7.4 \times 10^{-16}$ at 1 s.

# Part IV
# Pushing forward the stability limits

In this part is exposed what has been at the core of this thesis project, namely the implementation of a cavity-assisted non-destructive detection system of atoms trapped in an optical lattice. The motivation for such a development lays in the need to push forward the current stability limits of our strontium clocks: Dick effect, detection noise and quantum projection noise. These limitations and related challenges are exposed in section 8, where an explanation can be found about why a non-destructive detection system can help for increasing the clock stability. So far, our detection system was based on fluorescence techniques, resulting in a systematic destruction of the trap, i.e. an expulsion of all the atoms trapped in the lattice. This trap destruction mechanisms are investigated in details in section 9. Before moving to the non-destructive system, a characterization of our standard fluorescence detection is provided in section 10. Then, section 11 gives mathematical derivations of all the expressions required for the understanding and the implementation of the non-destructive system. Section 12 provides the details of the system's implementation and the main results. While being promising for reducing the Dick effect, the system we demonstrate suffers from serious limitations preventing it from entering the quantum regime , which is necessary to mitigate the quantum projection noise. This is discussed in section 13. After that, some basic considerations about how the quantum projection noise could be reduced in microwave clocks are presented in section 14 along with a discussion about whether or not such techniques can be applied directly to optical lattice clocks. Finally, section 15 reports on the very early stage of the development of a system compatible with the quantum regime.

## 8 Stability limitation and challenges

Three effects are currently limiting the stability performances of cold neutral atoms optical clocks. The Dick effect, the detection noise and the quantum projection noise. The Dick effect is discussed in section 8.1 along with some very promising strategies that are expected to make possible achieving significant reduction of it. The quantum projection noise is introduced in section 8.2. Some elementary considerations are given regarding the detection noise in section 10 but its contribution to the instability is given at the end of section 8.2, since it is derived the same way as that of the quantum projection noise. The hierarchy between these three effects is discussed in section 8.3.

### 8.1 Dick effect

The Dick effect can be interpreted as the down conversion of clock laser high frequency noise to lower frequencies region of the spectrum due to an aliasing effect stemming from the discrete sampling of the clock laser frequency by the atom interrogation [105]. Two approaches can be drawn to address this issue. On the one hand one could work on the reduction of the clock laser frequency noise at the frequencies contributing most to Dick effect, which can be shown to be the harmonics of the clock cycle frequency. On the other hand one could take a *dual* approach and consider tailoring the clock cycle frequency in such a way that the sensitivity to high frequency noise in the clock laser frequency is minimized, independently on the particular clock laser noise spectrum. For typical clock laser noise spectrum, the Dick effect monotonously decreases with the clock duty cycle. While some hard work along the line drawn by the first approach is currently led at SYRTE in particular, the main goal of this thesis was to explore the second one and will be discussed here in deeper details.

#### 8.1.1 Dick effect for a Rabi interrogation

In a simplistic view overlooking atom-environment coupling effects, the Hamiltonian driving the atom dynamics during the clock-atom interaction stage can be considered to be

$$\hat{H} = -\hat{\mathbf{d}}.\hat{\mathbf{E}} \times \Pi_T(t) \tag{226}$$

where $\Pi_T(t) = 1$ for $t \in [0, T]$, 0 for $t \notin [0, T]$ is the time profile function *enveloping* the interaction. This type of interactions leads to Rabi oscillations when the atom is considered a two level system (TLS), for

which the square of the probability amplitude corresponding to the excited state is given by

$$P_e(T) = \frac{\Omega^2}{\tilde{\Omega}^2} \sin^2\left(\frac{\tilde{\Omega}}{2}T\right) \quad , \qquad \tilde{\Omega} = \sqrt{\Omega^2 + \Delta^2} \tag{227}$$

with $\Omega$ the on-resonance Rabi frequency and $\Delta$ the detuning between the driving field and the atomic transition. The above formula is valid for the amplitude and the frequency of $\hat{\mathbf{E}}$ being constant over time. But concerned by DE, one has to take into account fluctuations of the clock field frequency while still considering amplitude fluctuations negligible.

$$\omega_{CL} \longrightarrow \omega_{CL} + \delta\omega(t)$$

Such fluctuations lead to a change $\delta P(T)$ in the probability given by 227, meaning that the actual probability reads

$$P_e(T) \longrightarrow P_e(T) + \delta P(T)$$

The fluctuations $\delta P(T)$ can be expressed as [104]

$$\delta P(T) = \frac{1}{2}\int_0^T g(t)\delta\omega(t)\ dt \tag{228}$$

$g(t)$ being the sensitivity function for this particular type of interrogation.

This concept can be extended to cases where the interaction is enveloped by a time profile function assuming a form more complex than the square window assumed in the case of Rabi interrogation.

The usefulness of the sensitivity function for stability characterization appears clearly when considering its Fourier components

$$g_m = \frac{1}{T_c}\int_0^{T_c} g(t)e^{-2\pi i m t/T_c}dt \tag{229}$$

since it can be shown it contributes to the Allan deviation (AD) according to [Philipp]

$$\sigma_y^2(\tau) = \frac{1}{\tau g_0^2}\sum_{m=1}^{\infty} |g_m|^2 S_{\mathrm{CL}}(m/T_c) \tag{230}$$

$S_{\mathrm{CL}}(f)$ being the one-sided power spectral density of the relative frequency fluctuations of the free running clock laser. It can be shown that for a $\pi$-pulse, i.e. such that $\Omega\tau_R = \pi$ ($\tau_R$ the clock interrogation pulse duration) and a detuning $\Delta = \Delta\nu/2$, $\Delta\nu$ the width of the transition for the given clock power, the Fourier components of the sensitivity function can be approximated as

$$g_m = \frac{2d\cos(\pi m d)}{\pi\left(1-(2md)^2\right)} \tag{231}$$

with $d = \tau_R/T_c$ the duty cycle. Hence, for large $m$, we asymptotically have

$$\left|\frac{g_m}{g_0}\right|^2 \lesssim \frac{1}{16m^4d^4} \tag{232}$$

As seen on Figure 39, the normalized Fourier components do not display any divergences or irregular behaviors for small values of $m$, meaning that for clock laser frequency noise spectra not increasing drastically for small values of $m$, the Allan deviation behavior is dominated by the part of this noise spectrum where the normalized Fourier components of the sensitivity functions is upper bound given in 232 suggesting the closer the duty cycle $d$ can be brought to unity, the lower the contribution of the clock laser noise to the instability will be.
There are actually several options to mitigate the Dick effect. The conceptually most straightforward option is probably working at reducing the clock laser frequency noise itself, and this track is actually currently explored by many optical clocks groups, including our laboratory at SYRTE. But it turned out that the current limitation to the currently dominant contribution to the clock laser frequency noise is the thermal of the high reflection coatings of the ultra stable cavity mirrors used to short term stabilize the clock laser. Short term means here that the cavity reaches its minimal instability within a range of

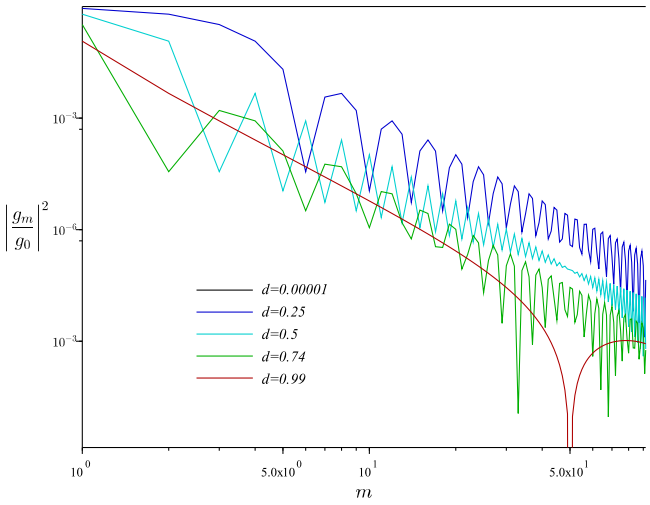


Figure 39: Some normalized Fourier components $|g_m/g_0|^2$ as a function of $m$ for duty cycles $d = 0.00001$, 0.25, 0.5, 0.74 and 0.99. It is apparent that the higher $d$, the lower the contribution to $\sigma_y(\tau)^2$. With our standard fluorescence detection system which kicks the atoms out the trap and thus requires a reloading stage, we typically run sequences with duty cycles between 0.3 and 0.4 (between the light and dark blue curves).

integration times of the same order of the clock cycle time. Bringing the noise lower than this is actually very challenging and we decided to explore an other alternative which has been at the core of the work carried out in the frame of this thesis.

Based on the analysis carried out in [105] and summed up above, we decided to dedicate a lot of efforts to push the duty cycle closer to unity. The duty cycle being defined as $d = \tau_R/T_c$, $\tau_R$ the duration of the interaction between the clock laser and the atoms and $T_c$ the total duration of a full clock cycle, including all stages of atom trapping, cooling, state preparation, interrogation and detection, we are left with two options: extend the interrogation time or reduce the duration of the stages not involved in the interrogation itself.

The first option is already fully explored and has reached its limit, at least in the currently operated Rabi scheme. Indeed, in order to maximize the sensitivity of the clock lock feedback system to clock laser frequency changes, the detuning of the clock laser relative to the atomic transition is set to $\Delta = \Delta\nu/2$ where the corresponding error signal slope is maximal. But one has to be careful to make sure that the frequency region explored by the clock laser be confined within the linear part of the error signal profile (see Figure; 40). On top of the *effective* exploration of this profile mimicked by the detection noise, the expanse of the explored region of the error signal scales as the noise amplitude of the clock laser. But for given detection and clock laser frequency noises, the narrower the transition, the larger the region of the error signal explored. Hence, since the width of the transition scales as $1/\tau_R$, the longer the interrogation, the wider the explored region of the error signal, even though this is partially compensated by the fact that the Dick effect would be reduced resulting from the increase of the duty cycle, meaning that the *effective* explored region would be slightly contracted[52]. Thus, there is an optimal interrogation duration beyond which the explored range of the error signal is no longer linear, resulting in a degradation of the stability. For our system, this nominal interrogation time lays within the 150 - 200 ms range.
Regarding the second option, trapping, cooling, state preparation and detection already have been optimized as far as possible and it seems there is no simple way to contract them further. The idea here is simply to get rid of the trap loading stage. Indeed, one of the most time consuming stage of the cycle

[52] *effective* because the Dick effect induces a folding of the high frequencies regions of the noise spectrum into the region where the clock clock is highly sensitive. Hence, the frequencies explored by the clock laser are still the same, but the sensitivity is decreased for higher duty cycles, i.e. for higher $\tau_R$

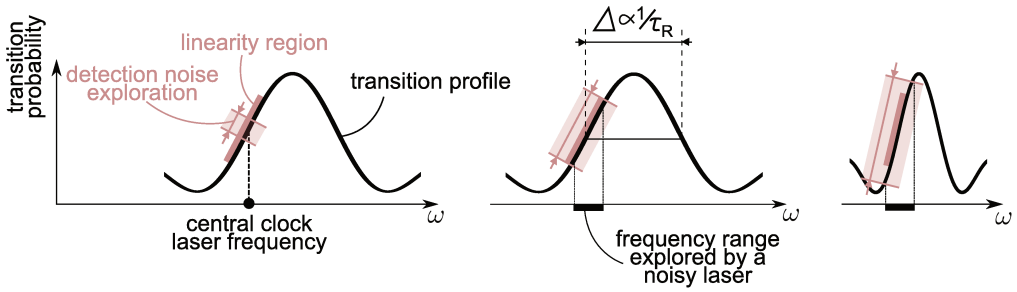


Figure 40: Schematic plots of the transition probability as a function of clock laser frequency $\omega$. The pink bar represents the region where the probability is linear with the clock laser frequency. The pale filled rectangle represents the region explored due to noises of different nature. *Left):* The laser is assumed noiseless, the exploration of the profile being due to detection noise only and is confined to a linear region. *Center):* Due to laser frequency noise added to the detection one, the linear region is fully explored. We note that the width of the transition profile scales as $\Delta \propto 1/\tau_R$. *Right):* When $\tau_R$ is too large, the transition width too low and explored range for the same amount of noise exceeds the linear region, resulting in a stability degradation.

is the loading of the trap, which represents $\sim 40\%$ (typically 200 ms out of a total 500 ms cycle) of each clock cycle, meaning typical duty cycles around 40% (200 ms of clock interrogation against 200 ms of loading + 100 ms of cooling, optical pumping and detection). This is necessary as far as the atoms are kicked out from the trap at the final detection stage, which performs the projective measurement of the atomic final state. Finding a way of measuring the final atomic state without pushing them out of the trap would eventually lead to a significant increase of the duty cycle (i.e. taking it closer to unity) and therefore to a reduction of the Dick effect contribution to the clock instability. This was achieved via the implementation of our classical non destructive detection scheme described in section 11.

As discussed in section 12.4 the rms[53] noise of this new detection system is about 4 atoms in 1 $\mu$s, time duration over which each atom scatters in average a sufficiently low number of photons not to be kicked out the trap. However, this non destructive detection scheme could be used in a destructive configuration, i.e. with detection time $\tau_d$ far larger than the $\mu$s range. From section 12.4, the typical decay time of the atoms off the trap for the non destructive scheme is around 0.1s (the decay is actually not exponential so a standard decay time is not well defined, see equation 270.). Hence, typical detection times $\tau_d \simeq 0.1$ ms could be achieved. Assuming a white noise for the detection, the rms noise scales as $1/\sqrt{\tau_d}$, and noise of around 0.4 atom could be accessible. Note that for such resolution some other effects overlooked till now should be taken into account such as the differential decay between the two clock states for example.

The current camera fluorescence detection system has a noise of roughly 30 atoms (see section 10) for typically 750 atoms trapped after a loading time of 200 ms giving a signal to noise ratio (SNR) of about 25. An equivalent SNR would in principle be achievable with our new system with 10 atoms only. Assuming a linear loading of the trap, this number of atoms would be reached in 3 ms only. Our *drain-repumpers* [105] loding scheme is linear for times $> 10$ ms (which is one of the advantages of this scheme compared to the standard *red MOT* loading used in other groups [76]). Hence, such a number of atoms could be reached in around 10 ms, meaning a 10 fold reduction of the loading stage duration, leading to duty cycles of $\sim 60\%$

### 8.1.2 Ramsey interrogation

In the frame of this thesis, Rabi interrogation only has been used. However, we expect that making benefit from pushing the non destructive detection to the quantum regime will rely on a Ramsey interrogation. Indeed, the main strategy to beat the standard quantum limit relies on the implementation of quantum non-demolition measurement (QND) that consists in successive probings of the atomic state while keeping its coherence. In other words, a QND measurement is a series of engineered Rabi interrogations, Ramsey interrogation being a prototype of such series, with two subsequent Rabi interrogations.

[53] root mean square

This is the reason we recall here basics results regarding such interrogation schemes.

For a Ramsey interrogation, the timing profile enveloping the interaction Hamiltonian is $\Pi_T(t) = 1$ for $t \in [0, T_p] \cup [T, T + T_p]$, 0 otherwise, meaning the sequence is made of two Rabi pulses of duration $T_p$ separated by a Ramsey time $T_R$. In the case the two Rabi pulses are $\pi/2$-pulses, i.e. such that $\Delta = 0$ and $\Omega T_p = \pi/2$, the Fourier components of the sensitivity function take approximatively the form

$$g_m = \frac{2(1 + T/2T_p)(\cos(m\pi d/(1 + 2T_p/T))) - \cos(m\pi d)}{d((2md)^2 - (T_c/2T_p)^2)} \tag{233}$$

where the duty cycle is now given by $d = (2T_p + T)/T_c$. Now $g_m$ depends on both $d$ and the ratio $T_p/T$. The main features of this sensitivity function in terms of stability degradation are discussed in [105] and are just summed up hereafter.

First, the behavior of the normalized Fourier components is in $m^{-2}$ instead of $m^{-4}$, but only for $m$ lower than $m_R = (2 + T/T_p)/d$ above which the components behaves again as $m^{-4}$. This means that for a unity duty cycle, i.e. in the limit of a vanishing dead time, the Ramsay interrogation always gives a stronger reduction of the Dick effect. However, for duty cycles of around 40% achievable so far with our standard camera fluorescence detection system, which interrogation technique gives the best result depends on the LO noise spectrum. In our case, all gain due to switching to Ramsey interrogation would have been canceled by technical detection noises. This is the reason why only Rabi interrogations have been used for the standard operation of the clock so far. However, as discussed above, we expect reaching duty cycles close or even above 60 % for which the Ramsey operation may provide better results than the Rabi scheme.

## 8.2 Quantum projection noise

The work achieved so far to increase the duty cycle looks promising and we expect significant gains in lowering the clock instability. However, this reduction can not be pushed to arbitrary low levels as the stability would at a certain point reach the so called standard quantum limit imposed by the quantum projection noise (QPN). The QPN is nothing but the fact that for the clock laser frequency steering process to be performed, one needs to infer probability amplitudes determining a binomial process from a finite number of experiments. A binomial process is characterized by the probability distribution of its two possible outcomes, say $a$ and $b$, $p(a)$ and $p(b) = 1 - p(a)$. The direct link between this probabilistic definition and the statistics of an experiment is given by

$$p(a) = \lim_{N\to\infty} \frac{N_a}{N} \tag{234}$$

where $N$ is the total number of experiments performed, $N_a$ ($N_b$) the number of experiments with outcome $a$ ($b$) and $N = N_a + N_b$. The problem arises from the finite number $N$ of experiments performed. The discrepancy between the actual value $p(a)$ that one aim at measuring and its experimental statistical estimate $N_a/N$ for $N$ finite contributes to the clock instability (since the difference $p(a) - N_a/N$ differs from a series of measure to another, it does not introduce a constant bias and thus contribute to the clock instability and not to the (in-)accuracy budget).

In the case of neutral atoms optical clocks, the $N$ experiments of each series are performed simultaneously. Indeed, at the end of the interrogation stage of the cycle, each of the atoms trapped in the lattice is found in the coherent superposition $\alpha|g\rangle + \beta|e\rangle$, $|g\rangle$ and $|e\rangle$ being the clock ground and excited states respectively. Afterward, a projective measurement is performed, sending each atom in state $\alpha|g\rangle + \beta|e\rangle$ to $|g\rangle$ with probability $|\alpha|^2$ or to $|e\rangle$ with probability $|\beta|^2$. We then measure the number of atoms projected onto $|g\rangle$ and $|e\rangle$ and estimate the probabilities $|\alpha|^2 = p(g) \sim N_g/N$, $N_g$ being the number of atoms detected in state $|g\rangle$ at the end of the process, $N$ the total number of atoms trapped in the lattice at the moment of the detection (and proceed the same way for $|\beta|^2$).

The statistical definition of the probability

$$\lim_{N\to\infty} \left( p(e) - \frac{N_e}{N} \right) = 0 \tag{235}$$

suggests that it should be possible to arbitrarily reduce the QPN by jut increasing $N$, i.e. the total number of atoms trapped in the lattice. Indeed the standard deviation of the binomial variable $N_e$ is $\sigma_e = \sqrt{Np_e(1-p_e)}$. Hence, the standard deviation of the experimentally induced estimate $\overline{p}_e = N_e/N$ of $p_e$ is

$$\sigma_{\text{QPN}} = \frac{\sigma_e}{N} = \sqrt{\frac{p_e(1-p_e)}{N}} \tag{236}$$

where $N$ is the number of statistical experiments performed, i.e. the number of atoms probed during a given interrogation pulse. As mention in section 8.1.1, the highest sensitivity for the clock laser feedback is obtained for a detuning $\Delta = \Delta\nu/2$ ($\Delta\nu$ the width of the resonance as resolved by the clock laser) for which the transition probability is $p_e = 1/2$ leading to $\sigma^2_{QPN} = 1/(4N)$. Evaluating the contribution of this noise on the probability measure $p_a$ to the Allan deviation of the clock laser frequency requires investigating how it combines with other lock parameters within the lock loop. This was done in [105], where it is shown that for a resonance profile $h(\omega)$ with contrast $C$[54] the one side fractional frequency noise PSD reads

$$S_y(f) = \left(\frac{1}{\omega_0 C(\partial h/\partial\omega)}\right)^2 S_{QPN}(f) \tag{237}$$

where the partial derivative of $h$ should be taken at half-resonance width detuning and where $S_{QPN}(f)$ is the one side PSD of the probability $p_e$ and is given by (see [105])

$$S_{QPN}(f) = 2T_c\sigma^2_{QPN} \tag{238}$$

For Rabi interrogations the resonance profile is the same as the transition Rabi transition probability, i.e. $h = P_e(T)$ and from equation 227 we have

$$\frac{\partial h}{\partial\omega} = \frac{\Delta\Omega_1^2T^4}{\pi^4} = \frac{\Delta T^2}{\pi^2} \approx \frac{0.8\times T}{\pi^2} \tag{239}$$

where we used $\Omega_1 T = \pi$ for a $\pi$-pulse ($\Omega_1$ the Rabi frequency of the transition for the given electric field amplitude and polarization) and the ralation $\Delta \times T \approx 0.8$. Finally considering the total number of atoms probed at each interrogation is constant, i.e. considering that $N$ does not vary significantly from interrogation to another, the contribution of the QPN to the in loop clock laser Allan variance is (see equation 22)

$$\sigma^2_{y,QPN}(\tau) = \frac{\pi^4 2}{C^2\omega_0^2\Delta^2T^4}\frac{T_c}{\tau}\sigma^2_{QPN} \approx \frac{1}{1.28\times C^2\nu_0^2T^2}\frac{T_c}{\tau}\frac{1}{4N} \tag{240}$$

Note that the exact same derivation is valid for the detection noise as well, since the only specification on the QPN noise to work 240 out was that it was white, which is the case for the detection noise. Figure 41 shows the behavior of $\sigma^2_{y,QPN}(\tau)$ for $\tau = 1$ s as a function of $T$, $T_c$ and $N$ varying within a realistic range of values.

## 8.3 Instability contributions hierarchy

When operated with the standard fluorescence detection technique destroying the trap at each cycle, the typical number of atoms loaded in the lattice is such that the Dick effect contribution dominates significantly all types of technical noises as well as the QPN (see Figure. 43 where it is seen that for Rabi times larger than 3 ms the Dick effect, i.e the clock laser frequency noise, dominates the QPN.). In other words $\sigma_y(\tau = T_c) \simeq \sigma_{\text{Dick}}$. However, the implementation of the non destructive detection system is expected to enable a strong reduction of the Dick effect to such a low level that the system could reach a point where the QPN can no longer be overlooked, at least if the clock is operated with the current typical number of atoms (a few thousands). Increasing the number of atoms could be a solution *a priori* since the QPN scales as $1/\sqrt{N}$. However, this would inevitably increase the atomic density, i.e. the number of atoms per lattice site, and the strontium-strontium collision shift might then no longer be overlooked (see section 4.6.4). The strategy for future development is then based on cavity-assisted spin squeezing, as briefly outlooked in section 14.

[54] here $h$ has maximum 1 and the actual measured profile is $h$ rescale by $C$. In other, the maximum transition probability measured is $C$, when the off transition background is zero.

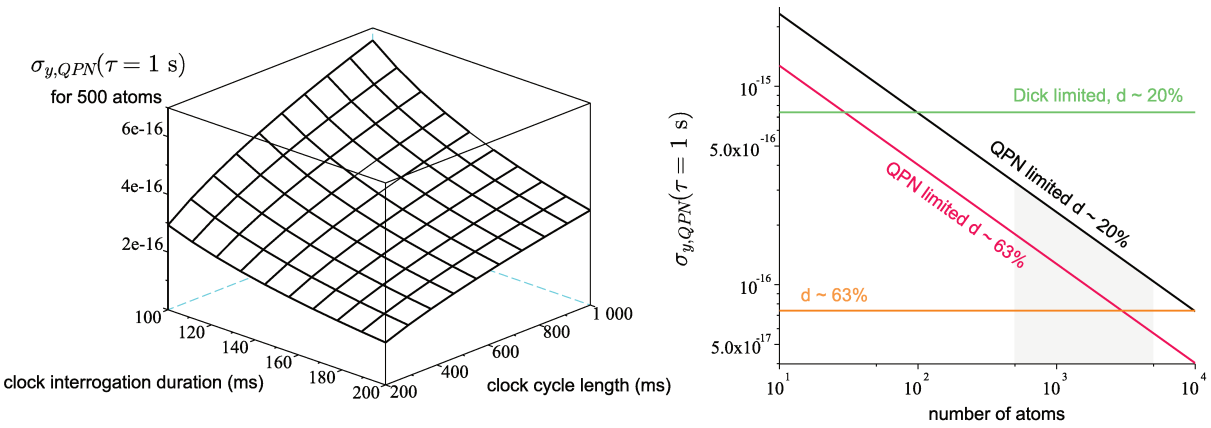


Figure 41: The left-side plot shows $\sigma^2_{y,QPN}(\tau = 1\ s)$ as a function of the clock interrogation duration $T$ and the clock full cycle duration $T_c$ for a Rabi interrogation scheme. The right-side plot shows the behavior of $\sigma^2_{y,QPN}(\tau = 1\ s)$ as a function of the number of atoms $N$ for a duty cycle $d \sim 20\%$, which corresponds to the typical values currently realized, and $d \sim 63\%$, which is expected duty cycle we could implement with our non destructive detection scheme. For both curves the total interrogation lasts 200 ms, which is what is currently implemented. We represented as well the current Dick effect limited Allan deviation of our two clocks, measured via the three-cornered hat method (see 7.2.3) for $d \sim 20\%$. The value used for $d \sim 63\%$ is estimated from the behavior given in 230, i.e. rescaling $\sigma_y(\tau = 1\ s)$ as $d^2$. The clocks are typically operated with $500 \lesssim N \lesssim 5000$ which is represented by the gray area on the graph. Hence, while the current Allan deviation at 1 s is dominated by the Dick effect contribution for $d \sim 20\%$, it is expected this will no longer be the case with a $d \sim 63\%$ duty cycle.

### 8.3.1 Expected stability improvements

Because a poor lifetime of the atoms in the lattice of about $\tau_L \simeq 400$ ms for the the SrB clock, on which we developed the detection system, we could not yet benefit from its non destructivity, the time the atoms are sufficiently many in the trap being to short to perform even two consecutive interrogations. But we can roughly estimate the expected gain for a lifetime $\tau_L \simeq 10$ s, as that of our second strontium clock Sr2. Sr2 is nominally operated with a 500 ms MOT [55] and a 200 ms interrogation Rabi pulse for a total cycle length close to the second, i.e. a duty cycle $d \simeq 20\%$. This means a cycle without lattice loading would last some 300 ms (200 ms of clock interrogation + 100 ms of cooling, optical pumping and detection). Hence, for a 10 s lattice lifetime, it would be possible to proceed to 33 cycles of 300 ms before loosing half of the atoms, each of which with a 200 ms interrogation pulse. In order to have a sufficient number of atoms at the last cycle, the lattice should initially be loaded with a high number of atoms[56], say with a 500 ms loading time. This would result in an effective duty cycle $d \simeq 63\%$, which is an increase by more than a factor 3. Remembering the normalized Fourier components involved in the Dick effect contribution to the squared Allan deviation (see equation 230) scales as $1/d^4$ (see equation 232), this would result in an instability reduction by a factor 9, assuming the spectral property of the clock laser noise are the same around the harmonics of $\nu_c = 1/T_c$ for both cycle lengths corresponding to the actual scheme and that with the non destructive detection.
Equation 236 suggests that increasing the number of atoms in the lattice should allow for the reduction of the QPN contribution to an arbitrary low level. However it turns out that this approach leads to other systematics effects such as cold collisions within lattice sites, the effect of which is still to be fully characterized. Moreover, increasing the number of atoms in the lattice requires increasing the trap depth $U_0$, making lattice light shifts more difficult to deal with (see 5 section for details). Thus, beating the QPN limit while preserving the accuracy budget demands relying on other resources (see section 14).

[55] corresponding to loading stage of $\simeq 600$ ms including the repumping from the two meta-stable states $^3P_0$ and $^3P_2$ to the ground state $^1S_0$

[56] The initial number of atoms can not actually increased above a certain threshold beyond which the non destructive detection system is no longer working, as is discussed in section 12.4

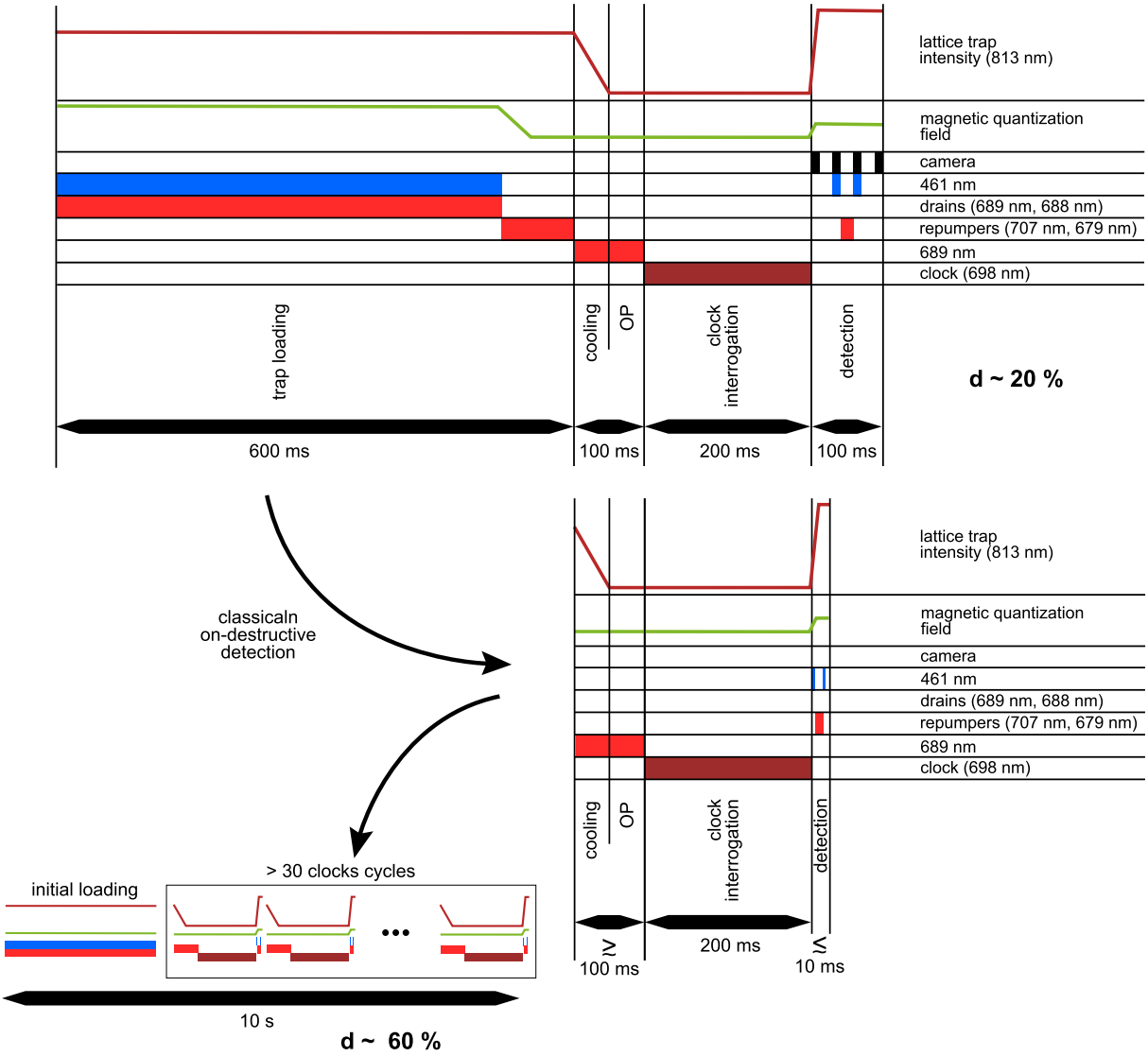


Figure 42: Schematic representation of the Sr2 clock as it is operated now and how it is expected to be after the implementation of our non-destructive detection system (the SrB cock sequence is very similar to this as well). Top graph: the current sequence lasts around 1 s, composed as 600 ms of trap loading, 100 ms of cooling and optical pumping (OP), 200 ms of clock interrogation and finally 100 ms of fluorescence camera detection, resulting in a duty cycle of about 20%. Bottom right: After implementation of the non-destructive detection, the loading stage is dropped out, and the detection itself is carried out much quicker, resulting in a total cycle duration of roughly 300 ms, corresponding to a duty cycle of about 66%.Bottom left: with a trap lifetime of 10 s and an initial loading stage of 500 ms, it should be possible to carry out over 30 successive cycles 300 ms each, giving an effective duty cycle above 60%.

### 8.3.2 Measurement of detection, clock laser induced and quantum projection noises

In this section we present our experimental characterization of the three main sources of noise degrading our clock stability: the detection noise, the clock laser frequency noise and quantum projection noise. All these measurements where performed measuring the fluorescence signal stemming from the trapped atoms illuminated by a probe and collected by a Hamamatsu 9200 C camera (see section 10 for details about the fluorescence CCD camera detection system). Hence, all the measurement are limited by the corresponding detection noise, meaning that the noise stemming from any other effect will be visible only if higher than the detection noise. Hence we start with characterizing the detection noise. We then

explore the clock laser frequency noise contribution and finally measure the quantum projection noise.

**1)** *Detection noise*

In the paragraph "Signal to noise ratio analysis" of section 10.1 we characterize the detection noise for the fluorescence detection using a Hamamatsu 9200 C camera. IN order to isolate the detection noise from the clock laser noise and the quantum projection noise we measure it with the clock laser off resonance, i.e. at frequencies where the transition probability $p_e$ vanishes. Its variance then reads (see 301)

$$\sigma_D^2 = 2\frac{\Sigma_{P_p}^2}{N_c^2} \tag{241}$$

where $\Sigma_{P_p} \sim 5500$ camera counts accounts for the camera dark noise and where the $N_c$ is the total number of counts, i.e. dark noise plus atom's fluorescence. Hence the corresponding noise scales as $1/N_c$. The corresponding curve is reporter on Figure. 43 (blue trace) along with the measured values (blue dots).

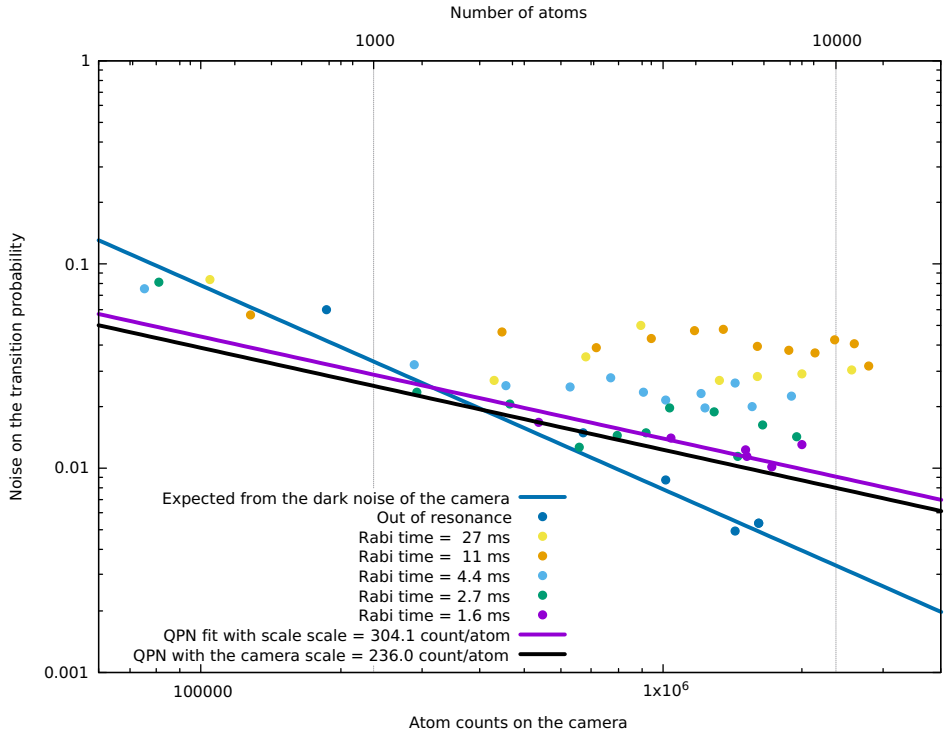


Figure 43: **Noise on the transition probability**. *Blue line:* predicted transition probability noise $\sigma_{p-e} = \sigma_D = \sqrt{2}(\Sigma_{P_p}/N_s)$ for $p_e = 0$ (off resonance). *Blue dots:* measured detection noise for $p_e = 0$. *Color dots:* measured $\sigma_{p_e}$ for $p_e = 1/2$ for different Rabi times $\tau_R$. *Black line:* predicted quantum projection noise contribution $\sigma_{QPN} = 1/(2\sqrt{N})$ to $\sigma_{p_e}$ for $p_e = 1/2$ based on a camera counts calibration of 236 counts per atom. *Purple line:* Fitted quantum projection noise based the $\tau_R = 1.6$ ms measurements apparently scaling as $1/\sqrt{N_c}$. This fit provides an independent calibration of the camera counts conversion factor of 304 counts per atoms.

**2)** *Clock laser noise*

To evaluate the effect of the clock laser noise on the transition probability we need to work at non zero transition probability. Since the clock is nominally operated at $p_e = 1/2$, we characterize the clock laser induced noise at this value. This is achieved setting the pulse duration, i.e. the Rabi time $\tau_R$, and the clock power, i.e. the Rabi frequency $\Omega_1$ in such a way that $\Omega_1\tau_R = \pi$ while setting the clock laser frequency half a resonance width away from the center of the transition line. As depicted in Figure. 40, for a given clock laser frequency noise excursion, the steeper the resonance profile, the larger the measured transition probability excursion. In other words, the broader the resonance profile, the lower

the sensitivity to clock laser frequency noise. Since the transition profile width scales as $1/\tau_R$, we expect the noise on the transition probability readout to increase with the Rabi time. We measured the noise on the transition probability for different Rabi times $\tau_R$ and different number of atoms (see color points on Figure. 43). For Rabi times and number of counts such that this noise dominate the detection noise (blue line) and the quantum projection noise (purple and black lines, see below) the clock laser induced noise is rather flat, meaning it does not depend on the number of atoms. We see that for $\tau_R \geq 4.4$ ms the noise on the probability always lays above the quantum projection noise. Indeed, for number of counts such that the quantum projection noise would be equivalent or even would dominate the clock laser noise contribution, the total noise on the probability is limited by that of the detection, and the corresponding data are "lifted" by the detection noise, i.e. they lay on the blue line.

**2)** *Quantum projection noise*

The transition probability noise due to the quantum projection is given by 236 and scales as $1/\sqrt{N_c}$. From our calibration of atoms number in function of number of counts it is possible to draw the corresponding line (black line) on Figure 43. For $\tau_R = 1.6$ ms, we see that the probability noise (purple dots) scales as $1/\sqrt{N_c}$ as well, meaning the noise is dominated by the quantum projection effect. We notice an offset between the purple dots and the black line. We can interpret this offset in two ways. First, it could be due to the fact the quantum projection effect, for this Rabi time and over this region of number of atoms, is higher than the detection noise and the clock laser induced noise but without dominating them sufficiently for them to be totally negligible. In other words, we have to keep the full expression $\sigma_{p_e} = \sqrt{\sigma_D^2 + \sigma_{CL}^2 + \sigma_{QPN}^2}$ where the subscripts $_D$ and $_CL$ refer to detection and clock laser respectively, without dropping $\sigma_D^2$ and $\sigma_{CL}^2$, resulting in slightly higher values than $\sigma_{QPN}$. Second, it could be due to a small error in our estimation of the atoms number to number of counts conversion factor. The purple line is a fit of the purple dots with a function scaling as $1/\sqrt{N_c}$, resulting in an estimation of this factor providing a value of 304 counts per atom, independent of that carried out in section 10.1 that gives 236 counts per atoms (i.e. $1/\beta = 236$, see 10.1).

## 8.4 Cavity assisted detection as a solution to both limitations

As mentioned in section 8.1 there are two strategies aiming at reducing the Dick effect: reducing the clock laser frequency noise and reducing the duty cycle. While current efforts are currently made in various laboratories [77], including SYRTE, to reduce the clock laser frequency noise, which is understood as being dominated by Brownian thermal fluctuations of the ultra stable cavity mirror coatings, the present work addressed the second solution. Our solution relies on a cavity assisted detection scheme based on dispersive properties of atom-light interaction. While operated in the classical regime, this scheme is referred to as classical non destructive detection (CNDD), and is described in section 11. Classical here means that the trap is not destroyed in the sens that the number of photons scattered per atoms sufficiently low for the atoms not to be pushed out of the trap while their internal state coherence induced by the clock interrogation is lost (all the atoms are left in the ground state at the end of the detection). Keeping the atoms enables a fast repetition of clock cycles with almost no dead time, i.e. a duty cycle close to unity and therefore a reduction of the Dick effect.

Moreover, pushing this detection scheme in its quantum regime (QNDD) is expected to overcome the QPN problem as well. Indeed, with the QNDD scheme, less than one photon is scattered per atom during the detection, meaning that the coherence of the atomic internal state is partially preserved over the process, in a sens discussed in the QNDD section. This is a key feature to achieve quantum non demolition (QND) measurement, which might be the way to perform sub-standard quantum limit measurement, i.e. measurement with noise lower that the QPN limit.

Hence, cavity assisted non destructive detection techniques stand as a powerful tool to address simultaneously both Dick effect and QPN noise limitations.

# 9 Trap destruction mechanism

In this section we first expose, in section 9.1, the reason why, using a fluorescence based detection system, we could not get rid of the trap reloading stage at each clock interrogation cycle, which is the dominant contribution to the dead time of the cycles, amounting to roughly half of the total cycle duration, keeping our duty cycle below the 50% level. We then move to a careful analysis of the trap destruction phenomena in section 9.2 in order to draw out some basics criteria determining the required features for a non destructive detection system and finally show how these criteria rule out our two fluorescence detection system currently at disposal and compute the expected heating and loss rates for our non destructive detection scheme. This section also includes a detailed discussion about the heating mechanism and how it varies from one geometry to another. A brief conclusion about the usefulness of the expressions obtained is given in section 9.3.

## 9.1 Standard fluorescence detection

Our strategy in addressing the Dick effect stability limitation consists in increasing the duty cycle of the clock sequence by avoiding having to reload the trap after each clock interrogation. To explain why a reloading stage has been inevitable so far, we recall the basics of Rabi clock interrogation of the atoms by the LO and the transition probability readout based on standard fluorescence detection. The atoms are initially all in the clock ground state $|g\rangle$ and end, up after the interaction with the LO field[57], in the coherent normalized superposition $\alpha|g\rangle + \beta|e\rangle$. The useful information used to steer the LO frequency is the probability $|\beta|^2$. In the frame of standard fluorescence[58] detection technique, the probabilities are read out by shining a powerful resonant probe (adjusted to the $^1S_0 \rightarrow {}^1P_1$ transition in our case). This results in projecting each atom in state $\alpha|g\rangle + \beta|e\rangle$ onto $|g\rangle$ or $|e\rangle$ with respective probability $|\alpha|^2$ or $|\beta|^2$. The atoms projected into $|g\rangle$ fluoresce while those sent to $|e\rangle$ do not. The measurement of the fluorescence signal is then proportional to $|\alpha|^2 N$, $N$ the total number of atoms. Because the probe shone to the atoms is powerful, all the fluorescing atoms undergo a large number of absorption-emission cycles and are eventually kicked out from the trap. The atoms left in state $|e\rangle$ are then pumped down via intermediate states, ending up in state $|g\rangle$. A second probe pulse is then sent to the remaining atoms yielding a fluorescence signal proportional to $|\beta|^2 N$, which, again, are kicked out from the trap. The useful quantity is then obtained combining the two measurements results as

$$|\beta|^2 = \frac{|\beta|^2 N}{|\alpha|^2 N + |\beta|^2 N}, \text{ since } |\alpha|^2 + |\beta|^2 = 1 \tag{242}$$

The extraction of the useful information required for operating the clock is then obtained at the cost of kicking all the atoms out of the trap, thus demanding the repetition of the trap loading stage at each interrogation cycle.

## 9.2 Trap destruction by photon scattering

A first step on the way to prevent trap destruction is the understanding of its mechanisms. The atoms are trapped in the lattice that consists in a linear sequence of potential wells, or lattice sites, resulting of the dipolar interaction between the atomic dipole and the standing wave electromagnetic field of the lattice light. The lattice can be considered translationally invariant over a few hundreds of sites along its longitudinal direction ($\sim$ hundreds of $\mu m$). The clock is nominally operated with the lattice tuned at the so-called *magic wavelength* at which both clock levels polarizabilities are equal, resulting in an equal trapping potential for both levels[59] meaning that, in this configuration, the trapping of an atom does not depend on its internal degree of freedom[60] but only on its external, kinetic, degree of freedom. As soon as an atom has its kinetic energy close to or higher than the site potential well depth, it is likely to escape it.

There are mainly three ways for a trapped atom to gain kinetic energy. i) Trap amplitude fluctuations, when occurring close to twice the harmonic motion frequency of the atoms in the trap, can result in

[57] this general view is valid for both Rabi and Ramsey interrogation scheme.
[58] absorption techniques are based on the same phenomena described hereafter
[59] the existence of this *magic wavelength* ensures the possibility of having each clock level undergoing the same lattice induced light shift and therefore to cancel the resulting clock transition shift, at least to the first order in trap depth.
[60] at least to the first order trap intensity or trap depth

heating and eventually losses of the atoms if the kinetic energy acquired goes above the trap depth. One can actually relates the loss rate $\Gamma_L$ of trapped atoms to the motional oscillations frequency $\nu_L$ resulting from the harmonic trapping by the lattice and the relative noise spectral density of the lattice intensity $S_L(f)$ as [107]

$$\Gamma_L = \pi^2 \nu_L^2 S_L(2\nu_L) \tag{243}$$

Such fluctuations may typically occur when the lattice light lock to the trap depth enhancement cavity is not tight enough, the cavity converting the fluctuating lattice-to-cavity frequency mismatch into intra cavity field amplitude fluctuations. ii) Collisions hot atoms and molecules found in the residual vacuum background gas, which is explored in details in section 6. iii) Photon scattering, i.e. the acquisition of extra momentum via photon absorption-emission process, which is treated hereafter.

As mentioned at the beginning of section 8.3, full benefits from the implementation of the non destructive detection is possible only if the lifetime of the atoms in the lattice is sufficiently large to allow several clock cycles to be successively performed before the trap be depleted. Typical durations of cycle when non destructive detection is used are expected to last around 300 ms. We then need to make sure the loss rates due to point i) and ii) are not limiting the life time of the atoms in the cavity to shorter than at least a few seconds. It turns out that the loss rate is dominated by hot collisions with residual background gas and that it is sufficiently low on second clock (Sr2) whereas it is too high on our first clock (SrB) on which was implemented the detection system in its prove of principle development stage (see section 8.3).

As sketched out in section 9.1 the reason we systematically destroy the trap at the end of the clock cycle with a standard fluorescence detection system is the high power required for the probabilities reading out. In this section we explore in greater details how this mechanism works starting from energy and momentum conservation relations during photon absorption and emission by the atoms.

### 9.2.1 Absorption momentum transfer for free atoms

In the case of a free atom illuminated by a laser probe , for a photon to be absorbed, both the following energy and momentum conservation relations should be fulfilled

$$\mathbf{k}_f = \mathbf{k}_i + \mathbf{k}_{ph} \tag{244}$$

$$E_f = E_i + \hbar\omega \tag{245}$$

where $E_{f,i}$, $\mathbf{k}_{f,i}$ are the final (just after the absorption) and initial (just before) momenta and energy of the atom, $\mathbf{k}_{ph}$ the absorbed photon momentum. Absorption momentum transfer always occurs in the same direction, that dictated by the orientation of the probe. For free atoms (not trapped), this transfer direction corresponds to the probe direction, given by the probe orientation. Taking the motional degree of freedom into account, 245 demands

$$E_{f,i} = \frac{\hbar^2 \mathbf{k}_{f,i}^2}{2m} + E_{e,g} \tag{246}$$

$E_{e,g}$ being the internal electronic energy levels of the excited and ground state of the transition of interest. Thus

$$\hbar\omega = \frac{\hbar^2(\mathbf{k}_f^2 - \mathbf{k}_i^2)}{2m} + E_e - E_g \tag{247}$$

and defining the Bohr transition frequency as $\omega_0 = (E_e - E_g)/\hbar$

$$\hbar\omega = \hbar\omega_0 + \frac{\hbar^2 \mathbf{k}_{ph}^2}{2m} - \mathbf{k}_i.\mathbf{k}_{ph}\frac{\hbar^2}{m} \tag{248}$$

with $E_{\mathrm{D}} = -\mathbf{k}_i.\mathbf{k}_{ph}\frac{\hbar^2}{2m}$ the Doppler shift and $E_r = \frac{\hbar^2 \mathbf{k}_{ph}^2}{2m}$ the recoil shift or energy recoil, i.e. the amount of energy provided by the incoming photon required for the momentum to be conserved, independent of the initial motion of the atom.

### 9.2.2 Absorption momentum transfer in the Lamb-Dicke regime

For atoms trapped in a uni-dimensional (1D)lattice, both the internal and external degrees of freedom are to be taken into account. When the atoms temperature is such that their kinetic energy amounts to a fraction of the trap depth, the region of the lattice potential they explore can be considered quadratic and their motion is suitably described by a three-dimensional quantum harmonic oscillator. For 1D lattices, the confinement is much higher in the longitudinal direction, say $z$, than in the transverse ones, i.e. in the $x-y$ plane, where it is defined by the transverse Gaussian profile of the lattice laser mode. The external degrees of freedom can thus be described as states of the form $|n_x, n_y, n_z\rangle = |n_x\rangle \otimes |n_y\rangle \otimes |n_z\rangle$ where the $|n_j\rangle$ is an eigenstate of the of the 1D quantum harmonic oscillator in direction $j = x,\ y,\ z$. The total state of the atom is then given by combinations of states of the form $|\psi\rangle = |\xi\rangle \otimes |n_x, n_y, n_z\rangle$, where $\xi = g$ for the internal ground state of the considered transition, $e$ for the excited one. We thus expect a laser probe to possibly drive transition between $|g\rangle \otimes |n_x, n_y, n_z\rangle$ and $|e\rangle \times \left|n'_x, n'_y, n'_z\right\rangle$. The matrix elements of the driving Hamiltonian corresponding to these transitions are proportional to factors of the form $\langle n_z| e^{-ik_z\hat{z}} |n'_z\rangle$ [106, 136], $k_z$ the probe wave vector $z$-component[61]. For a strong confinement in the $z$-direction the spatial distribution of the wave function in this direction is very small, meaning the corresponding momentum wave function is very large in the $p_z$ direction and thus is approximately invariant under $p_z$ translation, i.e. under the action of the operator $e^{-ik_z\hat{z}}$. Hence, by orthogonality of the harmonic oscillator eigenstates,

$$\langle n_z| e^{-ik_z\hat{z}} |n'_z\rangle \simeq \langle n_z|n'_z\rangle = 0 \tag{249}$$

meaning the coupling between $|n_z\rangle$ and $|n'_z\rangle$ mediated by the absorption of a probe photon is much weaker than that corresponding to a pure internal transition occurring without change of external degrees of freedom.

Hence we consider there is no momentum exchange between probe field and atoms in the longitudinal direction of the lattice, i.e. that momentum transfers occur in the transverse direction only (the longitudinal component of the momentum is absorbed by the lattice itself). We then decompose the momenta $\mathbf{k}$ in to $\mathbf{k}_z + \mathbf{k}_\perp$ where $\mathbf{k}_z$ points along the $z$ direction (longitudinal component), to which the lattice is aligned, while $\mathbf{k}_\perp$ lays in the transverse $x-y$ plane. This leads to the decomposition of the energy recoil into $E_r$ as $E_r = E_\perp + E_z$ with

$$E_\perp = \frac{\hbar^2(k_{ph,x}^2 + k_{ph,y}^2)}{2m} = \frac{\hbar^2 \mathbf{k}_{ph,\perp}^2}{2m} \tag{250}$$

$$E_z = \frac{\hbar^2 k_{ph,z}^2}{2m} \tag{251}$$

This means the momentum gained by an atom considering the absorption transfer only (the emission is treated in the next paragraph) after $n_\gamma$ absorptions amounts to

$$\mathbf{k}_f - \mathbf{k}_i = n_\gamma \mathbf{k}_{ph,\perp} \tag{252}$$

### 9.2.3 Emission momentum transfer

Since we are interested in the destructive effect of the fluorescence readout detection probe, we restrict our study to the corresponding ${}^1S_0 \to {}^1P_1$ transition. Each time an atom absorbs a photon it re-emits it in a random direction[62] after a typical time laps $\tau = \Gamma^{-1}$, $\Gamma$ the linewidth of the considered transition, which is about 32 MHz. Taking this into account, after $n_\gamma$ absorption/re-emission cycles the atom momentum gain reads

$$\mathbf{k}_f - \mathbf{k}_i = n_\gamma \mathbf{k}_{ph,\perp} - \sum_{q=1}^{n_\gamma} \mathbf{k}_{q,\perp} \tag{253}$$

with $\mathbf{k}_q$ the momentum of the $q^{th}$ photon re-emitted by the atom. In order to avoid pushing the atoms to fast away from their location at the beginning of the detection, the detection beam, or probe beam,

[61] This formula is actually valid in the restricted case of a probe beam collinear to the longitudinal direction of the lattice, but a more general treatment here would be cumbersome since we are only interested in a qualitative description of the phenomenon, which is the same as in the collinear case.

[62] The re-eimission is actually randomly distributed in space for free atoms when it occurs when no field polarizes it. However, in the general case of concern here the probe field is kept on during the whole detection process and therefore polarizes the atoms along its polarization. The re-emission distribution is then that of the dipole emission pattern. This is taken into account further in the development.

is retro-reflected back onto the same incoming path. This means each atom absorbed roughly the same number of photons from the direct probe as from the retro-reflected one. Let say that for $n_\gamma$ absorbed with momentum $\mathbf{k}_{ph}$, $n'_\gamma = n_\gamma(1-\varepsilon)$ with momentum $\mathbf{k}'_{ph} = -\mathbf{k}_{ph}$ are absorbed, and the momentum gain per atom then reads

$$\mathbf{k}_f - \mathbf{k}_i \simeq \varepsilon n_\gamma \mathbf{k}_{ph,\perp} - \sum_{q=1}^{2n_\gamma} \mathbf{k}_{q,\perp} \tag{254}$$

When the retro-reflection is well prepared, the difference between the number of photons absorbed per atom stemming from the direct and retro-reflected beams is small compared to each of these numbers i.e. $n_\gamma - n'_\gamma \ll n_\gamma$ or $\varepsilon \ll 1$.

### 9.2.4 Heating and loss rates

Computing the heating and losses rates requires knowing the distribution of kinetic energy gain for a given probe geometry as a function of the photon absorption rate. This is done first by deriving the transfer momentum distribution. We start with a simplified model assuming an isotropic radiation pattern, then consider the standard dipole radiation distribution and finally discuss if further effects induced by the cavity (such as Purcell effect) should or not be overlooked.

How the absorption transfered momenta and the emission transfered momenta combine to give the kinetic energy growth rate of the trapped atoms depends on the relative geometry between probe and lattice. Indeed the energy gain is given by

$$E = \frac{\hbar^2}{2m}\left(\varepsilon n_\gamma \mathbf{k}_{ph,\perp} - \sum_{q=1}^{2n_\gamma} \mathbf{k}_{q,\perp}\right)^2 \tag{255}$$

that can be written as

$$E = \frac{\hbar^2}{2m}\left(A - B + C\right) \tag{256}$$

with

$$A = \varepsilon^2 n_\gamma^2 \mathbf{k}_{ph,\perp}^2 \qquad B = 2\varepsilon n_\gamma \mathbf{k}_{ph,\perp}.\sum_{q=1}^{2n_\gamma} \mathbf{k}_{q,\perp} \qquad C = \left(\sum_{q=1}^{2n_\gamma} \mathbf{k}_{q,\perp}\right)^2 \tag{257}$$

whose hierarchy depends on the size of $\varepsilon n_\gamma$ as well as the relative size of $\mathbf{k}_{ph,\perp}$ compared with $\varepsilon n_\gamma$. Indeed

$$\langle A \rangle = \varepsilon^2 n_\gamma^2 k_{ph}^2 \sin(\zeta) \tag{258}$$

with $\zeta$ the angle between detection probe and lattice,

$$\langle B \rangle = 2\varepsilon n_\gamma \mathbf{k}_{ph,\perp}.\left\langle \sum_{q=1}^{2n_\gamma} \mathbf{k}_{q,\perp} \right\rangle = 0 \tag{259}$$

and

$$\langle C \rangle = \sum_{q=1}^{2n_\gamma}\sum_{r=1}^{2n_\gamma} \langle \mathbf{k}_{q,\perp}.\mathbf{k}_{r,\perp} \rangle = \sum_{q=1}^{2n_\gamma} \langle \mathbf{k}_{q,\perp}^2 \rangle = 2n_\gamma \frac{2k_{ph}^2}{3} \tag{260}$$

the uncorrelation between the different emissions directions ensuring $\langle \mathbf{k}_{q,\perp}.\mathbf{k}_{r,\perp} \rangle = 0$ for $q \neq r$ and the $2/3$ factor stemming from the isotropy of the re-emission process[63]. Hence the ratio $A/C$ scales as

$$\frac{A}{C} \propto \varepsilon^2 n_\gamma \sin(\zeta) \tag{261}$$

For a standard fluorescence projective detection, the probe is not collinear to the lattice, with typical values $\zeta \sim \pi/2$ and for retro-reflected probe well overlapped to the incoming one $\varepsilon n_\gamma$ can be reasonably small such that both the $A$ and the $C$ terms have to be taken into account. As shown further in this

[63] This factor is slightly changed when considering the dipole radiation pattern instead.

section the $A$ term gives a deterministic kinetic energy increase whereas the $C$ terms leads to a stochastic behavior. Hence, the actual hierarchy between the two terms can be determined when the readout fluorescence signal is obtained using a photomultiplier tube, which conserved the time evolution of the signal (see section 10). In the cavity-assisted configuration described in section 11 the probe is perfectly collinear to the lattice, i.e. $\sin(\zeta) = 0$, making the $C$ term dominant.

In the next paragraphs we evaluate the heating and loss rates for 1) the collinear probe (i.e. when the $C$ term dominates the dynamics) and 2) the non collinear case, first assuming a simplified isotropic radiation pattern and in a second step in the more elaborate case of a dipole radiation pattern.

**Spherical radiation pattern**

**1)** *Collinear probe beam*

As enhanced above, in the case of a probe collinear to the lattice, the absorption contribution to the energy transfer vanishes ($\sin(\zeta) = 0$ and thus $A = 0$) and the growth of the kinetic energy is a random process since it relies on the re-emission of the absorbed photon randomly in all direction of space (in the case of our isotropic assumption for the radiation pattern). The atomic momentum growth is then given by

$$\mathbf{k}_f - \mathbf{k}_i = -\sum_{q=1}^{2n_\gamma} \mathbf{k}_{q,\perp} \tag{262}$$

The assumed isotropy of the re-emission pattern means that the emitted momentum distribution is evenly distributed over the three direction of space

$$\langle \mathbf{k}_q^2 \rangle = \sum_{i=1,\dots,3} \langle k_{q,i}^2 \rangle = 3 \times \langle k_{q,j}^2 \rangle = k_{ph}^2, \;\; j = 1,2,3 \tag{263}$$

where we used that the size of the emitted momentum equals that of the absorbed one, i.e. $k_q = k_{ph}$. By the central limit theorem this leads to a distribution for the cumulated absorbed momentum $i^{th}$ component $k_i = \sum_{q=1}^{n_\gamma} k_{q,i}$

$$p\left(k_i\right) = \frac{1}{\sqrt{2\pi\sigma^2}} e^{-\frac{k_i^2}{2\sigma^2}} \tag{264}$$

where $\sigma^2 = n_\gamma k_{ph}^2/3$. The probability for an atom to be ejected from the trap via photon scattering after $n_\gamma$ absorption/re-emission cycles is given by the probability for an atom to end up with a kinetic energy higher than the trap depth $U_0$. In order to compute the heating rate we then need the kinetic energy growth distribution as a function of $n_\gamma$ which, from 264, reads

$$p\left(E_K = \frac{\hbar^2 K_\perp^2}{2m}\right) = \int dk_x dk_y dk_z \; p\left(k_x\right) p\left(k_y\right) p\left(k_z\right) \delta\left(K_\perp^2 - (k_x^2 + k_y^2)\right) \tag{265}$$

where $\delta$ is the Dirac distribution, $K_\perp = \sqrt{2mE_K/\hbar^2}$ the accumulated momentum in the transverse direction such that the kinetic energy gain of the atoms is $E_K$. The integrals in the transverse and longitudinal directions decouple into $I_\perp \times I_z$ with

$$I_\perp = \int dk_x dk_y \; p\left(k_x\right) p\left(k_y\right) \delta\left(K_\perp^2 - (k_x^2 + k_y^2)\right) \tag{266}$$

$$I_z = \int dk_z \; p\left(k_z\right) = 1 \tag{267}$$

Computing $I_\perp$ in polar coordinates and using the Delta distribution property $\delta(a^2 - x^2) = (\delta(x-a) + \delta(x+a))/|a|$ we get

$$I_\perp = \frac{1}{\sigma^2} e^{-\frac{E_K/E_r}{2\sigma^2}} \tag{268}$$

The distribution of the kinetic energy accumulated during the process then reads

$$p(E_K) = \frac{1}{\sigma^2} e^{-\frac{E_K/E_r}{2\sigma^2}} \tag{269}$$

For an ensemble of trapped atoms all with initial kinetic energy $E_i$, the fraction remaining trapped after having absorbed $n_\gamma$ is $\beta = p(E_i + E_K < U_0)$, i.e.

$$\beta(E_i) = \int_0^{U_0 - E_i} p(E_K) dE_K \tag{270}$$

which gives, for an initial distribution of kinetic energy $p(E_i)$

$$\beta = \int p(E_i)\beta(E_i) dE_i \tag{271}$$

**2)** *Non collinear probe beam*

In the case the probe is not collinear to the lattice, not only the re-emitted photons contribute to the atomic momentum increase and the transverse part of the absorbed momenta has to be taken into account. The absorbed photons contribution to the momentum increase amounts to, after a time such that in average each atom has absorbed $n_\gamma$ photons from the incoming probe,

$$\mathbf{k}_{\text{abs}} = \varepsilon n_\gamma \mathbf{k}_{ph,\perp} \tag{272}$$

In order to simplify the treatment we assume this momentum growth can be considered deterministic, amounting to neglecting the fluctuations in number of photons absorbed over a given time from atom to atom. The momentum accumulated per atom is then given by equation 254. The probability of the cumulated momentum $i^{th}$ component has to take into account the deterministic contribution given by equation 272 and then reads

$$p(k_i) = \frac{1}{\sqrt{2\pi\sigma^2}} e^{-\frac{\tilde{k_i}^2/k_{ph}^2}{2\sigma^2}} \qquad \text{with} \quad \tilde{k_i} = k_i - \varepsilon n_\gamma k_{ph} \sin(\zeta) \tag{273}$$

As before, this is obtained computing the $I_\perp$ in polar coordinates $(k, \eta)$ with this corrected expression for $p(k_i)$ leading to

$$I_\perp = \frac{1}{2\pi\sigma^2} \int k \, dk \, d\eta \, \exp\left\{ -\frac{k^2 - 2kK_{n_\gamma}(\sin(\eta) + \cos(\eta)) + K_{n_\gamma}^2}{2\sigma^2} \right\} \delta\left(K_\perp^2 - k^2\right) \tag{274}$$

where $K_{n_\gamma} = \varepsilon n_\gamma k_{ph} \sin(\zeta)$. We then have

$$p(E_K) = \frac{1}{2\pi\sigma^2} \; e^{-\frac{E_K/E_r}{2\sigma^2}} \; e^{-\frac{E_{n_\gamma,\perp}/E_r}{2\sigma^2}} \; \Theta(\varepsilon, \zeta, E_K) \tag{275}$$

where $\Theta(\varepsilon, \zeta, E_K)$ accounts for the fact that because of the deterministic momentum "drift" $\varepsilon n_\gamma k_{ph} \sin(\zeta)$, the integral yielding $p(E_K)$ is carried out along a close circle in the transverse momentum space, as before, but not centered at the center of the joint distribution proportional to $p(k_x)p(k_y)$ (see Figure. 44).

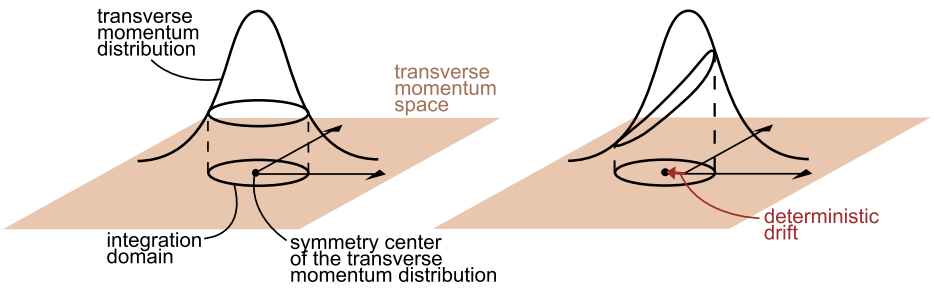


Figure 44: Asymmetry introduced by the deterministic drift resulting from a non-perfectly overlapped detection probe back-reflection.

This asymmetry contribution is given by

$$\Theta(\varepsilon, \zeta, E_K) = \int_0^{2\pi} d\eta \, \exp\left\{ LK_\perp \left( \sin(\eta) + \cos(\eta) \right) \right\} \tag{276}$$

where $L = K_{n_\gamma}/\sigma^2$, the dependency on $E_K$ being encapsulated in $K_\perp = \sqrt{2mE_K/\hbar^2}$. When $LK_\perp$ is small compared to unity, i.e. when the deterministic drift contribution to the accumulated momentum is small compared to that provided by transverse re-emission, the asymmetry correction can be approximated to the second order in $LK_\perp$ as

$$\Theta(\varepsilon,\zeta,E_K) \simeq \int_0^{2\pi} d\eta \left\{1 + LK_\perp\big(\sin(\eta)+\cos(\eta)\big) + \frac{(LK_\perp)^2}{2}\big(\sin(\eta)+\cos(\eta)\big)^2\right\} = 2\pi\left(1+\frac{(LK_\perp)^2}{2}\right) \tag{277}$$

which can be expressed as a function of the energies involved: the total accumulated energy $E_K$ whose distribution we are investigating, the recoil energy $E_r$ and the deterministic drift accumulated energy $E_{n_\gamma,\perp} = K_{n_\gamma}^2\hbar^2/2m$ as

$$\Theta(\varepsilon,\zeta,E_K) \simeq 2\pi\left(1+\frac{1}{2}\frac{E_{n_\gamma,\perp}E_K}{E_r^2(2n_\gamma/3)^2}\right) \tag{278}$$

Finally, the accumulated energy distribution is given by

$$p(E_K) = \frac{e^{-\left(\frac{E_{n_\gamma,\perp}/E_r}{2\sigma^2}\right)}}{\sigma^2}\, e^{-\frac{E_K/E_r}{2\sigma^2}}\left(1+\frac{1}{2}\frac{E_{n_\gamma,\perp}E_K}{E_r^2(2n_\gamma/3)^2}\right) \tag{279}$$

Note that this deterministic drift effect can occur only when operating the fluorescence detection. In such a case, the number of photon scattered per atoms during the detection pulse is so large that most of the collected signal stem from photons scattered by atoms that already have left the trap and for which the Lamb-Dicke condition where only the transverse momentum momentum contribute to heating is not valid, making such departure from the distribution given equation 269 very hard to observe.

**Dipole radiation pattern**

Taking into account that the trapped atoms are polarized by both the lattice and detection probe fields, the radiation, or re-emission, pattern can no longer be considered spherically symmetric. The re-emission is dominated by the effect of the detection probe which is operated at a broad resonance, while the lattice is far detuned, meaning that it can be assumed not inducing any emission, and we therefore consider the atomic dipole as being due to the probe field only. The radiation pattern depends on the probe field polarization that we consider linear in the following. Because the probe is not collinear to the lattice the angle $\eta$ between the probe polarization and the lattice longitudinal axis can assume a wide range of values. For a probe-to-lattice angle $\zeta$, we have $\eta \in [(\pi/2)-\zeta, \pi/2]$. In a coordinate system $(x',y',z')$ with the probe polarization aligned to the $z'$ direction, the dipole radiation probability density reads $p(\theta') = (3/8\pi)\sin^2\theta'$, where the corresponding spherical coordinate system has been labeled $(\theta',\phi')$ (see Figure. 45).

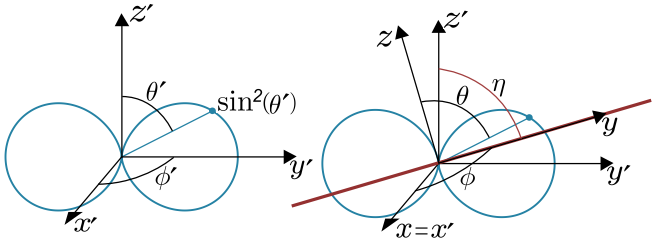


Figure 45: Spherical coordinate representation of the dipole radiation pattern ($z'-x'$ plane slice represented in blue) "tilted" with respect to the lattice direction (red line).

If we choose the $y'$ such that it lays in the plane defined by the probe polarization and the longitudinal axis of the lattice, we can define a system of coordinate $(x,y,z)$ such that $y$ points along the lattice longitudinal direction and such that $x' = x$ (see Figure. 45). It turns out that with such a choice, the $(x,y,z)$ system is obtained from the $(x',y',z')$ system by a rotation around the $x = x'$ axis by an angle, for a probe-to-lattice angle $\eta$, $\alpha = (\pi/2)-\eta$. The corresponding angular coordinate $(\theta,\phi)$ then relate to the primed coordinates via

$$\sin\theta'\cos\phi' = \sin\theta\cos\phi \tag{280}$$

$$\sin\theta'\sin\phi' = \cos\alpha\sin\theta\sin\phi - \sin\alpha\cos\theta \tag{281}$$

$$\cos\theta' = \sin\alpha\sin\theta\sin\phi + \cos\alpha\cos\theta \tag{282}$$

In the un-primed angular coordinates system the radiation pattern then reads

$$p\left(\theta,\phi\right)=\frac{3}{8\pi}\sin^2\left(\arccos\left(\sin\alpha\sin\theta\sin\phi+\cos\alpha\cos\theta\right)\right) \tag{283}$$

In the case of a probe polarization orthogonal to the lattice, i.e. $\eta=\pi/2$ we have $\alpha=0$ and this expression obviously reduces to

$$p\left(\theta,\phi\right)=\frac{3}{8\pi}\sin^2\left(\theta\right) \tag{284}$$

Therefore, for an emission wave vector of size $k_{ph}$ and pointing in direction $(\theta,\phi)$ its transverse components, i.e. that in the $x-z$ plane orthogonal to the lattice direction $y$, reads

$$k_\perp(\theta,\phi)=\sqrt{k_{ph,x}^2+k_{ph,z}^2}=k_{ph}\sqrt{\sin^2\theta\cos^2\phi+\cos^2\theta} \tag{285}$$

from where we can compute the average

$$\langle k_\perp^2\rangle=\int d\Omega\ p(\theta,\phi)k_\perp^2(\theta,\phi)=\frac{3p_{ph}^2}{8\pi}\int d\theta\ d\phi\ \left(\sin^5\theta\cos^2\phi+\sin^3\theta\cos^2\theta\right)=k_{ph}^2\frac{4\pi-2}{10\pi}\simeq\frac{k_{ph}^2}{3} \tag{286}$$

which yields approximately the same result as for the isotropic radiation pattern divided by a factor 2. We indeed expected a reduction since the dipole radiation disfavors emission in the probe polarization direction which is included into the transverse plane containing the contribution to the momentum increase. In order to get the probability distributions of the two transverse components, here in the $x$ and $z$ directions, we split the integral given in equation 286 and get

$$\langle k_x^2\rangle=\frac{2}{5}k_{ph}^2\longrightarrow\sigma_x^2=2n_\gamma\frac{2}{5}k_{ph}^2=\frac{6}{5}\sigma^2 \tag{287}$$

$$\langle k_z^2\rangle=\frac{1}{10\pi}k_{ph}^2\longrightarrow\sigma_z^2=2n_\gamma\frac{1}{10\pi}k_{ph}^2\simeq0.1\times\sigma^2 \tag{288}$$

where $\sigma_x^2$ and $\sigma_z^2$ are the variance of the corresponding normal distribution obtained from the central limit theorem for $n_\gamma(2+\varepsilon)\sim2n_\gamma$ absorbed. The drop by roughly a factor 10 in the variance for the contribution in the probe polarization direction, i.e. in the $z$ axis, is striking whereas a small increase in the $x$ axis contribution can be seen, stemming from the dipole radiation particular profile.

As in the isotropic case, the computation of the heating rate is obtained calculating the probability density of the accumulated kinetic energy. We restrict the study to the perfectly overlap retro-reflected probe, i.e. neglecting any deterministic drift contribution (see equation 273) leading to

$$p\left(E_K=\frac{\hbar^2K_\perp^2}{2m}\right)=\int dk_x\ dk_z\ p(k_x)p(k_z)\ \delta\left(\frac{2mE_K}{\hbar^2}-(k_x^2+k_z^2)\right) \tag{289}$$

where again we consider the integral over the longitudinal direction provides a unit factor[64]. Because the variances in $x$ and $z$ direction differ, the computation is more involving and the distribution is given by

$$p\left(E_K=\frac{\hbar^2K_\perp^2}{2m}\right)=\frac{1}{2\pi\sqrt{\sigma_x^2\sigma_z^2}}\int d\theta\ d\phi\ \sin\theta\ \exp\left\{-K_\perp^2\left(\frac{\sin^2\theta\cos^2\phi}{2\sigma_x^2}+\frac{\cos^2\theta}{2\sigma_z^2}\right)\right\} \tag{290}$$

## 9.3 Conclusion

From an experimental point of view, there only two geometries realized on our setups. For the standard fluorescence detection the probe propagation axis is orthogonal to the trap but not its polarization, i.e. $\eta\neq\pi/2$ and further computations would be required to obtained a workable expression for the distribution $p\left(E_K\right)$. Moreover, when operated with the camera the decay of the trapped atom population in the ground state is not resolved in time and the heating rate by photon scattering is so high that the trap is entirely destroyed at each detection step. For a fluorescence detection achieved with the photomultiplier tube, the trap decay is resolved in time and one could used the above developments to check our level of understanding of the trap destruction mechanisms (but keeping in mind that most of the photons detected are emitted by atoms already falling out the trap). For example, keeping the simplified

[64] In the isotropic treatment, the longitude direction was along the $z$ axis whereas here it coincides with the $y$ axis

isotropic radiation pattern, one could be able to see the decay dependency on the overlapping between the incoming and retro-reflected probe beams as we expect from inserting 279 in 270.

The second geometry is that of the non destructive scheme where the probe is collinear to the trap and thus has its polarization orthogonal to it. As discussed in section 12.4 a fit using 270 combined with 269 give much better results than a simple exponential fit. We could even go further using numerically computed decay obtained using the dipole radiation pattern instead of the isotropic one, i.e. using 290 instead of 269.

# 10 Detection systems characterizations

In this section we characterize the two detection systems based on fluorescence at our disposal: a CCD camera (section 10.1) and a photo-multiplier tube (section 10.2).

## 10.1 The Hamamatsu 9200 C camera

Till recently we used a Hamamatsu 9200 C camera to detect the fluorescence signal emitted by the atoms when shone with a probe (resonant with the $^1S_0 \rightarrow {}^1P_1$ transition at 461 nm) without having a proper calibration in terms of absolute numbers of atoms. Indeed, the useful information for the clock operation is the transition probability $p_e$ (see 9.1) that can be obtained with a relative number of atoms, i.e. based on the number of *counts* detected by the camera. The camera provides a matrix of pixels each assigned a value proportional to the number of photons it collects (see figure 46). The camera *counts* is just the summation over all the pixels of their individual values. The quantity $N$ in equation 242 ca be exchange with any value proportional to $N$, as the number of camera counts $N_c$. However, comparison with our two other detection systems (photomultiplier and on destructive detection) requires evaluating the noise of the detection in terms of absolute number of atoms. It could as well be useful to evaluate the average number of atoms per lattice site in which is determinant for cold collisions process.

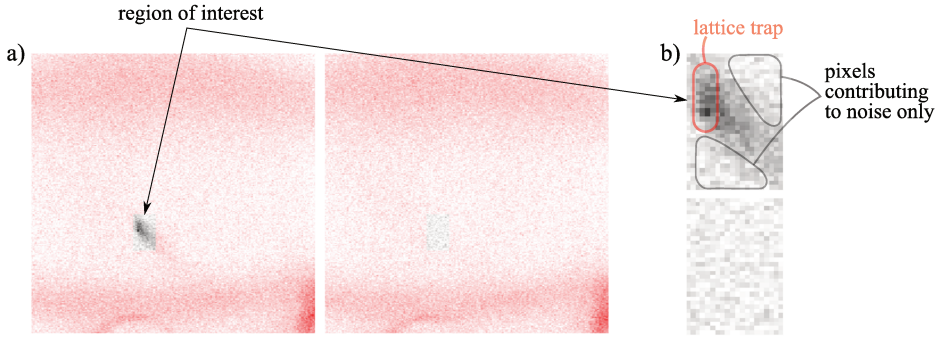


Figure 46: **Camera counts**. The camera provides pictures or pixels matrices. Each pixel is assigned a value proportional to the number of photon it collects over the detection duration. **a)**: Two of the four matrices of pixels provided by the camera at each detection stage (see section 4.4). The higher this number, the darker the pixel. The first picture is taken while the atoms are trapped and the detection probe is on while the second one is taken with probe on only (in order to allow for the differential cancellation of the stray light induced by the environment and the probe). The camera *counts* is then defined as the summation of each pixel's value over the whole matrix. Each pixel introduces some noise, i.e. counts fictitious photons or miss actual photons. In order to minimize this noise, the summation is restricted to pixels within a *region of interest* (of typically $20 \times 40$ pixels), represented on picture **b)**. On this particular shot, it is possible to distinguish the vertically oriented lattice trap (top-left of the top picture). However, because of a mis-overlap of the incoming and the retro-reflected detection probes, a large part of the atoms are blown towards the bottom-right, requiring enlarging the region of interest, and therefore increasing the noise due to pixels contributing to the noise only and not to the signal.

### 10.1.1 Camera counts calibration

In order to calibrate the camera counts in terms of absolute atoms number, we mimic the atomic cloud fluorescence source using a laser beam focused at the location of the cloud, in the absence of atoms in the chamber. This allows for a precise calibration of the number of camera counts as a function of the power collected by the camera, in a geometrical configuration similar to that of an actual fluorescing atomic cloud. Then we compute the fluoresced power within the camera aperture angle as a function of both the number of atoms and the detection probe power. Finally, combining the two results with a saturation parameter calibration, we obtain the atoms number as a function of the number of camera counts.

**1)** *Number of counts as a function of the power collected by the camera.*

A laser beam stemming from the probe light source (i.e. having the same spectral properties) with divergence $\alpha_0 = 0.091$, power $P_\ell = 0.26$ nW and focused at the atomic cloud location is oriented towards the camera, which aperture we call $\alpha$ (see Figure 47 ) giving a number of counts $N_c^\ell \simeq 1.3 \times 10^6$.

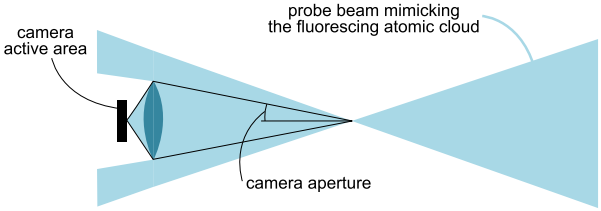


Figure 47: Probe beam mimicking the fluorescing atomic cloud.

Assuming a Gaussian beam profile and considering the camera objective distance to the focus point $z$ is significantly larger than the Rayleigh range $z_R$ the field amplitude in the plane containing the camera objective first lens reads

$$|E(r,z)| = E_0 \frac{z_R}{z} e^{-r^2 z_R^2 / w_0^2 z^2} \tag{291}$$

where $r$ is the coordinate in the radial (i.e. transverse) direction perpendicular to the beam optical axis and $w(z)$ is the beam waist at distance $z$ from the focus. That the beam has divergence $\alpha_0$ means that, since $z \gg z_R$, $w(z) \sim w_0 z / z_R \sim \alpha_0 z$ i.e. $z_R^2 w_0^2 \sim 1/\alpha_0^2$. The power through a surface within the plane transverse to the beam propagation axis at a distance $z$ from the focus defined by an aperture $\alpha$ is equal to the the integral of the field intensity over the surface defined by $(z, 0 \leq r \leq \alpha z, 0 \leq \theta \leq 2\pi)$ in cylindrical coordinates (see Figure. 47), i.e. $P_{\text{col}}^\ell = \int_0^{2\pi} \int_0^{\alpha z} I(z,r) r dr d\theta$ where $I(z,r) \equiv I(z,r,\theta) \propto |E(z,r)|^2$. Hence, the ratio between the collected power within the aperture $\alpha$ of the camera to the total power of the beam is given by

$$\frac{P_{\text{col}}^\ell}{P^\ell} = \frac{\int_0^{2\pi} \int_0^{\alpha z} e^{-2r^2/\alpha^2 z^2} r dr d\theta}{\int_0^{2\pi} \int_0^{\infty} e^{-2r^2/\alpha^2 z^2} r dr d\theta} = 1 - e^{-2(\alpha/\alpha_0)^2} \tag{292}$$

The camera and vacuum chamber optics, the amount of power collected by the camera reads

$$P_{\text{col}}^\ell = \eta P_\ell \left(1 - e^{-2(\alpha/\alpha_0)^2}\right) \tag{293}$$

where $\eta$ accounts for the optical losses and the efficiency of the camera detector. Hence, the ratio $\gamma$ of the number of camera counts $N_c^\ell$ over the collected power $P_{\text{col}}$ reads

$$\gamma = \frac{N_c^\ell}{P_{\text{col}}^\ell} = \frac{N_c^\ell}{\eta P_\ell \left(1 - e^{-2(\alpha/\alpha_0)^2}\right)} \simeq \frac{N_c^\ell}{2\eta P_\ell} \left(1 + \left(\frac{\alpha_0}{\alpha}\right)^2\right) \tag{294}$$

**2)** *Fluoresced power as a function of atoms number and probe power.*

The total power radiated by $N$ atoms for saturation parameter $s$ is

$$P_{\text{at}} = \frac{\Gamma}{2} \frac{hc}{\lambda} \frac{s}{1+s} N \tag{295}$$

$\lambda$ and $\Gamma/(2\pi)$ being the wavelength and spectral width of the considered probed transition. In our geometry the probe polarization is orthogonal to the atom cloud-camera axis. Hence, taking into account the dipole radiation distribution of the fluorescence signal this corresponds, for small solid angles $d\Omega$, to a power

$$\frac{dP}{d\Omega} = \frac{3}{8\pi} P_{\text{at}} \tag{296}$$

Therefore, the corresponding power collected by the camera of aperture $d\Omega = \pi\alpha^2$ is

$$P_{\text{col}} = \frac{3}{8} \alpha^2 \eta P_{\text{at}} \tag{297}$$

Combining this with the camera counts calibration in terms of power we get the number of counts $N_c$ as a function of the number of atoms $N$

$$N_c = \gamma P_{\text{col}} = \frac{N_c^\ell}{P_{\text{col}}^\ell}\frac{3}{8}\alpha^2\eta\frac{\Gamma}{2}\frac{hc}{\lambda}\frac{s}{s+1}N \tag{298}$$

Since the loss factor $\eta$ appears in both the numerator and the denominator via $P_{\text{col}}^\ell$ it cancels out and there is no need for an experimental estimation of it. We then get the counts-to-atoms conversion factor $\beta$ as a function of the saturation parameter

$$\beta = \frac{N}{N_c} = \frac{1}{\gamma}\frac{8}{3\alpha^2}\frac{2}{\Gamma}\frac{\lambda}{hc}\frac{s+1}{s} \tag{299}$$

**3)** *Saturation parameter calibration.*

In practice the detection probe power is stabilized by a power locking system. A portion of the probe beam is sent to a photo diode whose output is compared to a voltage reference. A proportional-integrator feed back circuit then keeps this difference at zero level. Adjusting the voltage reference then allows us to control the probe power. Measuring the amount of fluoresced light by the atoms in camera counts unit as a function of the probe power allows for a direct experimental calibration of the dependency of the saturation parameter $s$. Figure 48 shows the number of camera counts as a function of the detection probe power $P_p$ for a steady state MOT shined by the probe. It is then proportional to $s/s+1$ and allows for a direct estimation of $s(P_p)$.

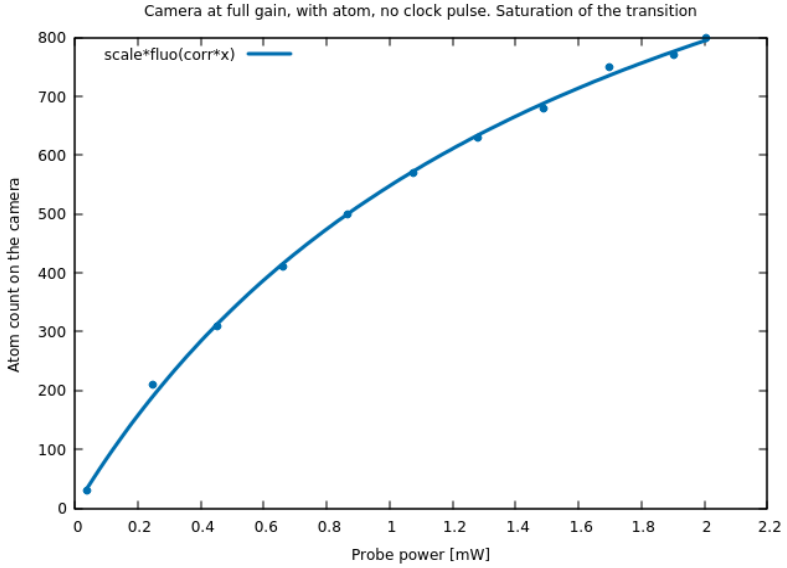


Figure 48: Experimental estimation of the saturation parameter as a function of the detection probe power. The number of counts on the camera is the average number of counts for a MOt in the steady state while shined by the detection probe It scales as $s/1+s$

For a typical probe power of $P = 1.97$ mW, the experimentally calibrated saturation parameter is 1.23, giving a counts-to-atoms conversion factor $\beta \simeq 0.0042$ atom per count.

### 10.1.2 Signal to noise ratio analysis

As explained in section 9.1, the useful signal for the clock laser steering requires two subsequent detections of atoms in internal ground trapped in the lattice, spaced by a few ms. In order to minimize the error in atoms counting due to noise stemming from electron accumulation within the sensor during the MOT loading stage or to stray light and background residual illumination, two extra pictures are added to the detection sequence, ending up in a four pictures series, denoted A,B,C and D. The first picture , A, is taken to flush the electrons accumulated within the sensor active area. The second one, B, detects the

fluorescence of the trapped atoms projected by the probe onto the clock ground state. The third one, C, detects the atoms pumped down from the excited clock state. The last one, D, measures the background, including the probe stray, and is used to remove the corresponding counts from pictures B and C. The transition probability $p$ is then obtained as

$$p = \frac{D - C}{(B - C) + (D - C)} \tag{300}$$

where $B$, $C$ and $D$ represent the integral of the signal of each pixel of pictures $B$, $C$ and $D$ restricted to the region of interest. However, despite this precaution, we are left we residual noise mainly due to electronic noise and dark counts intrinsic to the camera and, to a lesser extent, to background fluctuations[65].

Here we explore the statistics of this residual noise. This analysis is carried out with the camera parameters usually used for the clock operation: exposure = 1.0, binning = 4×4, full frame and with region of interest spanning the pixels defined as $x \in [88, 105]$ and $y \in [140, 168]$.

In order to investigate the camera noise we evaluate the statistics of the number of counts during a large number of slots, each of which lasting typically 30 s[66]. This measurements are performed in various configurations. We explore different values for the gain of camera, and carry out the measurement with and without probe light sent to the chamber as well as with and without atoms trapped in the MOT (the lattice being always kept off). In other words, for each configuration, we get a series of series of data points $x_{i,j}$, $i \in \{1, ..., N\}$, $j \in \{1, ..., M\}$ where the index $i$ stands for the number of the slot measured (with $N$ the total number of slots) for a given configuration and $j$ for the number of the data point ($M$ being the number of data points acquired over a 30 s slots). We then extract the average $X_i = (1/M) \sum_j x_{i,j}$ and the standard deviation $\sigma_i = \sqrt{(1/M) \sum_j \left(x_{i,j}^2 - X_i^2\right)}$.

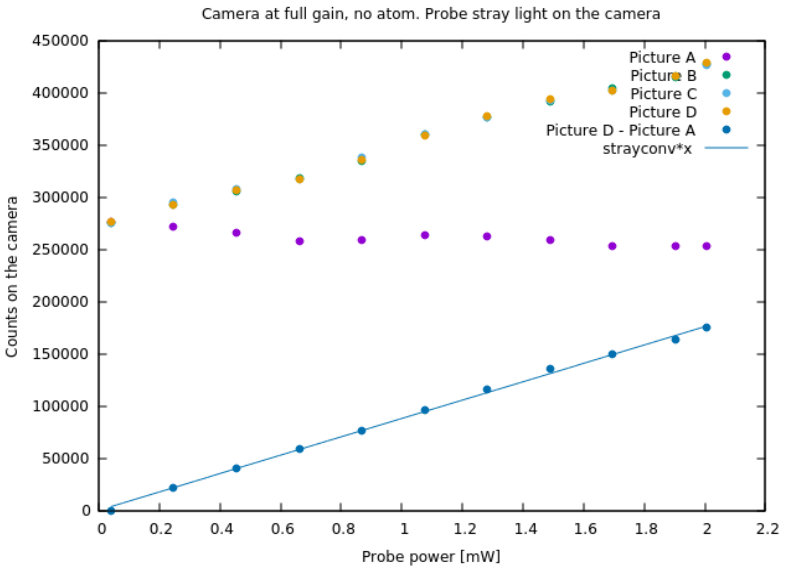


Figure 49: Average camera counts as a function of the probe power.

We explore the dependence of the camera counting statistics varying the gain and the probe power independently[67]. This is the reason all the measurements reported in this paragraph are carried out with camera gain g = 255, while the probe power $P_p$ only is varied. It is apparent on Figure 50 that the average number of camera counts $X_i$ scales linearly with the power, but with a large offset of the same order as the signal itself, which is here even when no light is sent to the camera (we checked carefully that this offset actually does not stem from residual illumination and that it is not due to light impinging onto

[65] As an example, the aliasing of the 50 Hz laboratory illumination light is not addressed by this technique and operating the clock with room lights on severely degrades the atoms counting statistics.

[66] Note that this means that we consider the noise as being ergodic, i.e. with statistics within 30 s slots invariant under time translation

[67] we expect these two dependences to be independent one from an other

the camera). To remove this offset, we then need to make the difference between these different images as expressed in 300. The noise on each of them is then crucial. This is the reason why we investigate the behavior of the $\sigma_i$ as a function of $P_p$, as shown on Figure 50.

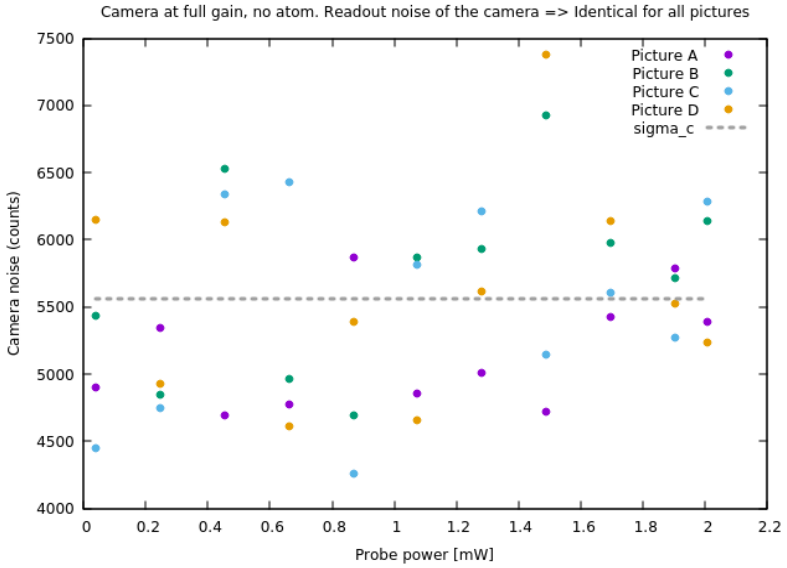


Figure 50: Camera readout noise

It turns out that the noise, as characterized by $\sigma_i$, is independent of the exposure to stray light, as can be seen on Figure 50. More precisely, the averages $\Sigma_{P_p} = (1/N)\sum_i \sigma_i$ of the $\sigma_i$ for different probe powers $P_p$ depart from each other by amounts lower than a few percents. From the counts-to-atoms conversion factor estimated at the beginning of section 10.1, the typical value $\Sigma_{P_p} \sim 5500$ counts corresponds to approximately 23 atoms for a probe power of 1.97 mW.

We now want to explore the camera gain parameter and choose the one maximizing the signal to noise ration (SNR). We then fix the probe power and follow the same protocol as above but his time varying the camera gain within an interval ranging from g = 0 to g = 255. The results are depicted in Figure 51 where it is apparent that the highest SNR$\simeq$ 33 is achieved with maximum gain $g = 255$ but as well that the SNR does not degrade significantly for lower gains (e.g. SNR $\simeq$ 27 for $g \simeq 130$).

### 10.1.3 Detection noise

We now briefly investigate how the noise on each camera picture contribute to the detection noise, i.e. the noise on the probability as obtained from equation 300. Applying the error propagation formula to equation 300 leads, for a probe power $P_p$, to a detection noise of variance

$$\sigma_D^2 = \left(2 - 6p_0 + 6p_0^2\right) \frac{\Sigma_{P_p}^2}{N_c^2} \tag{301}$$

where the total number of counts $N_c$ is given by $N_c = (B - C) + (D - C)$, $p_0$ is the averaged measured probability, and $\Sigma_{P_p}$ the camera noise for the given power and area of interest (see previous paragraph).

### 10.1.4 Applicability to classical non destructive detection.

The camera we use for the standard fluorescence detection probes less than 1% of the total solid angle spanned by the re-emissions. Hence, for a total number of photons $n_\gamma$ scattered per atoms during the detection compatible with keeping the atoms trapped, i.e. $n_\gamma \lesssim 100$ for a trap depth of $200 \times E_{r,813}$, a number of photons close to or even below unity would reach the detector for each atom. This means that even with quantum efficiency equal to one, CNDD is out of reach for this particular configuration.

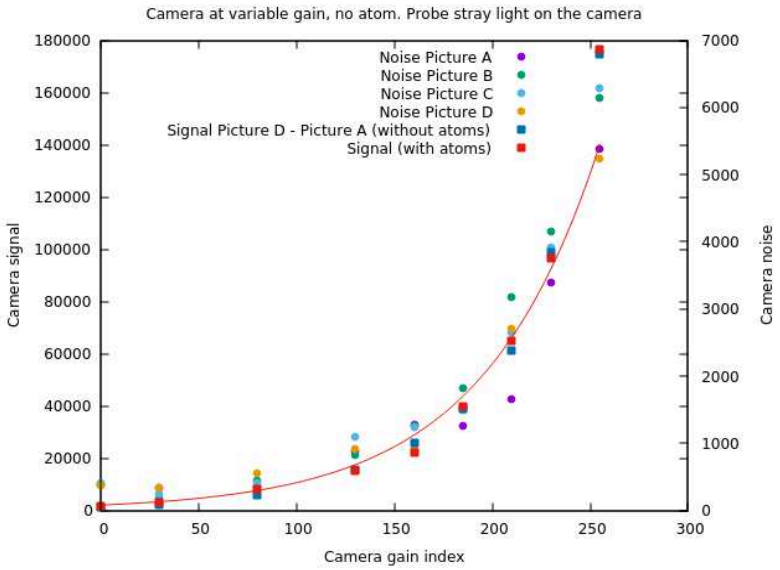


Figure 51: Signal and noise as function of camera gain $g \in [0, 255]$.

## 10.2 Photo multiplier tube

We explored as well the possibility of using a photo multiplier tube (PMT) detector as an alternative to the camera. The main difference is that the camera signal stems from the integration over the detection time while keeping the spatial resolution of the physical signal, whereas the PMT signal stems from the integration over the spatial variables and keeps the time profile of the physical signal. A typical PMT measurement signal is depicted in Figure 52. This particular feature has two direct implications. It offer the possibility to implement a time averaging method based on combining integration and fit techniques allowing for an increased signal to noise ratio (SNR), as discussed in section (10.2.2). It means as well that a PMT might be used, in principle, for the implementation of a non destructive detection, as discussed in section 10.2.1.

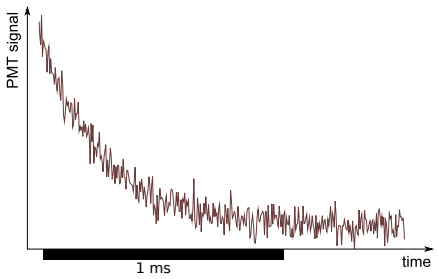


Figure 52: A typical time trace of a PMT detection.

Note that, being based on the time-resolved feature of the signal it provides, the following analysis can be applied to the non destructive detection system presented in section (11).

### 10.2.1 Photo multiplier tube for non destructive detection

In this section we explore theoretically the possibility of using a PMT for non destructive detection techniques. For this study, we assume the PMT noise is not dramatically dominated by its electronic noise and that a photon noise limited detection is possible for the rate of photon scattering considered hereafter. However this assumption is not verified for our particular device, which is by far dominated by its electronic noise.

The preservation of the time profile of the atomic signal allows for the monitoring of the trap destruction, as suggested on Figure. 52, allowing us to resolve the atoms number decay. Whether the PMT can indeed be used as a CNDD system depends on the possibility to carry out the measurement fast enough for the

atoms not to scatter to many photons while keeping the detection and shot noises low enough for the signal to noise ratio (SNR) not to be dramatically degraded. The strategy adopted here is to study the SNR of the detection system varying the detection pulse duration while keeping the average number of photons scattered per atom $n_\gamma$, i.e. the trap destructivity, constant.

In the following we first study how the PMT signal is expected to depend on the probe pulse duration, then investigate the behavior of two noise sources, the electronic PMT noise as well as the photon shot noise.

**Signal**
For a given radiation power $P$ sent to the PMT active area, the average number of photons reaching the detector over a time interval of duration $t$ is

$$\langle N_P(t)\rangle = \frac{Pt}{h\nu} \tag{302}$$

If $\tau_0$ is the raise time of the detector, or equivalently if its detection bandwidth is $\tau_0^{-1}$, the average current it provides would then be given by

$$i(\tau_0) = a\frac{P\tau_0}{h\nu} \tag{303}$$

with $a$ a conversion factor encompassing the the quantum efficiency of the detector. We want to explore the signal to noise ratio of the PMT detection system for a given trap destructivity, i.e. for a fixed number $n_\gamma$ of photons scattered per atom during the detection, as a function of the probe pulse duration $t$. This means that the power collected by the PMT has to scale accordingly. Moreover, one needs to include a geometrical factor accounting for the fact that the PMT detects only the photons scattered by the atoms within its aperture $\pi\alpha^2$. The first lens of the PMT objective being set at roughly 15 cm from the position of the atom cloud and having a diameter of 2.5 cm, we have $\alpha^2 \sim 0.007$ i.e. $\pi\alpha^2 \ll 4\pi$. Assuming the probe polarization is orthogonal to the PMT orientation, i.e. that the orientation of the PMT corresponds to that where the dipolar radiation pattern is maximal and equal to $3/(8\pi)$, this geometrical factor is $3\alpha^2/8$. In the end, the collected power reads

$$P(n_\gamma, t) = \frac{3\alpha^2}{8}\frac{n_\gamma h\nu}{t} \tag{304}$$

corresponding to an average PMT output current

$$i(\tau_0, t) = an_\gamma\frac{3\alpha^2}{8}\frac{\tau_0}{t} = a\tau_0\frac{P(n_\gamma, t)}{h\nu} \tag{305}$$

which is our detection signal. We now want to explore how the corresponding noise depends on the pulse duration $t$. To do so we consider only two sources of noise: the PMT intrinsic electronic noise (stemming from thermal noise in resistor and dark counts mainly) and the photon shot noise.

**Electronic noise**
For the electronic noise we consider a white noise with amplitude $\sigma_{e,0}$ within a bandwidth of $\tau_0^{-1}$. Hence, when integrated over the probe pulse of duration $t$ it reduces to

$$\sigma_e(t) = \sqrt{\frac{\tau_0}{t}}\sigma_{e,0} \tag{306}$$

**Photon shot noise**
In a standard picture, the photon shot noise is dealt with in the same way as the electronic noise as briefly exposed above. But since we are scaling the radiated power according to 304, the standard view needs to be modified. Indeed, the white spectral properties of the shot noise commands a scaling as $t^{-1/2}$, as for the electronic noise, but we know from quantum optics it has to scale as the square root of the collected power. We then express it as

$$\sigma_p(t) = b\sqrt{\frac{P}{th\nu}} = \frac{b}{t}\sqrt{\langle N_P(t)\rangle} \tag{307}$$

with $b$ a scaling factor. Since we know how to describe the photon noise for coherent light fields, we would like to link the photon noise of the radiation collected by the PMT to that of the coherent probe field. In order to do so, we view the scattering and the geometric filtering by the device aperture as an effective

loss process of photons. Indeed, for a probe power $P_p$, the number of photons scattered per atoms within a time interval of duration $t$ is

$$n_\gamma = \frac{t\Gamma}{2}\frac{AP}{1+AP} \qquad \text{where } A = \frac{\Gamma^2}{4P_{\text{sat}}\Delta^2} \tag{308}$$

with $P_{\text{sat}}$ the saturation power (for the given geometry), $P$ the optical power and $\Gamma$ the natural width of the probed transition. Hence, for a given number of photons $n_\gamma$ scattered per atom over the whole detection process of duration $t$, the probe power needs to be set to

$$P_p(n_\gamma, t) = \frac{1}{A}\frac{1}{(\Gamma t/2n_\gamma) - 1} \tag{309}$$

Hence, only a fraction $\eta = P(n_\gamma, t)/P_p(n_\gamma, t)$ of the probe power sent to the atoms reaches the PMT active area, with

$$\eta(n_\gamma, t) = \frac{3\Gamma}{16}\alpha^2 h\nu A\left(\frac{2n_\gamma}{\Gamma t} - 1\right) \tag{310}$$

As developed in section 12.3.3, this loss process induce a degradation of the SNR that can be accounted for by adding the corresponding partition noise which in this case simply consists in rescaling the expression given in equation 307 by a factor $\sqrt{\eta}$, leading to

$$\sigma_p(t) = \frac{b}{t}\sqrt{\eta(t)\langle N_{P_p}(t)\rangle} \tag{311}$$

where we dropped out the dependency in $n_\gamma$ to lighten the notations. We note that from equation 302

$$\eta(t)\langle N_{P_p}(t)\rangle = \frac{P(t)}{P_p(t)}\frac{P_p(t)t}{h\nu} = \frac{t}{a\tau_0}i(t) = \frac{P(t)t}{h\nu} = \frac{3\alpha^2}{8}n_\gamma = \langle N_P\rangle \tag{312}$$

where we emphasize that $\langle N_P\rangle \equiv \langle N_P(t)\rangle$ does not depend on the detection duration $t$ since $\langle N_P\rangle$ is precisely the quantity we keep unchanged through our investigation.

**Signal to noise ratio**

Assuming the electronic and the photon noise are independent, the total noise is then given by

$$\sigma(t) = \sqrt{\sigma_e^2(t) + \sigma_p^2(t)} = \sqrt{\frac{\tau_0}{t}\sigma_{e,0}^2 + \frac{b^2}{t^2}\langle N_P\rangle} \tag{313}$$

leading to

$$\text{SNR} = \frac{(a/t)\langle N_P\rangle}{\sqrt{(\tau_0/t)\sigma_{e,0}^2 + (b^2/t^2)\langle N_P\rangle}} \tag{314}$$

Thus, when the probe pulse is short enough for the noise to be dominated by the photon shot noise, the SNR can be approximated by the more simple form

$$\text{SNR} \simeq \frac{a}{b}\sqrt{\langle N_P\rangle} = \frac{a}{b}\sqrt{\frac{3\alpha^2 n_\gamma}{8}} \tag{315}$$

which does not depend on the detection duration. Note that estimating the rise time $\tau_0$ of the detector allows for a direct measurement of the conversion factor $a$ using 303 and of $\sigma_{e,0}$ as well via 306 and that for a detector with accessible photon noise limited regime, the factor $b$ can be measured using 307.

**Applicability to classical non destructive detection**

As said at the beginning of this section, for a typical trap depth $U_0 \sim 200E_{r,813}$, each atom should scatter less than 100 photons for the trap to be preserved. This means that the number of photon collected by the PMT for each atom is of the order of

$$\langle N_P\rangle = \frac{3\alpha^2}{8}n_\gamma \lesssim 0.3 \tag{316}$$

which is unrealizable, even with a unitary quantum efficiency.

### 10.2.2 Counting atoms with the PMT

The previous development focused on the expected behavior of the PMT SNR in the perspective of the possibility of using it for classical non destructive detection, based on the assumption that the detector could be operated in a photon noise limited configuration. However, real measurements show that the electronic noise of the detector is by far dominant over the photon noise for realistic detection duration. Indeed, the noise of all time traces such that depicted in Figure. 52 is independent on the signal amplitude, i.e. is the same at the beginning and at the end of the fluorescence signal decay, meaning it does not depend on the amount of fluoresced photons detected. In this section, we discuss a strategy to get, based on the PMT signal, a detection with a better SNR than that obtained with the CCD camera.

As mentioned in the introduction of section 10.2, this strategy is based on the combination of integration and fit techniques. The first idea was to save the time trace $s(t)$, compute its integral and relate it to the corresponding number of atoms via a calibration factor. The problem of this approach is that one has to choose the time duration over which is carried the integral. Let say the time trace starts at $t_0$ and lasts till $t_1$. Then one would compute

$$X_s = \int_{t_0}^{t} s(t')\ dt' \tag{317}$$

with $t \leq t_1$. To make sure the whole decay profile is integrated, one has to make sure that $t - t_0$ is significantly larger than the decay time $\tau$. But if the integral is carried out for $t$ too large, the part of the signal stemming from the fluorescence is zero and the only contribution to the integral is the electronic noise component of the signal. Hence, the choice of the upper bound of the integral is crucial for optimizing the SNR of the detection.

Our strategy to cope with this problem is as follows. We first take a large number $N_t$ of traces $s_i(t)$, $i = 1, .., N_t$, such the one depicted in Figure 52. We then consider each of them as being the sum of the effective atomic signal (i.e corresponding to the counting of the fluoresced photons reaching the PMT) $u_i(t)$ and the electric noise $e_i(t)$. Note that this decomposition is theoretical while the only measurable is $s_i(t)$. We sum all this traces and obtain

$$S(t) = \sum_{i=1}^{N_t} s_i(t) = \left(\sum_{i=1}^{N_t} u_i(t)\right) + \left(\sum_{i=1}^{N_t} e_i(t)\right) = U(t) + E(t) \tag{318}$$

The $u_i(t)$ components are supposed to be very close to each other, with small variations corresponding to fluctuations in the number of atoms trapped in the lattice. Hence, $U(t)$ scales as $N_t$. On the other hand, the electronic noise of each trace are independent from each other meaning $E(t)$ scales as $\sqrt{N_t}$. The SNR of the summed signal $S(t)$ then scales as $\sqrt{N_t}$. We then compute numerically the integral $X_S$ of $S$ over a time interval significantly larger than the decay time $\tau$

$$X_S = \int_{t_0}^{t} S(t')\ dt' \tag{319}$$

and use it to get a normalized decay profile $\tilde{S}(t)$

$$\tilde{S}(t) = \frac{S(t)}{X_S} \tag{320}$$

Note that quantities as $X_s$ and $X_S$ play the same role as the number of counts $N_c$ for the camera, and one can thus work out a conversion factor $a_X$ from *unit area under the curve*[68] to number of atoms $N_{at}$, as is done in section 10.1.1 for the camera. This conversion factor is typically expressed in atom per $V.s$. Normalizing this conversion factor by $X_S$, we end up with a conversion factor $a_{\tilde{S}}$ assigning a number of atoms to the normalized profile $\tilde{S}(t)$ (thus expressed in umber of atoms directly).

Once this conversion factor has been computed, the normalized profile $\tilde{S}(t)$ is used to fit the traces measured during the clock operation, with a scaling factor $A_{\text{sc}}$ as unique free parameter. The number of atoms $N_{\text{at}}$ is then obtained as

$$N_{\text{at}} = A_{\text{sc}} \times a_{\tilde{S}} \tag{321}$$

[68] for PMT signals measured in Volts, the unit of *area under the curve* is typically V.s

# 11 Cavity assisted classical non destructive detection (CNDD)

As the standard fluorescence detection, the classical non destructive measurement (CNDD) belongs to the class of projective measurements. Each atom, in the state $\alpha|g\rangle + \beta|e\rangle$ is projected onto $|g\rangle$ with probability $|\alpha|^2$ or onto $|e\rangle$ with probability $|\beta|^2$. Here as well, the quantum state is *destroyed* but if one manages to get sufficient information out of the system to estimate the probability amplitudes $|\alpha|^2$, $|\beta|^2$ with a number of scattered photons $n_\gamma$ sufficiently low, all or most of the probed atoms remain in the trap and the trap is not destroyed, justifying the the *non destructive* qualification. From section 9.2.4 we know that the average energy gain per atom in the CNDD configuration, which is achieved with the probe collinear to the lattice, can roughly be estimated, for an average of $n_\gamma$ photons scattered per atom over the detection pulse, as

$$\langle E \rangle = \frac{n_\gamma}{m} \frac{\hbar^2 k_{ph}^2}{3} \tag{322}$$

For the atoms to be kept in the trap, the average number of photons scattered should be such that

$$\langle E \rangle \lesssim U_0 \tag{323}$$

where $U_0$ is the trap depth. Hence the $n_\gamma$ should not exceed the generous upper bound

$$\frac{3m}{\hbar^2 k_{ph}^2} U_0 = \frac{3}{2} \frac{U_0}{E_{r,461}} \tag{324}$$

$E_{r,\lambda}$ being the energy recoil for a photon of wavelength $\lambda$ expressed in nm. Since we have $E_{r,813}/E_{r,461} \simeq 0.32$, this means that, for a trap depth $U_0 = 200 \times E_{r,813}$, $n_\gamma$ should not exceed 100. In this section we explore a new detection system such that a sufficient amount of information about the atoms internal states can be obtained from such a low number of scattered photons.

The structure of this chapter is as follows. Section 11.1 introduces the basic idea underpinning the cavity-assisted non-destructive detection system: the collinear transport of the information about the atomic population as a phase imprinted by the atoms onto a cavity mode field. It also gives an extensive derivation of the expression of this phase shift, since it is a key ingredient for the understanding of the system working principle as well as for the interpretation of the measured signals. The expressions for this measured signals are derived in section 11.2.

## 11.1 Phase imprint: collinear transport of information

### 11.1.1 Limitation of camera and PMT for CNDD

It appears clearly that the impossibility to achieve CNDD with the camera or the PMT is mainly due to a too low number of photons to be collected due to the fact that only a fraction $3\alpha^2/8$ (amounting, for our particular geometries, to about $X\%$ for the camera, 0.7% for the PMT) of the photons scattered are seen by the detectors which can not be compensated by increasing the total number of scattered photons which has to be kept lower than typically 100 photons per atom. Thus, in order to keep the number of detected photons above unity and sufficiently higher than the corresponding noise floor of the chosen detector, while keeping the total number of photons scattered lower than the destruction threshold, an other configuration is needed where none of the information about the atomic states is wasted into unprobed direction of space. This is the reason we moved to our cavity assisted CDNN scheme, where a *collinear transport* of the information is achieved.

Instead of collecting the scattered photons them-selves, one could measure the phase shift imprinted by the atoms onto the probe field. In a semi-classical picture, where the internal atomic degrees of freedom only are quantized, the field being classical, the phase imprint onto the field induced by its interaction with the atoms does not depend on the re-emission direction, and the information can be thought of as propagating collinearly with the probe field and not spread in all directions of space.

### 11.1.2 Phase imprinted by the atoms on the probe field

In the semi-classical picture the linear part of polarization density $\mathbf{P}$ induced in a medium by the propagation of a field $\mathbf{E} = \mathbf{E}^+ + \mathbf{E}^-$ (with $\mathbf{E}^\pm = E_0 e^{\pm i(\omega t - k_0 z)}$, $k_0$ the vacuum wavenumber) reads

$$\mathbf{P} = \rho \left( \alpha \mathbf{E}^+ + \alpha^* \mathbf{E}^- \right) \tag{325}$$

with $\alpha$ the polarizability of the medium given by

$$\alpha = \frac{d^2}{\hbar}\frac{\Delta + i\Gamma/2}{(\Gamma/2)^2 + \Omega_1^2 + \Delta^2} \tag{326}$$

The resulting classical field is a superposition of the incoming one and that stemming from the polarization of the medium, or that of the atom cloud, and reads $\mathbf{E}(z,t) = \mathbf{E}_0(e^{i(\omega t - kz)} + c.c.)$ with $k = n(\omega)k_0$, where

$$n(\omega) = \sqrt{1 + \frac{\alpha(\omega)\rho}{\varepsilon_0}} \sim 1 + \frac{\alpha(\omega)\rho}{2\varepsilon_0} \tag{327}$$

The imaginary part of $n(\omega)$ accounts for the damping of the field amplitude due to absorption within the atomic cloud and can be dropped out for the study of the phase imprint. The change in $k$ induced by the presence of the atoms then reads

$$\Delta k = k - k_0 \sim k_0\frac{\alpha(\omega)\rho}{2\varepsilon_0} \qquad \alpha(\omega) = \frac{d^2}{h}\frac{\Delta}{(\Gamma/2)^2 + \Omega_1^2 + \Delta^2} \tag{328}$$

Using $k_0 = 2\pi/\lambda$ and

$$\Gamma = \frac{8\pi^2 d^2}{3\varepsilon_0 \lambda^3 \hbar} \tag{329}$$

the corresponding phase shift acquired through a cloud of length $l$ and uniform atomic density $\rho$ is

$$\phi_{at} = l\Delta k \sim \ l\rho\lambda^2 \ \frac{3}{2}\frac{1}{4\pi}\frac{(\Gamma/2)\Delta}{(\Gamma/2)^2 + \Omega_1^2 + \Delta^2} \tag{330}$$

that can be equivalently expressed as

$$\phi_{at} = l\rho \ \delta\phi_t = \frac{N_a l}{V}\delta\phi_t \qquad \delta\phi_t = \lambda^2\frac{3}{2}\frac{1}{4\pi}\frac{(\Gamma/2)\Delta}{(\Gamma/2)^2 + \Omega_1^2/2 + \Delta^2} \tag{331}$$

Assuming a Gaussian transverse distributions for both atomic density and light intensity profile at the atomic cloud input

$$\rho_\perp(r) = \rho_0 e^{\frac{-r^2}{2r_0^2}}, \qquad E_\perp(r, z=0) = E_{\perp,0}e^{\frac{-r^2}{w_0^2}} \tag{332}$$

we end up with a field profile at the cloud output, i.e. after passing through the atomic assembly, expressed as

$$E_\perp(r, z=l) = E_{\perp,0}e^{\frac{-r^2}{w_0^2}}e^{i(k_0 l + \Delta\phi(r))} \tag{333}$$

where $\Delta\phi(r)$ is defined as $\phi_{\text{at}}$ in 330 but with $\rho_\perp(r)$ instead of $\rho$ and taking into account the radial dependency of $\Omega_1 \equiv \Omega_1(r)$ defined by the transverse *detuned* saturation parameter

$$s(r,\Delta) = I(r)/I_{sat}(\Delta) = \frac{\Omega_1^2(r)}{\Delta^2 + \Gamma^2/4} \tag{334}$$

Note that 333 is valid assuming the cloud is located at the waist of the probe and has length $l \lesssim z_R$, $z_R$ the Reyleigh range of the probe. In this case the equiphase surfaces in the cloud region of space coincide with transverse planes and the free field phase depends on the longitudinal coordinate $z$ only and not on the radial one $r$. with $\rho_0$ defined from the total number of atoms in the cloud $N_a$ as

$$N_a = \int_0^\infty \rho(r)2\pi l r dr = 2\pi r_0^2 l\rho_0 \tag{335}$$

one gets (see [105])

$$\phi_{at} = \delta\phi_t\frac{N_a}{S}, \qquad S = 2\pi\left(r_0^2 + (w_0/2)^2\right) \tag{336}$$

This means that even though the phase imprinted by the atoms onto the probe field does depend on the radial coordinate $r$, the overall phase shift can be expressed as resulting from a uniform contribution normalized by the cross section factor $S$. The phase shift imprinted per atom onto the probe can then be expressed as

$$\phi_{at} = N_a\phi_{at,0}\frac{\Delta(\Gamma/2)}{\Delta^2 + \Omega_1^2/2 + (\Gamma/2)^2} = N_a\phi_{at,0}\frac{\Delta(\Gamma/2)}{\Delta^2 + (\Gamma/2)^2}\frac{1}{1+s(\Delta)} \tag{337}$$

Using the standard saturation parameter

$$s = \frac{I}{I_{\text{sat}}} = \frac{2\Omega_1^2}{\Gamma^2} \tag{338}$$

we get the alternative expression (used in [144])

$$\phi_{at} = N_a \phi_{at,0} \frac{2}{\Gamma} \left( \frac{\Delta}{1 + 4\Delta^2/\Gamma^2 + s} \right) \tag{339}$$

which behaves as $1/\Delta$ for large detunings and low saturation.

Note that since the ${}^1S_0 - {}^1P_1$ natural width does not resolve the Zeeman structure of the involved levels, one should actully compute for $\phi_a t$ a summation of terms of the same form but spanning each possible transition $|F, m_F\rangle \to |F', m'_F\rangle$. This was done in [105]. The resulting profile depends on the polarization of the ground state (i.e. in which $m_F$ state there are prepared). The global shape is left unchanged for atoms prepared in $m_f = +9/2$ needs to be rescaled and its the zero crossing is shifted by approximately $0.15 \times \Gamma$.
f

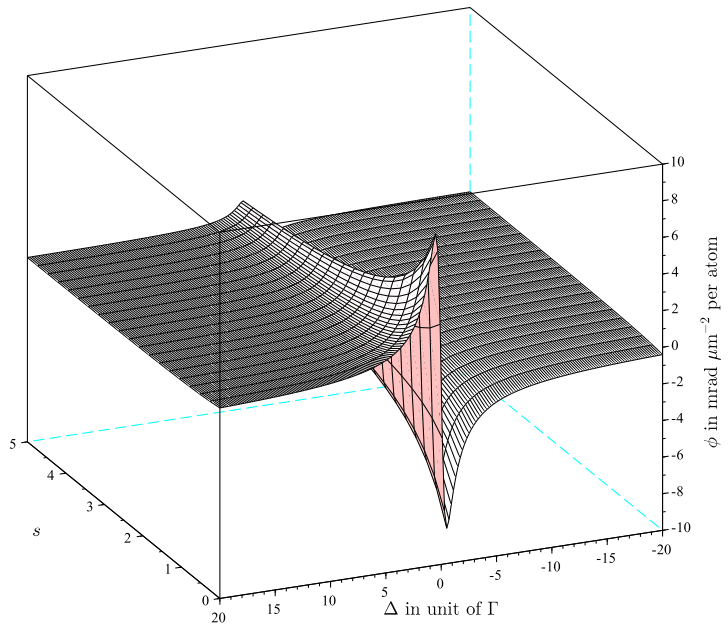


Figure 53: Dependence on the atom imprinted shift $\phi_{at}(s, \Delta)$ as given by formula 337 as a function of the saturation parameter $s(\Delta)$ as expressed in 334 and the detuning $\Delta$ here expressed in unit of $\Gamma = 2\pi\delta\nu$ with $\delta = 32$ MHz the ${}^1S_0 - {}^1P_1$ transition natural width.

The phase mediated measurement of the ground state atomic population was demonstrated in [109] inserting the atomic cloud in one arm of a Mach-Zender interferometer. However, in order to achieve sufficient SNR while keeping the atoms trapped, i.e. having a descent signal while having less than $\sim 100$ photons scattered par atoms over the detection pulse this scheme was not adequate. In order to amplify the sensitivity to phase shift induced by the presence of the atoms came up with the idea of immersing the system into a high probe resonant finesse cavity.

It turned out this was achievable with our vacuum setup since the lattice cavity, which is located inside the science chamber, has a finesse $F \sim 16000$ for the 461 nm probe selected for the CNDD.

## 11.2 CNDD algebra

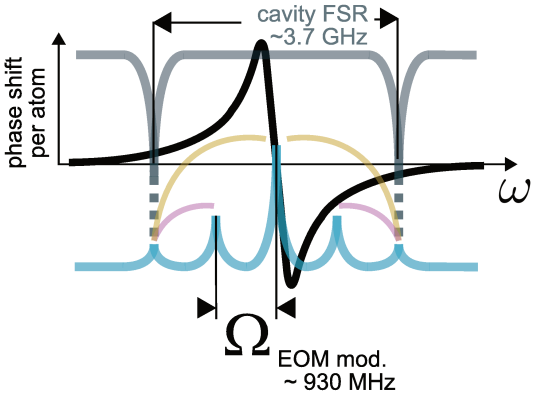


Figure 54: The cavity resonances, separated by one free spectral range $\delta_{\mathrm{FSR}} \approx 3.7$ GHz are represented upside down by the gray line. The probe carrier is set half way between two consecutive cavity resonances, and the EOM generated sidebands are separated by the EOM modulation frequency $\Omega \approx 930$ MHz, in such a way that the second order sidebands only are coupled to the cavity (blue line). The atomic response, or phase shift imprinted per atom onto the cavity coupled probe fields, is depicted by the black line It is anti-symmetric cantered at the probe carrier frequency.

The working principle of this cavity enhanced scheme is as follows (see Figures 54 and 55). The probe, resonant with the broad 32 MHz wide ${}^1S_0 \rightarrow {}^1P_1$ transition, is sent through an EOM modulated at $\Omega = \mathrm{FSR}/4$ with a depth $\beta$, $\mathrm{FSR} \simeq 3.8$ GHz being the free spectral range of the lattice cavity. The lattice cavity length is adjusted in such a way it is resonant with both the magic lattice light at 813 nm and the $\pm 2^{nd}$ order side bands (SBs) generated on the probe. Then nor the probe carrier nor the $\pm 1^{st}$ order SBs are coupled to the cavity and only the $\pm 2^{nd}$ order SBs, symmetrically detuned from the transition by $\Delta = \pm \mathrm{FSR}/2$, are entering the cavity and are seen by the atoms. Because of the anti-symmetry of the dispersive response of the atom as a function of detuning (see Figure 54), the shift induced on those two SBs have equal amplitudes but opposite signs

$$\phi_{at}(-\Delta) = -\phi_{at}(\Delta) \tag{340}$$

On the other hand, as is shown further in this section, the phase shift due to traveling through the cavity is the same for both of them

$$\phi_{\mathrm{cav}}(-\Delta) = \phi_{\mathrm{cav}}(\Delta) \tag{341}$$

This opposite symmetry for the two phase acquisition phenomena, that stemming from traveling through the cavity, the other imprinted by the atoms, is a key feature for our system. We discuss in the following how, collecting the beating of all the SBs coming back from the cavity makes possible to get a signal dependent on the atomic phase shift only (demodulating the beatnote at $2 \times \Omega$) and an other one sensitive to the cavity-to-$2^{\mathrm{nd}}$ order sideband detuning only (demodulating the beatnote at $1 \times \Omega$), allowing for their simultaneous lock to the cavity and atoms population read-out.
In the next sections we discuss in details how are produced the locking and atomic signals and provide a full derivation of their mathematical expressions.

### 11.2.1 Generation of the probe sidebands and cavity-atoms response.

Throughout this section we use the complex representation of oscillating electric fields. The linearly polarized probe field at the electro-optic modulator (EOM) input (see Figure 55) reads

$$\mathbf{E}(z = 0, t) = \mathbf{E}_0 e^{-i\omega t} \tag{342}$$

where $\mathbf{E}_0$ is a complex components vector collinear to the EOM strong modulation crystal axis. The modulation of the index of refraction of the crystal in this axis induces a modulation of the propagating field wave number of the form

$$k(t) = k_0(1 + a\sin(\Omega t)) \tag{343}$$

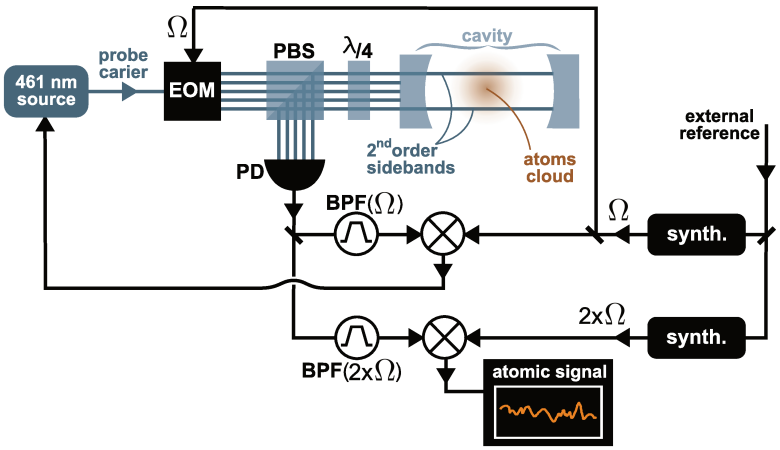


Figure 55: Simplified schematic of the non destructive detection setup. An external reference at 10 MHz feeds two synthesizers, one providing a signal at $\Omega$ the other at $2\Omega$. The $\Omega$ signal is partially sent to an EOM producing up to the $2^{nd}$ order sidebands (SB) on a probe carrier at 461 nm, resonant with a the broad ${}^1S_0 \rightarrow {}^1P_1$ transition, where $\omega$ equal to a forth of the cavity free spectral range is such that the $\pm 2^{nd}$ order SBs only are coupled to the cavity and are seen by the atoms. A polarizing beam splitter (PBS) combined to a $\lambda/4$ wave plate then drives the four SBs reflected from the cavity to a fast photodiode (PD) where they beat. The PD signal is then split into two parts. The first one is filtered around $\Omega$ (using a band pass filter (BPF)) and mixed down with an $\Omega$ local oscillator (LO) stemming from the first synthesizer and provides a probe-to-cavity locking signal fed back to the probe source. The second one, filtered around $2\Omega$, is mixed down with the $2\Omega$ LO and provides the atomic signal.

Assuming the length $l$ of the crystal is such that $l/(n_0 c) \ll 1/\Omega$, where $n_0$ is the average crystal index of refraction, $c$ the speed of light in vacuum and $\Omega$ the crystal index modulation frequency, i.e. that the modulated index of the crystal can be considered constant over the time it takes for the light to travel through it, the field at the EOM output reads

$$\mathbf{E}(l,t) = \mathbf{E}_0 e^{i(k(t)l-\omega t)} = \mathbf{E}_0 e^{i(k_0 l-\omega t)} \sum_{n=-\infty}^{\infty} J_n e^{in\Omega t} \tag{344}$$

where the $J_n \equiv J_n(\beta)$ are the Bessel coefficient for a modulation depth $\beta = lk_0 a$. The superposed probes fields (carrier and SBs) are then sent to the cavity from where they are reflected with respective coefficients $F_n = F(\omega + n\Omega)$

$$F_n = \frac{r(1-e^{2i\Phi_n})}{1-r^2 e^{2i\Phi_n}} \tag{345}$$

where $\Phi$ encompasses the shift acquired by the probe field along half a round trip in the cavity

$$\Phi_n = k_n L + \phi_{at,n} \tag{346}$$

$L$ the length of the cavity, $k_n = (\omega + n\Omega)/c$ and $\phi_{at,n}$ the atom phase shift imprinted onto the field component oscillating at $\omega + n\Omega$ and given by 337. From this stage of the propagation till the detector, the distance traveled by the beam (carrier plus SBs) is, say, $l'$. Then, at the detector, the field reads

$$\mathbf{E}(t, l+l') = \mathbf{E}_0 e^{i(k_0 l-\omega t)} \sum_{n=-\infty}^{\infty} J_n F_n e^{in\Omega t} e^{i(n\Omega/c)l'} \tag{347}$$

The corresponding intensity $I = |\mathbf{E}(t)|^2$ is collected on a fast photodiode, which can be expressed as

$$I = |\mathbf{E}_0|^2 \sum_p \sum_q J_p J_q F_p F_q^* e^{i(p-q)\Omega t} e^{i(p-q)(\Omega/c)l'} \tag{348}$$

that we can split into $\Omega$ harmonics components as $I = \sum_q I_{q\Omega}$ with

$$I_{q\Omega} = |\mathbf{E}|^2 \left( \sum_p J_p J_{p-q} F_p F^*_{p-q} e^{q\Omega t} e^{iq(\Omega/c)l'} + \sum_p J_p J_{p+q} F_p F^*_{p+q} e^{-iq\Omega t} e^{-iq(\Omega/c)l'} \right) \tag{349}$$

The $p$ index runs from $-\infty$ to $+\infty$ and relabelling $p$ as $p-q$ in the second sum we see that

$$\sum_p J_p J_{p+q} F_p F^*_{p+q} = \left( \sum_p J_p J_{p-q} F_p F^*_{p-q} \right)^* \tag{350}$$

and $I_{q\Omega}$ reads

$$I_{q\Omega} = |\mathbf{E}|^2 \left( e^{iq\Omega t} e^{iq(\Omega/c)l'} \sum_p J_p J_{p-q} F_p F^*_{p-q} + c.c. \right) \tag{351}$$

This signal is then mixed down with two local oscillators (LOs) $A_1 \sin\left(\Omega t + \tilde{\phi}_1\right)$ and $A_2 \sin\left(2\Omega t + \tilde{\phi}_2\right)$, with $\tilde{\phi}_n = \phi_n + n(\Omega/c)l'$, $\phi_n$ being let undetermined for the moment. This gives the two signals $S_{1\Omega}(\phi_1)$ and $S_{2\Omega}(\phi_2)$ expressed as

$$\begin{aligned}
S_{1\Omega}(\phi_1) &= |\mathbf{E}|^2 A_1 \frac{1}{2i} \left( e^{i(\Omega t + \tilde{\phi}_1)} - c.c. \right) && (352)\\
&\quad \times \left( e^{i\Omega t} e^{i(\Omega/c)l'} \sum_p J_p J_{p-1} F_p F^*_{p-1} + c.c. \right) && (353)\\
&= |\mathbf{E}|^2 A_1 \frac{1}{2i} \left( \sum_p J_p J_{p-1} F^*_p F_{p-1} e^{+i\phi_1} - c.c. \right) && (354)\\
&= |\mathbf{E}|^2 A_1 \frac{1}{2i} \Bigg[ \cos(\phi_1) \left( \sum_p J_p J_{p-1} F^*_p F_{p-1} - c.c. \right) && (355)\\
&\quad + i \sin(\phi_1) \left( \sum_p J_p J_{p-1} F^*_p F_{p-1} + c.c. \right) \Bigg] && (356)\\
&= |\mathbf{E}|^2 A_1 \Bigg[ \cos(\phi_1) \sum_p J_p J_{p-1} \mathrm{Im}\left( F^*_p F_{p-1} \right) && (357)\\
&\quad + \sin(\phi_1) \sum_p J_p J_{p-1} \mathrm{Re}\left( F^*_p F_{p-1} \right) \Bigg] && (358)
\end{aligned}$$

where we dropped out the terms oscillating at $2\Omega$ and kept the DC terms only, and

$$\begin{aligned}
S_{2\Omega}(\phi_2) &= |\mathbf{E}|^2 A_2 \Bigg[ \cos(\phi_2) \sum_p J_p J_{p-2} \mathrm{Im}\left( F^*_p F_{p-2} \right) && (359)\\
&\quad + \sin(\phi_2) \sum_p J_p J_{p-2} \mathrm{Re}\left( F^*_p F_{p-2} \right) \Bigg] && (360)
\end{aligned}$$

In order to minimize the destructivity of the detection system, the power seen by the atoms, i.e. that scales as $J_2^2$, must be kept sufficiently low. For this reason, we explore values of the modulation depth $\beta$ such that $|J_k J_l|$ can be neglected for $\sqrt{k^2+l^2} > 3$. Moreover, the useful signal we want to keep from $S_{1\Omega}(\phi_1)$ is the $\cos(\phi_1)$ term, which provides a PDH-like signal for the lock of the probe to the cavity as is discussed further (see section 11.2.4), meaning the demodulation phase is set such that $\phi_1 = 0$ rad. Noting that $J_{-p} = (-1)^p J_p$ and that each term $J_p J_{p-1} \mathrm{Im}(F^*_p F_{p-1})$ has its counterpart

$$J_{1-p} J_{-p} \mathrm{Im}(F^*_{1-p} F_{-p}) = -J_p J_{p-1} \mathrm{Im}(F^*_{1-p} F_{-p}) \tag{361}$$

appearing in the summation, $S_{1\Omega}$ (where we dropped out the dependency on $\phi_1 = 0$) simplifies to

$$\begin{aligned}
S_{1\Omega} &= |\mathbf{E}|^2 A_1 \Big[ J_2 J_1 \mathrm{Im}\left( F^*_2 F_1 - F^*_{-1} F_{-2} \right) && (362)\\
&\quad + J_1 J_0 \mathrm{Im}\left( F^*_1 F_0 - F^*_0 F_{-1} \right) \Big] && (363)
\end{aligned}$$

The same occurs for $S_{2\Omega}$ whose useful quadrature containing the atomic induced shift is obtained for $\phi_2 = 0$ as well (see section ), but without the sign flip

$$J_{2-p}J_{-p}\mathrm{Im}(F_{2-p}^* F_{-p}) = +J_p J_{p-2}\mathrm{Im}(F_{2-p}^* F_{-p}) \tag{364}$$

leading to[69]

$$S_{2\Omega} = |\mathbf{E}|^2 A_1 \Big[ J_2 J_0 \mathrm{Im}\left(F_0^* F_{-2} + F_2^* F_0\right) \tag{365}$$

$$+ J_1 J_{-1} \mathrm{Im}\left(F_1^* F_{-1}\right) \Big] \tag{366}$$

### 11.2.2 Half round trip phase shift

In order to go further in the analysis one needs being able to compute, or at least estimate, the phase factors $F_k$. This requires a detailed knowledge of the half round trip phase shift $\Phi$ accumulated by the field traveling through the cavity and interacting with the atoms which we derive in this section.

The probe carrier being set half way between two cavity resonances, we have

$$\frac{\omega_0}{2\pi} = \left(n + \frac{1}{2}\right)\frac{c}{2L_0}, \quad \text{with } n \text{ integer} \tag{367}$$

with $\omega_0$ the average probe carrier frequency and $L_0$ the average cavity length. The two $2^{nd}$ order SBs being simultaneously resonant with the cavity and separated by exactly one FSR, their frequencies $\omega_0 \pm 2\Omega_0$, $\Omega_0$ the average EOM feeding frequency, verify

$$\frac{\omega_0 \pm 2\Omega_0}{2\pi} = \left(n + \frac{1}{2} \pm \frac{1}{2}\right)\frac{c}{2L_0} \tag{368}$$

and therefore

$$\frac{\Omega_0}{2\pi} = \frac{1}{4}\frac{c}{2L_0} \tag{369}$$

The one way phase shift of the $k^{th}$ SB in the cavity then reads

$$\phi_k = \frac{1}{c}\left(\omega_0 + k\Omega_0\right)L_0 + \phi_k^{at} \tag{370}$$

Taking into account the possible fluctuations of these parameters, we consider $L = L_0 + \delta L$, $\omega = \omega_0 + \delta\omega$ and $\Omega = \Omega_0 + \delta\Omega$, leading to

$$\phi_k = \frac{1}{c}\left(\omega + k\Omega\right)L + \phi_k^{at} = \frac{1}{c}\left(\omega_0 + \delta_\omega + k\Omega_0 + k\delta_\omega\right)\left(L_0 + \delta L\right) + \phi_k^{at} \tag{371}$$

which gives to the first order in fluctuations

$$\phi_k \sim \frac{(\omega_0 + k\Omega_0)L_0}{c} + \frac{\omega_0 L_0}{c}\left(\frac{\delta\omega}{\omega_0} + \frac{\delta L}{L_0}\right) \tag{372}$$

$$+ \frac{k\Omega_0 L_0}{c}\left(\frac{\delta\Omega}{\Omega_0} + \frac{\delta L}{L_0}\right) + \phi_k^{at} \tag{373}$$

$$= \pi\left(n + \frac{1}{2} + \frac{k}{4}\right) + \pi\left(n + \frac{1}{2}\right)\varepsilon_\omega + \pi\frac{k}{4}\varepsilon_\Omega + \phi_k^{at} \tag{374}$$

with $\varepsilon_x = \left(\frac{\delta x}{x_0} + \frac{\delta L}{L_0}\right)$.

[69] where we note that not term in $J_{-1}J_1$ appears in the summation 359

### 11.2.3 Cavity response

From equation 345, the cavity response $F_k(\phi)$ is close to unity except when the one way phase shift is close to an integer multiple of $\pi$ and admits the first order expansion

$$F_k(\phi) \sim -i\sqrt{F}\phi \ [\pi] \qquad \text{for } \phi \sim 0 \ [\pi] \tag{375}$$

$$F_k(\phi) \sim 1 \qquad \text{otherwise} \tag{376}$$

Thus, since $\phi_0 \sim (n+1/2)\pi$, $\phi_{\pm 1} \sim (n+(1/2)\pm 1/4)\pi$ and $\phi_{\pm 2} \sim (n+1/2\pm 1/2)\pi = 0 \ [\pi]$ we have

$$F_{0,\pm 1} \sim 1 \tag{377}$$

$$F_{\pm 2} \sim -i\sqrt{F}\left(\pi\left(n+\frac{1}{2}\right)\varepsilon_\omega \pm \pi\frac{1}{2}\varepsilon_\Omega + \phi^{at}_{\pm 2}\right) \tag{378}$$

### 11.2.4 PDH-like error signal

The cos quadrature of the $S_{1\Omega}$ signal stemming from the down mixing of the beating signal at frequency $\Omega$ is, see equation 362, a combination of $F_1F_0^* - F_0F_1^*$ and $F_2F_1^* - F_{-1}F_{-2}^*$. From equation 377

$$F_1F_0^* - F_0F_1^* = 0 \tag{379}$$

$$F_2F_1^* - F_{-1}F_{-2}^* = F_2 + F_{-2} = -i\sqrt{F}\left((2n+1)\pi\varepsilon_\omega + \phi^{at}_{+2} + \phi^{at}_{-2}\right) = -i\sqrt{F}(2n+1)\pi\varepsilon_\omega \tag{380}$$

where we used the antisymmetry of the dispersive atomic response $\phi_{at}(-\Delta) = -\phi_{at}(\Delta)$, i.e. $\phi^{at}_{-2} = \phi^{at}(-2\Omega) = -\phi^{at}(+2\Omega) = \phi^{at}_{+2}$. Finally

$$S_{1\Omega}(\phi_1) = -|\mathbf{E}|^2 A_1 J_1 J_2 \pi\sqrt{F}(2n+1)\varepsilon_\omega \tag{381}$$

Hence $S_{1\Omega} \propto \varepsilon_\omega$ and is insensitive to the presence of the atoms and thus can be used as an error signal for a feedback loop acting on the probe carrier frequency $\omega$ to keep $(\omega \pm 2\Omega)L/c = 0 \ [\pi]$ for small variations $\delta L$ of the cavity length $L$ and small variations of the probe carrier frequency $\omega$, i.e. to keep $\varepsilon_\omega \simeq 0$.

### 11.2.5 Atomic signal

Here again, considering $F_{\pm 1} \sim 1$, the $J_1J_{-1}$ term of $S_{2\Omega}$ cancels out and we are left we a term proportional to

$$\mathrm{Im}(F_2F_0^* + F_0F_{-2}^*) = \mathrm{Im}(F_2 + F_{-2}^*) = \mathrm{Im}(F_2 - F_{-2}) = -2\sqrt{F}\left(\pi\varepsilon_\Omega + \phi^{at}_{+2}\right) \tag{382}$$

The full expression of $S_{2\Omega}$ reads

$$S_{2\Omega} = -2|\mathbf{E}|^2 A_2 J_0 J_2 \sqrt{F}\left(\pi\varepsilon_\Omega + \phi^{at}_{+2}\right) \tag{383}$$

Whether $S_{2\Omega}$ can be used as a "good" atomic signal signal depends on the relative size of the two components of the signal: $\varepsilon_\Omega$ and $\phi^{at}_{+2}$. In section 11.1.2 we estimated the phase imprinted by one atom to the probe field to typically a few hundreds of nrad. The typical size of $\varepsilon_\Omega$ is discussed in section 12.3.1 where it is shown that, for our experimental parameters, the noise induced by fluctuations in cavity length and EOM modulation frequency is at least one order of magnitude lower than the signal of a single atom.

### 11.2.6 Atom-probe coupling homogeneity

In this section we discuss the fact that, because the atoms are trapped in the lattice and therefore are located around the center of each lattice site, and that the relation between the sidebands standing-waves periodicity and that of the lattice are commensurate but as the ratio of two large numbers (see section 12.1.3), some atoms might be probed by different fields and this give different contributions to the phase shift measured. This is the problem of atom-probe coupling inhomogeneity.

We express the effect of the cavity and the atoms on each sideband field, labeled $k$, via the cavity reflectivity coefficients $F_k$ given in equation 345 in which appear the atom imprinted phase shifts $\phi^{at}_k$, which are derived in section 11.1.2 based on a development found in [105]. This development had been carried out for a single frequency probe. One of the first step of the treatment was to compute the

polarization $\mathcal{P}(t)$ induced by the probe on the atomic cloud, i.e. to compute the polarizability $\alpha(\omega)$, the computation of which was based on finding the steady state solutions of the Von Neuman equation

$$\frac{d\hat{\rho}}{dt} = -\frac{i}{\hbar}\left[\hat{H}, \hat{\rho}\right] \tag{384}$$

where the interaction component of the Hamiltonian is given by

$$\hat{H}_{\text{int}} = -\mathbf{d}\cdot\mathbf{E} + \Gamma \tag{385}$$

where $\Gamma$ is non hermitian and accounts for the spontaneous decay from excited to ground state. An important point to solve the steady state solution for $\hat{\rho}$ is that the electric field $\mathbf{E}$ rotates at only one frequency $\omega$, i.e. $\mathbf{E} = \mathbf{E}_0(\mathbf{r})e^{i(\omega t - \mathbf{k}\cdot\mathbf{r})} + c.c.$, where $\mathbf{E}_0(\mathbf{r})$ is the complex field amplitude vector, whose size depends on the location $\mathbf{r}$. This is critical for the treatment since the solution for $\hat{\rho}$ is obtained in the rotating frame, i.e. replacing the component $\rho_{eg}$ by $\tilde{\rho}_{eg} = \rho_{eg}e^{i\omega t}$, which finally leads to the expression $\alpha(\omega)$ as expressed in 326. In our case two probes (both the 2$^{\text{nd}}$ order side bands created by the EOM induced phase modulation of the carrier) are sent to the atoms which then experience a field

$$\mathbf{E} = \left(\mathbf{E}_{+2}(\mathbf{r})e^{i(\omega_{+2}t - \mathbf{k}\cdot\mathbf{r})} + c.c.\right) + \left(\mathbf{E}_{-2}(\mathbf{r})e^{i(\omega_{-2}t - \mathbf{k}\cdot\mathbf{r})} + c.c.\right) \tag{386}$$

containing the two optical frequencies $\omega_{\pm 2} = \omega \pm 2\Omega$, from where it is no longer possible to define a rotating frame *canceling* the time dependence of the field. A complete treatment would provide a polarizability $\alpha(\mathbf{E}_{+2}, \omega_{+2}, \mathbf{E}_{-2}\omega_{-2})$ that would depend on the position $\mathbf{r}$ via its dependence to $\mathbf{E}_{\pm 2}$. This tough problem was addressed by B. R. Mollow in [110] back in 1972 where he derived a solution in the case where one of the two fields has its amplitude much smaller than the other, i.e. making a perturbative treatment of the problem. The problem can be addressed within the frame of the *quantum regression theorem* [111] whose handling requires dedicated skills and is far beyond the frame of this thesis.

However, in the case where the excited state is only weakly populated (i.e. for low detuned saturation parameter, such that spontaneous decay happen much faster than pumping the ground state into the excited one), the dynamics is linear and the effect of each probe sideband coupled to the cavity can be considered individually and then summed up. Hence, each of the two probes oscillating at $\pm\omega_{\pm 2}$ is phase shifted by the effect induced by the polarizability $\alpha(\omega_{\pm 2})$, and the two resulting polarization field are added

$$\mathcal{P}(\mathbf{E}_{+2}, \omega_{+2}, \mathbf{E}_{-2}\omega_{-2}) \approx \mathcal{P}(\mathbf{E}_{+2}\omega_{+2}) + \mathcal{P}(\mathbf{E}_{-2}\omega_{-2}) = \alpha(\omega_{-2})\mathbf{E}_{+2} + \alpha(\omega_{-2})\mathbf{E}_{-2} \tag{387}$$

In other words, the shift on the probe at $\omega_{+2}$ is obtained from $\phi_{at}(\omega_{+2})$, itself obtained from $\alpha(\omega_{+2})$, the same being considered for the probe at $\omega_{-2}$, simultaneously. This approach consists then in considering that the atoms polarizability is $\alpha(\omega_{+2})$ and $\alpha(\omega_{-2})$ at the same time, which of course is valid only in the weakly excited state population regime.

To check that all the atoms contribute equally to the phase shift, i.e. that the contribution does not depend on the position along the cavity axis, we check that the sum of the field amplitude can be considered constant over the region of the trap where the atoms are located. Consider, for the sake of simplicity, the case of an empty plane mirror Fabry-Perrot cavity injected by a linearly polarized plane wave field

$$E(z,t) = E_0(e^{i(kz-\omega t)} + c.c.) \tag{388}$$

Assuming a reflectivity $r$ for the mirrors, the field at location $z_0$ reads

$$E(z_0,t) = E_0\left(e^{-i\omega t}\left[e^{ikz_0}\sum_n r^{2n}e^{2inkL} + e^{ik(2L-z_0)}\sum_n r^{2n}e^{2inkL}\right] + c.c.\right) \tag{389}$$

where the first term of the square bracket accounts for the components of the intra-cavity field arriving in $z_0$ in the sens of increasing $z$, the second one for those arriving backward. This equation simplifies to

$$E(z_0,t) = E_0\left(e^{-i\omega t}\left(e^{-ikz_0} + e^{ik(2L-z_0)}\right)\frac{1}{1-r^2e^{2ikL}} + c.c.\right) \tag{390}$$

Coming back to our two probes, they are both resonant with the cavity and are separated by one free spectral range $\Delta_{\text{FSR}} = c/(2L)$. Hence, their frequencies and wave numbers read

$$k_{+2} = 2\pi\,(n+1)\,\frac{1}{2L}, \qquad k_{-2} = 2\pi n\frac{1}{2L} \tag{391}$$

for some integer $n$. Around the middle point of the cavity, i.e. at $z_0 = L/2 + \delta\ell$, we then have, assuming $n = 2p$ is odd

$$k_{-2} z_0 = \pi p \left(1 + \frac{2\delta\ell}{L}\right) \tag{392}$$

$$k_{-2}(2L - z_0) = \pi p \left(3 - \frac{2\delta\ell}{L}\right) \tag{393}$$

leading to

$$e^{ik_{-2}z_0} + e^{ik_{-2}(2L-z_0)} = e^{ip\pi} 2\cos\left(2p\pi\frac{\delta\ell}{L}\right) \tag{394}$$

For the other probe sideband, we have

$$k_{+2} z_0 = \pi p \left(1 + \frac{2\delta\ell}{L}\right) + \pi\left(\frac{1}{2} + \frac{\delta\ell}{L}\right) \tag{395}$$

$$k_{-2}(2L - z_0) = \pi p \left(3 - \frac{2\delta\ell}{L}\right) + \pi\left(\frac{3}{2} - \frac{\delta\ell}{L}\right) \tag{396}$$

and therefore

$$e^{ik_{+2}z_0} + e^{ik_{+2}(2L-z_0)} = -e^{ip\pi} 2\sin\left((1+2p)\pi\frac{\delta\ell}{L}\right) \tag{397}$$

The total field at $z_0 = L/2 + \delta\ell$ then reads, assuming an equal amplitude for the two probes sidebands at the cavity input,

$$E(L/2 + \delta\ell, t) = E_0 \frac{2}{1 - r^2}\left(\cos\left(2p\pi\frac{\delta\ell}{L}\right)\cos(\omega_{-2}t) + \sin\left((1+2p)\pi\frac{\delta\ell}{L}\right)\cos(\omega_{+2}t)\right) \tag{398}$$

The cavity length is around 4 cm and the two probes have wavelengths close to 461 nm, thus, $2p = n \simeq 10^5$, thus $1 + p \sim p$, meaning that, close to the cavity middle point, the two fields are in quadrature over a sufficient large range for the . On each of this oscillating field $\mathbf{E}_{\pm\mathbf{2}}$ the atoms, at a given location along the cavity axis $L + \delta\ell$, will imprint a phase shift $\phi_{\pm 2}$ of opposite sign (because of the antisymmetry of the atomic response as a function of the detuning $\Delta$) and scaling proportionally to the field intensity, i.e, $\phi_{\pm 2} = \pm\alpha(\Delta)|E_{\pm 2}|^2$ (fro low saturation parameter, see equation 337). Since the signal measured $S_{2\Omega}$ is proportional to the difference between the phase shift imprinted on each sideband, each atom located at position $z$ along the cavity axis contributes to the signal as

$$\chi(z) = \alpha(\Delta)\left(|E_{+2}(z)|^2 + |E_{-2}(z)|^2\right) \tag{399}$$

which is plot on Figure 56 over a range spanning about 100 lattice sites centered at the cavity middle-point (i.e. at half cavity length along the cavity axis). Over this range the total variations of $\chi(z)$ are lower than 0.5%, meaning that all the atoms, what ever being their locations $z$, contributes the same way to the total signal. In other words, the probe-to-atom coupling can be considered homogeneous.

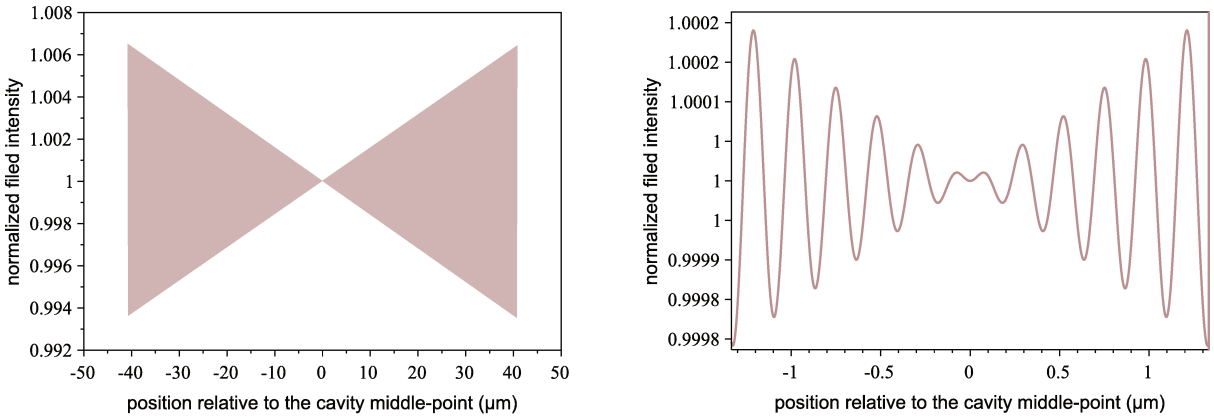


Figure 56: *left)*: envelop of the sum of the two sidebands fields intensities profiles normalized by $|2E_0/(1-r^2)|^2$, i.e. $|\cos\left(2p\pi\frac{\delta\ell}{L}\right)|^2 + |\sin\left((1+2p)\pi\frac{\delta\ell}{L}\right)|^2$. *Right)*: Zoom in the left picture around the cavity middle-point to check their is no aliasing problem in the left side plot: the intensities sum profile modulations are perfectly resolved at the expected 461/2 nm scale.

# 12 CNDD implementation

We now move to the description of the implementation of the non-destructive detection system discussed in its theoretical aspect in the previous chapter. The experimental setup is presented in section 12.1. The adjustment protocols of the main experimental parameters are discussed in section 12.2. Section 12.3 is dedicated to the investigation of the noises of the systems and the resulting expected signal-to-noise-ratios. Finally, our main results are presented in section 12.4.

## 12.1 Setup

We represent on Figure 57 only the sub-system of the whole experiment involved in the non destructive detection implementation. Each component of the setup is described in some details in the following sub-sections.

### 12.1.1 The in-vacuum cavity stabilization

The in vacuum cavity is kept resonant to the lattice light stemming from a Titanium-Sapphire laser. To do so, its length is tuned via a PZT actuator which driving voltage is obtained from a PDH lock scheme (see [30]). The residual fluctuations of the cavity length allowed by the lock are discussed in section 12.3.1. The Titanium-Sapphire light is frequency stabilized on a transfer cavity, itself referenced to a atomic spectroscopy signal.

The geometry of the system is such that the rigidity of the in-vacuum cavity allows for a variety of mechanical modes to be naturally excited. Indeed, the mechanical connection between the two cavity mirrors is a sequence of mechanical links, junctions and contacts with a complex topology (see gray components on Figure 58) allowing for certain acoustic modes to be excited by environmental acoustic noise sources. Some of those modes induce longitudinal deformation of the cavity. Most of them have their frequencies within the locking bandwidth, which is limited by the bandwidth of the PZT coupled to the whole mechanical system marked by a resonance that was measured to be at approximately 22 kHz. However, natural vibrations mode at 20 kHz are visible on the open loop response of the system (see Figure 59). As a result, when the gain of the feedback is sufficiently high for the vibration modes within the lock bandwidth to be compensated, the effective gain at the mode at 20 kHz is far too large due to the proximity of the PZT resonance at 22 kHz, resulting in strong over-oscillations. The solution we found was then to set a lowpass filter on the error signal driving the PZT correction. This way, we could keep the gain for lower frequencies sufficiently high while drastically reducing it for frequencies approaching the resonance at 22 kHz and thus prevented over oscillations from occurring.

Beside the fact that lattice amplitude fluctuations resulting from an imperfect cavity-to-lattice lock could reduce the lifetime of the atoms (when oscillations occur at multiple or integer fractions of atoms harmonic oscillations in the trap potential sites), it could have limited the possibility of locking the probe sidebands used for the non destructive detection. This is discussed further in this section[70]

### 12.1.2 The probe light

The probe light is picked up from a light line stemming from a doubling cavity providing a 461 nm light beam from an amplified 922 nm extended cavity laser diode source. A part of the 461 nm light is sent to an saturated absorption spectroscopy setup which signal is used to tune the PZT of the 922 nm extended cavity diode laser. A large amount of the 461 nm light is devoted to the MOT cooling and to the Zeeman slower used to load the trap[71].

The non destructive probe light is picked up from this MOT-Zeeman arm. It is first rooted through a double pass acousto-optic modulator (AOM) that is used in the probe SB-to-cavity lock. It then passes through an electro-optic modulator (EOM) modulated at

$$\Omega = \Delta_{\mathrm{FSR}}/4 \sim 937 \text{ MHz} \tag{400}$$

with depth $\beta \sim 0.2-0.3$ (see hereafter for values adjustment details) that produces the required sidebands (SB), as explained in section 11.2. It is then coupled to a polarization maintaining fiber and sent to the

[70] see **The probe sidebands lock to the cavity** paragraph.
[71] a part of this light is as well sent to the spectroscopy stage, and to the fluorescence detection system

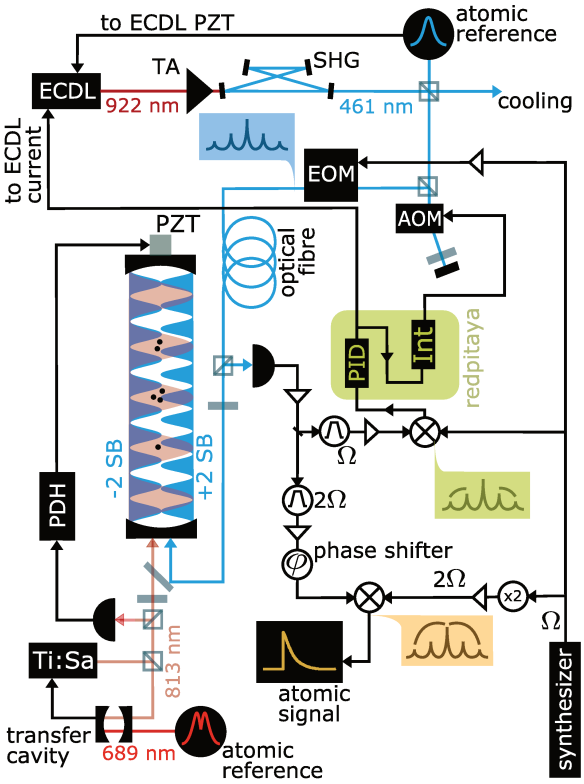


Figure 57: Here is a very schematic view of the sub-system involved in the implementation of the non destructive detection. The extended cavity diode laser (ECDL on the picture) provides around 20 mW of 922 nm light that is amplified in an optical tapered amplifier (TA) to 450 mW feeding a frequency doubling cavity (SHG) providing with 150 mW of 461 nm light (blue line). This light is dispatched to the Zeeman slower, MOT (cooling), spectroscopy and detection systems. The blue spectroscopy (atomic reference) is used to keep the 461 nm light referenced to the ${}^1S_0 - {}^1P_1$ atomic transition. This is achieved generating a correction feeding the Piezzo (PZT) actuator tuning the ECDL cavity length. A portion of the 461 nm light is picked up and sent towards the non destructive detection system. It passes twice through an acousto-optic modulator (AOM) used to tune the frequency of the probe carrier, then through an electro-optic modulator (EOM) producing the first and second order probe sidebands ($\pm 2$ SB). It is then routed through a polarization maintaining fiber (optical fiber) to the cavity stage. Their it runs back and forth to and from the cavity through an optical setup described further in this section. The beatnote of all the probe sidebands is detected by a fast photodiode which signal is amplified and then split into two arms. One arm is dedicated to the generation of the PDH-like correction signal used to lock the probe second order sidebands to the cavity, using a Redpitaya FPGA platform. The other one is dedicated to the generation of the atomic signal. The signals used to modulate the EOM and down mix the two photodiode signals for the generation of the useful signals stem from a common source as explained further in the section.

vacuum cavity stage. In order to make sure the requirement 400 is fulfilled, we scan the length of the cavity by scanning the voltage supplying one of its two PZT actuator. The observed cavity throughput signal typically looks like that depicted in Figure 60, *a)*. We then change the EOM modulation frequency $\Omega$ till having the $+2^{nd}$ and $-2^{nd}$ order SBs of two consecutive carriers merging. When this happens, the corresponding throughput signal doubles in amplitude: the two merged SBs add up one to another (see Figure 60 *b)* and Figure 61).

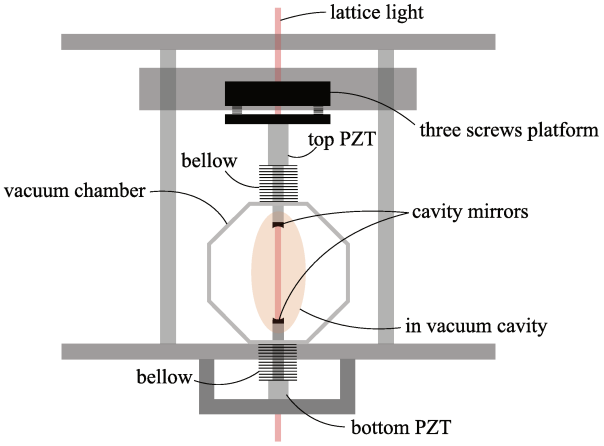


Figure 58: This schematic view of the in-vacuum cavity system make visible the potential lack of rigidity of the cavity due to the complex geometry and topology of its structure. The two mirrors cavity are linked via a set of mechanical connection, links and junctions (all parts represented in black and gray) allowing for a large variety of mechanical modes to be excited, resulting in cavity geometry instabilities.

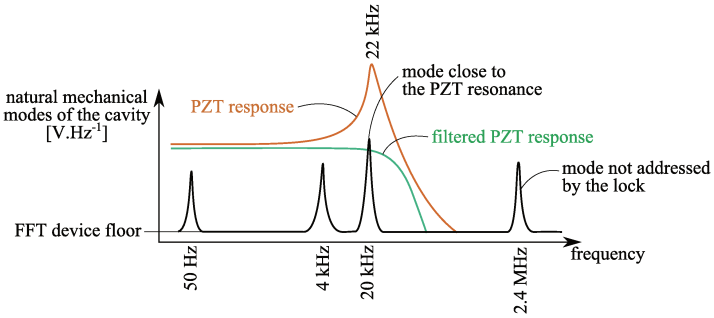


Figure 59: Here is a schematic plot of the FFT of the un-locked cavity throughput signal. The main resonance are displayed (see black line). The 50 Hz resonance stems from the associated electronics system, but some others at 4 kHz and 20 kHz stem from mechanical deformation of the system due to lack of rigidity of the mechanical system (see Figure 58). The response of the PZT exhibits a resonance at 22 kHz, setting the limit to the lock bandwidth. When the feedback gain is sufficient, the oscillations at 50 Hz and 4 kHz are compensated by the lock system but, on the other hand, the fluctuations at 22 kHz are enhanced because of the proximity of the PZT response resonance at 22 kHz (orange line). Setting a first order lowpass filter with cutoff frequency just below 20 kHz resulted in an effective gain strongly reduced around the PZT resonance and removed the over-oscillations. The 2.4 MHz fluctuations are not addressed by the PZT lock. They probably stem from a slight over-oscillation of the lattice lock to the transfer cavity or from the lattice power lock.

### 12.1.3 Tri-chromatic cavity

The atoms are trapped in the 1D vertical lattice at the magic wavelength $\lambda_m \sim 813$ nm consisting in a standing wave built-up in an in-vacuum cavity of length $L \sim 4$ cm and mirrors curvature of 25 mm giving a waist of 50 $\mu$m at $\lambda_m$ , for which the finesse is $\mathcal{F} \sim 160$. For the 461 nm probe light, the waist is $w_0 = 38$ $\mu$m for a finesse of approximately $\mathcal{F} \sim 1.6 \times 10^4$. Note that the cavity has to be resonant with three different wavelengths: the lattice magic wavelength $\lambda_m \simeq 813$ nm and the two probe sidebands $\lambda_{\pm 2} \simeq 461$ nm. This requires the length $L$ of the cavity to be an integer multiple of the three wavelength

$$L = n_m \frac{\lambda_m}{2} = n_{-2} \frac{\lambda_{-2}}{2} = n_{+2} \frac{\lambda_{+2}}{2} \tag{401}$$

Note that once the EOM modulation frequency $\Omega$ as been tuned as described in the previous paragraph and that the two probe sidebands are merged (see Figure 60), the second equality is directly verified as soon as the first one is. Thus, the tri-chromaticity problem reduces to a bi-chromaticity problem. The

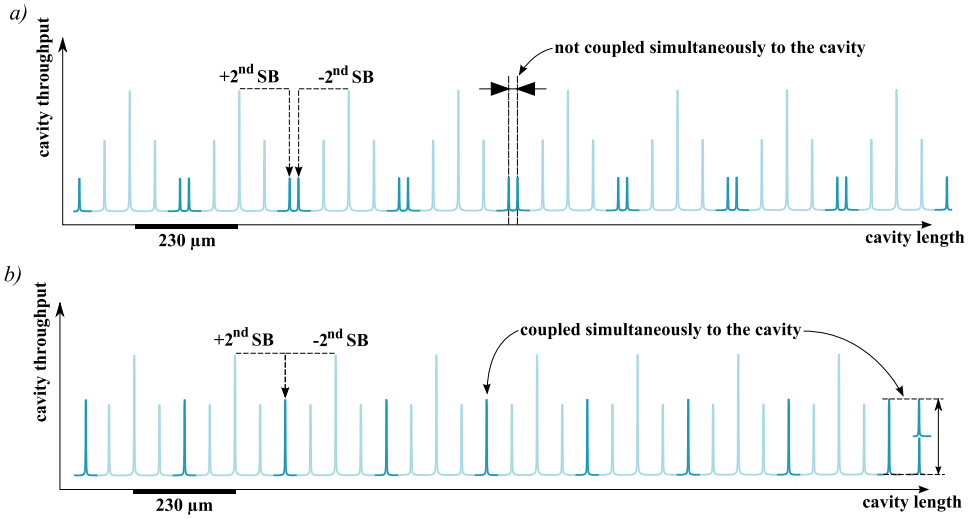


Figure 60: Cavity throughput as a function of the cavity length modulated by a triangular shape signal. Two successive resonances of the carrier (highest pick for low EOM modulation depth) are separated by $\lambda/2 \approx 230$ nm. *a)* shows a configuration where the EOM modulation frequency $\Omega$ is slightly lower than a forth of the cavity free spectral range. *b)* shows the behavior when $\Omega$ is adjusted to a forth of the free spectral range. In this configuration the $\pm 2^{nd}$ order sidebands are simultaneously coupled to the cavity and the corresponding throughput intensity is twice as large as when they are not merged.

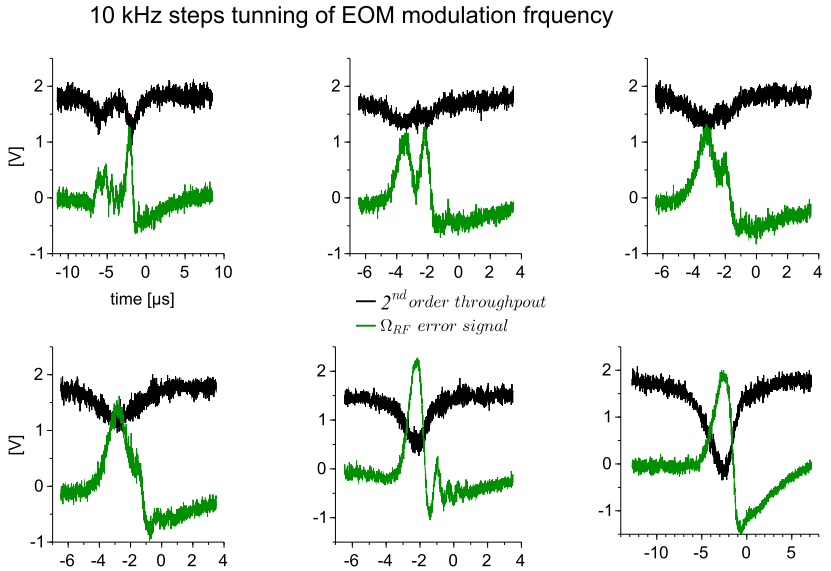


Figure 61: These plots show the cavity throughput intensity corresponding to the $\pm 2^{nd}$ order sidebands (black trace) and the PDH-like error signal (green) as a function of time, or equivalently as a function of the cavity length since it is triangularly modulated in time. When the two resonances are close one from another by a distance of the order of a linewidth, the PDH-like signal is distored but when the two merge, it recovers its nominal shape and the throughput intensity of the merged sidebands doubles. We use these two criteria to tune the EOM modulation frequency.

equation above is then equivalent to having the ratios $(\lambda_m/\lambda_{\pm 2})$ to a rational number, i.e.

$$\frac{\lambda_m}{\lambda_{-2}} = \frac{n_{-2}}{n_m} \text{ or equivalently } \frac{\omega_{-2}}{\omega_m} = \frac{n_{-2}}{n_m} \tag{402}$$

which is not the case in general. The wavelength $\lambda_m$ can not be changed since it has to be *magic*. On the other hand, possible small tuning are possible on $\omega_{\pm 2}$. Indeed, one could change the cavity length $L$, resulting in a change in $\Omega = c/8L$, and thus in $\omega \pm 2 = \omega_0 \pm 2\Omega$. Hence, if no solution is found for a given $L$, it might be possible to fulfill the requirement given by 402 for a well chosen length $L + \delta L$. Further more, the profile of the atomic phase imprint on the probe fields is such that it is not very sensitive to mis-tuning of the carrier by a few MHz. Such a tunning is realized experimentally by tunning the frequency feeding a double pass AOM, allowing for a tunning range of no more than a few MHz. This means we could translate the probe carrier frequency by an amount $\delta\omega$ of the order of a few MHz. The bi-chromaticity requirement can then be restated as

$$\frac{\omega_0 - \frac{c}{4(L_0+\delta L)} + \delta\omega}{\omega_m} = \frac{n_{-2}}{n_m} \tag{403}$$

To the first order in $\delta L$ this reads

$$\frac{\omega_0 - \frac{c}{4L}}{\omega_m} + \varepsilon \approx \frac{n_{-2}}{n_m} \ , \qquad \varepsilon = \frac{\delta\omega - \frac{c\delta L}{4L^2}}{\omega_m} \tag{404}$$

For $\delta\omega \approx 5$ MHz, $\delta\omega/\omega_m \approx 2.5 \times 10^{-8}$. Ideally, we would like to be able to achieve the bi-chromaticity condition by adjusting the extension of a PZT, starting from a randomly chosen cavity $L_0 \simeq 4$ cm. Thus, $\delta L$ is typically of the order of a few tens or hundreds of microns. Hence $(c\delta L/4L^2)/\omega_m \approx 10^{-7}$. This means the ratio $n_{-2}/n_m$ has to approximate $(\omega_0 - \frac{c}{4L})/\omega_m$ by closer than $10^{-7}$. For a cavity length of roghly 4 cm, $n_{-2}$ and $n_m$ are of the order of $10^5$, meaning they can *a priori* approximate whatever a number by closer than $10^{-5}$, which might be not sufficient.

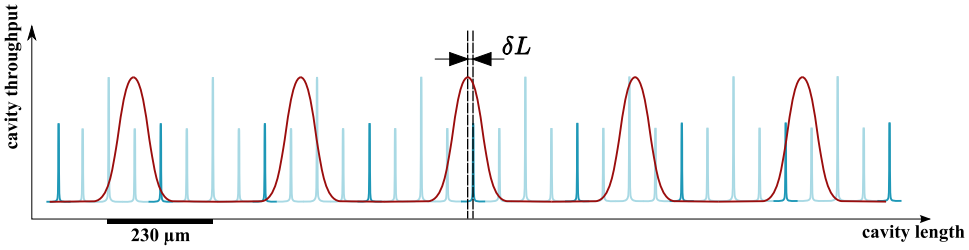


Figure 62: Cavity tri-chromaticity. The probe light resonances are represented in light blue, the overlapped second-order sidebands being slightly darker. The lattice light resonances are depicted in red. Since the lattice frequency can not be changed (has to be at the magic wavelength), and since the distance between the probe second-order sidebands is determined by the cavity FSR, i.e. by the cavity length $L$, the only free paramters we are left with are the probe carrier frequency and the cavity length. Once $\delta L$ has been set to a value such that the probe overlapped second-order sidebands and the lattice have resonances close enough (see text), the probe carrier frequency is adjusted by at most a few MHz via a double pass AOM in such a way that these three resonances occur for the same cavity length: the cavity is tri-chromatic.

However, we can check numerically if condition 403 can be fulfilled. Indeed, if such $n_{-2}$ and $n_m$ exist, they are given by

$$n_m = \left[\frac{2L}{\lambda_m}\right], \qquad n_{\pm 2} = \left[\frac{2L}{\lambda_{\pm 2}}\right] \tag{405}$$

where the square brackets stand for the entire part function that gives the largest integer number smaller than the considered number. We then need to find the values $\delta L$ for which the following inequality holds

$$f(L) = \left| \frac{\omega_0 - \frac{c}{4L_0}}{\omega_m} - \frac{\left[\frac{2L}{\lambda_{\pm 2}}\right]}{\left[\frac{2L}{\lambda_m}\right]} \right| \leq \varepsilon \approx 10^{-7} \tag{406}$$

The function $f(L)$ is displayed in Figures 63 and 64 for $L$ spanning intervals centered around $L = L_0 = 4$ cm with excursions of 2 $\mu$m, 9 $\mu$m 50 $\mu$m (corresponding to typical excursions of PZT available commercially) as well as 1000 $\mu$m respectively. One can see that over an excursion of a $\delta L = 2$ microns

(Figure 63, left plot) it is likely not to find a length $L =$ satisfying condition 406. On the 9 $\mu$m excursion plot (Figure 63, right plot), we see this condition is fulfilled once. For a 50 $\mu$m excursion (Figure 64, left plot), we see this condition is fulfilled three times. Two know whether this results are statistically representative, we plot $f(L)$ for a 1 mm excursion (Figure 64), where it is apparent that condition 406 is fulfilled regularly, in average 2 or 3 times over whatever a 100 $\mu$m interval. It even occurs that one could realize $f(L) \lesssim 10^{-12}$ at roughly once each 200 $\mu$m. Making sure we could tune the length of the cavity using a PZT to match the bi-chromaticity condition without having to do it manually[72] would then require a PZT actuator providing excursion of a 50 microns at least.

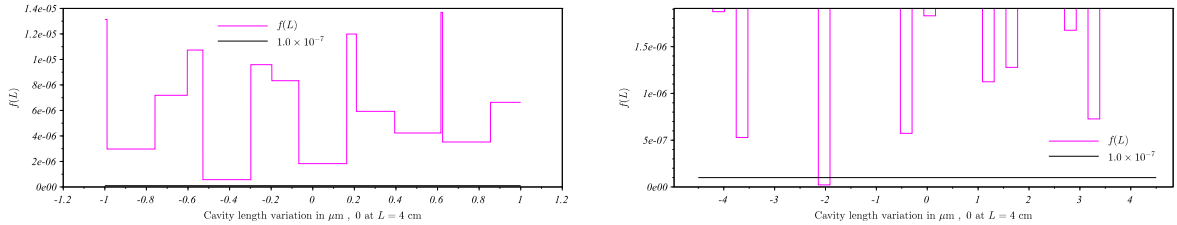


Figure 63: representation of $f(L)$ over intervals centered around $L = L_0 = 4$ cm of length 2 $\mu$m (left) and 9 $\mu$m (right). The black line represents the value $f(L) = 10^{-12}$ above which the bi-chromaticity condition can not be matched. Hence, for a PZT excursion of 2 $\mu$m $L_0 = 4$ cm, the condition is inaccessible. For 9 $\mu$m, the condition can be matched only once.

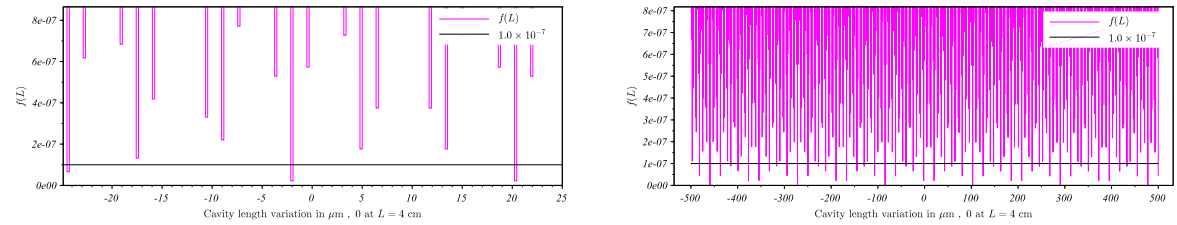


Figure 64: representation of $f(L)$ over intervals centered around $L = L_0 = 4$ cm of length 50 $\mu$m (left) and 1000 $\mu$m (right). It is apparent for the 1000 $\mu$m excursion graph that the bi-chromaticity condition is ful-filled 2 or 3 times over whatever an interval of lentgth 100 $\mu$m.

Initially[73], the vacuum cavity was endowed with two PZT, one at the top the other at the bottom, each with a maximal excursion of $\sim 2$ $\mu$m (they typically allowed for the scanning of the cavity over a bit more than 4 lattice light resonance, corresponding to 1.6 $\mu$m). We then installed, at the top side of the cavity, a new long range PZT (Noliac, NAC2124-H30) that consisted in a 30 mm stack of 15 PZT ring units. Each unit was 2 mm high and provided and excursion of 3.3 $\mu$m, resulting in a total maximal excursion of roughly 50 $\mu$m. However, after a few months of operation it broke, mainly because of its length resulting in a too strong torque. We then replaced it with a 1 cm high Thorlabs (PK44LA2P2) with 9 $\mu$m excursion only, but more compact and robust. This excursion was nevertheless sufficient to catch an operative bi-chromaticity cavity length. The procedure is then as follows: tune manually the cavity length to reach one of the points where $f(L) \lesssim 10^{-7}$ and then, correct for long term drifts[74] with the top, long excursion PZT.

### 12.1.4 The PDH-like setup

Their, a typical PDH setup is used. The beam, linearly polarized, goes through a polarizing beam splitter. The probe polarization is such that all the light goes through the cube. It then passes through a

[72] Our setup is such that a manual tuning is possible. However, it can not be done without having to re-align the cavity which is time consuming.

[73] i.e. at the beginning of this thesis period.

[74] We noticed that, mainly due to thermal dilations, the cavity length can vary by a few microns over a day.

quarter wave plate making its polarization circular, goes to the cavity from where it is reflected according to 345. It passes back through the quarter wave plate which this time makes it polarization linear again but orthogonal to that it had at the fiber output. The probe is then deflected by the polarizing beam splitter and its intensity is collected by a fast photodiode.

### 12.1.5 Generation of the signals

The signal provided by the photodiode, described in 11.2.1 is first amplified and then split into two arms, the "PDH" arm and the "atomic" arm at the end of which each signal is mixed down with a local oscillator at the corresponding frequency.

*1) The three local oscillators*

The local oscillators as well as the FR signal feeding the EOM are provided by a common source whose single output at $1\Omega$ is split into three. The first part is sent to an RF amplifier and then feeds the EOM producing the probe sidebands. A second is adjusted in power and sent to the "PHD" arm mixer. The third is sent to the "atomic" arm mixer.

*2) The atomic signal*

In the "atomic" arm the signal is filtered around $2\Omega$ to keep only the $I_{2\Omega}$ component of the intensity signal given in 349. It then amplified and passes through a phase shifter, used to tune its phase relatively to that of the local oscillator used to mix it down and obtain the quadrature of interest $S_{2\Omega}(\phi_1 = 0)$ (see section 11.2.4). This is our atomic signal, whose calibration is discussed in section 12.2.4.

*3) The PDH-like error signal*

In the "PDH" arm the signal is filtered around $1\omega$ then amplified and finally mixed down with the $1\Omega$ local oscillator. The relative phase between the two being set adjusting the "PDH" arm cables length. The signal is the PDH-like signal described in 11.2.4.

### 12.1.6 The probe light sidebands lock to the cavity

The PDH-like error signal is then sent to a FPGA board used as a proportional-integrator-derivator unit. The FPGA device we use is a commercial redpitaya platform endowed with two analog inputs and two analog outputs rating up to 50 MHz. We programmed it in such a way it mimics the analog setup usually provided at SYRTE by our electronics department. The main advantage of using this scheme is that it allows for a computer controlled real time adjustment of its parameters: gain and sign for the integrator, the proportional and the derivator.

## 12.2 System parameters adjustment

### 12.2.1 Adjustment of $\Omega$

The theoretical value of $\Omega$ is first estimated from the formula $\Omega = \Delta_{FSR}/4 = c/(8L) \sim 937$ MHz for an estimated value of $L \sim 4$ cm for the cavity length. we then finely tune this value looking at the profile of the PDH-like locking signal while scanning the cavity length (varying one of the cavity PZT voltage): when the two SBs are simultaneously coupled to the cavity with an overlap better than a linewidth ($\sim 200$ kHz) the signal amplitude is twice as large as in the disjoint case while its shape is minimally distored (see Figures 61 and 60).

### 12.2.2 Choice of $\beta$

The value of $\beta$ has to be chosen taking into account two aspects of the detection operation. First, as discussed in the trap destruction section, we want to minimize the number of probe photons scattered during the detection, i.e. to minimize the amount of probe power in the $\pm 2^{nd}$ order SBs. This pushes towards minimizing $\beta$. Second, in order for the SNR not to be limited by the electronic noise of the

detector, the detection has to be operated in the photon shot noise limited regime. The photon shot noise scales as $\sqrt{I_\Omega}$ where $I_\Omega \propto |J_1 J_2|$, which puts a lower bound

$$\beta > \beta_{SN} \tag{407}$$

For an estimate of $\beta_{SN}$ see the noise analysis section. Furthermore, depending on the particular set amplification chain, there is a minimal amplitude required for the PDH-like signal used to lock the probe to the cavity. This signal scales as $|J_0 J_2|$. It turned out this was the strongest constraint, forcing $\beta \gtrsim 0.2$.

### 12.2.3 Calibration of $\beta$

The calibration of $\beta$, which is required to compute the intracavity probe power needed for the $\phi^{at}$ estimation, is performed in the following way. The normalized power $\bar{p}_i$ of each SB $i \geq 0$[75] is measured with a PD at the cavity output: the PD voltage $V_i$ read on the scope for each SB is rescaled dividing by $N = \sum_{i=0,1,2} \varepsilon_i V_i$, where $\varepsilon_0 = 1$ because there is only one $0^{th}$ order SB, the carrier, $\varepsilon_1 = 2$ because there are two $1^{st}$ order SBs and $\varepsilon_2 = 1$ because even though there are two $2^{nd}$ order SBs, the corresponding voltage already contains a factor 2 because the $\pm 2^{nd}$ order SBs are simultaneously coupled to the cavity (note that when it is not the case, one has to take $\varepsilon_2 = 2$ for the second order sidebands, see comment of 65). The normalized power in each sideband $i$ is then

$$\bar{p}_{|i|} = \frac{\alpha_i V_i}{N} \tag{408}$$

$\alpha_{0,1} = 1$, $\alpha_2 = 1/2$ (again because the power in the $2^{nd}$ order SBs is measured twice. If they are not simultaneously coupled to the cavity, one takes). We thus have $\sum_i u_i \bar{p}_i = 1$, where $u_i$ is the number of $i^{th}$ order sidebands, i.e. $u0 = 1$ , $u_{i\neq 0} = 2$ and $\bar{p}_i \simeq |J_i(\beta)|^2$. We then obtain $\beta$ fitting the relation

$$\bar{p}_i = |J_i(\beta)|^2 \tag{409}$$

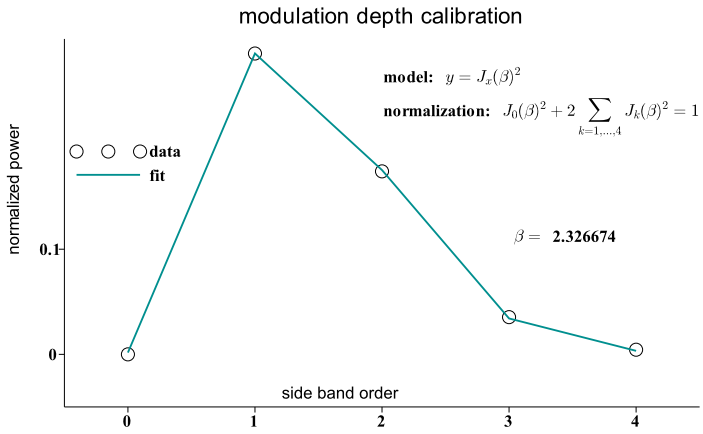


Figure 65: Typical fit of the normalized measured Bessel coefficients. The agreement is by far sufficient for our purpose. Note that for this particular fit, we used $\varepsilon_{i\neq 0} = 2$ because the measure was made with no sidebands merged (i.e. simultaneously coupled to the cavity).

### 12.2.4 Voltage to phase slope calibration

The phase shift imprinted by the atoms onto the probe field results in a voltage offset on the $S_2$ signal stemming from the down-mixing at $2\Omega$ of the RF beatnotes collected onto the fast PD (see **CNDD algebra** section). Thus one needs to know the voltage to phase slope calibration factor $\alpha$ (rad.V$^{-1}$)

$$\Delta\phi = \alpha \Delta V$$

[75] the sidebands of opposite order carry the same power, so we can get the modulation depth considering the positive orders only

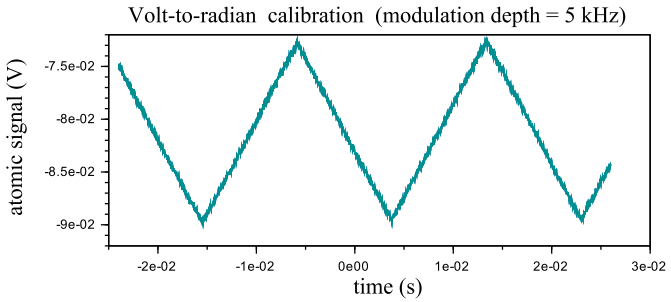


Figure 66: Here is displayed the "atomic signal" obtained with the probe $2^{nd}$ order sidebands locked to the cavity while modulating the radio-frequency signal sent to the electro-optic modulator $\Omega(t) = \Omega_0 + \delta\Omega(t)$ where $\Omega_0$ is equal to a forth of the cavity free spectral range $\Delta_{\rm FSR}$, i.e. $\Omega_0 \approx 930$ MHz, and where $\delta\Omega(t)$ is a triangular modulation of amplitude 5 kHz (i.e. 5 kHz $\leq \delta\Omega(t) \leq$ 5 kHz). The peak-to-peak amplitude of this *fake* "atomic signal" is $S_{2\Omega} \approx 15$ mV. Hence, for this particular configuration, the Volt-to-rad conversion factor is $\alpha \approx 720$ $\mu$radV$^{-1}$.

This is done taking advantage of the equivalent role played by $\phi^{at}_{\pm 2}$ and $\phi^{\Omega}_{\pm 2}$ in the contribution to $S_{2\Omega}$. Indeed, when no atoms are present in the cavity

$$S_{2\Omega} \propto \phi_{+2} - \phi_{-2} = 2\phi^{\Omega}_{+2} = \pi\varepsilon_{\Omega} = \pi\left(\frac{\delta\Omega}{\Omega_0} + \frac{\delta L}{L_0}\right) \tag{410}$$

hence, triangle-modulating $\Omega$ with a pick-to-pick amplitude $\Delta\Omega$ sufficiently low that the response $S_{2\Omega}(t)$ is linear in $|\delta\Omega(t)| < \Delta\Omega$ we can deduce the conversion factor

$$\alpha = \frac{\pi(\delta\Omega/\Omega_0)}{S_{2\Omega}}$$

where $S_{2\Omega}$ is given in Volt. Typical values are, e.g., 40 mV$_{ppk}$ for a 6 kHz modulation depth (i.e. -6 kHz$< \delta\Omega <$ 6 kHz) giving $\alpha \simeq 1$ mradV$^{-1}$. For our typical set of parameters (total probe power reaching the PD of $P_{\rm opt} \sim 4$ mW and a waist at the atom position $w = 38$ $\mu$m) for which we expect a shift of $\sim 150$ nrad per atom, this give a calibration of roughly $7 \times 10^3$ atoms per Volt.

## 12.3 Noise and SNR analysis

### 12.3.1 residual cavity length fluctuations and EOM modulation induced noise

Formally, because of sharing the same odd symmetry, $\phi^{\Omega}_{\pm 2}$ plays the same role as $\phi^{at}_{\pm 2}$ in the atomic signal $S_{1\Omega} \propto \phi^{\Omega}_{+2} + \phi^{at}_{+2}$. This means that the noise introduced by EOM feeding frequency fluctuations $\delta\Omega$ around its target value $\Omega_0 = \Delta_{FSR}/4$ can not be distinguished from fluctuations in number of detected atoms. It is then crucial to make sure it is small enough not to degrade the detection SNR.

The one way phase fluctuations on the atomic signal is

$$\phi^{\Omega}_{+2} = \frac{\pi}{2}\varepsilon_{\Omega} = \frac{\pi}{2}\left(\frac{\delta\Omega}{\Omega_0} + \frac{\delta L}{L_0}\right) \tag{411}$$

We need an estimate of both $\delta\Omega$ and $\delta L$.
Estimation of $\delta L$ relays on the analysis of the cavity-to-lattice lock in-loop PDH error signal $\varepsilon_{Lat}(t)$. Indeed, for a cavity finesse $\mathcal{F}_{Lat}$ for the lattice light and a lattice frequency assumed constant over time, the cavity length difference separating the maximum from the minimum of the PDH signal is (see Figure 67)

$$\Delta L_{\rm PDH} = \frac{\lambda_{Lat}}{2\mathcal{F}_{Lat}} \tag{412}$$

where $\lambda_{lat}$ is the lattice wavelength and the corresponding PDH signal slope giving the variation of the PDH signal, as read in Volt on the scope, as a function of the cavity length variation $\delta L$ is

$$\alpha = 2\frac{\Delta V_{\rm PDH}}{\Delta L_{\rm PDH}} \tag{413}$$

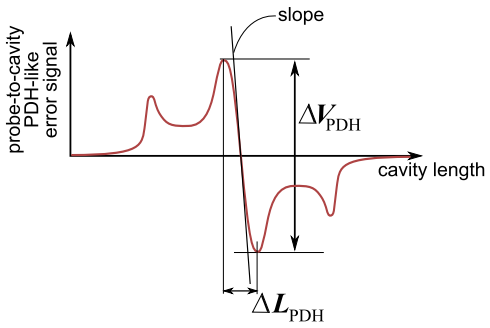


Figure 67: A typical PDH signal profile as a function of the cavity length. The length difference separating the two main extrema is given by $\Delta L_{\mathrm{PDH}} = (\lambda_{lat}/2\mathcal{F}_{lat})$. The slope in the linear region centered at the zero crossing is given by $\alpha = 2\Delta V_{\mathrm{PDH}}/\Delta L_{\mathrm{PDH}}$

where $\alpha$ is expressed in $\mathrm{Vm}^{-1}$ and the cavity length variations $\delta L$ can be deduced by the PDH error signal variations $\delta\varepsilon_{Lat}$ as

$$\delta L = \frac{\delta\varepsilon_{Lat}}{\alpha} = \frac{\lambda_{Lat}}{4\mathcal{F}_{Lat}\Delta V_{\mathrm{PDH}}}\delta\varepsilon_{Lat} \tag{414}$$

In our case $\lambda_{Lat} = \lambda_m = 813$ nm (from equation 411) and $\mathcal{F}_{Lat} = 160$ giving a PDH signal width of $\Delta L_{\mathrm{PDH}} \sim 6$ nm and $\Delta V_{\mathrm{PDH}} \sim 1$ V i.e. $\alpha^{-1} \sim 3\ \mathrm{nmV}^{-1}$. Typical fluctuations of the in-loop PDH error are $\delta\varepsilon_{Lat} \sim 150$ mV giving tpical length fluctuations $\delta L \sim 450$ pm. For our cavity of length $L_0 \sim 4$ cm, this leads to relative fluctuations

$$\frac{\delta L}{L_0} \sim 1.125 \times 10^{-8} \tag{415}$$

that is a contribution of $\sim 18$ nrad to the one way phase shift experienced by the probe field in the cavity, to be compared to the 94 nrad imprinted per atom in the configuration presented in [our paper].

Regarding the noise introduced by fluctuations of the EOM modulation frequency $\Omega$, its contribution amounts to

$$\frac{\pi}{2}\frac{\delta\Omega}{\Omega_0} \tag{416}$$

thus, for it to be of the same order of magnitude as the phase imprinted per atom of about 100 nrad, $\delta\Omega$ needs be as large as

$$\delta\Omega \sim 2\Omega_0\frac{200\ \mathrm{nrad}}{\pi} \sim 64\ \mathrm{Hz} \tag{417}$$

### 12.3.2 Photodetection noises

There are mainly four sources of noise involved in the detection chain. The first one is due to very quantum properties of the light to be detected and relates to the photon statistics, this is the so called photon shot noise, or photon noise. It is revealed by the detection but is intrinsic to the light incident to the detector. The second one stems from the photo-current process itself, i.e. from the statistics of electron-hole pairs production at the arrival of a photon to the photodetector conversion area and is encoded in the quantum efficiency. The third one is the losses, that can be accounted for introducing the so-called *partition noise* (see 12.3.3). The forth and last one is due to the electronic noise produced along the amplification chain, including transimpedance noise, i.e. thermal noise within the resistor converting the photodiode current into a voltage to be amplified. These four types of noises are isolated and investigated in the following paragraphs.

**The photon noise**

The operator of the quantized field beating at the photodetector assumes the general form

$$\hat{E} = \hat{E}^+ + \hat{E}^- \tag{418}$$

where $\hat{E}^- = \hat{E}^{+\dagger}$ and $\hat{E}^+$ assumes the general multimode decomposition

$$\hat{E}^+ = i\sum_k \sqrt{\frac{\omega_k}{2\varepsilon_0 V}}\hat{a}_k^\dagger\ e^{i(\omega_k t - kr)} = \sum_k \hat{E}_k^+\ e^{i(\omega_k t - kr)} \tag{419}$$

where the summation spans over all possible wave numbers $k$. Identifying the modes coefficients, we have the definition for the $\hat{E}_k^+$

$$\hat{E}_k^+ = i\sqrt{\frac{\omega_k}{2\varepsilon_0 V}}\hat{a}_k^\dagger \tag{420}$$

Note we represented the field as a scalar quantity, assuming all modes are co-propagating in the same direction and are in the same polarization state. Dealing with laser light sources, we can assume each mode $k$ is in a Glauber coherent state $|\alpha_k\rangle$, each satisfying the eigenvalue equation $\hat{a}_k |\alpha_k\rangle = \alpha_k |\alpha_k\rangle$, and therefore write the multi-mode light state impinging onto the photo detector as $|\alpha\rangle = \otimes_k |\alpha_k\rangle$. Accounting for probe spectrum we restrict the distribution of the $\alpha_k$ in a somehow ideal way. We consider in the following that $\alpha_k$ does not vanish only for $k = k_0 + nk_\Omega$, $n \in \mathbb{Z}$, $k_0 = \omega/c$ being the probe carrier wave number and $k_\Omega = \Omega/c$. This means the mode corresponding to the theoretical EOM produced side bands are populated. All the others are in vacuum states $|\alpha = 0\rangle$. This is an idealized view since it consists in assuming the side bands line width are infinitely narrow. The power in each side band of mode $k$ relates to the modulus of $\alpha_k$ in the following way. The optical power $P_k$ in mode $k$ is proportional to the number of photons $n_k$ in this mode, for a duration unit $\tau$

$$P_k = \frac{n_k}{\hbar\omega_k}\frac{1}{\tau} \quad , \qquad n_k = \langle\alpha_k| \hat{a}_k^\dagger \hat{a}_k |\alpha_k\rangle = |\alpha_k|^2 \tag{421}$$

We now define, for whatever an operator $\hat{A}$ and a state $|\psi\rangle$, the fluctuation operator $\delta\hat{A}_\psi$ as

$$\delta\hat{A}_\psi = \hat{A} - \langle\psi| \hat{A} |\psi\rangle \tag{422}$$

from where it directly follows that

$$\langle\psi| \delta\hat{A}_\psi |\psi\rangle = 0 \tag{423}$$

The operator $\delta\hat{A}_\psi$ encompasses the fluctuations of the expectation value of $\hat{A}$ for a system in state $|\psi\rangle$ while having zero average. Indeed

$$\sigma_A^2(\psi) = \langle\psi| \hat{A}^2 |\psi\rangle - \langle\psi| \hat{A} |\psi\rangle^2 = \langle\psi| \delta\hat{A}_\psi^2 |\psi\rangle \tag{424}$$

In the following we write $\delta\hat{A}$ instead of $\delta\hat{A}_\psi$ in order to lighten the notations, except in case of ambiguity. We thus define for each mode $k$, considering implicitly a coherent state $|\alpha_k\rangle$,

$$\delta\hat{a}_k \equiv \delta\hat{a}_{k,\alpha_k} = \hat{a}_k - \alpha_k \quad , \qquad \delta\hat{E}_k^+ \equiv \delta\hat{E}_{k,\alpha_k}^+ = i\sqrt{\frac{\omega_k}{2\varepsilon_0 V}}\delta\hat{a}_k^\dagger \tag{425}$$

The multimode decomposition of $\hat{E}^+$ can therefore be expressed as

$$\hat{E}^+ = \sum_k \left(E_k^* + \delta\hat{E}_k^\dagger\right) e^{i(k\Omega t - kr)} \tag{426}$$

where we used the assumption $\omega_k = k\Omega$ and where

$$E_k = \langle\alpha_k| \hat{E}_k^+ |\alpha_k\rangle = i\alpha_k^*\sqrt{\frac{\omega_k}{2\varepsilon_0 V}} \quad , \qquad \hat{E}_k^+ = i\sqrt{\frac{\omega_k}{2\varepsilon_0 V}}\hat{a}_k^\dagger \tag{427}$$

The total field intensity operator $\hat{I}$ then reads

$$\hat{I} = \hat{E}^+\hat{E}^- = \sum_{k,l}\left[\left(E_k^* + \delta\hat{E}_k^\dagger\right)\left(E_l + \delta\hat{E}_l\right)\right] e^{i\Omega_{kl}t} \tag{428}$$

$$= \sum_{k,l}\left[E_k^* E_l + E_k^*\delta\hat{E}_l + E_l\delta\hat{E}_k^\dagger + \delta\hat{E}_k^\dagger\delta\hat{E}_l\right] e^{i\Omega_{kl}t} \tag{429}$$

with $\Omega_{kl} = \Omega_l - \Omega_k = (l-k)\Omega$. From where we get the expectation value $\langle\hat{I}\rangle$ of the field intensity, taken on the multimode state $\otimes_k |\alpha_k\rangle$

$$\langle\hat{I}\rangle = \sum_{k,l}\left(E_k^* E_l + \langle\delta\hat{E}_k^\dagger\delta\hat{E}_l\rangle\right) e^{i\Omega_{kl}t} \tag{430}$$

Summation 428 can be re-written as in section 11.2.1, i.e. as

$$\hat{I} = \sum_q \hat{I}_q \tag{431}$$

where

$$\hat{I}_q = \sum_k \Bigg( \left[ E_k^* E_{k+q} + E_k^* \delta\hat{E}_{k+q} + E_{k+q} \delta\hat{E}_k^\dagger + \delta\hat{E}_k^\dagger \delta\hat{E}_{k+q} \right] e^{iq\Omega t} \tag{432}$$

$$+ \left[ E_k^* E_{k-q} + E_k^* \delta\hat{E}_{k-q} + E_{k-q} \delta\hat{E}_k^\dagger + \delta\hat{E}_k^\dagger \delta\hat{E}_{k-q} \right] e^{-iq\Omega t} \Bigg) \tag{433}$$

that can be decomposed onto its two quadratures as

$$\hat{I}_q = \sin(q\Omega t)\, \hat{I}_q^S + \cos(q\Omega t)\, \hat{I}_q^C \tag{434}$$

where

$$\hat{I}_q^S = i \sum_k \left[ E_k^* \left( E_{k+q} - E_{k-q} \right) + E_k^* \left( \delta\hat{E}_{k+q} - \delta\hat{E}_{k-q} \right) \right. \tag{435}$$

$$\left. + \delta\hat{E}_k^\dagger \left( E_{k+q} - E_{k-q} \right) + \delta\hat{E}_k^\dagger \left( \delta\hat{E}_{k+q} - \delta\hat{E}_{k-q} \right) \right] \tag{436}$$

and

$$\hat{I}_q^C = \sum_k \left[ E_k^* \left( E_{k+q} + E_{k-q} \right) + E_k^* \left( \delta\hat{E}_{k+q} + \delta\hat{E}_{k-q} \right) \right. \tag{437}$$

$$\left. + \delta\hat{E}_k^\dagger \left( E_{k+q} + E_{k-q} \right) + \delta\hat{E}_k^\dagger \left( \delta\hat{E}_{k+q} + \delta\hat{E}_{k-q} \right) \right] \tag{438}$$

The expectation value for each quadrature for a system in multimode state $\otimes_k |\alpha_k\rangle$ then reads

$$\langle \hat{I}_q^S \rangle = i \sum_k \left( E_k^* \left( E_{k+q} - E_{k-q} \right) + \langle \delta\hat{E}_k^\dagger \left( \delta\hat{E}_{k+q} - \delta\hat{E}_{k-q} \right) \rangle \right) \tag{439}$$

$$\langle \hat{I}_q^C \rangle = \sum_k \left( E_k^* \left( E_{k+q} + E_{k-q} \right) + \langle \delta\hat{E}_k^\dagger \left( \delta\hat{E}_{k+q} + \delta\hat{E}_{k-q} \right) \rangle \right) \tag{440}$$

We now compute the fluctuations

$$\left( \sigma_q^X \right)^2 = \left\langle \left( \hat{I}_q^X \right)^2 \right\rangle - \left\langle \hat{I}_q^X \right\rangle^2 \tag{441}$$

$X = S,\ C$, i.e. the photon noise of each quadrature. For the computation of $\left\langle \left( \hat{I}_q^X \right)^2 \right\rangle$, we write a hierarchized summation

$$\left\langle \left( \hat{I}_q^X \right)^2 \right\rangle = \sum_{j=0}^{4} A_j^X \tag{442}$$

$$\tag{443}$$

where we packed in each $A_j^X$ all the terms of order $j$ in fluctuation operators $\delta\hat{E}_k^{(\dagger)}$. Remembering that $\langle \delta\hat{E}_k^{(\dagger)} \rangle = 0$, for whatever a mode $k$, we then have $A_1^X = 0$. Hence, for the *sin* quadrature, we have

$$A_0^X = \mp \left\langle \sum_{k,l} E_k^* E_l^* \left( E_{k+q} \mp E_{k-q} \right) \left( E_{l+q} \mp E_{l-q} \right) \right\rangle \tag{444}$$

$$A_1^X = 0 \tag{445}$$

$$A_2^X = \mp \Bigg\langle \sum_{k,l} \Bigg( 2 \times \left[ E_k^* \left( E_{k+q} \mp E_{k-q} \right) \delta\hat{E}_l^\dagger \left( \delta\hat{E}_{l+q} \mp \delta\hat{E}_{l-q} \right) \right] \tag{446}$$

$$+ E_k^* \left( E_{l+q} \mp E_{l-q} \right) \left( \delta\hat{E}_{k+q} \mp \delta\hat{E}_{k-q} \right) \delta\hat{E}_l^\dagger \tag{447}$$

$$+ E_l^* \left( E_{k+q} \mp E_{k-q} \right) \delta\hat{E}_k^\dagger \left( \delta\hat{E}_{l+q} \mp \delta\hat{E}_{l-q} \right) \Bigg) \Bigg\rangle \tag{448}$$

where the upper *sign* in $\mp$ stands for the $I_q^S$ quadrature, the lower one for the $I_q^C$ quadrature. There is *a priori* no need to go further in the computation since terms of higher order in $\delta\hat{E}_k^{(\dagger)}$ are negligible compared to that of second order. To go further in the computation of $A_2$ we investigate the factors assuming the form $\langle\delta\hat{E}_k^{(\dagger)}\delta\hat{E}_l^{(\dagger)}\rangle$.

First, assuming the noise in each mode $k$, encompassed by $\delta\hat{E}_k$ in state $|\alpha_k\rangle$, is statistically independent on that of the other modes, we have, for $k \neq l$

$$\langle\delta\hat{E}_k^{(\dagger)}\delta\hat{E}_l^{(\dagger)}\rangle = \langle\delta\hat{E}_k^{(\dagger)}\rangle\langle\delta\hat{E}_l^{(\dagger)}\rangle = 0 \tag{449}$$

Therefore, only the terms with a factor $\langle\delta\hat{E}_k^{(\dagger)}\delta\hat{E}_l^{(\dagger)}\rangle$ where $k = l$ may not vanish.
Second, Remembering that $\delta\hat{E}_k^{(\dagger)} \propto \delta\hat{a}_k^{(\dagger)}$, we can check which of these remaining terms vanish replacing $\delta\hat{E}_k$ with $\delta\hat{a}_k$

$$\begin{aligned}
\langle\delta\hat{a}_k\delta\hat{a}_k\rangle &= \langle\alpha_k|\,(\hat{a}_k-\alpha_k)(\hat{a}_k-\alpha_k)\,|\alpha_k\rangle && (450)\\
&= \langle\alpha_k|\,\hat{a}_k^2 - 2\alpha_k\hat{a}_k + \alpha_k^2\,|\alpha_k\rangle && (451)\\
&= \alpha_k^2 - 2\alpha_k^2 + \alpha_k^2 = 0 && (452)
\end{aligned}$$

$$\begin{aligned}
\langle\delta\hat{a}_k^\dagger\delta\hat{a}_k\rangle &= \langle\alpha_k|\,(\hat{a}_k^\dagger-\alpha_k^*)(\hat{a}_k-\alpha_k)\,|\alpha_k\rangle && (453)\\
&= \langle\alpha_k|\,\hat{a}_k^\dagger\hat{a}_k - \alpha_k^*\hat{a}_k - \alpha_k\hat{a}_k^\dagger + |\alpha_k|^2\,|\alpha_k\rangle && (454)\\
&= |\alpha_k|^2 - 2|\alpha_k|^2 + |\alpha_k|^2 = 0 && (455)
\end{aligned}$$

$$\begin{aligned}
\langle\delta\hat{a}_k^\dagger\delta\hat{a}_k^\dagger\rangle &= \langle\alpha_k|\,(\hat{a}_k^\dagger-\alpha_k^*)(\hat{a}_k^\dagger-\alpha_k^*)\,|\alpha_k\rangle && (456)\\
&= \langle\alpha_k|\,\hat{a}_k^{\dagger 2} - 2\alpha_k^*\hat{a}_k^\dagger + \alpha_k^{*2}\,|\alpha_k\rangle && (457)\\
&= \alpha_k^{*2} - 2\alpha_k^{*2} + \alpha_k^{*2} = 0 && (458)
\end{aligned}$$

but, using the general commutation formula $\hat{a}_k\hat{a}_k^\dagger = [\hat{a}_k,\hat{a}_k^\dagger] + \hat{a}_k^\dagger\hat{a}_k$ and $[\hat{a}_k,\hat{a}_k^\dagger] = 1$, we get

$$\begin{aligned}
\langle\delta\hat{a}_k\delta\hat{a}_k^\dagger\rangle &= \langle\alpha_k|\,(\hat{a}_k-\alpha_k)(\hat{a}_k^\dagger-\alpha_k^*)\,|\alpha_k\rangle && (459)\\
&= \langle\alpha_k|\,\hat{a}_k\hat{a}_k^\dagger - \alpha_k^*\hat{a}_k - \alpha_k\hat{a}_k^\dagger + |\alpha_k|^2\,|\alpha_k\rangle && (460)\\
&= \langle\alpha_k|\,[\hat{a}_k,\hat{a}_k^\dagger] + \hat{a}_k^\dagger\hat{a}_k - \alpha_k^*\hat{a}_k - \alpha_k\hat{a}_k^\dagger + |\alpha_k|^2\,|\alpha_k\rangle && (461)\\
&= \langle\alpha_k|\alpha_k\rangle + |\alpha_k|^2 - 2|\alpha_k|^2 + |\alpha_k|^2 = 1 && (462)
\end{aligned}$$

Hence, only the terms where $\delta\hat{a}^\dagger$ appears at the right of $\delta\hat{a}$, or equivalently those where $\delta\hat{E}^\dagger$ appears at the right of $\delta\hat{E}$, do not vanish. Taking these two remarks into account, $A_2$ reduces to

$$\begin{aligned}
A_2^X = \mp\Bigg(&\sum_k E_k^*\,(E_{k+2q} \mp E_k)\,\langle\delta\hat{E}_{k+q}\delta\hat{E}_{k+q}^\dagger\rangle && (463)\\
&\mp\sum_k E_k^*\,(E_k \mp E_{k-2q})\,\langle\delta\hat{E}_{k-q}\delta\hat{E}_{k-q}^\dagger\rangle\Bigg) && (464)
\end{aligned}$$

meaning that only the line 448 in the expression of $A_2^X$ does not vanish. From 425 and the above computations, we have

$$\langle\delta\hat{E}_k\delta\hat{E}_k^\dagger\rangle = \frac{\omega_k}{2\varepsilon_0 V} = \frac{\omega+k\Omega}{2\varepsilon_0 V} \simeq \frac{\omega}{2\varepsilon_0 V} \tag{465}$$

the last approximation being justified by the fact that the optical carrier frequency $\omega$ is in the optical range while the EOM modulation frequency $\Omega$ is in the GHz frequency domain.

Noticing that the daggered fluctuation operators appearing in $\langle\hat{I}_q^X\rangle$ are always on the left side of the non-daggered ones, the above argument can be use to simplify the expression $\langle\hat{I}_q^X\rangle$ as well into

$$\langle\hat{I}_q^X\rangle = i\sum_k E_k^*\,(E_{k+q} \pm E_{k-q}) \tag{466}$$

and therefore

$$\langle \hat{I}_q^X \rangle^2 = \sum_{k,l} E_k^* E_l^* \left(E_{k+q} \mp E_{k-q}\right)\left(E_{l+q} \mp E_{l-q}\right) = A_0 \tag{467}$$

We now have all the ingredients to express $\sigma_q^{X2}$ in a simplified and more workable form Hence, we are left with

$$\sigma_q^{X2} = \langle \hat{I}_q^{X2} \rangle - \langle \hat{I}_q^X \rangle^2 \simeq A_2^X \simeq \mp \frac{\omega}{2\varepsilon_0 V} \sum_k E_k^* \left(E_{k+2q} \mp 2E_k + E_{k-2q}\right) \tag{468}$$

$$= \mp \frac{\omega}{2\varepsilon_0 V} \sum_k \left(2\mathrm{Re}\left(E_k^* E_{k+2}\right) \mp 2|E_k|^2\right) \tag{469}$$

the first approximation stemming from dropping out $A_{3,4}^X$ and the second one from 465.

We then need to relate this general form to that used in our CNDD theoretical development. More precisely we need to chose the right complex values for the $\alpha_k$. We require the classical expressions for each quadrature for the different frequency components of the total intensity to match their quantum expectation values counterparts, i.e. we require

$$I_q = \langle \hat{I}_q \rangle \tag{470}$$

where $I_q$ is given by equation 351. Combining definition 427 and definition 432 and using the fact that $\langle \delta \hat{E}_k^{(\dagger)} = 0$ we get

$$\langle \hat{I}_q \rangle = \left\langle \sum_k \left( \left[ E_k^* E_{k+q} + E_k^* \delta \hat{E}_{k+q} + E_{k+q} \delta \hat{E}_k^\dagger + \delta \hat{E}_k^\dagger \delta \hat{E}_{k+q} \right] e^{iq\Omega t} + h.c. \right) \right\rangle \tag{471}$$

$$= \sum_k \left( E_k^* E_{k+q} e^{iq\Omega t} + c.c. \right) \tag{472}$$

$$\simeq \frac{\omega}{2\varepsilon_0 V} \sum_k \left( \alpha_k \alpha_{k+q}^* e^{iq\Omega t} + c.c. \right) \tag{473}$$

Comparing with the expression of $I_q$ as provided in eq. [ref.], this means

$$\alpha_k = \sqrt{\frac{2\varepsilon_0 V}{\omega}} e|E| J_k F_k^* \qquad \text{which is equivalent to} \qquad E_k = i|E| J_k F_k \tag{474}$$

From 466 the quadratures intensities read

$$I_q^X = \langle \hat{I}_q^X \rangle = i \sum_k E_k^* \left(E_{k+q} \mp E_{k-q}\right) = i \left( \sum_k E_k^* E_{k+q} \mp \sum_k E_{k+q}^* E_k \right) \tag{475}$$

which, using the identification 474, leads to the two specific expressions

$$I_q^S = -2\mathrm{Im}\left( \sum_k E_k^* E_{k+q} \right) = -2|E|^2 \sum_k J_k J_{k+q} \mathrm{Im}\left(F_k^* F_{k+q}\right) \tag{476}$$

and

$$I_q^C = 2\mathrm{Re}\left( \sum_k E_k^* E_{k+q} \right) = 2|E|^2 \sum_k J_k J_{k+q} \mathrm{Re}\left(F_k^* F_{k+q}\right) \tag{477}$$

Combining 474 with the expression 468 of $\sigma_q^{X2}$ leads to

$$\sigma_q^{X2} = \mp 2\langle \delta \hat{E} \delta \hat{E}^\dagger \rangle |E|^2 \sum_k \left( J_k J_{k+2q} \mathrm{Re}\left(F_k^* F_{k+2q}\right) \mp J_k^2 |F_k|^2 \right) \tag{478}$$

Hence the signal to noise ratio (SNR) for the two quadratures take the general form

$$\mathrm{SNR}^S = \frac{I_q^S}{\sqrt{\sigma_q^{S2}}} = \frac{\sqrt{2}|E| \sum_k J_k J_{k+q} \mathrm{Im}\left(F_k^* F_{k+q}\right)}{\sqrt{\langle \delta \hat{E} \delta \hat{E}^\dagger \rangle \sum_k \left( J_k^2 |F_k|^2 - J_k J_{k+2q} \mathrm{Re}\left(F_k^* F_{k+2q}\right) \right)}} \tag{479}$$

while similar computations gives for the *cos* quadrature

$$\mathrm{SNR}^C = \frac{I_q^C}{\sqrt{\sigma_q^{C2}}} = \frac{\sqrt{2}|E|\sum_k J_k J_{k+q}\mathrm{Re}\left(F_k^* F_{k+q}\right)}{\sqrt{\langle\delta\hat{E}\delta\hat{E}^\dagger\rangle\sum_k\left(J_k^2|F_k|^2 + J_k J_{k+2q}\mathrm{Re}\left(F_k^* F_{k+2q}\right)\right)}} \tag{480}$$

As shown in section 11.2.3, when both the probe second order sidebands are close to be at resonance with the cavity $F_{k\neq\pm2} \approx 1$ whereas $F_{\pm2}$ is purely imaginary, meaning that $\mathrm{Re}\left(F_k^* F_{k+2q}\right) \approx 0$. Furthermore, the non destructive detection scheme is operated at low modulation depth $\beta$ meaning that $J_k \gg J_{k+1}$. Finally, only the term in $J_0^2$ is kept in $\sigma_q^{X2}$ i.e.

$$\sigma_q^{X2} \sim 2\langle\delta\hat{E}\delta\hat{E}^\dagger\rangle|E|^2 J_0^2 \tag{481}$$

As shown in section 11.2.4, the PDH-like error signal used to lock the second oprder probe sidebands to the cavity is the *sinus* quadrature of $I_{q=1}$, i.e. $I_1^S$, that reads

$$I_1^S \sim 2|E|^2 J_1 J_2 \mathrm{Im}\left(F_2 - F_{-2}^*\right) = -2|E|^2 J_1 J_2\sqrt{F}(2n+1)\pi\varepsilon_\omega \tag{482}$$

giving a signal-to-noise-ratio for the PDH-like error signal

$$\mathrm{SNR}^{\mathrm{PDH}} = \frac{\sqrt{2}|E|J_1 J_2\sqrt{F}\varepsilon_L}{J_0\sqrt{\langle\delta\hat{E}\delta\hat{E}^\dagger\rangle}} \tag{483}$$

For the atomic signal component of the intensity collected at the photodetector, i.e. $I_2^S$, the noise is the same as before, i.e. dominated by the carrier beating with the vacuums at frequency $\omega \pm q\Omega$, which does not depend on the value of $q$, and is given by 481, whereas the atomic signal reads (see section 11.2.5)

$$I_2^S \sim 2|E|^2 J_0 J_2 \mathrm{Re}\left(F_2 + F_{-2}^*\right) = 2|E|^2 J_0 J_2\sqrt{F}\left(\pi\varepsilon_\Omega + \phi_{+2}^{\mathrm{at}} - \phi_{-2}^{\mathrm{at}}\right) \tag{484}$$

giving a signal-to-noise-ratio

$$\mathrm{SNR}^{\mathrm{at}} = \frac{\sqrt{2}|E|J_2\sqrt{F}\left(\pi\varepsilon_\Omega + \phi_{+2}^{\mathrm{at}} - \phi_{-2}^{\mathrm{at}}\right)}{\sqrt{\langle\delta\hat{E}\delta\hat{E}^\dagger\rangle}} \tag{485}$$

Note that we can express the noise on the atomic signal induced by the photon noise, i.e. $\sigma_2^X$, as an effective atom shift $\phi_n$, i.e. such that the total signal, including the noise, be written as

$$I_2^S = 2|E|^2 J_0 J_2\sqrt{F}\left(\pi\varepsilon_\Omega + \phi_{+2}^{\mathrm{at}} - \phi_{-2}^{\mathrm{at}}\right) + \sigma_2^S = 2|E|^2 J_0 J_2\sqrt{F}\left(\pi\varepsilon_\Omega + \phi_{+2}^{\mathrm{at}} - \phi_{-2}^{\mathrm{at}} + \phi_n\right) \tag{486}$$

giving

$$\phi_n = \frac{\sigma_2^S}{2|E|^2 J_0 J_2\sqrt{F}} = \frac{\sqrt{\langle\delta\hat{E}\delta\hat{E}^\dagger\rangle}}{J_2|E|\sqrt{2F}} \tag{487}$$

But, $\hat{E}^+ = i\sqrt{\omega/2\varepsilon_0 V}\hat{a}^\dagger$ and $\delta\hat{E} = i\sqrt{\omega/2\varepsilon_0 V}\delta\hat{a}$. Moreover, $\langle\delta\hat{a}\delta\hat{a}^\dagger\rangle = 1$ hence, for a coherent state $|\alpha\rangle$, $|E| = \sqrt{\langle\hat{E}^+\hat{E}^-\rangle} = (\omega/2\varepsilon_0 V)|\alpha| = (\omega/2\varepsilon_0 V)\sqrt{N}$, $N$ being the average number of photons in the mode and relates to the total optical power $P$ incoming to the cavity and the measurement duration $T$ according to

$$N = \frac{PT}{\hbar\omega} \tag{488}$$

Therefore

$$\frac{|E|}{\sqrt{\langle\delta\hat{E}\delta\hat{E}^\dagger\rangle}} = \sqrt{N} = \sqrt{\frac{PT}{\hbar\omega}} \tag{489}$$

Finally, the effective atom shift noise due to photon noise can be expressed as

$$\phi_n = \frac{1}{J_2}\sqrt{\frac{\hbar\omega}{2FPT}} \tag{490}$$

Other expressions of practical interest can be derived for $\mathrm{SNR}^{\mathrm{at}}$ and $\phi_n$. Indeed, the intra-cavity power $P_c$, i.e. the power experienced by the atoms, relates to the incoming power $P$ according to

$$P = \frac{\pi}{4\mathcal{F}J_2^2}\, P_c \tag{491}$$

Therefore, since $\mathcal{F} = \pi\sqrt{F}/2$, equation 485 can be recast into

$$\mathrm{SNR}^{\mathrm{at}} = \sqrt{\frac{8\lambda P_c T\mathcal{F}}{\pi hc}}\left(\frac{\phi^{\mathrm{at}}_{+2} - \phi^{\mathrm{at}}_{-2}}{2}\right) \tag{492}$$

which the formula we used in [144] (where we have dropped out the $\pi\varepsilon_\Omega$ contribution due to fluctuations in the EOM modulation frequency and than can be considered a noise). For $\phi_n$ we get

$$\phi_n = \sqrt{\frac{hc}{\lambda}\frac{\pi}{\mathcal{F}}\frac{2}{P_c T}} \tag{493}$$

**Photodetector quantum efficiency**

As shown in the next paragraph, optical losses are detrimental to SNR, as accounted for by the denominator $\eta$ factor in eq. 541. A major source of losses in our system is the low quantum efficiency of our photodetector (PD) at the probe frequency: $\rho_{461} = 0.17$ AW$^{-1}$ according to the manufacturer. Our lab-made PD circuitry is as follows, as depicted in Fig. 68. The PD cathode is connected to a $V_b$ potential

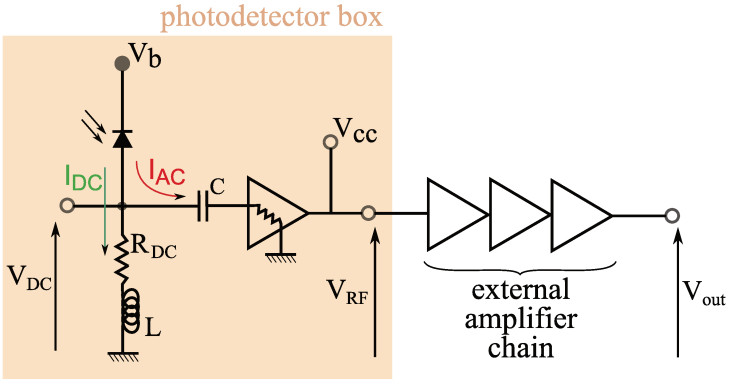


Figure 68: Schematic of our lab-made fast photodetector circuit.

point (the biasing voltage), its anode to a three branches node. One of the two "output" branches of this node, the DC branch, comprises a transimpedance resistor $R_{tr}$ (that we measured to be 220 Ω) in series with an transinductance $L_{tr}$ which end tip connects to the PD box ground. The other one, the AC branch, comprises a capacitance $C$ in series with an Era-2 drop-in monolithic amplifier with power gain $G$ and noise figure $N_f$ whose 50 Ω impedance output port is connected to both its biasing potential point of $V_{cc}$. The AC branch capacitor prevents the DC part of the PD current from running through, and saturate the monolithic amplifier, while the series LC circuit of the DC branch rejects all the AC components of the photocurrent into the AC branch. Hence, a direct measurement of the transimpedance voltage $V_{tr}$ gives the average photocurrent $i_{PD}$

$$\langle i_{PD}\rangle = \frac{V_{tr}}{R_{tr}} \tag{494}$$

For a probe optical power $P_{op}$ of 10 mW directly sent to the PD, we measure a transimpedance voltage of 300 mV which gives, for our 220 Ω transimpedance, an average photocurrent of 1.36 mA. The quantum efficiency of the detector being defined as

$$\rho = \frac{\langle i_{PD}\rangle}{P_{op}}$$

we obtain an estimated quantum efficiency of

$$\rho \simeq 0.136 \text{ AW}^{-1} \tag{495}$$

to be compared with the 0.17 AW$^{-1}$ manufacturer value.

If the PD photo current, i.e. the photo electron flux, were a faithful representation of the actual photon flux impinging onto it, then we would have

$$i_{\mathrm{PD},\delta t}(t) = \frac{eP_{\mathrm{op}}}{\hbar\omega} \tag{496}$$

This would give a ideal quantum efficiency, for our 461 nm probe

$$\overline{\rho} = \frac{e}{\hbar\omega} = 0.37 \text{ AW}^{-1}$$

i.e. $\overline{\rho} \sim 2.72 \times \rho$. This means that approximately one third of the photons incoming to the PD contribute to the effective photo current signal.

**Estimation of photon noise from average photo current measurement**
In the ideal case of a perfect transcription of the photon statistics into the PD current statistics, the photo current fluctuation variance would be a copy of that of the photons, rescaled by the ideal unitary quantum efficiency $\overline{\rho} = e/\hbar\omega$

$$\sigma_i^2 = \overline{\rho}^2 \sigma_{op}^2 \tag{497}$$

However, in the case of non unitary efficiency, i.e. in the case some impinging photons do not give rise to the injection of a photo electron into the detection circuit, the above formula has to be slightly modified. Noting the flux quantum efficiency, i.e. the fraction of the number of the incoming photons that are actually detected, as

$$\eta = \rho/\overline{\rho} \approx 0.37 \tag{498}$$

one can not just rescale $\sigma_i^2$ multiplying it by a factor $\eta^2$. As described in section 12.3.3, one has to add the *partition noise* to the non unitary quantum efficiency losses, leading to

$$\sigma_i^2 = \overline{\rho}^2 \left( \eta^2 \sigma_{op}^2 + \eta(1-\eta) \left(\hbar\omega\right)^2 \langle n_{ph} \rangle \Delta^2 \right) \tag{499}$$

with $\Delta$ the measurement bandwidth and where the average number of photon is given by $\langle n_{ph} \rangle = P_{op}/\Delta\hbar\omega$. Extracting $\sigma_{ph}^2$ from eq. 499 requires knowing $\sigma_i^2$. It can be obtained from the average photo current. We start from the standard relation

$$\boxed{\sigma_i^2 = 2e\langle i \rangle \Delta} \tag{500}$$

where $e$ is the electron charge and $\Delta$ the considered bandwidth, valid only in the case of Poissonian electron flux. In the most general case, Poissonian statistics of the incoming photons is not ensured and one as to consider that the noise on the photo current reproduce this possibly not Poissonian noise. We should then degrade it accordingly , leading to

$$\begin{aligned} \sigma_i^2 &= \eta^2 2e\langle i \rangle \Delta + \eta(1-\eta)\ e^2 \langle n_e \rangle \Delta^2 && (501)\\ &= \left(2\eta^2 + \eta(1-\eta)\right) e\langle i \rangle \Delta && (502)\\ &= \tilde{\eta} 2e\langle i \rangle \Delta && (503) \end{aligned}$$

In our case, $\overline{\rho} \sim 2.72 \times \rho$, $\tilde{\eta} \sim 0.3$. Inverting eq. 499 one gets

$$\sigma_{op}^2 = \left(\frac{\hbar\omega}{\eta}\right)^2 \left( \frac{2\tilde{\eta}}{e} \langle i \rangle - \frac{\eta(1-\eta)}{\hbar\omega} P_{op} \right) \Delta \tag{504}$$

However, assuming a coherent optical field state, these complication are not necessary and we have

$$\sigma_{op}^2 = (\hbar\omega)^2 \langle n_{ph} \rangle \Delta^2 = \hbar\omega P \Delta \tag{505}$$

and 499 reduces to

$$\boxed{\sigma_i^2 = \overline{\rho}^2 \eta \sigma_{op}^2 = \frac{e^2 \eta P}{\hbar\omega} \Delta} \tag{506}$$

where the Poissonian character of the statisctics is conserved, meaning that equation 500 is valid. For an input optical power of 10 mW, we measured an average photocurrent of 1.36 mA. Thus, for a bandwidth $\Delta = 1$ Hz, this gives

$$\sqrt{\sigma_{op}^2} \sim 6.6 \times 10^{-11} \text{ W}/\sqrt{\text{Hz}} \tag{507}$$

or in terms of photons number

$$\sqrt{\sigma_{ph}^2} \sim 1.61 \times 10^8 \ \left(\sqrt{\text{Hz}}\right)^{-1}$$

which is agreement with the theoretical value provided by the standard shot noise formula for coherent state $\sqrt{\sigma_{ph}^2} = \sqrt{P\Delta/\hbar\omega} \sim 1.56 \times 10^8$ photon per $\sqrt{\text{Hz}}$.

**PD electronic noise**

The main source of electronic noise within the PD circuitry is the so-called thermal, or Nyquist, noise. It stems from electrons agitation in resistors due the their unavoidable thermal excitation at non zero temperature $T$. It can be considered equivalently as shunt current or a series voltage (Figure 69) whose magnitudes depend on the considered bandwidth. They are given by

$$i_{th} = \sqrt{\frac{4k_B T \Delta_{\text{BW}}}{R}} \qquad\qquad v_{th} = \sqrt{4k_B T \Delta_{\text{BW}} R} \tag{508}$$

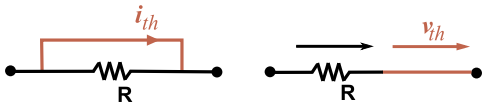


Figure 69: Two possible model for the thermal or Nyquist noise generated by any resistor. It could be represented by a shunt current (left) or a series voltage (right).

However, there is some controversy about how to account for this noise in a photodetector circuit. Here we propose four different approaches leading to sensibly different results. The three first approaches are derived from the thermal noise current $i_{th}$ and give results agreeing with each other up to within a factor 2. The forth one is based on the thermal noise voltage $v_{th}$.

*I. Thermal noise current approach*

The first of this approaches consists in considering that all the thermal noise contribution is that of the DC-arm resistor $R_{DC}$ of the photodector circuit (see Figure 68). The second consider a combination of the noise stemming from $R_{DC}$ to that stemming from the 50 Ω internal resistor of the detector box embedded monolithic amplifier (see Figure 70). The third one consider that thermal noise of the circuit is dominated by the *noise figure* contribution of the monolithic amplifier.

*1) $R_{DC}$ only thermal noise*

In our circuit, the actual value of $R_{DC}$ is 1 kΩ. However, because of the particular circuit topology, it reads 220 Ω when measured with a multimeter. Based on this value, the resulting thermal noise is

$$i_{th} = 8.66 \times 10^{-12} \text{ A in a band of 1 Hz} \tag{509}$$

*2) $R_{DC}$ plus 50 Ω amplifier thermal noise*

In our detector circuit configuration (see Fig. 70), the current thermal noise running through the AC arm reads

$$i_{th} = \sqrt{4k_B T \Delta_{\text{BW}}} \left( \frac{1}{\sqrt{R_{\text{AC}}}} + \frac{1}{\sqrt{R_{\text{DC}}}} \right) \frac{Z_{\text{DC}}}{Z_{\text{AC}} + Z_{\text{DC}}} \tag{510}$$

where $Z_{AC,DC}$ are the complex impedance of the corresponding arm. In our configuration $Z_{\text{DC}} = R_{\text{DC}} + jL\omega$ and $Z_{\text{AC}} = R_{\text{AC}} + 1/jC\omega$ where $R_{\text{AC}} \simeq 50$ Ω and $C$ is the capacitance set on the AC arm. For high frequencies, i.e. allowed to run through the $AC$-arm capacitance we can consider

$$\frac{Z_{\text{DC}}}{Z_{\text{AC}} + Z_{\text{DC}}} \approx 1 \tag{511}$$

leading to

$$i_{th} \simeq 2.7 \times 10^{-11} \text{ A in a band of 1 Hz} \tag{512}$$

*2) Amplifier noise figure thermal noise*

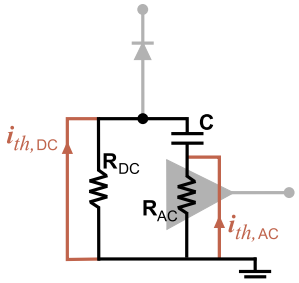


Figure 70: Schematic representation of the resistor circuit used to compute the photondetector thermal noise.

For this third approach we follow the derivation of [112]. It is based on a *noise figure* analysis of the monolithic amplifier behavior. Generally speaking, when a signal $s$ and its inherent noise $\sigma$ are sent to an amplifier, each of them is amplified with a gain $g$. However, the amplification process adds some noise $\sigma'$. This can be accounted for by considering the signal amplification gain $g$ is different from the noise amplification gain $g'$

$$s \longrightarrow gs \tag{513}$$
$$\sigma \longrightarrow g\sigma + \sigma' = g'\sigma \tag{514}$$

The amplifiers gain are most of the time given in terms of power gain $G = g^2$. Indeed, for typical signals $s$ in Volts or Ampère, the power scales as $S = s^2$ and 513 can be re-written as

$$S \longrightarrow GS \tag{515}$$
$$\sigma^2 \longrightarrow G\sigma^2 + \sigma'^2 = G'\sigma^2 \tag{516}$$

The noise figure, provided by most amplifier manufacturers, is then defined as

$$N_f = \frac{G'}{G} \tag{517}$$

and is most of the time given in dB unit, i.e.

$$N_f(dB) = \log_{10}(G') - \log_{10}(G) \tag{518}$$

The noise figure $N_f$ relates to the thermal noise in the following way (see [112, 113]). It is used to derive an effective noise temperature $T_R$ defined as

$$T_R = 290\left(10^{N_f(dB)/10} - 1\right) \tag{519}$$

For our monolithic Minicircuit Era-5+ amplifier (manufacturer data: $N_f \simeq 3.5$ dB), this gives an effective temperature of 360 K. This value is then used to compute the thermal noise in standard way for the 50 Ω impedance of the amplifier[76]. This leads to a *noise figure thermal noise*

$$i_{th} = 2 \times 10^{-11} \text{ A in a band of 1 Hz} \tag{520}$$

This leads to an estimation

$$i_{th} = (1.8 \pm 0.9) \times 10{-}11 \text{ A in a band of 1 Hz} \tag{521}$$

To relate this to the experiment, we consider the power dissipated by this current in the 50 $\omega$ transimpedance resistor $R_{amp}$ of the amplifier

$$P_{th} = i_{th}^2 \times R_{amp} \tag{522}$$

multiply it by the gain of the amplification chain[77] $G_{ch}$ and finally derive a voltage $V_{th}$, corresponding to that read on our fast Fourier transform (FFT) analyzer, assuming a 50 Ω transimpedance $R_{an}$ for the analyzer as well

$$V_{th}^2 = R_{an}R_{amp}G_{ch}i_{th}^2 \approx G_{ch} \times 8.1 \times 10^{-19} \text{ V}^2 \text{ in a band of 1 Hz} \tag{523}$$

[76] As noted in [112], this computation is accurate aslong as the 50 Ω impedance matching at the amplifier input is verified.
[77] whose first amplifier is the detector boxed monolithic amplifier.

or equivalently

$$V_{th} \approx \sqrt{G_{ch}} \times 9 \times 10^{-10} \text{ V}/\sqrt{\text{Hz}} \tag{524}$$

*II. Thermal noise voltage approach*

Here we consider only the $R_{DC}$ thermal noise voltage contribution which we assume is amplified by the amplifiers chain, leading to a amplified voltage noise

$$V_{th} = \sqrt{G_{ch} 4 k_B T R_{DC}} \approx \sqrt{G_{ch}} \times 1.9 \times 10^{-9} \text{ V}/\sqrt{\text{Hz}} \tag{525}$$

which is agreement with the value estimated above within a factor 2.

Our photodetector circuit includes a $\approx +20$ dB gain around 1 GHz, to which are added two amplifiers of $\approx +20$ dB each as well in the same frequency range, resulting in an amplifier chain power gain $G_{ch} \approx +60$ dB. We thus expect a voltage noise

$$V_{th} \approx 10^{-6} \text{ V}/\sqrt{\text{Hz}} \tag{526}$$

which is not that far from the measured value (see next paragraph and Figure 74) of

$$V_{th}^{meas} = 6.7 \times 10^{-7} \text{ V}/\sqrt{\text{Hz}} \tag{527}$$

Note that it is possible to use the models developed above the other way around to infer the value of $R_{DC}$ from a measurement of the electronic noise. We did this using the setup depicted in Figure 71. In this protocol, no light is sent to the detector and we directly measure the noise at the amplification chain output on a FFT analyzer providing us with the power spectral density of the signal. We measured a noise of -89 dBV$^2$/Hz. Subtracting the amplification chain gain (internal Era-5+ plus the three external amplifiers) $G_{ch}(\text{dB}) = 85$ dB we obtain a thermal noise

$$V_{th}^2(\text{dB}) = -174 \text{ dB} \tag{528}$$

Using our forth model, this gives a transimpedance

$$R_{DC} \approx 240 \ \Omega \tag{529}$$

close to the 220 Ω measured with the multimeter.


Figure 71: On the left: configuration used for a quick estimation of the thermal noise (electronic noise supposed to be dominated by its thermal contribution) plugged directly onto a wideband FFT. Right: typical expected profile for the photon noise spectrum. The noise diverges for frequency going to zero Hz. For higher frequencies (typically above a few hundreds of MHz) the should be flat till the detector cutoff frequency marking its bandwidth.

**Photon and electronic noise measurement**

The photon noise is expected to be flat, i.e. frequency independent. However, the noise density close to DC increases drastically because of power fluctuations of the light sources, and the response drops down at the PD frequency cut off. We then expect a behavior as the typical one displayed on right-side schematic plot of Figure 71. A direct measurement of the row PD signal on a spectrum analyzer shows the spectrum is flat from $\sim$ 100 MHz till the PD cut off at 2 GHz, which then corresponding to the

frequency range over which the photon noise is measurable. However, we use for the measurement a computer acquisition board plus a real-time FFT software providing us with spectra spanning a region going from 0 Hz to roughly 1 Mhz. Hence the spectrum region where he photon noise is visible is out of reach with our device. To *bring* the photon noise into an accessible region we beat the amplified photodetector signal with a signal at 1.8 GHz provided by a synthesizer (see Figure 72). The observed

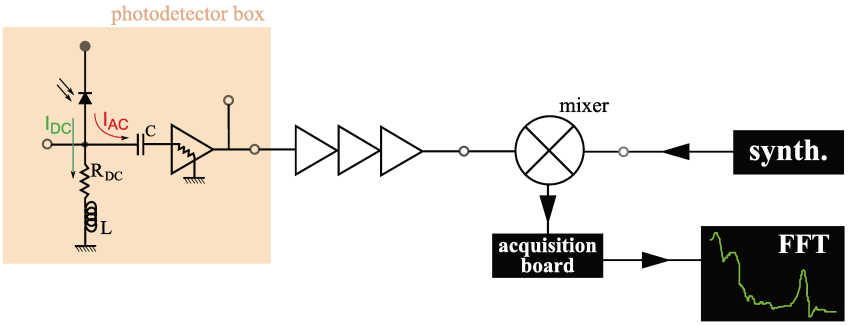


Figure 72: When no wideband FFT device is available (which is our case except when borrowed from other labs), one can not measure the photon noise directly at the detector amplification output. Indeed, typical photon noise spectrum start being flat far above 1 MHz which our computer-board FFT bandwidth. The signal has then to be mixed down to accessible region of the spectrum. In our particular case, the flat spectrum stretches from roughly 1 GHz to 2 GHz, the detector cutoff. We mix it down with a synthesizer provided local oscillator. The resulting signal can be used for noise analysis.

FFT spectra then correspond to the noise around a central frequency of roughly 1.8 GHz over a 1 MHz span. Hence, the mixed down signal samples a region where the noise has the right frequency-independent behavior, and the demodulated signal should be flat. However, due to low frequency noise induced by the amplification chain and the measurement device itself, the noise power spectral density of the mixed down signal displays the same typical behavior at low frequencies (see Figure 73). The idea is then to

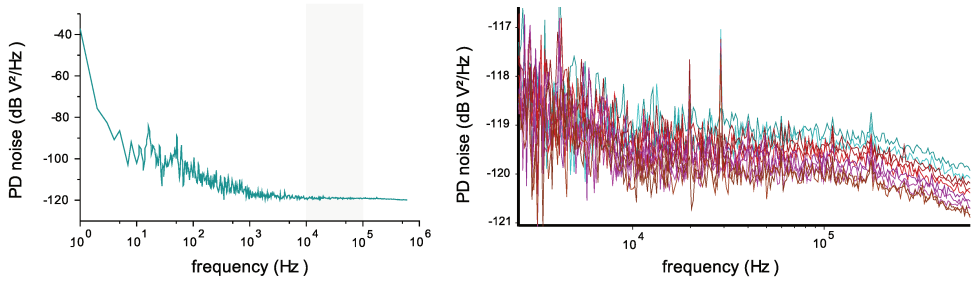


Figure 73: FFT of the detector noise down mixed to a frequency region accessible for our FFT ($0 < f < 1$ MHz). On the left-side, a typical trace with the large low frequency noise. Above 1 kHz the spectrum looks rather flat at this scale. On the right-side, a zoom into the seemingly flat region. The cutoff of the FFT device is clearly seen just above 100 kHz. The part of the signal we average to estimate the photon noise is located between 10 kHz and 100 kHz. In spite of the noise, we can guess the dependence in optical power, meaning the detection is photo noise limited (see analysis below).

average the FFT spectrum over a region where it is flat, typically over an interval ranging from 10 kHz to 100 kHz (see 73) and use this averaged value as the photon plus electronic noise measurement. We repeat this treatment for various values of optical powers, ranging from $\sim 50$ $\mu$W to a bit more than 10 mW, sent to the photodetector. The flat sections of the corresponding spectra obtained for a 1 Hz measurement bandwidth are displayed on Figure 73. The corresponding averages are presented on the right graph of Figure 74.
Assuming the electronic noise of the photodetector plus the amplifying chain does not depend on the optical power sent to the PD (this assumption means we consider the noise figure of the amplification

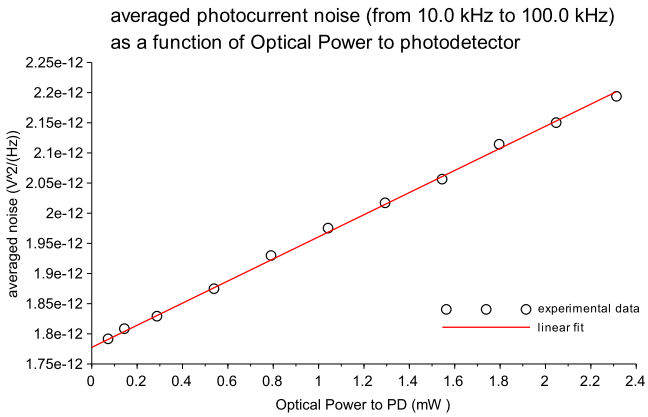


Figure 74: Variance of the total noise $\sigma^2_{el+ph}$ (electronic plus photon noise) computed from experimental data according to the protocol described above (averaging the flat section of the FFT spectra). It clearly can be decomposed as $\sigma^2_{el+ph} = \sigma^2_{el} + \sigma^2_{ph}$ with $\sigma^2_{el}$ a constant and $\sigma^2_{ph}$ scaling linearly with the optical power sent to the photodetector. The ift gives $\sigma^2_{el} = 1.778 \times 10^{-12}$ A$^2$/Hz and $\sigma^2_{ph} = 1.833 \times 10^{-10} \times P$ A$^2$/Hz, for $P$ expressed in W.

chain to be $N_f = +0$ dB) and is independent of the photon noise we consider the total noise $\sigma^2_{el+ph}$ to be the quadratic sum of the photon and electronic noises. Moreover, the photon noise is expected to scale as the square root of the optical sent to the detector. Hence our model is

$$\sigma^2_{el+ph} = \sigma^2_{el} + \sigma^2_{ph} = \sigma^2_{el} + a \times P \tag{530}$$

The noise data obtained as described above and displayed on Figure 74 can be indeed fitted by a function of this form, giving

$$\sigma^2_{el} = 1.778 \times 10^{-12} \text{A}^2/\text{Hz}, \qquad \sigma^2_{ph} = 1.833 \times 10^{-10} \times P \text{ A}^2/\text{Hz, for } P \text{ expressed in W} \tag{531}$$

from where we deduce the ratio

$$\frac{\sigma^2_{ph}}{\sigma^2_{el}} = \frac{e^2\eta^2 P/(\hbar\omega)}{4k_B T/R_{DC}} \approx \frac{aP}{b} \tag{532}$$

that provides an other way to estimate $\eta$ using the value $R_{DC}$ obtained in 529 as

$$\eta = \sqrt{\frac{a}{b}\frac{4k_B T\hbar\omega}{e^2 R}} \approx 0.34 \tag{533}$$

which is compatible with the estimation made earlier from the DC photocurrent $\eta \approx 0.37$.

Knowing the probe detuning to resonance, the amount of power in the probe carrier and having a good calibration for the EOM modulation depth $\beta$, it is possible to translate the measured noise in units of atoms. The result is shown on Fig. 75. It becomes apparent on this figure that below an incoming optical of 10 mW the photon noise is not dominating the electronic one but that they are on the same order of magnitude.

**detector bandwidth characterization**

If the power sent to the detector is large enough for the photon shot noise to dominate over the electronic noise of the detector circuit, the spectral response of the detector is expected to present a characteristic three-stages spectrum. At low frequencies, the noise is dominated by typical low frequency noise, exploding close to DC. Then, the spectrum displays a flat response that stretches over several decades corresponding to he photon shot noise, which is white and does not depend on frequency. Finally, the response drops suddenly after the cut off frequency $\nu_c$. This is indeed what we observe. The measured spectrum can therefore be used to infer the cut off frequency, which in the case of our CNDD detector is circa 2 GHz.

Since fast detector, with bandwidth of several GHz are hardly found on the market for 461 nm, we made our first attempts for our second detection scheme (see section 14) with our 2 GHz bandwidth detector even though the scheme requires ideally a BW of 6 GHz.

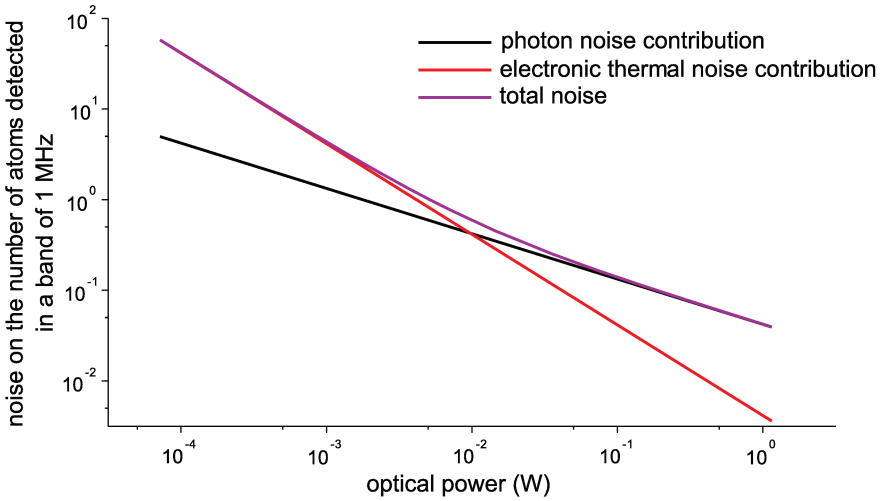


Figure 75: We plot the photon noise in unit of atoms obtained from 490 combined with 337 (black line). From our measurement of the photon and thermal electronic noise we know their ratio as a function of the incoming optical power $P$ (see equation 532). We can then estimate the electronic contribution to the noise in atom unit (red line). The sum of these two contributions is represented in purple. We see that for optical power below 10 mW (typical powers used are indeed below this limit) the photon noise is not dominant.

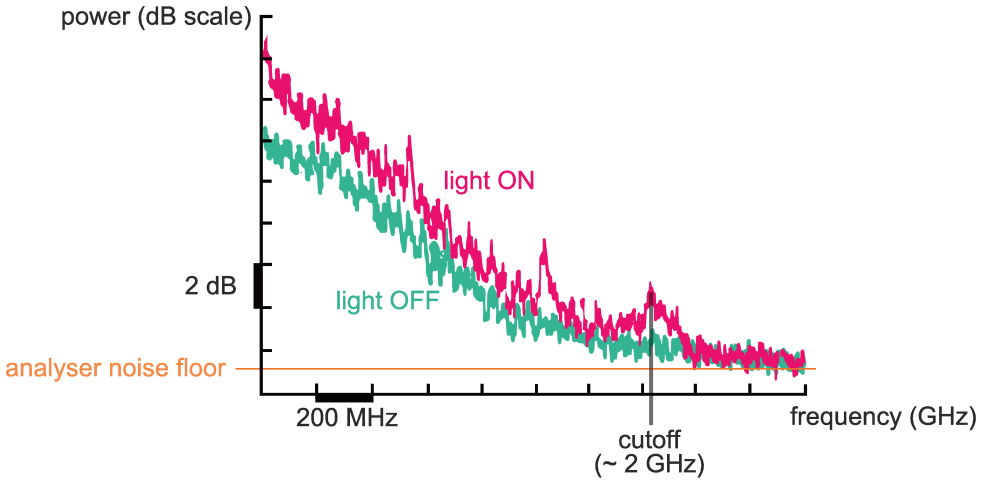


Figure 76: Photodector bandwidth measurement. This graph represents the spectra (in logarithmic scale) of the photodetector signal as directly measured at the lab-made box output (see figure 68) with a commercial spectrum analyser. The measurement covers frequencies ranging from 600 MHz to 2.6 GHz. The green spectrum was measured with no light reaching the detector, the noise profile being due to thermal and amplification noise. The red spectrum xas obtained with 5 mW of 461 nm light incoming to the detector. The difference between the two corresponds to the photon shot noise, which should be flat, i.e. should not depend on the frequency. In practice this feature is altered due to DC noise (not visible here because the spectrum starts at 600 MHz) the non-flatness of the amplification (gain depending on frequency) and the limited bandwidth of the photodetector (see figure 71). Indeed, after the cutoff frequency, the noise is expected to drops abruptly. From this graph we deduce the cutoff occurs around 2 GHz.

### 12.3.3 Optical losses

The discussion presented in this section is based on the standard modelling of optical losses as a beam splitter dynamics (e.g. in [114]).

From a classical view point, optical losses just consist in a renormalization of the fields amplitudes by a factor accounting for the light power losses occurring all along the light path way: mainly partial reflections, absorptions and diffractions. When it comes to considering intrinsic light quantum noise, one has to be more careful. Indeed, each element at which a power loss occurs might be formally represented as an unbalanced beam splitter with field amplitude transmission and deflection coefficients $t$ and $d$, with $d = \sqrt{1-t^2}$ to ensure energy conservation, with only one input ports fed with light. This means that, for an input field $E_{in,1}$ at the beam splitter ports 1 and no field at port 2, the output fields at ports 3 and 4 would be given by $E_3 = tE_1$ and $E_4 = dE_1$. Translating this directly into the quantum optics formalism would lead to $\hat{a}_3 = t\hat{a}_1$. If such were the case, we would end up with

$$[\hat{a}_3, \hat{a}_3^\dagger] = [t\hat{a}_1, t\hat{a}_1^\dagger] = t^2 \neq 1 \tag{534}$$

meaning the beam splitter operator would not be unitary. This problem is solved defining the beam splitter operation as

$$\begin{pmatrix} \hat{a}_3 \\ \hat{a}_4 \end{pmatrix} = \begin{pmatrix} t & -d^* \\ d & t^* \end{pmatrix} \begin{pmatrix} \hat{a}_1 \\ \hat{a}_2 \end{pmatrix} \tag{535}$$

with $|t|^2 + |d|^2 = 1$. With this definition we recover the required quantized field commutation relation (see appendix C)

$$[\hat{a}_3, \hat{a}_3^\dagger] = 1 \tag{536}$$

From equation 535, we have $\hat{a}_3 = t\hat{a}_1 - d^*\hat{a}_2$ which suggests that, in opposition to the classical picture, the filed at port 2 plays a important role and can not be overlooked even for a field of vanishing amplitude, i.e. in a vacuum state. From equation 535 we get for the output field intensity at port 3 (appendix C)

$$\langle \hat{n}_3 \rangle = |t|^2 \langle \hat{n}_1 \rangle \tag{537}$$

Th fluctuations $\sigma_3^2$ in this intensity are given by (appendix C)

$$\sigma_3^2 = |t|^4 \sigma_1^2 + |t|^2 |d|^2 \langle \hat{n}_1 \rangle \tag{538}$$

whereas a classical treatment would have suggested $\sigma_3^2 = |t|^4 \sigma_1^2$. This means that the losses contribute to the total noise adding an excess noise $|t|^2|d|^2\langle \hat{n}_1 \rangle$, the so-called *partition noise*. An intuitive way to grasp this effect is to look at the random *sorting* process occurring at the beam splitter. Considering the beam incoming to the beam splitter as a flux of pointwise particles, or photons, with random arrival times (with a poissonian distribution of the time interval length separating to successive photons, in the case of a coherent light state), we can think of the beam splitter action as deflecting randomly some photon to the non used output port, in a proportion given by the intensity deflection coefficient $D = |d|^2$. It is clear that if their is no correlation between the arrival times of the photons and the sorting process at the beam splitter, this can only turn the photon statistics more noisy, as can be seen on Figure 77. As shown above, this is actually due to the effect of the vacuum introduced on the non used input port.

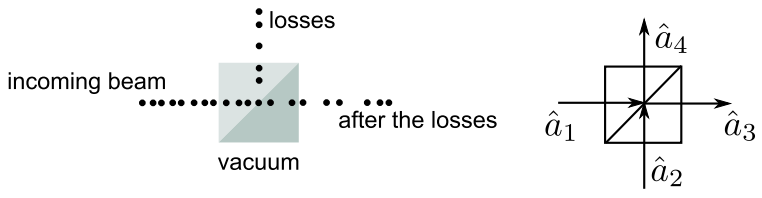


Figure 77: Optical losses can be modeled as the dynamics induced by an imbalanced beam splitter. A classical view consists in seeing the beam splitter as sorting out randomly some photons, in a proportion given by the optical losses considered. The quantum description requires taking into account the vacuum state at the unused port ($\hat{a}_2$ on the right-side picture)

The SNR at the output port 3 then relates to that at input port 1 as

$$\mathrm{SNR}^{\mathrm{out}} = \frac{\langle \hat{n}_3 \rangle}{\sqrt{\sigma_3^2}} = \frac{\langle \hat{n}_1 \rangle}{\sqrt{\sigma_1^2 + |d/t|^2 \langle \hat{n}_1 \rangle}} = \frac{1}{\sqrt{1 + |d/t|^2 \langle \hat{n}_1 \rangle / \sigma_1^2}} \frac{\langle \hat{n}_1 \rangle}{\sqrt{\sigma_1^2}} = \sqrt{\eta}\ \mathrm{SNR}^{\mathrm{in}} \tag{539}$$

where $\eta = \left(1 + |d/t|^2 \langle \hat{n}_1 \rangle / \sigma_1^2\right)^{-1}$ accounts for all the optical losses occurring between the cavity and the photodetector, including solid state losses such the quantum efficiency of the chip, electron-hole recombination and others.

In the case of a coherent input field state we have $\sigma_1^2 = \langle \hat{n}_1 \rangle$ and equation 538 reduces to

$$\sigma_3^2 = |t|^2 \langle \hat{n}_1 \rangle \left( |t|^2 + |d|^2 \right) = |t|^2 \langle \hat{n}_1 \rangle = |t|^2 \sigma_1^2 \tag{540}$$

Moreover, $\eta = |t|^2$ which is the fraction of the number of photons not lost over the lossy propagation process modeled by the beam splitter scheme discussed just above. Accounting for the losses for the PDH-like cavity locking signal and the atomic detection signal, we just add this detrimental factor to the expressions established above (see equations 483 and 485).

$$\mathrm{SNR}^{\mathrm{PDH}} = \sqrt{\eta}\ \frac{2\sqrt{2}|E|J_1 J_2 \sqrt{F}\varepsilon_L}{J_0 \sqrt{\langle \delta\hat{E}\delta\hat{E}^\dagger \rangle}} \qquad \mathrm{SNR}^{\mathrm{at}} = \sqrt{\eta}\ \frac{2\sqrt{2}|E|J_2 \sqrt{F}\phi_2^{\mathrm{at}}}{\sqrt{\langle \delta\hat{E}\delta\hat{E}^\dagger \rangle}} \tag{541}$$

## 12.4 Results

In this section we report on the experimental implementation of our first version of the cavity-assisted non-destructive detection scheme which is as well detailed in our publication (see 17).

On Figure 78 is displayed the time trace of the atomic signal $S_{2\Omega}$ (see 11.2.5) in both units of phase shift (i.e. rad) and number of atoms. The actual trace was readout on an oscilloscope (with 70 MHz bandwidth). The conversion from voltage to radian is obtained via the conversion factor determined according to the protocol described in section 12.2.4 and in this particular case gives 1 $\mu$rad per mV. The conversion from phase shift to number of atoms is based on formula 339 and amounts to approximately 5.28 atoms per $\mu$rad.

The sequence used for this detection demonstration is close to a nominal sequence except it does not include clock interrogation. Hence, all the atoms probed are in the clock ground state. The non destructive probe pulse was synchronized with the sequence via a TTL signal that turns on the double pass AOM used for the slow corrections of the probe-to-cavity feedbackloop (see Figure 57) and triggered the locking system. This means that before the TTL step, there is no probe light coupled to the cavity. It takes about 10 $\mu$s for the locking system to catch the resonance. Afterward, the signal fluctuates strongly for roughly 100 $\mu$s before reaching a much more stable behavior. We interpret this fluctuating stage as being due to the fact that at the beginning of the lock of the probe to the cavity there so many atoms trapped in the lattice that the total phase they imprint on each of the probe sidebands pulls them away from each other by an amount larger than their cavity line width. Indeed, from the graph displayed on figure 78, we see the lock is not working above 90 $\mu$rad, corresponding to 75 % of the maximal coupling in filed amplitude (see figure 79). Hence, for such a phase shit imprinted by the atom, each probe sideband is pulled away from the cavity resonance by approximately a forth of its line width and the lock is not efficient. In this regime, the approximation used for the cavity responses $F_k(\phi)$ (see equations 345 and 377) are not valid and the immunity of $S_{2\Omega}$ to fluctuations in $\varepsilon_\omega$, i.e. in probe-to-cavity frequency mismatch is not realized. Hence, the strong fluctuations seen over the first 100 $\mu$s are somehow a measure of this mismatch. It should then be in principle possible to check this looking at the correlations between the atomic signal $S_{2\Omega}$ and the PDH-like error signal $S_{1\Omega}$ used to lock the probe sidebands to the cavity.

We fitted the time trace with both an exponential decay function (gray line, Figure 78) and the heating function given by equation 270. The heating function fits much better the data, giving us some confidence in the model we derived (the main difference with an exponential decay stemming from taking into account the fact that no momentum is absorbed by the atoms in the lattice longitudinal direction). On the parameter of the heating function is $n_\gamma$ , i.e. the number of photon absorbed per atom since the beginning of the decay. Hence, the fit provides us with this number, which in this particular case

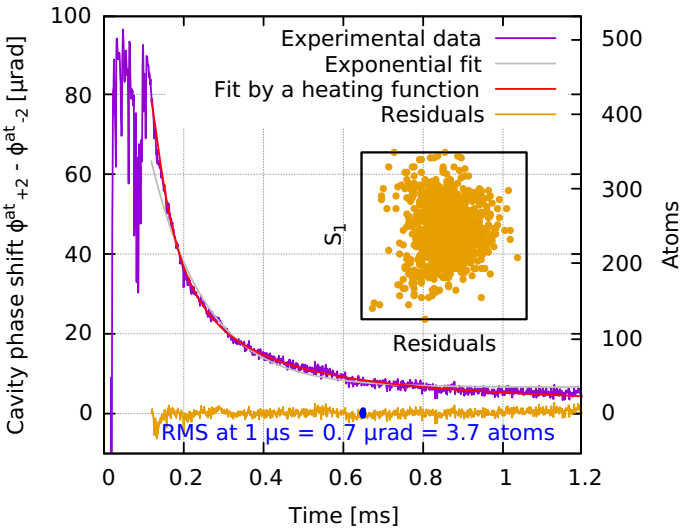


Figure 78: Time trace of the atomic signal. The purple line represents the measured phase shift imprinted by the trapped atoms in the ground state (left axis) or equivalently the number of atoms in the ground state (right axis, the conversion factor between this two quantities being that given by equation 339) as a function of time (the lock of the detection probe to the cavity being triggered at $t = 0$). The grey line is an exponential decay fit, the red one the fit by the heating function given by equation 270 and the yellow line its residual. The inset graph shows the PDH-like error signal used to lock the probe to the cavity as function of the residual. It is apparent there is no correlation between these two quantities, confirming the immunity of the atomic signal to first-order fluctuations in cavity length (see section 11.2.5). This single 1.2 ms measurement is a succession of 1 $\mu$s non-destructive measurements. Indeed, over 1 $\mu$s, the fitting by the heating function (red line) gives an amount of 38 photons scattered per atom in average, meaning that over that period the rate of kinetic energy growth is not sufficient to expel them from the trap.

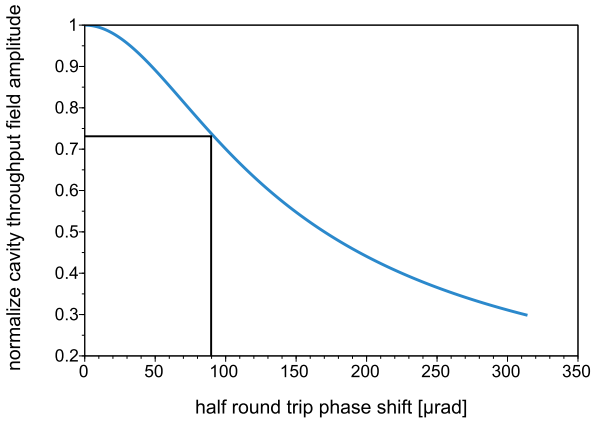


Figure 79: Normalized cavity throughput amplitude as a function of the half round trip phase shift for a finesse of 16000. For a phase shift of 90 $\mu$rad, as that imprinted by the atoms at the beginning of the measurement reported on figure 78, the throughput probe field amplitude is almost a forth lower than its maximum.

amounts to an average of 38 photons absorbed per atom in 1 $\mu$s.

The residual of the fit gives a stable rms noise over the whole decay of approximately 3.7 atoms for an integration time of 1$\mu$s (oscilloscope parameter), i.e. in a 1 MHz bandwidth. Note that our theoretical prediction based on a measurement of the photon noise and the electronic noise of the detector gives a noise of roughly 0.5 atom in a band of 1 MHz (see figure 75). There is then agreement in order of

magnitude, and a more careful analysis of the noise (in particular the electronic noise) along with an better estimation of the optical losses along the way from the cavity to the detector could probably give better results.

The corresponding detection noise is reported on Figure 80 along with the camera and photomultiplier tube detection noise as well as the quantum projection noise contributions to the probability measurement noise. It is seen we expect an improvement by approximately a factor 7.5. Extrapolating the lines to lower values of number of atoms, this contribution is below that of the quantum projection noise for an number of atom counts on the camera higher than roughly 20 000, corresponding to approximately 70 atoms, which is reachable with our system (for more than 450 atoms, the probe sidebands lock to the cavity fluctuates to much for the scheme to be operational, see Figure 78).

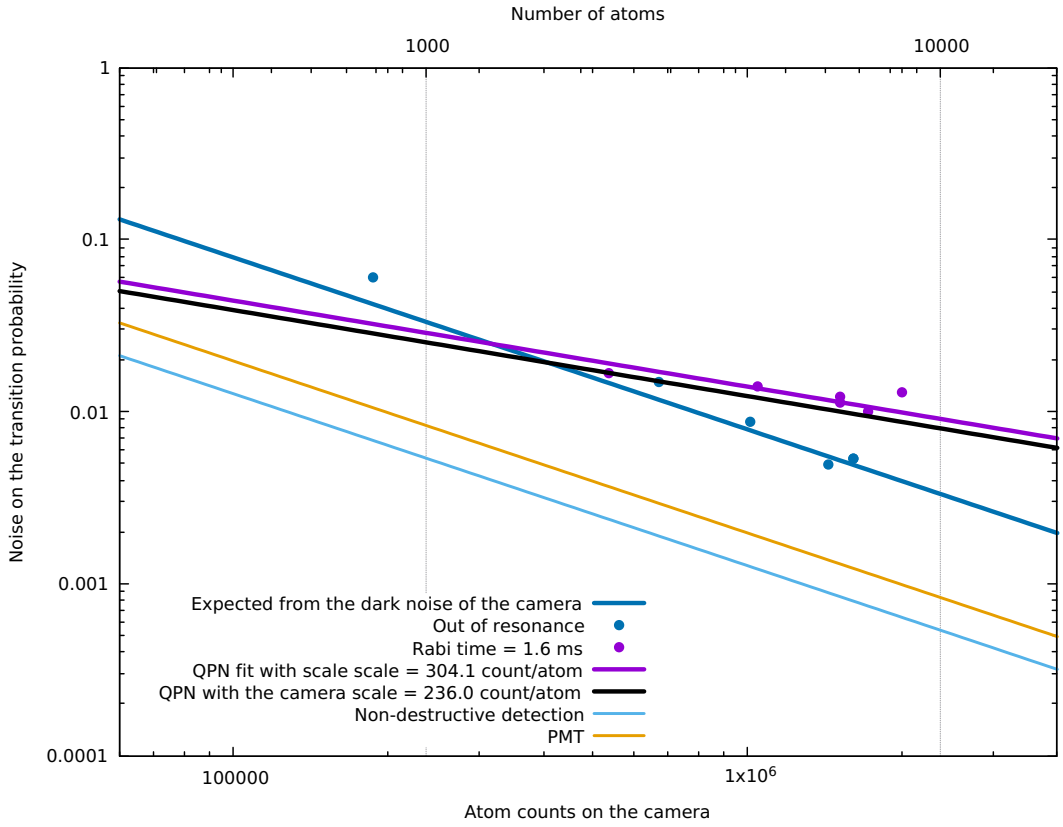


Figure 80: This graph represents the quantum projection noise and the detection noise contributions to the total noise on the measure of the transition probability (see section 8.3.2) as a function of the number of atoms probed. The non-destructive detection noise (light blue) lays a factor 7.5 below the fluorescence detection (dark blue), and a factor 1.5 below the photo multiplier tube (PMT) detection (yellow trace). Note that in addition to having a lower detection noise than the fluorescence and the PMT scheme, the cavity-assisted detection scheme is non destructive. It can be seen as well that for a number of atoms as low as 42 ($= 10^4 \times 0.0042$, where $10^4$ is the number of atoms at which the non-desctructive detection noise crosses the quantum projection noise, 0.0042 being the camera counts/number of atoms conversion factor), to be compared to around 100 ($2.4 \times 10^4$ camera counts) for the PMT and 1700 ($4 \times 10^5$ camera counts) for the fluorescence.

# 13 Limitations of the CNDD scheme

We were able to achieve with the CNDD scheme a $SNR(t = 1\ \mu s) \sim 135$ for about 500 atoms trapped in the lattice with an RMS noise of approximately 3.7 atoms within 1 $\mu$s, duration over which an average of 38 photons were scattered per atoms. Entering the quantum regime requires scattering less than 1 photon per atom during the detection. Extrapolating the CNDD results to a detection pulse of duration $T = 1/38\ \mu s \sim 26$ ns, during which each atom would scatter 1 photon in average, assuming white noise, the expected $SNR(T)$ would be $SNR(T) = SNR(t = 1\ \mu s)/\sqrt{38} \sim 23$ which is still sufficient to monitor the QPN limit for a total number of $\sim 500$ atoms. Indeed, QPN $= \sqrt{N_{at}}$, i.e. for 500 atoms QPN $\sim 22.3 \lesssim 23$. Nevertheless, their are no available electronics allowing us to perform such short measurement. For a detection pulse of 1 $\mu$s, which sounds feasible even though demand, entering the quantum regime requires a photon scattering at least 38 times smaller. There are two ways one could think of to reduce the scattering rate: *i)* reduce the power of the SBs coupled to the cavity and seen by the atoms, *ii)* increase the probe SBs detuning to the ${}^1S_0 \rightarrow {}^1P_1$ transition. Indeed, the number of photon scattered per atom per unit of time scales,in the case of large detuning which corresponds to our operational configuration, as

$$n_\gamma \propto \frac{\Omega_0^2}{\Delta^2}$$

where $\Omega_0^2 \propto P_{opt}$.

As mentioned earlier the first option requires lowering the modulation depth $\beta$ which is impossible within this scheme since it is already set to its lower bound a sufficient PDH-like error signal amplitude demands. The second option is not affordable nether since the detuning $\Delta$ from the ${}^1S_0 \rightarrow {}^1P_1$ transition is set by the cavity geometry through the relation

$$\Delta = \frac{\Delta_{FSR}}{2} = \frac{c}{4L}$$

giving $\Delta \sim 1.87$ GHz for $L \sim 4$ cm. The two mirrors of the in-vacuum cavity are mounted on two bellows which could be compressed or extended by no more than half a centimeter each, meaning a maximal length reduction of 1 cm, giving an upper bound for the detuning $\Delta_{max} \sim 2.5$ GHz, i.e. a factor $\sim 1.34$ in detuning resulting in a dividing factor 1.8 in terms of number of scattered photon per atom, ridiculus compared to the reduction target by a factor $\sim 40$.

## 13.1 Overcoming the CNDD scheme limitations

In order to overcome the limitations inherent to our CNDD scheme preventing from entering the quantum regime, we came up with new ideas strongly inspiered by what we had achieved so far. The main trick here is to keep the same cavity geometry, i.e. $L \sim 4$ cm, but spanning $3 \times \Delta_{FSR}$ istead of one only, and coupling the $4^{th}$ order SBs to the cavity instead of the $2^{nd}$ ones.

The first direct gain of this new scheme, referred to hereafter as the quantum non destructive detection (QNDD) scheme, is that the detuning relative to the ${}^1S_0 \rightarrow {}^1P_1$ transition is now $\Delta \sim 3 \times \frac{\Delta_{FSR}}{2} \sim 5.6$ GHz, resulting in a reduction by a factor $3^2 = 9$ compared to the CNDD scheme.

The second advantage of this scheme is that it allows the same amplitude for the PDH-like locking signal while a much lower intensity for the fields coupled to the cavity i.e. seen by the atoms. This is discussed in details in the 15.3.2 section.

# 14 Quantum non demolition detection (QNDD)

The current stabilities of our two strontium optical clocks are Dick effect limited at $4.7 \times 10^{-16}$ at 1 s (see section 7.2.3). However, as pointed out in section 8.3, we expect from the implementation of our cavity assisted non destructive measurement reported in section 11 a reduction by roughly one order of magnitude of the Dick effect. Moreover, as depicted on Figure 80, the detection noise contribution to the probability readout is expected to be below that of the quantum projection noise (QPN) for more than 70 atoms (more than a factor 2 below for more than 200 atoms). Based on our simulated Allan deviation QPN contributions (see Figure 41) we expect the QPN to be the next stability limitation for a number of atoms below $\sim 3000$. As elaborated in section 8.2, the QPN can be seen as stemming from the fact that classical measurements are projective, i.e. result in the collapse of the wave function corresponding to the detected quantity, combined with the fact that the outcomes of these projections are uncorrelated from atom to atom. Hence, there are at least two aspects one could try to elaborate on. Going to non projection measurement regimes and/or inducing some correlations between the atoms states. Various alternatives have been successfully explored for the realization of detection beating this limitation in the context of atomic clocks. However most of them have been implemented on clocks based on alkali atoms such as Cesium or Rubidium [121, 122, 123] and only a few in the context of optical clocks [130].

In this section we briefly exposed the main concepts and strategies developed to beat the quantum projection noise in the context of cavity assisted measurement. Because of lack of time to dedicate to theoretical developments, we harnessed the problem with an intuitive approach and started to set a setup that we think may allow for pushing our cavity-assisted detection system to the quantum regime of non destrucivity. The setup, based on similar conceptions as that presented in section 12.1, is exposed as well.

## 14.1 Quantum projection noise and spin squeezing

In this paragraph we expose in the broad lines the link between quantum projection noise and spin squeezing.

Any quantum two level system can be seen as a 1/2-spin, which is in particular the case for our idealized two-level clock system, where the clock state of each atom is described within a two-dimensional vector space spanned by the clock ground and excited states $|g\rangle$ and $|e\rangle$. In other words, the clock state $|\psi\rangle$ of any atom can be expressed as a unitary vector

$$\psi = a\,|g\rangle + b\,|e\rangle \qquad\qquad |a|^2 + |b|^2 = 1 \tag{542}$$

The 1/2-spin Pauli matrices $\sigma_i$ can then be defined as in the case of spin$-1/2$ particles. For example

$$\sigma_z = \frac{1}{2}\begin{pmatrix} 1 & 0 \\ 0 & -1 \end{pmatrix} = \frac{1}{2}\left(|g\rangle\langle g| - |e\rangle\langle e|\right) \tag{543}$$

They obey the usual commutation relations

$$[\sigma_i, \sigma_j] = i\varepsilon_{ijk}\sigma_k \tag{544}$$

For an ensemble of $N$ atoms, each with 1/2-spin operator $\mathbf{j}_n$, we define the total spin $\mathbf{J}_N$ operator as

$$\mathbf{J} = \sum_n \mathbf{j}_n \tag{545}$$

Its components $\mathbf{J}_i$ follow the same commutations rules as the $\sigma_i$, resulting in the uncertainty relations

$$(\Delta J_y)^2\,(\Delta J_z)^2 \geq \frac{1}{4}|\langle J_x\rangle|^2 \tag{546}$$

In an idealized vision, the clock pulse brings all the atoms trapped in the lattice from the ground state to a nearly balanced superposition of ground and excited state

$$|\psi_n\rangle\,|g\rangle \longrightarrow \frac{|g\rangle + |e\rangle}{\sqrt{2}} \tag{547}$$

The many-body state of the set of all the trapped atoms then reads

$$|\Psi\rangle_N = \left(\frac{|g\rangle + |e\rangle}{\sqrt{2}}\right)_1 \otimes \left(\frac{|g\rangle + |e\rangle}{\sqrt{2}}\right)_2 \otimes \ldots \otimes \left(\frac{|g\rangle + |e\rangle}{\sqrt{2}}\right)_{n=N} \tag{548}$$

Such state satisfies the minimum uncertainty relationship and $(\Delta J_z)^2 = (\Delta J_z)^2 = N/2$ which corresponds to our $\sigma_e = \sqrt{Np_e(1-p_e)}$ in the case of the balanced superposition $|\Psi\rangle_N$, i.e. with $p_e = 1/2$, from which we deduced the quantum projection noise itself (see section 8.2). Hence, pulling the stability below the QPN limits requires finding a way to achieve $(\Delta J_z)^2 < N/2$, or

$$\frac{\Delta J_z}{|\langle \mathbf{J} \rangle|} = \frac{1}{\sqrt{2N}} = \frac{1}{\sqrt{2}}\sigma^2_{\text{QPN}} \tag{549}$$

We note here that there is no necessity to refer to any projection effect to get this limitation, and it is usually called the standard quantum limit (SQL). Spin squeezing then consists in reducing the noise on the measured quantity, in our case $J_z$, below this limitation. Note that, since the uncertainty relation given above must hold, meaning that squeezing the noise in the direction $z$ can be only at the expense of an noise increase in the $y$ direction. Spin squeezing can be characterized in different ways. One of the most widely used characterization is the parameter $\xi_z$ defined as [115]

$$\xi_z^2 = \frac{N(\Delta J_z)^2}{\langle J_x \rangle^2 + \langle J_y \rangle^2} \tag{550}$$

which goes below unity for squeezed states.

## 14.2 Spin squeezing and entanglement

As mentioned in the previous paragraph, they is no need to resort on the concept of projection measurement to derive the SQL. However, we give here a hint about how spin squeezing makes the link between the SQL and the concept of projective measurement. This requires the concept of entanglement that we recall here briefly. A $N$-body pure state $|\Psi\rangle_N$ is said to be separable if and only if it can be expressed under the form

$$|\Psi\rangle_N = |\psi\rangle_1 \otimes ... \otimes |\psi\rangle_{n=N} \tag{551}$$

where each $|\psi\rangle_n$ accounts for the state of a single particle. A state is said to be entangled when it is not separable. For example, the coherent spin state defined by equation 548 is separable. It can be shown [116] that each time there is squeezing, there is entanglement. Hence, only entangled states can provide spin squeezing, i.e. $\xi < 1$. We can see, with a very simple example how entanglement relates to projection. Consider the coherent spin state defined as in equation 548 with two atoms only

$$|\Psi\rangle_2 = \frac{|gg\rangle + |ge\rangle + |eg\rangle + |ee\rangle}{2}, \qquad |uv\rangle = |u\rangle \otimes |v\rangle \tag{552}$$

which we know is SQL limited. When performing a projective measurement each of the 2-body term in the sum can be obtained with equal probability 1/4. As mentioned in the previous paragraph, the transition probability is obtained from the estimation $p_e = N_e/(N_e - N_g)$ which is a measure of $J_z$, $N_e$ and $N_g$ being respectively the number of atoms projected onto $|e\rangle$ and $|g\rangle$. Then, the probability to find $p_e = 0$ is 1/4, as well as for $p_e = 1$ and is 1/2 for the "right" one[78], i.e. $p_e = 1/2$. Meaning the noise on $p_e$ is large: $\sigma^2_{p_e} = 1/8$. On the other hand, considering the entangled state

$$|\Phi\rangle_2 = \frac{|eg\rangle + |ge\rangle}{\sqrt{2}} \tag{553}$$

the only possible outcome for $p_e$ is 1/2 (with unit probability) and therefore $\sigma_{p_e} = 0$ meaning there is no noise on $p_e$. Note that for this case $\xi_z^2 = 0 < 1$ meaning $|\Phi\rangle$ is a squeezed state. This case is of course too simple to infer any general result but hints about the link between correlation of the projections, entanglement and squeezing. Somehow, a squeezed spin state is such that if projectively measured, it leads to a reduced variance.

The whole game is then to find a way to go from $|\Psi\rangle_2$, state to which takes the clock pulse[79], to $|\Phi\rangle_2$.

[78] i.e. that corresponding to the definition $p_e = |b|^2$, where $b$ is the probability amplitude appearing in $|\psi\rangle = a|g\rangle + b|e\rangle$.
[79] Note that the clock pulse itself might induce some atom-to-atom entanglement.

## 14.3 Nonlinear Hamiltonians

Most of spin squeezing realization rely on non-linear Hamiltonians [125, 126, 127, 118, 119] typically involving terms like $\chi J_z^2$ or $\chi(J_xJ_y + J_yJ_x)$ [117]. Many experimental realization based on this type of Hamiltonians have demonstrated over the last decades. The non-linearity can stem from various sources such as collisions (typically for "spontaneous" spin squeezing in Bose-Einstein condensates) or interactions with a shared laser field, the latter being the case for most of the clock demonstration. Here we present the common one axis technique widely used to squeeze the spin $J_z$ corresponding to microwave transitions between hyperfine levels of alkali ground states.

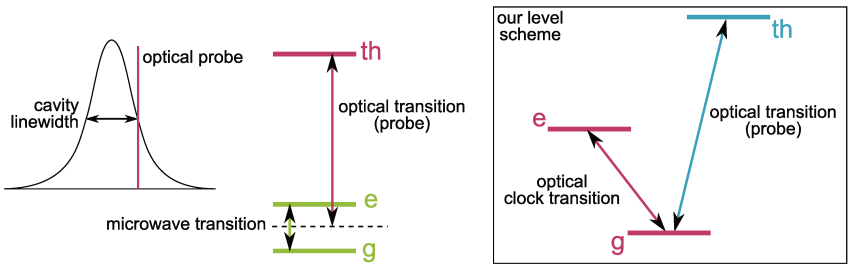


Figure 81: On the left-side: typical scheme used for the emergence of the squeezing non-linear Hamiltonian for microwave clocks. The atoms are stored in an optical cavity. An optical probe coupling the two clock states $|g\rangle$ and $|e\rangle$ to a third state $|th\rangle$ is tuned in such a way it is at equal detuning from both the $|g\rangle \rightarrow |th\rangle$ and $|e\rangle \rightarrow |th\rangle$ transitions. The cavity is set in such a way it is detuned from resonance with the probe by half a linewidth, to maximize the sensitivity to variations in probe phase and the linearity of the response. Adiabatically eliminating the third state gives that the phase shift imprinted on the probe by the atoms is proportional to $J_z$. But because of the phase discriminant impose by the cavity and the fact the cavity is half a linewidth away from resonance with the probe, the number of photons in the cavity mode is proportional to the phase imprint, and therefore proportional to $J_z$. But the atom-field interaction Hamiltonian is proportional to $J_z\hat{n}$, $\hat{n}$ the number operator for the cavity field. Hence the Hamiltonian is proportional to $J_s^2$, which provides the squeezing non-linearity. Right-side: In our atomic level and probe scheme, such a trick can not be used, since there is no way to couple the two clocks state using the intermediate third state. In other words, there is no field mediated coupling, and one has to resort on other techniques.

With alkali atoms, one can implement cavity-assisted spin squeezing using an optical transition. Consider an alkali atom with level structure as that shown in Figure 81 where $|g\rangle$ and $|e\rangle$ represent the hyperfine levels of the ground state used as a clock transition[80] and $|th\rangle$ a third level separated from $|g\rangle$ and $|e\rangle$ by an optical transition at frequency $\nu$. The atoms are place in an optical cavity into which laser light at frequency $\nu$ is partially coupled in the sens that it is detuned from the cavity resonance by half a cavity line width as shown on picture 81. The idea is to tune the optical frequency $\nu$ half way between the two $|g\rangle \rightarrow |tg\rangle$ and $|e\rangle \rightarrow |th\rangle$ optical transitions (see 81). It can be shown [120, 121] that if the number of photon in the cavity is sufficiently small the third state $|th\rangle$ can be adiabatically eliminated, resulting in an atom-field interaction Hamiltonian of the form

$$\hat{H} = \chi c^\dagger c J_z \tag{554}$$

The point here is that the presence of the atoms changes the local index of refraction inside the cavity, shifting the cavity-to-probe resonance as discussed in section 11. Due to this shift, the probe-to-cavity coupling is altered, resulting in a change of the number of photons stored in the cavity. But the shift itself depends on the number of atoms in the cavity and their internal state (the polarizability bieng different for $|g\rangle$ and $|e\rangle$). It turns out that when the probed frequency $\nu$ is precisely half-way between the two transitions, the shift is proportional to the population difference between the two states, i.e. is proportional to $J_z$. For a cavity-to-probe detuning of half a cavity line width this results in a number of

[80] as that used for the S.I. definition of the second

photons in the cavity $\langle c^\dagger c \rangle$ proportional to $J_z$. Finally, we end up with an interaction Hamiltonian of the form

$$\hat{H} = \Lambda J_z^2 \tag{555}$$

which is the non-linearity required for the squeezing to occur. Note that to keep the probe-to-cavity detuning constantly proportional to $J_z$ one has to measure the shift induced by the atoms in the probe field and to feedback the probe frequency. This is the reason why this method is often referred to as cavity feedback squeezing.

However, this technique can not be used when $|g\rangle$ and $|e\rangle$ are separated by an optical transition and one has to resort on other tricks. Cavity spin squeezing of the Strontium clock transition has been demonstrated using cavity resonant at the clock light it self [130], even in the case no field is coupled to the cavity (the vacuum state of the cavity mode induces the squeezing) [129] and some proposals were done for a lattice induced squeezing [134]. Regarding our levels scheme[81] where the cavity mode is close to the $|g\rangle \rightarrow |th\rangle$ transition frequency but does not address the clock excited state $|e\rangle$, proposal have been made [131, 132, 128] and future development of our clocks will probably be based on such pioneering works. We recommend as well the careful reading of [133] whose central ideas are given in the next paragraph.

## 14.4 Atom counting via non-demolition measurement

The idea of non-demolition measurement, i.e. measurement without projection of each individual atomic state in order to get information about the global many-body state only, is to couple the system whose state is investigated (here the total spin state component $J_z$) to a *meter* (in our case the probe sidebands fields coupled to the cavity), and operate a strong, i.e. projective, measurement of this meter. In our case the coupling system and meter is provided by the field atom interaction and can be reduced to its dipole approximation form. This strong measurement would present variance as well. Hence, implementing a non-demolition measurement system is beneficial only if the variance on the meter measurement is smaller than that obtainable from a direct projective measurement of the system. This is addressed in the particular case of cavity-assisted atom counting, which is our case, in [133] where a careful derivation of the variance of the filed phase shift measurement is derived as a function of the relevant parameters characterizing the system. This treatment accounts for the free-space scattering of field photons thus resulting in projection of the individual atom emitting the photon out of the cavity mode. We encourage for the investigation in this direction for the next development step for the realization of a sub-quantum projection noise stability clock.

Our contribution reduces to the experimental implementation of a scheme minimizing the number of photons scattered into free-space, aiming at less than one photon scattered in average per atom over the detection time, which is exposed below.

[81] our in-vacuum has a high finesse for the $^1S_0 \rightarrow {}^3P_0$ transition and we are bound to resort on it unless planning heavy modifications of the setup, which is hardly compatible with metrological activities

# 15 QNDD scheme

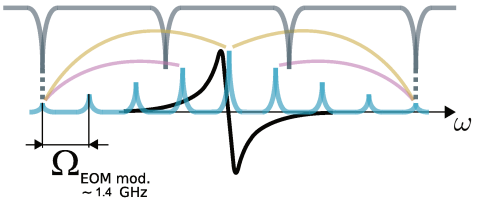


Figure 82: The cavity resonances, separated by $\Delta_{\mathrm{FSR}}$, are represented upside-down by the gray line. The probe carrier is set half way between two cavity consecutive resonances. The sidebands are generated by an EOM which modulation frequency is $\Omega = (3/8)\Delta_{\mathrm{FSR}} \approx 1.4$ GHz. The EOM modulation depth is such that the forth order sidebands can not be neglected. Because of the factor 3/8 the 8 sidebands and the carrier (blue line) span a range covering 3 cavity free spectral ranges and the $4^{th}$ order sidebands only are coupled to the cavity. As in the CNDD scheme, the atomic response is anti-symmetric centered at the carrier resonance. The beatnote at $3\Omega$ (pink links) provides the PDH-like error signal used to lock the sidebands to the cavity, while that at $4\Omega$ (yellow links) carries the atomic information.

As mentioned in section 13, the main problem of the non destructive detection system presented in section 11 that prevent it reaching the quantum regime, i.e. a regime where the presence of the atom is detected without projection, is that it is not possible to operate it in a configuration such that the number of photon scattered over the detection pulse is less than unity. Here by *scattered* we mean scattered in an incoherent way, i.e. in such a way that the re-emitted photon is not scattered within the probe mode. Our solution consists in decreasing the photon scattering rate by both increasing the prob-to-atomic resonance detuning and lowering the power coupled to the cavity (see section 13). The probe sidebands frequencies relate to the cavity resonances as shown in Figure 82.

## 15.1 Cavity and atomic signals

In this section we derived the expressions for the PDH-like cavity signal as well as the atomic signal. The derivation is similar to that given in section 11.

As in the CNDD scheme, the probe field is first phase modulated through an EOM modulated at frequency $\Omega$ and depth $\beta$, is then directed to the cavity and reflected back towards a fast detector where all the beatnotes at all the $\Omega$ harmonics frequencies are collected, resulting in an intensity $I$ that splits into $\Omega$ harmonics components as

$$I = \sum_{q=-\infty}^{\infty} I_{q\Omega} \tag{556}$$

with

$$I_{q\Omega} = |\mathbf{E}|^2 \left( \sum_p J_p J_{p-q} F_p F_{p-q}^* e^{iq\Omega t} + \sum_p J_p J_{p+q} F_p F_{p+q}^* e^{-iq\Omega t} \right) \tag{557}$$

One of the main differences from the CNDD case stems from the fact that here the $4^{th}$ order SBs only are coupled to the cavity, meaning that the factors encompassing the phase shift due to cavity round trips and the atoms polarizability $F_q$ all equal unity unless $q = \pm 4$ for which the approximation $F_{q=\pm 4}(\Phi) \sim -i\sqrt{F}\Phi[\pi]$ holds.

Moreover, in the QNDD scheme, the PDH-like error signal is obtained down mixing $I$ at $3 \times \Omega$ and the atomic signal comes from a demodulation at $4 \times \Omega$.

## 15.2 QNDD PDH-like error signal

### 15.2.1 Half round trip phase shift

In this scheme the $4^{th}$ order sidebands are coupled to the cavity and separated by $3\Delta_{\mathrm{FSR}}$ then covered by $8\Omega$, $\Omega$ being the EOM modulation frequency. Hence

$$\Omega = \frac{8}{3}\frac{c}{2L}, \qquad \omega_k = 2\pi\left(\left(n+\frac{3}{2}\right)+k\frac{3}{8}\frac{c}{2L}\right) \tag{558}$$

and, allowing for fluctuation in cavity length $L = L_0 + \delta L$, probe carrier frequency $\omega = \omega_0 + \delta\omega$ and EOM modulation frequency $\Omega = \Omega_0 + \delta\Omega$, we have for the half round trip phase shift of sideband $k$

$$\phi_k = \pi\left(\left(n+\frac{3}{2}\right)+k\frac{3}{8}\right)+\pi\left(n+\frac{3}{2}\right)\varepsilon_\omega + k\pi\frac{3}{8}\varepsilon_\Omega + \phi^{at}_{\pm 4} \tag{559}$$

### 15.2.2 PDH-like cavity locking signal

As said above, the locking signal is obtained demodulated the intensity collected on the fast detector at $3\times\Omega$, i.e. multiplying $I_{3\Omega}$ by $A_3\sin(3\Omega t+\phi_3)$ leading to

$$S_{3\Omega} = |\mathbf{E}|^2\frac{A_3}{2i}\left(e^{i(3\Omega t+\phi_3)} - c.c.\right) I_{3\Omega} \tag{560}$$

Proceeding the same as in the CNDD case, this leads to

$$S_{3\Omega}(\phi_3) = |\mathbf{E}|^2 A_3\Bigg(\sin(\phi_3)\sum_q J_q J_{q-3}\mathrm{Re}\left(F_q F^*_{q-3}\right) \tag{561}$$

$$-\cos(\phi_3)\sum_q J_q J_{q-3}\mathrm{Im}\left(F_q F^*_{q-3}\right)\Bigg) \tag{562}$$

here again, as for 361, for each pair of indices $(q, q-3)$, its counterpart $(3-q,-q)$ appears as well in the summation, and because of Bessel's coefficients parity

$$J_{3-q}J_{-q}\mathrm{Im}\left(F_{3-q}F^*_{-q}\right) = -J_q J_{q-3}\mathrm{Im}\left(F_{3-q}F^*_{-q}\right) \tag{563}$$

and the above summation running from $-\infty$ to $+\infty$ can be rewritten as a positive only indices summation, leading to

$$S_{3\Omega}(\phi_3) = |\mathbf{E}|^2 A_3\Bigg(\sin(\phi_3)\sum_{q\geq 0} J_q J_{q-3}\mathrm{Re}\left(F_q F^*_{q-3} - F_{3-q}F^*_{-q}\right) \tag{564}$$

$$-\cos(\phi_3)\sum_{q\geq 0} J_q J_{q-3}\mathrm{Im}\left(F_q F^*_{q-3} - F_{3-q}F^*_{-q}\right)\Bigg) \tag{565}$$

Setting the demodulation phase $\phi_3$ to 0 $[\pi]$ we get

$$S_{3\Omega}(0) = -|\mathbf{E}|^2 A_3\sum_{q\geq 0} J_q J_{q-3}\mathrm{Im}\left(F_q F^*_{q-3} - F_{3-q}F^*_{-q}\right) \tag{566}$$

Since the $\pm 4^{th}$ order SBs only are coupled to the cavity in the QNDD scheme, all terms $F_q F^*_{q-3} - F_{3-q}F^*_{-q}$ vanish unless $q$ or $q-3=4$, since $F_q = 1$ for uncoupled SBs. Therefore $S_{3\Omega} \equiv S_{3\Omega}(\phi_3 = 0)$ reduces to

$$S_{3\Omega} = -|\mathbf{E}|^2 A_3 J_4 J_1 \mathrm{Im}\left(F_4 + F_{-4}\right) \tag{567}$$

$$= |\mathbf{E}|^2 A_3 J_4 J_1\sqrt{F}\left((2n+3)\pi\varepsilon\omega + \phi^{at}_{-4} + \phi^{at}_{+4}\right) \tag{568}$$

$$= |\mathbf{E}|^2 A_3 J_4 J_1\sqrt{F}\,(2n+3)\pi\varepsilon\omega \tag{569}$$

where we used the anti-symmetry of the atomic response $\phi^{at}_{-4} = -\phi^{at}_{+4}$ meaning that $S_{3\Omega}$ can be used as a error signal for the lock of the probe $4^{th}$ sidebands to the cavity.

### 15.2.3 Atomic signal

The atomic signal is obtained demodulating at $4 \times \Omega$, i.e. mixing the PD signal with a local oscillator $A_4 \sin(4\Omega t + \phi_4)$. Proceeding as above for the PDH-like error signal, but without sign flip in 563, we obtain

$$S_{4\Omega}(\phi_4) = |\mathbf{E}|^2 A_4 \Bigg( \sin(\phi_4) \sum_{q\geq 0} J_q J_{q-4} \mathrm{Re}\left(F_q F^*_{q-4} + F_{4-q} F^*_{-q}\right) \tag{570}$$

$$- \cos(\phi_4) \sum_{q\geq 0} J_q J_{q-4} \mathrm{Im}\left(F_q F^*_{q-4} + F_{4-q} F^*_{-q}\right) \Bigg) \tag{571}$$

Setting $\phi_4$ to 0 $[\pi]$, $S_{4\Omega} \equiv S_{4\Omega}(\phi_4 = 0)$ reads

$$S_{4\Omega}(0) = -|\mathbf{E}|^2 A_4 \sum_{q\geq 0} J_q J_{q-4} \mathrm{Im}\left(F_q F^*_{q-4} + F_{4-q} F^*_{-q}\right) \tag{572}$$

which reduces to

$$S_{4\Omega} = -|\mathbf{E}|^2 A_4 J_4 J_0 \mathrm{Im}\left(F_4 - F_{-4}\right) \tag{573}$$

$$= |\mathbf{E}|^2 A_4 J_4 J_1 \sqrt{\mathcal{F}} \left(3\pi\varepsilon_\Omega + 2\phi^{at}_{+4}\right) \tag{574}$$

which can then be used as an atomic signal.

## 15.3 QNDD implementation

### 15.3.1 Radiofrequency source

For the realization of the previous non destructive detection setup we rely for the radiofrequency source at $\Omega = \Delta_{\mathrm{FSR}}/4 \approx 930$ MHz on a commercial synthesizer (model) ranging from DC to 1.2 GHz. However, for this new scheme the required modulation frequency is of the order of $\Omega = 3\Delta_{\mathrm{FSR}}/ \approx 1.4$ GHz which is out of reach of our available device. Instead of going for a heavy *over kill* high cost device we decided to use a evaluation board for a fractional-N/Integer-N PLL Frequency Synthesizer (Analog Device, ADF 43-50) which is 10 cm by 10 cm board, 180 Euro (th be compared with the 5 k Euro for the upgraded version of our previous synthesizer), ranging from 137.5 MHz to 4.4 GHz with 4 outputs. It turned out that for a given set frequency, each output provides the 4 first harmonics of the set frequency. This is probably a disadvantage for most applpications but it is perfectly matching our needs. Indeed, we need a signal at $\Omega \approx 1.4$ GHz for the EOM modulation but as well one at $3\Omega \approx 4.2$ GHz used as a local oscillator for the down mixing of the PDH-like signal and one at $5.6\Omega \approx$. For the $3\Omega$ we directly use the third harmonics signal and for the $4\Omega$ signal we frequency double the second harmonic.

### 15.3.2 EOM modulation depth choice

Assuming we would operate the QNDD with the same total probe optical power as in the case of the CNDD, and considering the QNDD locking system would require the same SNR as the CNDD's, we chose $\beta_Q$, where the index $Q$ stands stands for QNDD, such that the PDH-like signal amplitude of the QNDD scheme is similar to that of the CNDD, for which it was set to its minimum. The locking signals of the two schemes are, respectively

$$S_{1,C} = |\mathbf{E}_C|^2 A_1 J_2(\beta_C) J_1(\beta_C) \mathrm{Im}\left(F_{2,C} - F^*_{-2,C}\right)$$

and

$$S_{3,Q} = |\mathbf{E}_Q|^2 A_3 J_4(\beta_Q) J_1(\beta_Q) \mathrm{Im}\left(F_{4,Q} - F^*_{-4,Q}\right)$$

where the indices $c$ and $Q$ stand for CNDD and QNDD respectively. The equal probe power assumption means that $|\mathbf{E}_C| = |\mathbf{E}_Q|$. The amplitudes of the down mixing local oscillators $A_{1,3}$ are determined by the specifications of the particular mixers used for the implementations. It turned out that for both setup, even though the mixers are not the same, they require an input power of +7 dBm, meaning that $A_1 = A_3$. Furthermore, when the relevant SBs are coupled to the cavity, we have

$$\mathrm{Im}\left(F_{2,C} - F^*_{-2,C}\right) = 2\phi^{\omega}_{+2,C}, \quad \mathrm{Im}\left(F_{4,Q} - F^*_{-4,Q}\right) = 2\phi^{\omega}_{+4,Q}$$

where $\phi^{\omega}_{+2,C}$ and $\phi^{\omega}_{+4,Q}$ do depend on the probe detuning $\delta\omega$ and therefore

$$\mathrm{Im}\left(F_{2,C} - F^{*}_{-2,C}\right) = \mathrm{Im}\left(F_{4,Q} - F^{*}_{-4,Q}\right)$$

In the end we are left with

$$\frac{S_{1,C}}{S_{3,Q}} = \frac{J_2(\beta_C)J_1(\beta_C)}{J_4(\beta_Q)J_1(\beta_Q)}$$

The assumption that the two locking systems require the same SNR demands this ratio to be close to unity, condition that rules the choice of $\beta_Q$. The smallest value compatible with a descent lock of the SBs to the cavity in the CNDD scheme $\beta_C \sim 0.2$ gives a lower bound $\beta_Q = 1.1$.

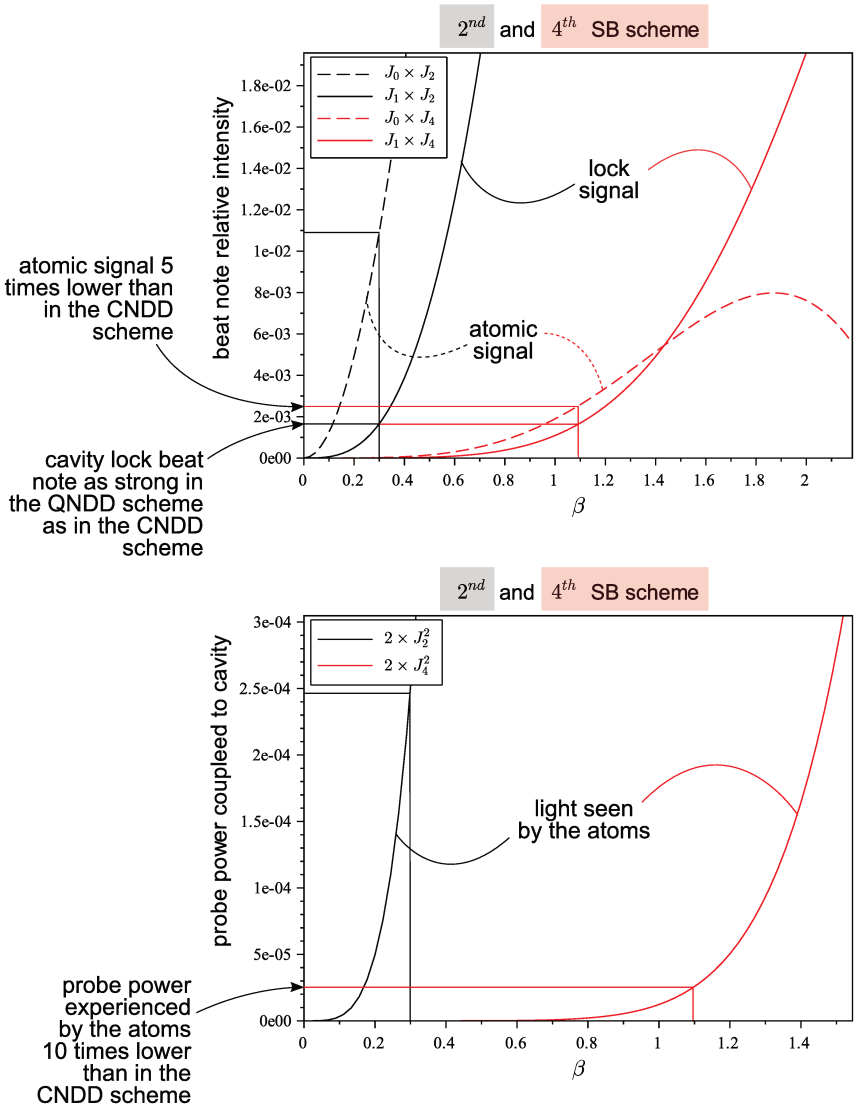


Figure 83: The top graph represents the simulation of the probe sidebands beatnotes relative intensities as a function of the EOM modulation depth $\beta$. The bottom one displays the simulated total power of the probe sidebands coupled to the cavity i.e. experienced by the atoms, as a function of $\beta$. The black traces correspond to the CNDD scheme (where the second-order sidebands are coupled to the cavity) and the red ones to the QNDD scheme (where the forth-order sidebands are coupled). The CNDD scheme was operated with $\beta \approx 0.3$. Our strategy for the QNDD scheme is to couple 10 times less power to the cavity, which corresponds to $\beta \approx 1.1$ (bottom graph). The atomic signal is then expected to be 5 times lower in power whereas the locking signal should be as strong as before, which is one of our requirements. Hence, operating the EOM at $\beta \approx 1.1$ is a good strategy to start with.

The amount of probe power coupled to the cavity, i.e. seen by the atoms, scales as $J_2^2(\beta_C)$ for the CNDD scheme and $J_4^2(\beta_Q)$ for the QNDD's. For $\beta_C = 0.2$ and $\beta_Q = 1.1$

$$\frac{J_4^2(\beta_Q)}{J_2^2(\beta_C)} \sim 0.1$$

meaning that the probe power seen by the atoms in the QNDD scheme is about 10 times lower than in the CNDD's, resulting in a reduction by a factor 10 in the number of photon scattered per atom per unit of time.

### 15.3.3 Merging the $4^{th}$ order sidebands in the cavity

As for the previous system, the probe sidebands used to detect the atoms, in this case the $4^{th}$ order's, have to be simultaneously coupled to the cavity. We use the same technique as exposed in section 12, meaning we look at the cavity throughput signal on an oscilloscope while scanning the length of the cavity by sending a triangle modulation voltage to one of the cavity locking PZT actuator and vary the EOM frequency till the two $4^{th}$ order sidebands merge. The difficulty here being that the EOM we use (Q-Big EO-T1500M3-VIS_TXC) has to be tuned in such a way that the modulation frequency matches its resonance to better than 13 MHz. Moreover, the synthesizer board we decided to use does not allow for a continuous tuning of its frequency. One has to change the frequency step by step, retuning the EOM resonance each time. On top of that, the modulation frequency for this scheme is set to $\Omega = 3\Delta_{\mathrm{FSR}}/8$ meaning that the full pattern ranging from the $-4^{th}$ order sideband till the $+4^{th}$ order's spans three cavity free spectral ranges. The corresponding cavity throughput monitored on the oscilloscope then overlaps with that next one, as shown on Figure 84. To identify which sideband corresponds to which pick on the cavity throughput signal we first modulate the EOM at low modulation depth in order to have the carrier and the first order sideband only on the oscilloscope trace. We then can identify both the carrier and the first order sidebands and the distance corresponding to $\Omega$ (EOM mod. freq. on picture 84). We then tune the modulation depth to a value such that the $4^{th}$ order sidebands are visible and look for picks located at position (i.e. time on the oscilloscope) translated by an integer number of the interval corresponding to $\Omega$. We then follow the same protocol as in section 12.1.2.

### 15.3.4 Preliminary results

We present very preliminary results obtained with this new scheme as seen on Figure 85. The behavior is comparable to that of the previous scheme, except that no strong fluctuations are seen just after the sidebands-to-cavity locked be efficient, which takes roughly 50 $\mu$s on this particular example, which is afterwards followed by the atom number decay due to heating. The atomic signal to noise ratio amounts to approximately 5 only during the decay. This is probably partially due to the 2 GHz cutoff frequency of the detector being far below the 5.6 HGz required. However, the noise when the probe light is turned on, i.e. for $t > 0$ on the graph, is larger than that for $t < 0$, meaning this noise is probably dominated by photon noise. Since the noise during the decay is roughly 3 times larger than when no atoms are left in cavity, we interpret it as being due to not perfect immunity of the atomic signal to cavity-to-probe frequency mismatch fluctuations probably due to an imperfect simultaneous coupling of the $4^{th}$ order sidebands to the cavity.
Note that the fast decay (the number of atoms decreases by a factor two in 50 $\mu$s, twice faster in the previous scheme, see 78) is due to the relatively high power we had to send to the cavity in order to have sufficient signal-to-noise ratio on the PDH-like signal for the locking to work. This high power requirement is mainly due the 2 GHz bandwidth of our detector, not allowing for a good restitution of the beatnote at $3\Omega \approx 4.2$ GHz that provides the locking error signal. We recently ordered a new detector with sufficient bandwidth and comparable quantum efficiency at 461 nm which is expected to allow us to enter the quantum regime of the non-destrucitve detection (see section 14).

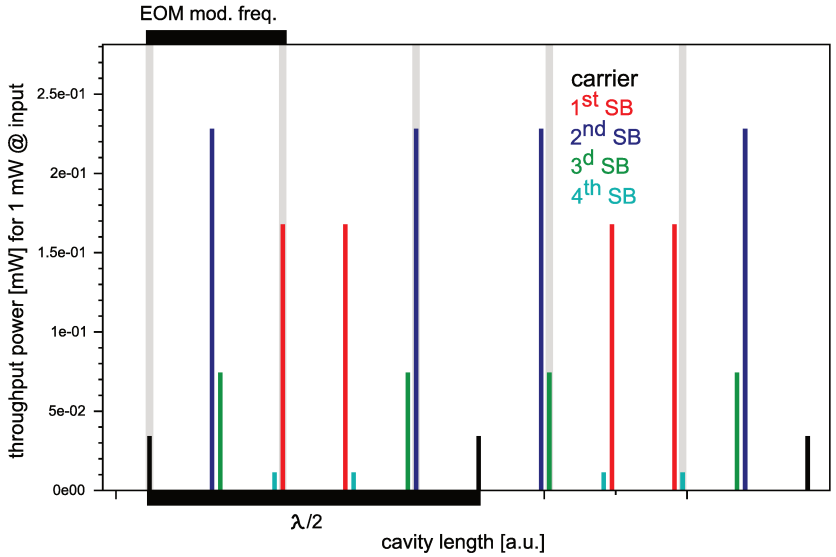


Figure 84: This plot represents cavity throughput power as a function of the cavity length $L$ for an incoming probe light whose phase is modulated (via an electro-optic modulator or EOM) at frequency  equal to $8/3$ of the cavity free spectral range $\Delta_{\mathrm{FSR}}$, and with a modulation depth $\beta$ sufficient for the forth order sidebands to be significant in amplitude. Because $> \Delta_{\mathrm{FSR}}$, the successive sidebands patterns seen when scanning $L$ overlap (which wa not the case in the previous scheme, see figure 60), making the identification of each sideband harder.

**Sidebands recognition protocol**: All the following steps should be done while scanning $L$ over more than a few halves of probe wavelength. i) identify the carrier turning the EOM modulation off. ii) identify the second order sidebands by turning the EOM modulation on but with a small modulation depth $\beta$ (such that the higher order sidebands are invisible). This allowes to measure the change $\delta L$ in cavity length corresponding to $\Omega$ ($\delta L$ is the distance separating a carrier resonance from the corresponding first order sidebands). iii) increase $\beta$ till having enough power in the forth order sidebands to be visible (at such modulation depths the carrier amplitude is significantly reduced). To identify the forth order sideband, start from a carrier resonance and translate the corresponding length (to the right or to the left) by $4\delta L$ where the forth order sideband resonance should be visible.

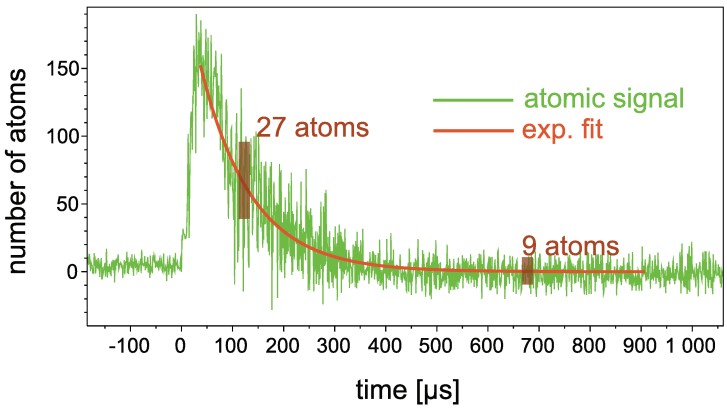


Figure 85: Preliminary results. Number of atoms in the clock ground state detected in the cavity as a function of the detection duration.

# 16 Conclusion and perspectives

This thesis work has been carried out on three fronts. First, it was done in the context of a time and frequency metrology institute and as such required a part of the work to be dedicated to "services", in this particular case as operating the clocks for contribution to TAI[82] and partially devoted to the stepping onward on the roadmap drawn by the CIPM recommendation in the perspective of a redefinition of the S.I. second. This required participating to continental scale clock comparison campaigns that where the occasions to confront the uncertainty budget established mainly by differential measurements varying the driving parameters of effects suspected to shift the clock frequency transition to the intransigence reality of the external world, i.e. the other clocks of the network, each claiming its own right on equal bases. These campaigns where as well great moments of satisfaction and the culmination of efforts of preparations always retributed. Each campaign brought its lot of unpredictable problems that could never have been detected without the comparisons and where actually revealed by them. Each time, the intense mobilization of the whole team allowed to cope with them. The complexity of such undertaking, involving several institutes dispatched over a whole continent and involving in each of them several teams is in itself a school for organization, team work and large system representation abilities. At the beginning of this work in the late 2015, the level of human attendance required for such events was high and demanded lab work to be sustained days and night for a period stretching over weeks. Thanks to efforts of the team worker involved for the implementation of automatized systems, the last campaign of 2018 was much less demanding, requiring a continuous human presence to watch over the clock but less and less to operate it.

Second, it included a large part dedicated to the re-assessment and the exploration of phenomena partially understood but still resisting to the assaults of the best theoreticians to be completely clarified. This was in particular the case for the hyperpoloarizability which is regularly remeasured (twice during my stay at SYRTE), each time with new ideas of implementations. Here again, each measurement, probing effects at the limit of visibility, requires the clocks to work at their nominal level of performances, which is in itself challenging. In this category enters as well the measurement of the hot collisions shifts which we are the first group to report on, for strontium based optical clocks. No new physics there, but the phenomena had been overlooked and the lack of theoretical tradition about this question when it comes to interpret it in terms of frequency shift made the region a bit blurry and uncertain as well as exciting because of being a door open to the unknown. We proposed our own approach to address the question and hope it will give rise to further development and understanding.

On a third ground, probably that to which I dedicated most of my work, lays the demonstration of the our cavity-assisted non destructive detection system. This systems offered several perspectives that can be summarized the following way. If used as a destructive probe, the integration of the decay signal can allow for a significant improvement in the atom number detection noise and therefore a reduction on the detection noise. It could be investigated to what extent this wold allow for a switch to a Ramsey interrogation scheme, since our choice to use a Rabi interrogation is based on the fact that the gain expected from a Ramsey would be mitigated by the risk of jumping from one fringe to the other because of detection noise. It could be used as well to achieve a detection noise of the same level as that obtained with the currently used camera detection but with a much smaller number of atoms, hence allowing for much shorter loading time and therefore higher duty cycle, then mitigating the Dick contribution to the clock instability. Nevertheless, we think the maximum benefit could be drawn out of it using on a non destructive bases, allowing for the strong reduction of the Dick effect, by almost one order of magnitude as enhanced in the text. This however would require finding a way to increase drastically the lifetime of the atoms in the trap, at least for a full benefit on our SrB clock on which the system was demonstrated. This scheme demonstrated compatibility with a quantum non demolition measurement in the sens that the its noise limitation are sufficiently low for the quantum noise to be resolved in a regime where less than one photon is scattered outside of the driving cavity mode during the detection pulse. Indeed, we proved an extrapolated noise lower than the square root of the number of atom in such a regime, which is precisely the level where lay the quantum limit. Moving to a quantum non demolition compatible configuration required new ideas and their implementations. We could not go that far in this direction but proved the system workability. Our first measurement with this improved scheme are promising and we hope the new detector will allow for a full benefit of the the scheme capabilities. However, how to implement a sequence that will effectively provide with a transition probability detection lower than the standard quantum limit is still an open question for the energy levels involved in our scheme. The main

[82] International atomic time

problem being probably the large width of the probing resonance, enhancing the scattering rate out of the cavity mode. Whether this is a limitation could probably be understood deriving a simple weak-interacting model based on an input-output formalism as usually done in the context of cavity-assisted quantum non demolition detections.

# 17 Publication

publication on the next page

New Journal of Physics
The open access journal at the forefront of physics

Deutsche Physikalische Gesellschaft DPG IOP Institute of Physics

PAPER • OPEN ACCESS

# A noise-immune cavity-assisted non-destructive detection for an optical lattice clock in the quantum regime

To cite this article: G Vallet *et al* 2017 *New J. Phys.* **19** 083002





New Journal of Physics
The open access journal at the forefront of physics

Deutsche Physikalische Gesellschaft DPG
IOP Institute of Physics

Published in partnership with: Deutsche Physikalische Gesellschaft and the Institute of Physics

OPEN ACCESS

RECEIVED
14 March 2017

REVISED
19 June 2017

ACCEPTED FOR PUBLICATION
29 June 2017

PUBLISHED
7 August 2017



PAPER

# A noise-immune cavity-assisted non-destructive detection for an optical lattice clock in the quantum regime

**G Vallet, E Bookjans, U Eismann[1], S Bilicki, R Le Targat and J Lodewyck**

SYRTE, Observatoire de Paris, PSL Research University, CNRS, Sorbonne Universités, UPMC Univ. Paris 06, LNE, 61 avenue de l'Observatoire F-75014 Paris, France

[1] Now with TOPTICA Photonics AG, Lochhamer Schlag 19, D-82166 Graefelfing, Germany.

**E-mail:** jerome.lodewyck@obspm.fr

**Keywords:** optical clock, frequency stability, optical lattice clock, non-destructive detection, spin squeezing

## Abstract

We present and implement a non-destructive detection scheme for the transition probability readout of an optical lattice clock. The scheme relies on a differential heterodyne measurement of the dispersive properties of lattice-trapped atoms enhanced by a high finesse cavity. By design, this scheme offers a 1st order rejection of the technical noise sources, an enhanced signal-to-noise ratio, and an homogeneous atom-cavity coupling. We theoretically show that this scheme is optimal with respect to the photon shot noise limit. We experimentally realise this detection scheme in an operational strontium optical lattice clock. The resolution is on the order of a few atoms with a photon scattering rate low enough to keep the atoms trapped after detection. This scheme opens the door to various different interrogations protocols, which reduce the frequency instability, including atom recycling, zero-dead time clocks with a fast repetition rate, and sub quantum projection noise frequency stability.

## 1. Introduction

The performance of a clock is characterised by its level of systematic uncertainty, frequency stability, and reproducibility. As such, optical lattice clocks (OLCs) are at the forefront of frequency metrology. Not only have they reached systematic uncertainties in the low $10^{-18}$ in fractional frequency units [1, 2], but they have proven to be reliable and reproducible as it has been demonstrated by various measurement and comparison campaigns [3, 4]. Albeit their success, the frequency stability of OLCs has not yet reached the quantum projection noise (QPN) limit, but is limited by the Dick effect, an aliasing effect between the frequency noise of the interrogation laser used to probe the clock transition (clock laser) and the cycle time of the experiment. OLCs have reached relative frequency stabilities in the low $10^{-16}/\sqrt{\tau}$ [1, 5], with $\tau$ being the averaging time expressed in seconds. This value is well above the QPN, which is below $10^{-17}$ at 1 s for an experimentally reasonable number of atoms of over $10^4$. However, in order to achieve a QPN-limited frequency stability in an OLC, the technical noise sources, i.e. the frequency noise of the clock laser and/or the dead time between consecutive measurements, have to be reduced.

Currently, the most stable clock lasers are frequency-locked to ultra-stable cavities, which have reached stabilities on the order of $10^{-16}$, using e.g. a long ultra-stable cavity [1, 5, 6] and a novel cryogenic single-crystal Si cavity [7]. To further push the frequency stability limit of the clock laser, new methods and techniques are being conceived, such as crystalline optical coatings [8], spectral hole burning in solid-state systems [9, 10] and novel laser sources [11]. As an alternative to improving the clock laser frequency noise, the Dick effect can be reduced by minimising the dead time in the clock cycle. For this, a dead-time free clock can be designed [5, 12], but this requires two separate atomic ensembles. Another approach is to implement a detection system able to preserve the lattice-trapped atoms, and therefore substantially reduce the dead time in the clock cycle devoted to loading atoms [13]. In this paper, we implement a cavity-assisted non-destructive detection technique in a Sr OLC. Its signal-to-noise ratio (SNR) also makes it suitable for quantum non-demolition measurements and therefore

opens the path to clock interrogation protocols based on weak measurements [14], as well as correlated quantum states in OLCs enabling frequency stabilities beyond the QPN limit [15–23].

### 1.1. Non-destructive detection methods in the dispersive regime

Dispersive measurement techniques are based on measuring the phase shift a probe beam acquires after passing through the atomic sample. They operate, in the far-detuned regime $\Delta \gg \Gamma$, with $\Delta$ being the detuning from resonance and $\Gamma$ the linewidth of the considered transition, and therefore have low photon scattering rates making them ideal for non-destructive measurements. In order to read out the induced phase shift, dispersive detection methods rely on interferometric techniques and require a stable phase reference. However, the advantage of a dispersive measurement is that all the information about the atomic population is gathered in the phase of the electromagnetic field of the mode of the probe beam, making it easy to collect and amplify with a cavity. In fluorescence based detection techniques, the atoms generally scatter in all directions, making it difficult to gather all the atomic information. In practice, this information loss is compensated by a large scattering rate, which leads to a large destructivity and consequently a substantial dead time in the clock cycle which needs to be devoted to trapping new atoms. The efficiency of dispersive measurement techniques has been exploited in various different cold and ultra-cold atom experiments and rely on various different interferometric techniques. Examples include phase contrast imaging of BECs [24], Mach–Zehnder interferometry [18, 25], heterodyne methods [26, 27], dual-colour homodyning [13, 28], cavity-based side-of-fringe methods [29, 30], and many more.

In this paper, we demonstrate a cavity-assisted non-destructive detection scheme based on a differential dispersive measurement. The scheme takes advantage of the parity of the dispersive atom-probe interaction such that it is to first order insensitive to technical noise sources, i.e. the probing laser frequency noise and vibrations [31]. Similar to a previously implemented non-destructive detection scheme in a Sr clock using a Mach–Zehnder interferometer [13], the presented detection scheme measures the difference between the phase shifts induced on two modulation sidebands with opposite detuning with respect to the $^1S_0$–$^1P_1$ transition. Since the induced atomic phase shifts have opposing signs, the atomic signal adds, while the technical noise is in common mode and is subtracted out. A major improvement of this new scheme is the cavity design, which brings substantial advantages for detecting atoms in OLCs. The cavity is used for both the generation of the optical lattice potential (813 nm) and the non-destructive probe (461 nm). The local oscillator, used as a phase reference for the dispersive measurement, is a common-mode strong carrier uncoupled to the cavity. This geometry constrains the alignment between the optical lattice potential and the probe beam requiring them to be overlapped, and therefore provides the necessary stability, robustness, and reproducibility required for operational OLCs. More importantly, the fundamental SNR of the detection system is improved by the square root of the cavity finesse $\mathcal{F} = 1.6 \times 10^4$ through the increased interaction length between the atoms and the probe light. A common issue with cavity-assisted detection schemes is the fact that the probe beam forms a standing wave in which the atoms are only optimally coupled to the probe light at anti-nodes. Schemes where the trapping lattice and the probing lattice have commensurable pitches [15, 32] are not applicable to OLCs because the trapping lattice frequency is constrained by the magic wavelength for which the clock transition is unperturbed. By creating two lattices with opposite phases, the differential scheme introduced in this paper ensures an homogeneous coupling in the longitudinal direction, as also discussed in [17].

## 2. Theory

The detection scheme considered in this paper relies on the dispersive properties of an atomic medium. The phase shift $\phi^{at}$ induced on the laser beam with detuning $\Delta$ from an atomic resonance with wavelength $\lambda$ passing through the atoms reads [13]:

$$\phi^{at} = \frac{N}{S}\frac{3\lambda^2}{2\pi}\frac{\Delta/\Gamma}{s + 4\Delta^2/\Gamma^2}, \tag{1}$$

where $N$ is the number of atoms in the fundamental clock state, $3\lambda^2/2\pi$ is the atomic cross-section, and $S$ is the cross-section of the cavity mode, averaged over the atomic ensemble. For an atomic sample of standard deviation $r_0$ probed by a Gaussian beam of waist $w_0$, $S = 2\pi(r_0^2 + w_0^2/4)$. $s$ is the saturation parameter, expressed by $s = P_c/(SI_{sat})$ where $P_c$ the power of the Gaussian beam, and $I_{sat} = \pi hc\Gamma/3\lambda^3$ is the saturation intensity. The measurement of $\phi^{at}$ therefore gives a measurement of $N$, from which the transition probability can be deduced using repumping methods [13].

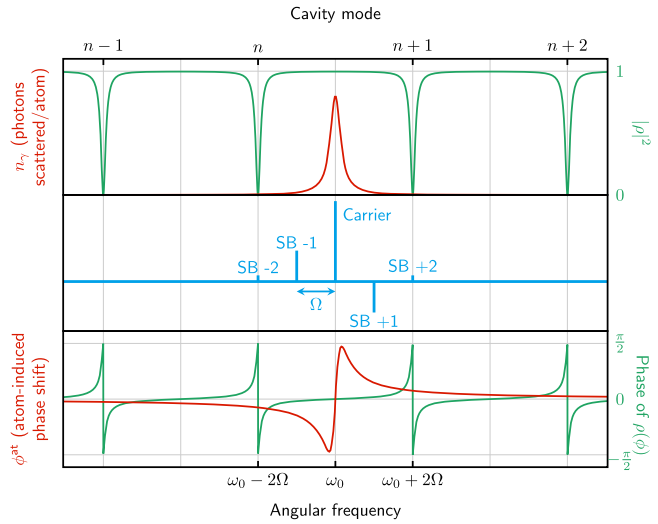


**Figure 1.** Illustration of the frequencies used in the setup. Top: reflection coefficient of the cavity (green trace) and scattering rate of the atoms (red trace). Middle: in-phase quadrature of the phase modulated electromagnetic field incident on the cavity, showing the parity of modulation sidebands. Only the second order modulation sidebands are coupled in the cavity, while the carrier acts as an uncoupled strong local oscillator. Bottom: phase of the reflection coefficient of the cavity (green) and atom induced phase shift (red). The odd parity of the atomic phase shift induces a displacement of the frequency of the $n$ and $n+1$ resonances of the cavity with opposite sign, resulting in a net signal when demodulating at $2\Omega = \mathrm{FSR}/2$. The displacement due to technical noise, however, induces a displacement with the same sign and therefore cancels out.

### 2.1. Noise insensitive detection

In the scheme presented in this paper, the phase shift $\phi^{at}$ is deduced from the measurement of the positions of the resonances of an optical cavity enclosing the atoms. The length of this cavity is noted $L = L_0 + \delta L$, where $L_0$ is the nominal cavity length and $\delta L$ are fluctuations around $L_0$. The cavity is illuminated with a laser beam of amplitude $|E_i|$, and angular frequency $\omega = \omega_0 + \delta\omega$, which is phase modulated with an angular frequency $\Omega = \Omega_0 + \delta\Omega$ and modulation depth $\beta$. The laser frequency and its modulation frequency are tuned such that the second order modulation side bands are resonant with two consecutive longitudinal modes of the cavity. The carrier is centred between these two modes:

$$\frac{\Omega_0}{2\pi} = \frac{1}{4}\frac{c}{2L_0}, \quad \text{and} \quad \frac{\omega_0}{2\pi} = \left(n + \frac{1}{2}\right)\frac{c}{2L_0}, \tag{2}$$

with $n$ being an integer. This configuration is schematically depicted in figure 1.

The phase shift $\phi_k$ of side band $k$ after a single pass in the cavity reads:

$$\phi_k = \frac{\omega + k\Omega}{c}L + \phi_k^{at} = \pi\left[n + \frac{1}{2} + \frac{k}{4} + \left(n + \frac{1}{2}\right)\epsilon_\omega + \frac{k}{4}\epsilon_\Omega\right] + \phi_k^{at}, \tag{3}$$

$$\text{with } \epsilon_\omega = \left(\frac{\delta\omega}{\omega_0} + \frac{\delta L}{L_0}\right), \text{ and } \epsilon_\Omega = \left(\frac{\delta\Omega}{\Omega_0} + \frac{\delta L}{L_0}\right), \tag{4}$$

where $\phi_k^{at} \equiv \phi^{at}(\omega + k\Omega)$ is the phase shift induced by the atoms on the sideband $k$. Because only the 2nd order sidebands are coupled to the cavity, the reflection coefficient of the cavity reads:

$$\rho_k \sim \begin{cases} -\mathrm{i}\frac{2\mathcal{F}}{\pi}\phi_k & \text{for } \phi_k \simeq 0\ [\pi] \Leftrightarrow k = 2\ [4] \\ 1 & \text{otherwise.} \end{cases} \tag{5}$$

The electric field $E_\mathrm{d}$ of the light collected by the detection photodiode can therefore be expressed as:

$$E_\mathrm{d} = \mathrm{e}^{\mathrm{i}\omega t}\sum_{k=-\infty}^{+\infty}\mathcal{E}_k\mathrm{e}^{\mathrm{i}k\Omega t}, \quad \text{with } \mathcal{E}_k = \rho_k J_k(\beta)|E_i|, \tag{6}$$

where $J_k$ are the Bessel functions of the first kind. This yields the AC photo-signal:

$$\mathcal{S} = E_\mathrm{d}E_\mathrm{d}^* = \sum_{m>0}\mathcal{S}_m, \text{ with} \tag{7}$$

$$\mathcal{S}_m = 2\Re\left[\mathrm{e}^{-\mathrm{i}m\Omega t}\sum_{k=-\infty}^{+\infty}\mathcal{E}_k\mathcal{E}^*_{k+m}\right], \tag{8}$$

which is composed of harmonics with frequencies $m\Omega$, each derived from various beatnotes between sidebands separated by $m\Omega$.

Assuming that the modulation depth $\beta$ is small, the signal at frequency $\Omega$ reads:

$$\mathcal{S}_1 = 2J_1(\beta)J_2(\beta)|E_i|^2\frac{2\mathcal{F}}{\pi}(\pi(n+1/2)\,\epsilon_\omega + \phi^{\mathrm{at}}_{+2} + \phi^{\mathrm{at}}_{-2})\sin\Omega t. \tag{9}$$

It arises from the beating of $\pm1$ order sidebands with $\pm2$ order sidebands. If the frequency of the laser carrier is tuned close to the atomic resonance, $\phi^{\mathrm{at}}_{+2} + \phi^{\mathrm{at}}_{-2}$ is approximately zero, due to the odd parity of the atomic response. As a result, $\mathcal{S}_1$ is a measurement of $\epsilon_\omega$, i.e. the relative laser frequency fluctuations with respect to the length of the cavity. This signal is thus used as an error signal to keep the laser frequency locked to the cavity resonance.

The signal at frequency $2\Omega$ reads:

$$\mathcal{S}_2 = \mathcal{S}_2^{\cos}\cos 2\Omega t + \mathcal{S}_2^{\sin}\sin 2\Omega t \quad \text{with} \tag{10}$$

$$\mathcal{S}_2^{\cos} = -2J_1^2(\beta)|E_i|^2, \tag{11}$$

$$\mathcal{S}_2^{\sin} = 2J_0(\beta)J_2(\beta)\frac{2\mathcal{F}}{\pi}(\pi\epsilon_\Omega + \phi^{\mathrm{at}}_{+2} - \phi^{\mathrm{at}}_{-2})|E_i|^2. \tag{12}$$

The $\mathcal{S}_2^{\sin}$ quadrature results from the beatnote between the carrier, used as a strong local oscillator, and the $\pm2$ order sidebands coupled in the cavity. The even parity of these modulation sidebands make this signal insensitive to residual length fluctuations of the cavity and frequency fluctuations of the laser. Combined with the odd parity of the atomic response ($\phi^{\mathrm{at}}_{+2} \simeq -\phi^{\mathrm{at}}_{-2}$), the even parity of the $\pm2$ order sidebands enables the detection of the atomic signal $\phi^{\mathrm{at}}_{+2} - \phi^{\mathrm{at}}_{-2}$. This signal is still sensitive to the relative mismatch between the cavity length and the modulation frequency $\epsilon_\Omega$, but it can be made negligible through an independent lock of the cavity length. Furthermore, this latter sensitivity can be used to scale the photo-signal to a phase unit by purposely detuning $\Omega$.

### 2.2. Shot noise analysis

Shot noise is the fundamental quantum noise on the quadratures of the electric field of coherent states. Its standard deviation only depends on the spatio-temporal geometry of the considered mode of the electric field. In the photodetection process, it is observed by its beatnote with an optical carrier.

Rewriting equation (6) to include the shot noise gives:

$$E_{\mathrm{d}} = \mathrm{e}^{\mathrm{i}\omega t}\sum_{k=-\infty}^{+\infty}(\mathcal{E}_k + \delta\mathcal{E}_k)\mathrm{e}^{\mathrm{i}k\Omega t}. \tag{13}$$

where $\delta\mathcal{E}_k$ is the shot noise on mode $\mathcal{E}_k$. Therefore, the shot noise of the signal $\mathcal{S}_m$ is:

$$\delta\mathcal{S}_m = 2\sum_{k=-\infty}^{\infty}\Re[(\mathcal{E}_{k-m}\delta\mathcal{E}^*_k + \mathcal{E}^*_{k+m}\delta\mathcal{E}_k)\mathrm{e}^{-\mathrm{i}m\Omega t}]. \tag{14}$$

Assuming a low phase modulation depth $\beta$, its component on the detection signal $\mathcal{S}_2^{\sin}$ hence reads:

$$\delta\mathcal{S}_2^{\sin} = 2J_0(\beta)|E_i|\Im[-\delta\mathcal{E}_2 + \delta\mathcal{E}_{-2}], \tag{15}$$

which has a standard deviation:

$$\sqrt{\langle\delta\mathcal{S}_2^{\sin 2}\rangle} = 2\sqrt{2}J_0(\beta)|E_i|\sqrt{\langle\delta E^2\rangle}, \tag{16}$$

given that the shot noise $\delta\mathcal{E}_2$ and $\delta\mathcal{E}_{-2}$ are uncorrelated and have an identical variance written $\langle\delta E^2\rangle$. The shot noise limited SNR therefore reads:

$$\mathrm{SNR} = \frac{\mathcal{S}_2^{\sin}}{\sqrt{\langle\delta\mathcal{S}_2^{\sin 2}\rangle}} = \frac{\sqrt{2}J_2(\beta)|E_i|}{\sqrt{\langle\delta E^2\rangle}}\frac{2\mathcal{F}}{\pi}\frac{\phi^{\mathrm{at}}_{+2} - \phi^{\mathrm{at}}_{-2}}{2}. \tag{17}$$

In this equation, the $\sqrt{2}J_2(\beta)|E_i|$ factor is the amplitude of the electric field coupled into the cavity, and $2\mathcal{F}/\pi$ is the phase enhancement factor of the cavity, already seen in equation (5).

Finally, given that for a coherent state $|E_i|/\sqrt{\langle\delta E^2\rangle} = 2\sqrt{N}$ with $N$ the number of photons in the mode, and taking into account the various optical losses in the detection process (the imperfect coupling into the cavity, the optical losses between the cavity and the photo-detector, and the quantum efficiency of the photo-detector, all combined into an effective efficiency $\eta$), equation (17) can be reformulated as:

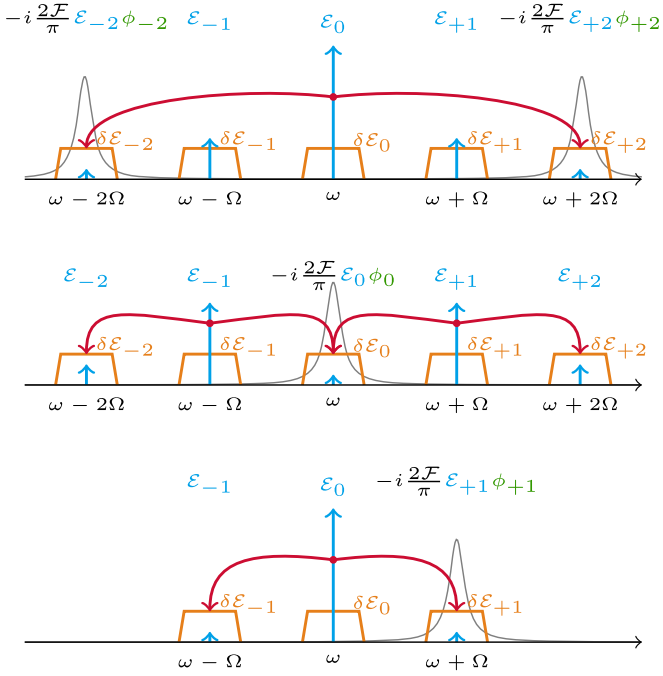


**Figure 2.** Illustration of the photon shot noise for different detection schemes. Blue arrows indicate the electric field reflected by the cavity, red arrows the beatnotes which compose the demodulated signal, grey curves the cavity modes, and orange boxes the shot noise in the detection bandwidth. Top: detection scheme proposed in this paper. Its SNR is given by equation (18) as a function of the intra-cavity power $P_c$. Middle: detection based on a PDH scheme. The first order sidebands are used as a local oscillator to detect the phase shift that the carrier coupled in the cavity experiences. Assuming that most of the detected optical power is in the first order sideband, equations (8) and (14) yield a SNR $\mathrm{SNR}_{\mathrm{PDH}} = \sqrt{2/3}$ SNR. The factor $\sqrt{2/3}$ comes from the fact that while the PDH scheme samples the signal and shot noise at frequency $\omega$, it also samples the shot noise but no signal at frequencies $\omega \pm \Omega$, hence a degraded SNR. Bottom: detection scheme in which a single optical sideband is coupled to the cavity. Its SNR reads $\mathrm{SNR}_{+1} = \sqrt{1/2}$ SNR. The $\sqrt{1/2}$ factor comes from the shot noise at frequency $\omega - \Omega$.

$$\mathrm{SNR} = \sqrt{\frac{4\eta P_c T\lambda}{hc}\frac{2\mathcal{F}}{\pi}}\,\frac{\phi^{\mathrm{at}}_{+2} - \phi^{\mathrm{at}}_{-2}}{2}, \tag{18}$$

where $T$ is the probing time, and $P_c$ is the total intra-cavity power held by both second order sidebands injected in the cavity. This expression is a factor $\sqrt{2\mathcal{F}/\pi}$ higher than the SNR of a dispersive detection scheme without a cavity [13], showing the cavity enhancement. The SNR (18) is identical to the SNR obtained when measuring the phase shift in the cavity with an homodyne beatnote between the signal transmitted by the cavity and a phase coherent local oscillator. Because the heterodyne scheme presented in this paper does not introduce additional shot noise, it is optimal with respect to the shot noise limit. This optimality comes from the fact that the two second order sidebands contain an atomic signal in addition to the shot noise. To illustrate this fact, figure 2 analyses other heterodyne detection schemes, including the well-known PDH scheme, which, in addition to being sensitive to cavity length and laser frequency fluctuations, feature a non-optimal SNR.

### 2.3. Non-destructivity

We recall that, in the detection scheme described here, the frequency of the optical carrier of the detection laser is close to the frequency of the atomic resonance. Therefore, the detunings of the second order modulation sibebands are opposite in sign, and are written as $\pm\Delta$. It is important to remark that because these two sidebands are injected into two consecutive modes of the cavity, the interference patterns they each form have opposing phases close to the centre of the cavity where the atoms are located. Therefore, the total intra-cavity power experienced by the atoms is homogeneous along the longitudinal direction. As the phase shifts of the two modulation sidebands are jointly measured by the heterodyne scheme presented here, the coupling between the atoms and the cavity modes, as well as the photon scattering rate, therefore do not depend on the position of the atoms along the axis of the cavity. This is a compelling feature of this detection scheme for OLCs, for which the trapping light has to be tuned to the magic wavelength, i.e. to a frequency which is incommensurable with the frequency of the detection light.

The heating rate of the atoms in the cavity is characterised by the photon scattering rate per atom:

$$n_\gamma = \frac{\Gamma}{2}\frac{s}{s + 4\Delta^2/\Gamma^2}. \tag{19}$$

The SNR can consequently be expressed as:

$$\mathrm{SNR} = \frac{\phi^{\mathrm{at}}_{+2} - \phi^{\mathrm{at}}_{-2}}{\delta\phi}, \tag{20}$$

with

$$\frac{1}{\delta\phi} = \sqrt{\frac{2\pi}{3}\frac{S}{\lambda^2}\eta n_\gamma T\frac{2\mathcal{F}}{\pi}}\sqrt{s + 4\Delta^2/\Gamma^2}. \tag{21}$$

Using the expression (1) for the atomic phase shift, the shot-noise limited SNR can be written in terms of the atom number resolution:

$$\mathrm{SNR} = \frac{N}{\delta N}, \tag{22}$$

with

$$\frac{1}{\delta N} = \sqrt{\frac{3}{2\pi}\frac{\lambda^2}{S}\eta n_\gamma T\frac{2\mathcal{F}}{\pi}}\sqrt{\frac{4\Delta^2/\Gamma^2}{s + 4\Delta^2/\Gamma^2}}. \tag{23}$$

For $s \ll 4\Delta^2/\Gamma^2$, the SNR depends only an a few experimental parameters, namely the atomic cross-section $3\lambda^2/2\pi$, the cavity cross-section $S$, the finesse $\mathcal{F}$, the detection efficiency $\eta$, and the number of scattered photons per atom $n_\gamma T$. If the latter is sufficiently low to prevent the atoms from escaping the trapping potential, the detection exhibits 'classical' non-destructivity. If the number of scattered photons is significantly lower than one, the detection lies in the quantum regime: it is able to weakly measure the atomic coherence. If the detection in the quantum regime can reach a detection noise smaller than the QPN, i.e. $\delta N \ll \sqrt{N}$, spin-squeezed states of the atomic ensemble can be generated to overcome the QPN. A cavity with a large finesse therefore helps reach this quantum regime.

The incoming probe beam on the cavity is composed of two cavity-coupled, weak $\pm 2$ modulation sidebands, but also of a strong carrier which acts as a local oscillator. Because a low destructivity implies a low power in the coupled sidebands, hence a low modulation depth, the destructivity of the non-cavity coupled but strong carrier also has to be considered because it is on-resonance with the atoms. The destructivity of the carrier due to residual off-resonant coupling into the cavity can be mitigated by purposefully introducing a non-zero detuning between the carrier and the atomic resonance, but sufficiently small as compared to the modulation frequency in order to preserve the homogeneous coupling of the atoms in the cavity. This condition is in practice always met, because once the cavity is injected with the trapping light at the magic wavelength, the frequencies of the resonances at the detection wavelength form a discrete set fixed by the incommensurable ratio between these frequencies. Also, the detection time can be decreased while keeping the product $P_c T$ constant, allowing for a larger modulation depth.

## 3. Experimental demonstration

### 3.1. Setup

We experimentally implemented the detection scheme proposed in this paper on one of the two operational $^{87}$Sr OLCs available at SYRTE, named Sr B. This clock features a systematic uncertainty of $4 \times 10^{-17}$, which has been confirmed by a relative frequency ratio measurement between Sr B and the other Sr clock (Sr 2), yielding

$$\frac{\nu_{\mathrm{Sr}_2} - \nu_{\mathrm{Sr}_\mathrm{B}}}{\nu_{\mathrm{Sr}}} = (2.3 \pm 7.1) \times 10^{-17}. \tag{24}$$

The frequency stability of Sr B is $10^{-15}$ for an integration time of 1 s, measured through a comparison with Sr 2 [3]. The aim of the non-destructive detection described in this paper is to improve this frequency stability.

The description of the clock system can be found in [3]. Here, we describe exclusively the parts of the experiment related to the detection scheme, shown on figure 3.

The main part of the detection scheme is an in-vacuum bi-chromatic build-up cavity used for both the optical lattice confining the Sr atoms in the Lamb–Dicke regime and the enhancement of the atomic phase shift imprinted on the non-destructive probe light. The cavity has a finesse of 180 at the trapping magic wavelength $\lambda_\mathrm{m} \simeq 813$ nm, which allows us to reach trapping depths as large as 2500 $E_{\mathrm{R},813}$, with $E_{\mathrm{R},813} = h^2/2m\lambda_\mathrm{m}^2$ being the recoil energy of Sr atoms of mass $m$. The finesse at the non-destructive detection wavelength 461 nm,

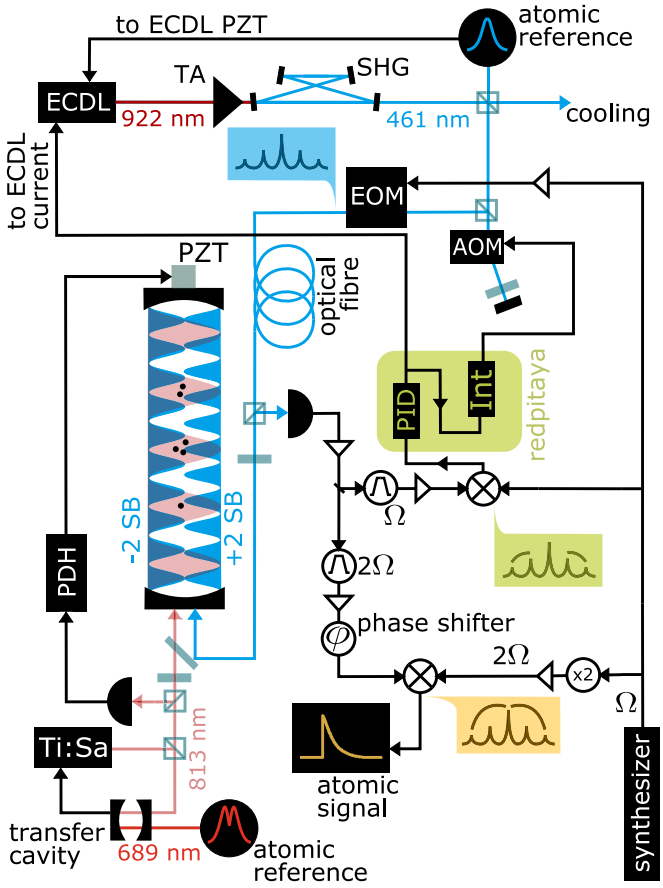


**Figure 3.** Schematic of the experimental setup. It shows the bi-chromatic high finesse cavity in which the atoms are trapped (magic wavelength at 813 nm) and probed (phase modulated laser at 461 nm). The second-order modulation sidebands form two out-of-phase standing waves in which the atoms are homogeneously coupled.

corresponding to the $^1S_0$–$^1P_1$ transition ($\Gamma = 2\pi \times 32$ MHz and $I_{sat} = 42.7$ mW cm$^{-2}$), is $\mathcal{F} = 1.6 \times 10^4$, which allows for a large enhancement of the detection signal. The two identical mirrors of the cavity are used as windows of the high vacuum system, and are adjusted by bellows to which piezo transducers (PZT) are attached. The length of the cavity is $L = 41$ mm, corresponding to a free spectral range (FSR) of 3.7 GHz. The radius of curvature of the mirrors is 25 mm, which gives a waist of 50 $\mu$m at 813 nm, and $w_0 = 38$ $\mu$m at 461 nm. Given that the typical transverse standard deviation of the atomic wavefunction is $r_0 = 10$ $\mu$m, the cavity cross-section is $S = 2.9 \times 10^3$ $\mu$m$^2$.

The 813 nm lattice light is provided by a titanium sapphire (Ti:Sa) laser. It is tuned to the magic wavelength $\lambda_m$ by a frequency-lock to an extended cavity diode laser (ECDL, not represented in figure 3) referenced to a transfer cavity, itself locked to a 689 nm source directly referenced to the Sr $^1S_0$–$^3P_1$ transition by saturated absorption spectroscopy. The length of the cavity is then locked to the magic wavelength lattice light via a standard Pound Drever Hall scheme acting on the PZT.

The 461 nm blue laser stems from a frequency doubled 922 nm ECDL. It is then dispatched to the first Sr cooling stage light system. Its frequency is locked to an atomic reference through a feedback loop onto the 922 nm ECDL PZT using a digital modulation lock. Part of the light is sent to the cavity for the non-destructive detection. Because the frequencies of both the 813 and 461 nm lasers are constrained, a double passed acousto-optic modulator (AOM) is used to tune the frequency of the 461 nm light to the resonances of the cavity. The laser beam is then phase modulated by an electro-optic modulator (EOM, provided by QuBig) at a frequency of one forth of the FSR, i.e. $\Omega = 2\pi \times 920$ MHz, in order to implement the heterodyne protocol described in section 2.1. After being cleaned through an optical fibre, the spatial mode of the laser is coupled to the cavity with an efficiency of $\eta_{cpl} = 0.82$.

Despite the fact that the cavity length and the laser frequencies are all locked to absolute references, the frequency difference between the 461 nm light and the resonances of the cavity fluctuates by much more than the cavity line-width, on time scales of tens of microseconds. This is due to the high finesse of the cavity, which is two orders of magnitude larger at 461 nm than at 813 nm. To keep the probe laser on resonance with the cavity, it is therefore necessary to implement a fast locking scheme of the laser frequency to the cavity length. For this,

we use the protocol described in section 2.1. The reflected signal is collected by a fast photodiode (OSIO FCI-125G-006HRL, with a specified bandwidth of 1.25 GS $s^{-1}$ and a quantum efficiency $\eta_{\rm det} = 0.46$) after an additional transmission efficiency $\eta_{\rm loss} = 0.65$, yielding an overall efficiency $\eta = \eta_{\rm cpl}\eta_{\rm det}\eta_{\rm loss} = 0.25$. The RF output signal of the photodiode is then split into two.

The first part is bandpass-filtered and demodulated at frequency $2\Omega$ in order to generate the atomic signal. This signal results from the beatnote of the reflected carrier acting as a strong local oscillator and the coupled second-order sidebands, and is given by equation (10). It is calibrated by applying a modulation on the modulation frequency $\Omega$, and the demodulation quadrature is adjusted in order to maximise the modulation signal using a mechanical phase shifter.

The second part is bandpass-filtered and demodulated at frequency $\Omega$. It contains the error signal given by equation (9) used to lock the 461 nm light frequency on the cavity. It results from the beatnote of the rejected first-order sidebands (local oscillator) and the coupled second-order sidebands. The servo loop uses a digital PID implemented on a FPGA based RedPitaya platform acting on the current of the 922 nm ECDL with a bandwidth larger than 1 MHz. This digital implementation also enables us to conditionally engage the integration stage of the PID with a TTL signal to accommodate with the fact that the blue light is turned off during the clock interrogation time. The correction signal is kept at zero by a second stage integrator acting on the AOM frequency. The aim of this lock is to keep the cavity in the linear regime for which the model developed in section 2.1, and especially equation (5) is valid. As long as this condition is fulfilled, the atomic signal is to first order insensitive to any offset or residual laser frequency noise and cavity length fluctuations, as shown by equation (10).

With the given experimental parameters, the theoretical shot noise limited resolution for a single scattered photon is

$$\delta N_{\rm th,SNL} = 3.3 \text{ atoms} \quad \text{for } s = 0, \text{ and } n_\gamma T = 1, \tag{25}$$

in principle enabling the entrance into the quantum non-destructivity regime with as little as a few tens of atoms.

### 3.2. Experimental results

The detection system is operated within the experimental cycle by illuminating the cavity with the phase modulated detection beam which has a total power $P_i = 4.3$ mW and a modulation depth $\beta \simeq 0.31$, such that the heterodyne lock system is robust enough. This gives a total intra-cavity power of $P_c = 4\eta_{\rm cpl}\mathcal{F}J_2^2(\beta)P_i/\pi = 10$ mW, a saturation parameter $s = P_c/SI_{\rm sat} = 8.1 \times 10^3$, and a photon scattering rate $n_\gamma = 38$ photons $\mu s^{-1}$. The atomic phase shift per atom is $\phi^{\rm at}_{+2}/N = -\phi^{\rm at}_{-2}/N = 94$ nrad/atom.

Figure 4 shows an acquisition of the atomic signal with atoms loaded in the optical lattice. At $t = 0$, the detection light is switched on. After a delay of 20 $\mu$s, the digital lock is able to stabilise the detection light on the cavity. However, the number of atoms, expected to be a few thousands, introduces a phase shift significantly larger than the linewidth $\pi/\mathcal{F} \simeq 200$ $\mu$rad of the cavity, so that the second order sidebands are no longer simultaneously injected in the cavity. The noise cancellation scheme presented in this paper is therefore not effective, and the atomic signal strongly varies with the laser frequency and cavity length fluctuations. As the atoms scatter photons, they escape out of the lattice trap. At $t \simeq 150$ $\mu$s, the number of atoms has sufficiently reduced such that the noise cancellation technique is effective, and the atomic signal becomes noise-immune (see inset of figure 4). The atomic signal then follows a decay that can be fit with a heating function [13]:

$$N(t) = N_0\left[1 - \exp\left(-\frac{U/E_{\rm R,461}}{n_\gamma t/3}\right)\right]. \tag{26}$$

This corresponds to a heating model for which the atoms are confined in the Lamb–Dicke regime in the longitudinal direction, and only acquire momentum in the transverse directions. The standard deviation of the fit residuals gives a resolution of:

$$\delta N_{\rm experimental} = 3.7 \text{ atoms}, \tag{27}$$

for an acquisition time of 1 $\mu$s, during which each atom scatters 38 photons. This shows the classical non-destructivity of the detection scheme, as this number of scattered photons is low enough not to push the atoms out of the lattice. Extrapolating to $n_\gamma T = 1$ yields $\delta N = 23$, enabling the entrance into the quantum regime for $N > 500$ atoms.

The value $\delta N_{\rm experimental}$ can be compared to the theoretical shot-noise limited resolution $\delta N_{\rm SNL} = 0.7$ atoms, obtained by evaluating equation (23) with the experimental parameters listed above, and $T = 1$ $\mu$s. An analysis of the dependence of the noise with the optical power reveals that the discrepancy between $\delta N_{\rm experimental}$ and $\delta N_{\rm SNL}$ is mostly due to electronic noise, and, to a lower extent, to a larger shot-noise than expected. We attribute the latter to extra losses in the photodetector. With an improved photodetector, we can therefore expect a five-fold improvement to the SNR.

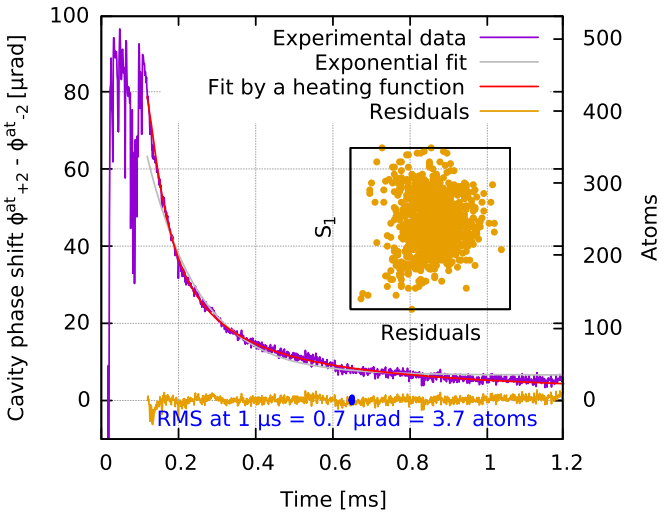


**Figure 4.** Atomic signal for a trap depth of $U = 750\ E_{R,461}$. The sampling rate is 1 MHz. After an initial settling time ($t \lesssim 150\ \mu s$) for which number of atoms is too large for the detection to work properly, the decay of the trapped atoms is fit by equation (26) in which a vertical and horizontal offset are added as fit parameters. The scattering rate given by the fit is $n_\gamma = 38$ photons $\mu s^{-1}$, in agreement with the value deduced from the optical power injected into the cavity. The grey curve shows that an exponential decay does not fit the experimental data as well as the heating function of equation (26). The inset shows that the redisuals of the fit and the error signal S1 of the lock of the laser on the cavity are mostly uncorrelated, which confirms that the atomic signal is noise-immune.

## 4. Prospects

The detection scheme demonstrated in this paper offers many perspectives for OLCs. First, exploiting the high SNR of the detection scheme can help run the clock with a lower number of atoms, and thus a shorter loading time. Figure 4 shows that a low detection noise can be reached even with as little as a few hundreds of probed atoms. As an example, we were able to load this amount of atoms with a total clock cycle time of 300 ms comprising a 150 ms clock probe pulse. Such a fast clock cycle can help reduce the clock dead time, hence the Dick effect, making the detection attractive, for instance, for transportable clock systems which do not have a high stability clock laser readily available. Furthermore, with a 50% duty cycle, it would be possible to operate a dead-time free clock using two atomic ensembles [5, 12] even with a clock laser that has a moderate coherence time. Exploiting the classical non-destructivity of the detection will allow us to further improve the duty cycle by recycling the atoms from clock cycle to clock cycle, thus reducing the contribution of the Dick effect to the clock instability.

Figure 4 also shows that the detection system, as demonstrated in this paper, can only detect up to about 500 atoms. This dynamic range is determined by the linewidth of the cavity, and is limited because of the large finesse of the cavity. Although, as discussed above, operating a clock with a small number of atoms can be an advantage for the frequency stability (lower Dick effect) and accuracy (lower frequency shift due to cold collisions), it is a drawback for a QPN-limited clock, as its frequency instability scales as $1/\sqrt{N}$. However, this limitation can be mitigated by several means. First, in a QPN limited clock, the excursion of the transition probability is small (on the order of $1/\sqrt{N}$), hence the number of detected atoms deviates from a constant expected value by a small amount only (provided that the number of atoms initially loaded in the clock is controlled, for instance using the non-destructive detection device). Despite its small dynamic range, the detection can be pre-tuned close to the expected atom number, and thus it is able to properly measure the transition probability. For instance, if the initial number of atoms can be controlled at the percentile level, the detection is suitable for a QPN-limited clock with 50 000 atoms. Second, the dynamic range of the detection system can be extended to detect more atoms by actively adjusting the modulation frequency $\Omega$ so that the two modulation sidebands are coupled into the cavity even when the resonances of the cavity are moved by more than their linewidth. Finally, the dynamic range of the detection can be increased by operating the detection scheme with a higher modulation frequency, and by addressing modes of the cavity separated by more than one FSR, without degrading the SNR.

Another challenge of the detection scheme presented in this paper is to reach a lower number of scattered photons. This can also be achieved by increasing the modulation frequency, or by further reducing the modulation depth, hence coupling less power to the cavity. Because locking the detection laser on the cavity by beating the first and second order sidebands, as proposed here, becomes challenging, another EOM could be used to generate an additional set of first order sidebands with sufficient power to obtain a sizable error signal.

Increasing the dynamic range and reducing the photons scattering rate can alternatively be achieved by probing the atoms close to the weak $^1S_0 - {}^3P_1$ inter-combination transition at 689 nm. It increases the SNR by a factor 1.5 (equation (23) shows that the SNR is proportional to $\lambda$, given that, for ultra-cold atoms, $S$ is proportional to $\lambda$), and enables the entrance to the regime for which the resonance linewidth is smaller than the cavity linewidth. However, the scheme proposed here relies on the fact that the non-destructive detection laser beam shares the same cavity mode as the lattice laser. In addition, the clock laser (698 nm) has also to be aligned with the lattice in order to probe the atoms in the tightly confined direction. Therefore, using the 689 nm transition requires a mirror coating with a high finesse at 689 nm, and simultaneously a large transmission at the wavelength of the clock transition at 698 nm, which is a technically very challenging requirement.

With the technical improvements proposed above, it will be possible to reach the quantum regime, in which entangled states of the atomic ensemble can help reach a sub-QPN frequency stability. The cooperativity of the atom-cavity system presented in this paper, defined by $\eta_0 = 6\mathcal{F}\lambda^2/\pi^3 w_0^2 = 0.45$ will allow for a significant amount of spin squeezing for the typical atom number of $10^4$ usually operated in OLCs.

## 5. Conclusion

In this paper, we have successfully implemented a cavity-assisted non-destructive detection scheme on an OLC with strontium atoms. For this, a single phase modulated laser beam is used to lock the laser on the cavity and to detect the atomic signal at the same time, via an heterodyne beatnote. This configuration makes the scheme simple and adapted to operational optical clocks. This detection scheme can measure the number of trapped atoms with a resolution of a few atoms, while scattering a number of photons sufficiently low for the atoms to remain trapped in the optical lattice. This classical non-destructivity will help improve the clock frequency stability by reducing the clock dead-time. Furthermore, simple technical improvements in the detection scheme will make it suitable to reach the quantum non-destructivity regime in which the clock stability can overcome the QPN limit.

## Acknowledgments

We acknowledge funding support from Agence Nationale de la Recherche (Labex First-TF ANR-10-LABX-48-01, ANR-16-CE30-0003-01), the European Metrology Research Programme (EXL-01 QESOCAS), the EMPIR 15SIB03 OC18, and Conseil Régional Île-de-France (DIM Nano'K). The EMRP is jointly funded by the EMRP participating countries within EURAMET and the European Union. The EMPIR programme is co-financed by the Participating States and from the European Union's Horizon 2020 research and innovation programme.

## References

[1] Nicholson T L *et al* 2015 Systematic evaluation of an atomic clock at $2 \times 10^{-18}$ total uncertainty *Nat. Commun.* **6** 6896
[2] Ushijima I, Takamoto M, Das M, Ohkubo T and Katori H 2015 Cryogenic optical lattice clocks *Nat. Photon.* **9** 185–9
[3] Lodewyck J *et al* 2016 Optical to microwave clock frequency ratios with a nearly continuous strontium optical lattice clock *Metrologia* **53** 1123
[4] Lisdat C *et al* 2016 A clock network for geodesy and fundamental science *Nat. Commun.* **7** 12443
[5] Schioppo M *et al* 2017 Ultrastable optical clock with two cold-atom ensembles *Nat. Photon.* **11** 48
[6] Häfner S, Falke S, Grebing C, Vogt S, Legero T, Merimaa M, Lisdat C and Sterr U 2015 $8 \times 10^{-17}$ fractional laser frequency instability with a long room-temperature cavity *Opt. Lett.* **40** 2112–5
[7] Kessler T, Hagemann C, Grebing C, Legero T, Sterr U, Riehle F, Martin M J, Chen L and Ye J 2012 A sub-40 mHz-linewidth laser based on a silicon single-crystal optical cavity *Nat. Photon.* **6** 687–92
[8] Cole G D, Zhang W, Martin M J, Ye J and Aspelmeyer M 2013 Tenfold reduction of brownian noise in high-reflectivity optical coatings *Nat. Photon.* **7** 644–50
[9] Chen Q-F, Troshyn A, Ernsting I, Kayser S, Vasilyev S, Nevsky A and Schiller S 2011 Spectrally narrow, long-term stable optical frequency reference based on a crystal at cryogenic temperature *Phys. Rev. Lett.* **107** 223202
[10] Leibrandt D R, Thorpe M J, Chou C-W, Fortier T M, Diddams S A and Rosenband T 2013 Absolute and relative stability of an optical frequency reference based on spectral hole burning *Phys. Rev. Lett.* **111** 237402
[11] Meiser D, Ye J, Carlson D R and Holland M J 2009 Prospects for a millihertz-linewidth laser *Phys. Rev. Lett.* **102** 163601
[12] Lodewyck J, Westergaard P G, Lecallier A, Lorini L and Lemonde P 2010 Frequency stability of optical lattice clocks *New J. Phys.* **12** 065026
[13] Lodewyck J, Westergaard P G and Lemonde P 2009 Nondestructive measurement of the transition probability in a Sr optical lattice clock *Phys. Rev.* A **79** 061401
[14] Kohlhaas R, Bertoldi A, Cantin E, Aspect A, Landragin A and Bouyer P 2015 Phase locking a clock oscillator to a coherent atomic ensemble *Phys. Rev.* X **5** 021011
[15] Hosten O, Engelsen N J, Krishnakumar R and Kasevich M A 2016 Measurement noise 100 times lower than the quantum-projection limit using entangled atoms *Nature* **529** 505
[16] Schleier-Smith M H, Leroux I D and Vuletić V 2010 Squeezing the collective spin of a dilute atomic ensemble by cavity feedback *Phys. Rev.* A **81** 021804

[17] Cox K C, Greve G P, Wu B and Thompson J K 2016 Spatially homogeneous entanglement for matter–wave interferometry created with time-averaged measurements *Phys. Rev.* A **94** 061601
[18] Oblak D, Petrov P G, Alzar C L G, Tittel W, Vershovski A K, Mikkelsen J K, Sørensen J L and Polzik E S 2005 Quantum-noise-limited interferometric measurement of atomic noise: towards spin squeezing on the Cs clock transition *Phys. Rev.* A **71** 043807
[19] Inoue R *et al* 2013 Unconditional quantum-noise suppression via measurement-based quantum feedback *Phys. Rev. Lett.* **110** 163602
[20] Leroux I D, Schleier-Smith M H and Vuletić V 2010 Orientation-dependent entanglement lifetime in a squeezed atomic clock *Phys. Rev. Lett.* **104** 250801
[21] Kuzmich A, Bigelow N P and Mandel L 1998 Atomic quantum non-demolition measurements and squeezing *Europhys. Lett.* **42** 481
[22] Wineland D J, Bollinger J J, Itano W M and Heinzen D J 1994 Squeezed atomic states and projection noise in spectroscopy *Phys. Rev.* A **50** 67–88
[23] Polzik E S and Ye J 2016 Entanglement and spin squeezing in a network of distant optical lattice clocks *Phys. Rev.* A **93** 021404
[24] Andrews M R, Mewes M O, van Druten N J, Durfee D S, Kurn D M and Ketterle W 1996 Direct, nondestructive observation of a bose condensate *Science* **273** 84–7
[25] Windpassinger P J, Oblak D, Petrov P G, Kubasik M, Saffman M, Garrido Alzar C L, Appel J, Müller J H, Kjærgaard N and Polzik E S 2008 Nondestructive probing of rabi oscillations on the cesium clock transition near the standard quantum limit *Phys. Rev. Lett.* **100** 103601
[26] Bernon S, Vanderbruggen T, Kohlhaas R, Bertoldi A, Landragin A and Bouyer P 2011 Heterodyne non-demolition measurements on cold atomic samples: towards the preparation of non-classical states for atom interferometry *New J. Phys.* **13** 065021
[27] Kohnen M, Petrov P G, Nyman R A and Hinds E A 2011 Minimally destructive detection of magnetically trapped atoms using frequency-synthesized light *New J. Phys.* **13** 085006
[28] Béguin J-B, Bookjans E M, Christensen S L, Sørensen H L, Müller J H, Polzik E S and Appel J 2014 Generation and detection of a sub-poissonian atom number distribution in a one-dimensional optical lattice *Phys. Rev. Lett.* **113** 263603
[29] Schleier-Smith M H, Leroux I D and Vuletić V 2010 States of an ensemble of two-level atoms with reduced quantum uncertainty *Phys. Rev. lett.* **104** 073604
[30] Zhang H, McConnell R, Ćuk S, Lin Q, Schleier-Smith M H, Leroux I D and Vuletić V 2012 Collective state measurement of mesoscopic ensembles with single-atom resolution *Phys. Rev. Lett.* **109** 133603
[31] Ye J, Ma L-S and Hall J L 1998 Ultrasensitive detections in atomic and molecular physics: demonstration in molecular overtone spectroscopy *J. Opt. Soc. Am.* B **15** 6–15
[32] Lee J, Vrijsen G, Teper I, Hosten O and Kasevich M A 2014 Many-atom cavity QED system with homogeneous atom-cavity coupling *Opt. Lett.* **39** 4005–8

# Appendices

## A Spherical tensors and the Wigner-Eckart theorem

Recalling the quantum investigation of neutral atoms energy structure, one remembers that the spherical symmetry of the Coulombian potential leads to a simplified treatment in the total electronic angular momentum operator $\hat{\mathbf{J}}^2$ eigenbasis $\{|j\rangle\}_{j\in\mathbf{N}}$ combined to that, $\{|m\rangle\}_{m=-j,...,+j}$, of its projection along one of the directions of space, labeled $z$, $\hat{J}_z$, leading to the orthogonal basis $\{|j,m\rangle\}$. This is of course possible because each of these two operators commute with each other and with the electronic Hamiltonian of a free atom. The aim of this section being accounting for energy levels changes due to the interaction with the lattice light, the atom can no longer be considered free, meaning that $\{|j,m\rangle\}$ is probably no longer a basis in which the full Hamiltonian is diagonal. However, the lattice induced energy levels shifts can be obtained from a perturbative treatment. As is shown in section B.2, the energy correction induced by the perturbation are given by linear combinations of products of terms of the form $\langle ajm|\,\hat{V}_\pm\,|a'j'm'\rangle$ where $a$ encompass all the parameters other than the angular parameters covered by the quantum numbers $j$ and $m$, and $\hat{V}_\pm$ are operators defined further in the section. The most powerful tool at our disposal to compute such products is the Wigner-Eckart theorem which, nevertheless, requires the operators $\hat{v}_\pm$ to be expressed as combinations of spherical irreducible tensors. In this paragraph we expose the basics of the spherical tensor decomposition, just what is needed to follow the calculation procedure of the energy level shifts, as well as the Wigner-Eckart theorem.

The paragraph is structured as follows. Basics definitions of Cartesian tensors are given, followed by an example suggesting the concept of irreducible tensor decomposition. Some similarities of the obtained form with the structure of angular momentum subspace is then highlighted motivating the definition of spherical tensors. A composition rule providing a tensor from two others is exposed and is applied to a particular of interest for the treatment of the polarizability shift. Finally, the Wigner-Eckart theorem is stated and applied to this particular example.

**Cartesian tensors and rotations.**
Cartesian coordinates of vectors obey certain well defined rules when undergoing rotations. The coordinates $V_i'$ of a rotated vector are given from its unrotated coordinates as

$$V_i' = \sum_j R_{ij} V_j \tag{575}$$

where $[R_{ij}]$ is the corresponding rotation matrix. Rotations are intimately related to angular momentum operators $\hat{\mathbf{J}}$ in the sens that $\hat{\mathbf{J}}$ is a generator for the spatial rotations and it turns out that equation 575 can be expressed as

$$\mathcal{D}^\dagger V_i \mathcal{D} = \sum_j R_{ij} V_j \tag{576}$$

where the rotation operator $\mathcal{D}$ is defined as

$$\mathcal{D} = \exp\left(-\sum_j \beta_j \hat{J}_j/\hbar\right) \tag{577}$$

where the $\beta_j$ depend on the particular rotation $[R_{ij}]$. Tensors $T$ can be seen as a generalization of vectors $V$ with a higher number $k$ of indices: $V_i \longrightarrow T_{i_1,...,i_k}$, $k$ being called the rank of the tensor. Hence vectors are rank-1 tensors. Cartesian coordinates of tensors as well obey a given set of rules when undergoing rotations and equation 576 generalizes to

$$\mathcal{D}^\dagger T_{i_1,...,i_k} \mathcal{D} = \sum_{j_1,...,j_k} R_{i_1 j_1} \cdots R_{i_k j_k} T_{j_1,...,j_k} \tag{578}$$

**Reducible and irreducible tensors**
It is apparent from equation 578 that in general rotations mix all of the Cartesian coordinates of the tensor on which it acts. Their is actually a smart way of decomposing a Cartesian rank-k tensor into components of rank $\ell = 0, ..., k$, such that rotations mix all the coordinates within each component but not between two different components.

It turns out that there is for each rank-k tensor $T^{(k)}$ a unique decomposition $\{T^{(\ell)}\}_{\ell=0,..,k}$ such that it is not possible to further decompose any of the components $T^{(\ell)}$ into sub-components that would not get mixed with each other under the action of rotations (see e.g. [140]). This minimal decomposition is called the irreducible decomposition. We now introduce the spherical basis $\{\mathbf{e}_{0,\pm}\}$ which presents several advantages with respect to the Cartesian one when it comes to handle irreducible decompositions of tensors. It is defined from the Cartesian basis vectors $\{\mathbf{e}_{x,y,z}\}$ as

$$\mathbf{e}_0 = \mathbf{e}_z \qquad\qquad \mathbf{e}_\pm = \mp\frac{\mathbf{e}_x - i\mathbf{e}_y}{\sqrt{2}} \tag{579}$$

In what follows, each irreducible decomposition of a rank-k tensor $T^{(k)}$ is given as a set of parameters $T_q^{(\ell)}$ where $\ell = 0,..,k$ and for each $\ell$, $q = -\ell,..,+\ell$. The $T_q^{(\ell)}$ are called the spherical irreducible tensor components of $T^{(k)}$. Expressing tensors in their irreducible spherical form is interesting for at least two general reasons, the first of which is that the Wigner-Eckart theorem has a manageable expression for tensors given in this form and the second being that it is easy to combine irreducible tensors given in spherical coordinates to get higher ranks tensors directly in irreducible form expressed in spherical coordinates as well, i.e. directly addressable by the Wigner-Eckart theorem, which will be very useful for our purpose. Moreover, for our particular purpose, this tensorial decomposition is very beneficial because it allows for the grasping of the whole complexity of the atomic structure within a few parameters, each of which depending on a particular set of experimental parameters. For example, for the first order lattice induced shift, as discussed in section 5.1, can be grasped in three parameters: the scalar, the vector and the tensor shift, each of them being correlated with well identified experimental effect.

**Combination rules and scalar product of irreducible tensors.**
When given in the spherical basis, the scalar of two rank-k irreducible tensors $U^{(k)}$ and $V^{(k)}$ is defined as

$$\left(U^{(k)} \cdot V^{(k)}\right) = \sum_{q=-k}^{k} (-1)^q U_q^{(k)} V_{-q}^{(k)} \tag{580}$$

which is compatible with the standard Euclidian scalar product of two vectors, i.e. of two rank-1 tensors. A very important result we just state here without proof is that two irreducible tensors with spherical coordinates $A_{q_1}^{(k_1)}$ and $B_{q_2}^{(k_2)}$ of respective ranks $k_1$ and $k_2$ can be combined, by tensorial product, to give an irreducible tensor $\{A^{(k_1)} \otimes B^{(k_2)}\}^{(k)}$ of rank $k = k_1 + k_2$ which spherical coordinates are given by

$$\{A^{(k_1)} \otimes B^{(k_2)}\}_q^{(k)} = \sum_{q_1,q_2} C^{kq}_{k_1 q_1, k_2 q_2} A_{q_1}^{(k_1)} B_{q_2}^{(k_2)} \tag{581}$$

where the $C^{jm}_{j_1 m_1, j_2 m_2} = \langle j_1 m_1, j_2 m_2 | jm; j_1 j_2 \rangle$ are the Clebsch-Gordan coefficients and where $k$ ranks from $|k_1 - k_2|$ to $k_1 + k_2$.

**Wigner-Eckart theorem**
As enhanced above, the irreducible components of tensors have been defined in relation to their behavior under the action of rotations, which are generated by $\hat{\mathbf{J}}$. It then would not be surprising that a part of their action as tensors would be related to that of $\hat{\mathbf{J}}$. In other words, considering two different rank-k tensors $U^{(k)}$ and $V^{(k)}$, their irreducible components $U_q^{(l)}$ and $V_q^{(l)}$ of rank $l \leq k$ would differ since $U^{(k)} \neq V^{(k)}$ but would share some common properties due to their common inherent relation to $\hat{\mathbf{J}}$. This separation between what stems from the relation to $\hat{\mathbf{J}}$ and what stems properly from the tensor represented is precisely what the Wigner-Eckart addresses (see e.g. [141]). As mentioned at the very beginning of section this section, the internal state of the unperturbed atoms is well described in the angular momentum basis $\{|jm\rangle\}$ which diagonalizes the unperturbed Hamiltonian. We anyway formally account for possible other degrees of freedom by adding a generic parameter $\alpha$ to the angular dependences and thus describe the atomic state using the extended basis $\{|ajm\rangle\}$. The Wigner-Eckart theorem then states that the matrix elements of any spherical tensor $T^{(k)}$ factorize into

$$\langle a'j'm'| T_q^{(k)} |amj\rangle = C^{j'm'}_{jm,kq} \frac{\langle a'j' \| T^{(k)} \| aj \rangle}{\sqrt{2j+1}} \tag{582}$$

meaning that the magnetic quantum number (i.e. the quantum numbers $m$, $m$' and $q$ related to $\hat{J}_z$) dependence is shared by all spherical tensors operators and is accounted for by the Clebsh-Gordan coefficient $\langle jm, kq | jm; kj' \rangle$. On the other hand, the part depending specifically on the particular tensor $T$,

quantum number $j$ and possibly on other parameters encapsulated in $a$ is independent on the magnetic quantum numbers. It is noted $\langle a'j' \| T^{(k)} \| aj \rangle$ and is called reduced matrix element.

As will been established in the next section, the Floquet perturbation theory provides corrections to the free atoms energy levels due to the interaction with the lattice light in the form of combinations of terms of the form $\langle a'j'm' | T_q^{(k)} | amj \rangle$. In sections 5.1 and 5.2 respectively dedicated to the polarizabillity and the hyperpolarizability, such combinations are recast using some algebraic tricks combined to the rules given by equations 580 and 581 and finally brought to a workable form using the Wigner-Eckart theorem.

# B Floquet perturbation theory

The equations derived in this section are well known from the theoretitians. The reason of the presence of this section here is to be found in the fact that tracing back the continuous conceptual and mathematical derivation leading to the theoretical results by which our experimental were motivated, we had to stop at what we perceived as a *dead end*, coming across the fatally sounding [63]

> [...] *With the help of the well known formulae of perturbation theory it can be presented as*
>
> $$U^{(4)}_{MM'} = -\langle\langle nJM|VGVGVGV|n'JM'\rangle\rangle \quad (583)$$
> $$+\langle\langle nJM|VGV|nJM\rangle\rangle\langle\langle nJM|VG^2V|nJM'\rangle\rangle \quad (584)$$
>
> *where*
>
> $$G = \sum_{n,k'} \frac{|n'k\rangle\rangle\langle\langle n'k|}{\mathcal{E}^0_{n'k} - E^0_{nj}} \quad (585)$$
>
> [...]

We found frustrating[83] not being able to link this track back to something familiar, especially knowing it was closely accessible from (a) perturbation theory, meaning there as only a small effort to provide for bridging the gap between what we already knew and the final result established by theoretician. Our curiosity has been driven by two things. First, standard perturbation theories are many, and even for those easily found in common textbooks, the expended formulae at the $4^{th}$ order, which is required for the hyperpolarizability treatment, are never provided. Second, the double bra-ket notation above did not look familiar to us, and we took the opportunity of learning something till know unknown to us.

## B.1 Motivation

The lattice induced shifts can be well studied within the frame of time-dependent perturbation theory. Indeed, the system Hamiltonian has the form

$$\hat{H}(t) = \hat{H}_0 + \hat{H}_I(t) \quad (586)$$

where all the time dependency of the total Hamiltonian is condensed in the perturbative part which, according to our discussion of section 5.0.2, is given by the dipole interaction $\hat{H}_I(t) = -\mathbf{d} \cdot \mathbf{E}(t)$, where the classical field oscillates at angular frequency $\omega$. Note that because we ruled out any magnetic field effects, the shifts is exclusively due to electric effects and is often reffered to as AC stark shift. The perturbation is then periodic and $\hat{H}_I(t+\tau) = \hat{H}_I(t)$ with $\tau = 2\pi/\omega$. Floquet perturbation theory, dealing with time-periodic Hamiltonians, is then particularly well appropriate to investigate successive corrections orders of the AC Stark shift [142, 143].

Note that if $\Psi$ is a solution of the Shrödinger equation

$$\hat{H}(t)\Psi = -i\hbar\frac{\partial\Psi}{\partial t}$$

its associated instantaneous energy will in general not be conserved because of the explicit time dependence of $\hat{H}(t)$ and it will be impossible to define a time independent energy shift as $\Delta E\ \Psi = \hat{H}(t)\Psi - E_0\Psi_0$, $E_0$ being the eigenvalue of $\hat{H}_0$ corresponding to its unperturbed eigenfunction $\Psi_0$. In order to overcome

[83] Nevertheless, this paper has been one of the most instructive among all we could find treating the hyperpolarizability

this problem, the energy of the perturbed system will be defined as the time average over one period $\tau$ of the expected value $\langle\Psi|\,\hat{H}(t)\,|\Psi\rangle$, denoted as

$$\langle\langle\Psi|\,\hat{H}(t)\,|\Psi\rangle\rangle = \frac{1}{\tau}\int_0^t \langle\Psi|\,\hat{H}(t)\,|\Psi\rangle\ dt = \frac{1}{\tau}\int_0^\tau \left(\int \Psi^*(\xi)\hat{H}(t,\xi)\Psi(\xi)\ d\xi\right)\ dt \tag{587}$$

where $\xi$ encompasses all the spatial and spin variables of the system, leading to the definition

$$\Delta E = \langle\langle\Psi|\,\hat{H}(t)\,|\Psi\rangle\rangle - E_0 \tag{588}$$

## B.2 Floquet theorem

Here we just remind the useful results of Floquet time dependent perturbation theory, without any derivation (following [142]).

Consider a system whose evolution is driven by the time dependent $\tau$-periodic Hamiltonian $\hat{H}(t+\tau) = \hat{H}(t)$. Its eigenfunctions $\psi(\xi,t)$ are solutions of the equation

$$\left[\hat{H} - \frac{i}{\hbar}\frac{\partial}{\partial t}\right]\psi(\xi,t) = 0 \tag{589}$$

and from Floquet theorem can be written as

$$\psi(\xi,t) = \phi(\xi,t)e^{i\mathcal{E}t/\hbar} \tag{590}$$

with $\mathcal{E}$ real and $\phi$ $\tau$-periodic solution of the Shrodinger type equation

$$\hat{\mathcal{H}}(t)\phi(\xi,t) = \mathcal{E}\phi(\xi,t) \tag{591}$$

with

$$\hat{\mathcal{H}}(t) = \hat{H}(t) - \frac{i}{\hbar}\frac{\partial}{\partial t}$$

Consider further that $\hat{H}(t)$ can be split into $\hat{H}_0 + V$ where $V$ only is time dependent (and $\tau$-periodic) such that the eigenvalues and eigenfunctions of $\hat{H}_0$ are well known

$$\hat{H}_0 f_n = E_n f_n(\xi) \tag{592}$$

and where the $\{f_n\}_{n\in N}$ form an orthonormal basis of the system Hilbert space, i.e. satisfy

$$\langle f_n|f_m\rangle = \delta_{m,n} \tag{593}$$

Note that from section A the index $n$ actually stands for the angular momentum quantum numbers as well for all possible other parameters, i.e. $n \equiv \{\alpha, j, m\}$, meaning $|f_n\rangle = |\alpha jm\rangle$. As above we define the unperturbed steady state Hamiltonian as

$$\hat{\mathcal{H}}_0(t) \equiv \hat{\mathcal{H}}(t) - V = \hat{H}_0 - \frac{i}{\hbar}\frac{\partial}{\partial t} \tag{594}$$

which eigenvalues and eigenfunctions satisfy, from Floquet theory,

$$\hat{\mathcal{H}}_0(t)\phi^{(0)}_{nq}(\xi,t) = \mathcal{E}^{(0)}_{nq}\phi^{(0)}_{nq}(\xi,t) \tag{595}$$

and are given by

$$\mathcal{E}^{(0)}_{nq} = E_n + q\omega \tag{596}$$

$$\phi^{(0)}_{nq}(t) = f_n(\xi)e^{iq\omega t} \tag{597}$$

where $\omega = 2\pi/\tau$, $q \in \mathbf{Z}$ where the $\phi^{(0)}_{n,q}$ form an orthonormal basis for a larger Hilbert space $\mathcal{S}$ including $\tau$-periodic functions, this space being endowed with the scalar product

$$\langle\langle\phi^{(0)}_{nq}|\phi^{(0)}_{n'q'}\rangle\rangle = \int_\Omega\int_0^\tau \phi^{(0)*}_{nq}(\xi,t)\phi^{(0)}_{n'q'}(\xi,t)d\xi dt = \delta_{n,n'}\delta_{q,q'} \tag{598}$$

The treatment is thereafter similar to standard time independent perturbation theory. Both the perturbed eigen energies and eigen functions are expanded in orders of perturbation as

$$\mathcal{E}_{nq} = \sum_k \mathcal{E}_{nq}^{(k)} \qquad \phi_{nq} = \sum_k \phi_{nq}^{(k)} \tag{599}$$

where the successive corrections verify $\langle\langle \phi_{nq}^{(0)} | \phi_{nq}^{(k)} \rangle\rangle = \delta_{0k}$. Inserting these expressions into 591 leads to

$$\left(\hat{\mathcal{H}}_0 - V\right) \sum_k \phi_{nq}^{(k)} = \sum_{k,l} \mathcal{E}_{nq}^{(k)} \phi_{nq}^{(l)} \tag{600}$$

which, equating left and right side terms of same order, gives the series of equations

$$\left(\hat{\mathcal{H}}_0 - V\right) \phi_{nq}^{(k)} = \sum_{l=0}^{k} \mathcal{E}_{nq}^{(l)} \phi_{nq}^{(k-l)} \tag{601}$$

from where one can compute the "extanded" expectation values

$$\langle\langle \phi_{n'q'}^{(0)} | \left(\hat{\mathcal{H}} - V\right) | \phi_{nq}^{(k)} \rangle\rangle$$

This allows for the calculation of the successive corrections which, when using the notation $|\phi_{n,q}^{(0)}\rangle \equiv |nq\rangle$, are given by

$$\mathcal{E}_{nq}^{(1)} = \langle\langle nq|V|nq\rangle\rangle \tag{602}$$

$$\mathcal{E}_{nq}^{(2)} = \sum_{n'q' \neq nq} \frac{\langle\langle nq|V|n'q'\rangle\rangle\langle\langle n'q'|V|nq\rangle\rangle}{\left(\mathcal{E}_{n'q'}^{(0)} - \mathcal{E}_{nq}^{(0)}\right)} \tag{603}$$

$$\mathcal{E}_{nq}^{(3)} = \sum_{n'q',n''q''} \frac{\langle\langle nq|V|n'q'\rangle\rangle\langle\langle n'q'|V|n''q''\rangle\rangle\langle\langle n''q''|V|nq\rangle\rangle}{\left(\mathcal{E}_{n'q'}^{(0)} - \mathcal{E}_{nq}^{(0)}\right)\left(\mathcal{E}_{n''q''}^{(0)} - \mathcal{E}_{nq}^{(0)}\right)} \tag{604}$$

$$- \sum_{n'q'} \frac{\langle\langle nq|V|nq\rangle\rangle\langle\langle nq|V|n'q'\rangle\rangle\langle\langle n'q'|V|nq\rangle\rangle}{\left(\mathcal{E}_{n'q'}^{(0)} - \mathcal{E}_{nq}^{(0)}\right)^2} \tag{605}$$

$$\mathcal{E}_{nq}^{(4)} = - \sum_{n'q'} \frac{\langle\langle nq|V|nq\rangle\rangle\langle\langle nq|V|n'q'\rangle\rangle\langle\langle n'q'|V|nq\rangle\rangle\langle\langle nq|V|nq\rangle\rangle}{\left(\mathcal{E}_{n'q'}^{(0)} - \mathcal{E}_{nq}^{(0)}\right)^3} \tag{606}$$

$$+ \sum_{n'q',n''q''} \frac{\langle\langle nq|V|nq\rangle\rangle\langle\langle nq|V|n'q'\rangle\rangle\langle\langle n'q'|V|n''q''\rangle\rangle\langle\langle n''q''|V|nq\rangle\rangle}{\left(\mathcal{E}_{n'q'}^{(0)} - \mathcal{E}_{nq}^{(0)}\right)^2\left(\mathcal{E}_{n''q''}^{(0)} - \mathcal{E}_{nq}^{(0)}\right)} \tag{607}$$

$$- \sum_{n'q',n''q''} \frac{\langle\langle nq|V|nq\rangle\rangle\langle\langle nq|V|n'q'\rangle\rangle\langle\langle n'q'|V|n''q''\rangle\rangle\langle\langle n''q''|V|nq\rangle\rangle}{\left(\mathcal{E}_{n'q'}^{(0)} - \mathcal{E}_{nq}^{(0)}\right)^2\left(\mathcal{E}_{n''q''}^{(0)} - \mathcal{E}_{nq}^{(0)}\right)} \tag{608}$$

$$- \sum_{n'q',n'',q'',n''',q'''} \frac{\langle\langle nq|V|n'q'\rangle\rangle\langle\langle n'q'|V|n''q''\rangle\rangle\langle\langle n''q''|V|n'''q'''\rangle\rangle\langle\langle n'''q'''|V|nq\rangle\rangle}{\left(\mathcal{E}_{n'q'}^{0} - \mathcal{E}_{nq}^{0}\right)\left(\mathcal{E}_{n''q''}^{0} - \mathcal{E}_{nq}^{0}\right)\left(\mathcal{E}_{n'''q'''}^{0} - \mathcal{E}_{nq}^{0}\right)} \tag{609}$$

$$- \sum_{n'q',n''q''} \frac{\langle\langle nq|V|n'q'\rangle\rangle\langle\langle n'q'|V|nq\rangle\rangle\langle\langle nq|V|n''q''\rangle\rangle\langle\langle n''q''|V|nq\rangle\rangle}{\left(\mathcal{E}_{n'q'}^{0} - \mathcal{E}_{nq}^{0}\right)^2\left(\mathcal{E}_{n''q''}^{0} - \mathcal{E}_{nq}^{0}\right)} \tag{610}$$

Note that the eigenvalues $\mathcal{E}_{nq}^{(0)}$ can not be interpreted as energies since $\hat{\mathcal{H}}_0$ is not an Hamiltonian. In analogy with the quasi momenta stemming from the Bloch theorem dealing with spatially periodic potentials, the eigenvalues $\mathcal{E}_{nq}$ are called quasi-energies. According to our definition of the energy shift given by eq. 588, the perturbed energy would be given rigorously by

$$E_n = \langle\langle \Psi | \hat{H}(t) | \Psi \rangle\rangle = \mathcal{E}_{nq} + \langle\langle nq | i\hbar \frac{\partial}{\partial t} | nq \rangle\rangle$$

Further analytical computations are possible due the particular form of the potential $V$ appearing in the energy correction expressions. Indeed, the harmonic potential induced by the field reads

$$V = V_-(\xi)e^{-i\omega t} + V_+(\xi)e^{i\omega t} \tag{611}$$

where $V_-(\xi) = -\mathbf{d}\cdot\boldsymbol{\varepsilon}^* E(\xi)$ with $\mathbf{d}$ the atomic dipole operator of the clock transition, $\boldsymbol{\varepsilon}$ the lattice field polarization and $E(\xi)$ its amplitude at location $\xi$ along the longitudinal lattice axis. and therefore

$$\langle\langle n'q'|V_\pm(\xi)e^{\pm i\omega t}|nq\rangle\rangle = \frac{1}{\tau}\int_{-\frac{\tau}{2}}^{\frac{\tau}{2}}\int \left[f_{n'}(\xi)e^{iq'\omega t}\right]^* V_\pm(\xi)e^{\pm i\omega t} f_n(\xi)e^{iq\omega t}d\xi dt \tag{612}$$

$$= \left(\frac{1}{\tau}\int_{-\frac{\tau}{2}}^{\frac{\tau}{2}} e^{i(1+q-q')\omega t}\right)\left(\int f^*_{n'}(\xi)V_\pm(\xi)f_n(\xi)d\xi\right) \tag{613}$$

$$= \delta_{q',q\pm1}\int f^*_{n'}(\xi)V_\pm(\xi)f_n(\xi)d\xi \tag{614}$$

$$= \delta_{q',q\pm1}\langle n'|V_\pm|n\rangle \tag{615}$$

Note that because $\hat{\mathbf{d}}$ is proportional to $\hat{\mathbf{r}}$ the integral 614 vanishes for states $|n\rangle$ and $|n'\rangle$ having the same parity. In particular, $\langle n'|V_\pm|n\rangle = 0$ which implies $\langle\langle nq|V|nq\rangle\rangle = 0$.

# C Beam splitter model of optical losses

As said in section 12.3.3, describing optical losses in a quantum frame requires modelling them as unitary beam splitter operation. In this representation, the mode $\hat{a}_1$ undergoing the losses is sent at the first port of the beam splitter, allong with a vacuum field in mode $\hat{a}_2$ at the second beam splitter port, the field attenuated by the losses in mode $\hat{a}_3$ being obtained at the third port and the lost photons being that leaving at the forth port (see figure 77). The modes at the different ports relate according to

$$\begin{pmatrix}\hat{a}_3\\ \hat{a}_4\end{pmatrix} = \begin{pmatrix}t & -d^*\\ d & t^*\end{pmatrix}\begin{pmatrix}\hat{a}_1\\ \hat{a}_2\end{pmatrix} \tag{616}$$

with $|t|^2 + |d|^2 = 1$. With this definition of the BS operator

$$[\hat{a}_3, \hat{a}_3^\dagger] = [t\hat{a}_1 - d^*\hat{a}_2, t^*\hat{a}_1^\dagger - d\hat{a}_2^\dagger] = |t|^2[\hat{a}_1,\hat{a}_1^\dagger] + |d|^2[\hat{a}_2,\hat{a}_2^\dagger] = |t|^2 + |d|^2 = 1 \tag{617}$$

For an input field in state $|\alpha\rangle$ at port 1, we thus have to consider as a total input field the joint state $|\alpha\rangle\otimes|0\rangle = |\alpha,0\rangle$ in order to account for the vacuum at port 2. The field average intensity at output port 3 is then

$$\langle\hat{I}_3\rangle = \langle\hat{n}_3\rangle \tag{618}$$

$$= \langle\hat{a}_3^\dagger\hat{a}_3\rangle \tag{619}$$

$$= \langle|t|^2\hat{a}_1^\dagger\hat{a}_1 - t^*d^*\hat{a}_1^\dagger\hat{a}_2 - td\hat{a}_2^\dagger\hat{a}_1 + |d|^2\hat{a}_2^\dagger\hat{a}_2\rangle \tag{620}$$

$$= |t|^2|\alpha|^2 \tag{621}$$

$$= |t|^2\langle\hat{n}_1\rangle \tag{622}$$

$$= |t|^2\langle\hat{I}_1\rangle \tag{623}$$

and

$$\langle\hat{I}_3^2\rangle = \langle\hat{a}_3^\dagger\hat{a}_3\hat{a}_3^\dagger\hat{a}_3\rangle = \langle\left(t^*\hat{a}_1^\dagger - d\hat{a}_2^\dagger\right)\left(t\hat{a}_1 - d^*\hat{a}_2\right)\left(t^*\hat{a}_1^\dagger - d\hat{a}_2^\dagger\right)\left(t\hat{a}_1 - d^*\hat{a}_2\right)\rangle \tag{624}$$

which is a 16 terms sum. Each term where $\hat{a}_2$ appears on the right side and/or $\hat{a}_2^\dagger$ on the left side vanish, because $\hat{A}_1\otimes\hat{A}_2\hat{a}_2\,|\alpha,0\rangle = 0$ and $\langle\alpha,0|\,\hat{A}_1\otimes\hat{a}_2^\dagger\hat{A}_2 = 0$ for whatever operators $\hat{A}_{1,2}$ acting on mode $1,2$. Hence, the only non vanishing terms are

$$|t|^4\langle\hat{a}_1^\dagger\hat{a}_1\hat{a}_1^\dagger\hat{a}_1\rangle = |t|^4|\alpha|^4 = |t|^4\langle\hat{n}_1^2\rangle$$

and

$$|t|^2|d|^2\langle\hat{a}_1^\dagger\hat{a}_1\hat{a}_2\hat{a}_2^\dagger\rangle = |t|^2|d|^2|\alpha|^2 = |t|^2|d|^2\langle\hat{n}_1\rangle$$

Therefore, the fluctuations $\sigma_3^2$ in intensity at output port 3 have magnitude

$$\sigma_3^2 = \langle\hat{I}_3^2\rangle - \langle\hat{I}_3\rangle^2 = |t|^4\left(\langle\hat{n}_1^2\rangle - \langle\hat{n}_1\rangle^2\right) + |t|^2|d|^2\langle\hat{n}_1\rangle = |t|^4\sigma_1^2 + |t|^2|d|^2\langle\hat{n}_1\rangle \tag{625}$$

# References


[1] T. J. Quinn, Practical realization of the definition of the metre, including recommended radiations of other optical frequency standards, Metrologia 40 103–33 (2001)

[2] Fritz Riehle et al., The CIPM list of recommended frequency standard values: guidelines and procedures, Metrologia 55 188–200 (2018)

[3] H. S. Margolis et al., Least-squares analysis of clock frequency comparison data to deduce optimized frequency and frequency ratio values, Metrologia 52 628–34 (2015)

[4] L. Robertsson et al., On the evaluation of ultra-high-precision frequency ratio measurements: examining closed loops in a graph theory framework. Metrologia 53 1272–80 (2016)

[5] IEEE - NASA symposium on short-term frequency stability, Goddard Space Flight Center, Grennbelt, Maryland (1964)

[6] J C Maxwell, in: Treatise on electricity and magnetism, Clarendon Press, Oxford, (book, 1873)

[7] D. W. Allan et al., Statistics of time and frequency data analysis, in: National Bureau of Standards monograph 140, Time and Frequency: theory and application, chap. 8.6.4.

[8] D. W. Allan, Statistics of atomic frequency standards, IEEE, (54) 221-230 (1966)

[9] J. Rutman, Characterization of phase and frequency instabilities in precision Frequency sources: fifteen years of progress, IEEE, (66) 1048-1075 (1978)

[10] J. A. Barnes, Characterization of frequency stability, IEEE Trans. Instrum. Meas. IM-20 105-120 (1971)

[11] J. Fiser, The cesium frequency standard (seminar), University of Ljubljan, Faculty of Mathematics and Physics (2014)

[12] A. D. Ludlow et al., Optical atomic clocks, Rev. of Modern Physics, vol 87 (2015)

[13] H. Katori et al., Ultrastable Optical Clock with Neutral Atoms in an Engineered Light Shift Trap, Phys. Rev. Lett. 91, 173005 (2003)

[14] D. J. Wineland et al., Experimental Issues in Coherent Quantum-State Manipulation of Trapped Atomic Ions, J. Res. Natl. Inst. Stand. Technol. 103, 259 (1998)

[15] Tomoya Akatsuka et al., Three-dimensional optical lattice clock with bosonic 88Sr atoms, Phys. Rev. A 81, 023402 (2010)

[16] A. Yamaguchi et al., A Strontium Optical Lattice Clock, Journal of the National Institute of Information and Communications Technology Vol.57 Nos.3/4 (2010)

[17] P. Morzynski et al., Absolute measurement of the 1S0− 3P0 clock transition in neutral 88Sr over the 330 km-long stabilized fibre optic link, Nature, ccientific Reports 5:17495, DOI: 10.1038/srep17495

[18] Tetsushi Takano et al., Precise determination of the isotope shift of 88Sr–87Sr optical lattice clock by sharing perturbations, Appl. Phys. Express 10 072801 (2017)

[19] R. Hobson, An Optical Lattice Clock with Neutral Strontium (PhD thesis), University of Oxford (2016)

[20] M. M. Boyd et al., Nuclear spin effects in optical lattice clocks, Phys. Rev. A 76, 022510 (2007)

[21] J. Lodewyck et al., Optical to microwave clock frequency ratios with a nearly continuous strontium optical lattice clock, Metrologia 53, 1123–1130 (2016), doi:10.1088/0026-1394/53/4/1123

[22] L. De Sarlo et al., A mercury optical lattice clock at LNE-SYRTE, Journal of Physics: Conference Series 723 (2016) 012017, doi:10.1088/1742-6596/723/1/012017

[23] I. Katori et al., Trapping of Neutral Mercury Atoms and Prospects for Optical Lattice Clocks, Phys. Rev. Lett. 100, 053001 (2008)

[24] M. Abgrall et al., Atomic fountains and optical clocks at SYRTE: Status and perspectives C. R. Physique 16 (2015) 461–470

[25] C. Philippe et al., 1.5 m - optical frequency standard iodine stabilized in the 10-15 range for space applications, 978-1-5386-2916-1/$31.00 (2017) IEEE

[26] R. Tyumenev et al., Comparing a mercury optical lattice clock with microwave and optical frequency standards, New J. Phys. 18 (2016) 113002

[27] P. Yun et al., High-Performance Coherent Population Trapping Clock with Polarization Modulation, Phys. Rev. A 7, 014018 (2017)

[28] H. L. Stover et al., Locking of laser oscillators by light injection, Appl. Phys. Lett. 8, 91 (1966)

[29] J. L. Hall et al., Delivering the same optical frequency at two places: accurate cancellation of phase noise introduced by an optical fiber or other time-varying path, Optics Letters, volume 19 number 21 (1994)

[30] E. D. Black, An introduction to Pound–Drever–Hall laser frequency stabilization, American Journal of Physics 69, 79 (2001); doi: 10.1119/1.1286663

[31] P. Lemonde et al., Hyperpolarizability Effects in a Sr Optical Lattice Clock, Phys. Rev. Lett. 96, 103003 (2006)

[32] N.Hinkley et al., An Atomic Clock with 10−18 Instability, Science 10.1126 1240420 (2013)

[33] G. P. Barwood et al., Agreement between two 88Sr+ optical clocks to 4 parts in 10-17, Phys. Rev. A 89, 050501(R) (2014)

[34] Y. Huang et al., Frequency Comparison of Two 40Ca+ Optical Clocks with an Uncertainty at the 10−17 Level, Phys. Rev Lett. 116, 013001 (2016)

[35] N. Huntemann et al., Single-Ion Atomic Clock with $3 \times 10-18$ Systematic Uncertainty, Phys. Rev. Lett. 116, 063001 (2016)

[36] S. Falke atal., A strontium lattice clock with 3x10−17 inaccuracy and its frequency, New Journal of Physics 16 073023 (2014)

[37] T.L. Nicholson Systematic evaluation of an atomic clock at 2x10-18 total uncertainty, Nature com. 6:6896 (2015), DOI: 10.1038/ncomms7896

[38] W. F. McGrew, A. D. Ludlow et al., Atomic clock performance beyond the geodetic limit, arXiv:1807.11282 (2018)

[39] D.B. Sullivan (2001). "Time and frequency measurement at NIST: The first 100 years". IEEE International Frequency Control Symposium. NIST. pp. 4–17.

[40] Essen, L.; Parry, J. V. L. (1955). An Atomic Standard of Frequency and Time Interval: A Cæsium Resonator. Nature. 176 (4476): 280–282. Bibcode:1955Natur.176..280E. doi:10.1038/176280a0

[41] S Weyers, V Gerginov, M Kazda, J Rahm, B Lipphardt, G Dobrev and K Gibble, Advances in the accuracy, stability, and reliability of the PTB primary fountain clocks, arXiv:1809.03362v1 (2018)

[42] T. Rosenband et al., Frequency Comparison of Two High-Accuracy $Al^+$ Optical Clocks, Phys. Rev. Lett. 104, 070802 (2010)

[43] S. G. Porsev et al., Optical clock comparison test of Lorentz symmetry, arXiv:1809.10742v1 (2018)

[44] A. Al-Masoudi et al., Noise and instability of an optical lattice clock Phys. Rev. A 92, 063814 (2015)

[45] M. Schioppo, A. D. Ludlow et al., Ultrastable optical clock with two cold-atom ensembles, Nature Photonics volume 11, pages 48–52 (2017)

[46] Campbell et al., A Fermi-degenerate three-dimensional optical lattice clock, Science 358, 90–94 (2017)

[47] T. Middelmann et al., High Accuracy Correction of Blackbody Radiation Shift in an Optical Lattice Clock, Phys. Rev. Lett. 109, 263004 (2012) 10.1103/PhysRevLett.109.263004

[48] K. Beloy et al., Atomic clock with 1×10−18 room-temperature blackbody stark uncertainty, Phys. Rev. Lett., 113:260801,(2014)

[49] I. Ushijima et al., Cryogenic optical lattice clocks, Nat Photon, 9:185–189, (2015)

[50] H. Ouerdane et al., S-wave and p-wave scattering in a cold gas of Na and Rb atoms, Eur. Phys. J. D 53, 27-32 (2009), https://doi.org/10.1140/epjd/e2009-00042-8

[51] N. D. Lemke et al., p-Wave Cold Collisions in an Optical Lattice Clock, Phys. Rev. Lett. 107, 103902 (2011)

[52] R. W. Boyd, Nonlinear Optics (book), Nonlinear Optics Series Elsevier (2008) ISBN: 0080485960, 9780080485966

[53] F. L. Kien *et al.*, Dynamical polarizability of atoms in arbitrary light fields: general theory and application to cesium*, Eur. Phys. J. D (2013), DOI: 10.1140/epjd/e2013-30729-x

[54] P. Rosenbusch et al., ac Stark shift of the Cs microwave atomic clock transitions, Phys. Rev. A 79, 013404 (2009)

[55] A. Khadjavi et al., Stark Effect in the Excited States of Rb, Cs, Cd, and Hg*, Physical Review Volume 161, number 5 (1968)

[56] S. G. Porsev, M. S. Safronova, Multipolar Polarizabilities and Hyperpolarizabilities in the Sr Optical Lattice Clock, Phys. Rev. Lett. 120, 063204 (2018)

[57] V. D. Ovsiannikov, Multipole, nonlinear, and anharmonic uncertainties of clocks of Sr atoms in an optical lattice, Phys. Rev. A 88, 013405 (2013)

[58] H. Katori, Strategies for reducing the light shift in atomic clocks, Phys. Rev. A 91, 052503 (2015)

[59] P. G. Westergaard et al., Lattice-induced frequency shifts in Sr optical lattice clocks at the 10−17 level. Phys. Rev. Lett. 106, 210801 (2011)

[60] C Shi et al., Polarizabilities of the 87Sr Clock Transition, Phys. Rev. A 92, 012516 (2015)

[61] S. G. Porsev et al., Possibility of an optical clock using the $6\ ^1S_0 \longrightarrow 6\ ^3P_0$ transition in $^{171,173}$Yb atoms held in an optical lattice, Phys. Rev. A 69, 021403(R) (2004)

[62] K.A.H. Van Leeuwen (book), Stark Effect Studies of Alkaline Earth Atoms, Drukkerij Elinkwijk B.V. - Uthrecht (1984)

[63] V A Davydkin and V D Ovsiannikov, The hyperpolarisability of an excited atom, J. Phys. B: At. Mol. Phys. 19 2071 (1986)

[64] N.L. Manakov et al., Atoms in a laser Field Physics Report (Review Section of Physics Letters) 141, No. 6, 319-433 (1986)

[65] J. D. Van der Waals, Dissertation, Leiden (1873)

[66] M. J. KLEIN, The historical origins of the Van Der Waals equation, Physica 73, 28-47 (1974)

[67] L. Diosi, 1995, Quantum Master Equation of a Particle in a Gas Environment, Europhys Lett. 30 (2). pp. 63-38 (1995)

[68] A. C. Vutha et al., Collisional frequency shift of a trapped-ion optical clock, Phys. Rev. A 96, 022704 (2017)

[69] K. Gibble, Scattering of Cold-Atom Coherences by Hot Atoms: Frequency Shifts from Background-Gas Collisions, Phys. Rev. Lett. 110, 180802 (2013) DOI: 10.1103/PhysRevLett.110.180802

[70] L. D. Landau and E. M; Lifshitz, Quantum Mechanics, non relativistic theory, Pergamon Press, London, 1958

[71] J. E. Bjorkholrn, Collision-limited lifetimes of atom traps, Phys. Rev. A vol. 38, number 3, (1988)

[72] C. W. Beer and R. A. Bernheim Hyperfine pressure shift of Cs atoms in noble and molecular buffer gases, Phys. Rev. A, Vol. 13, Number 3 (1976)

[73] D. E. Fagnan et al., Observation of quantum diffractive collisions using shallow atomic traps, Phys. Rev. A 80, 022712 (2009)

[74] K. Szymaniec1 et al., Prospects of operating a caesium fountain clock at zero collisional frequency shift, Appl. Phys. B 89, 187–193 (2007), DOI: 10.1007/s00340-007-2813-5

[75] R. Li et al., Improved accuracy of the NPL-CsF2 primary frequency standard: evaluation of distributed cavity phase and microwave lensing frequency shifts, Metrologia 48 (2011) 283–289, doi:10.1088/0026-1394/48/5/007

[76] X. Xu et al., Cooling and trapping of atomic strontium, J. Opt. Soc. Am. B/Vol. 20, No. 5/May (2003)

[77] W. Zhang et al., Ultrastable Silicon Cavity in a Continuously Operating Closed-Cycle Cryostat at 4 K, Phys. Rev. Lett. 119, 243601 (2017)

[78] S. Bilicki, Horloge à réseau optique au strontium: comparaison d'horloges pour des applications en physique fondamentale et échelles de temps, (PhD thesis) LNE-SYRTE, Observatoire de Paris-Meudon (2017)

[79] O. Lopez, Multiplexed Optical Link for Ultra-Stable Frequency Dissemination, Frequency Control Symposium (FCS), 2010 IEEE International, pp 639 - 641 (2010)

[80] Refimev clock comparison fiber network map

[81] N. Chiodo et al., Cascaded optical fiber link using the Internet network for remote clocks comparison, Optics Express Vol. 23, Issue 26, pp. 33927-33937 (2015) https://doi.org/10.1364/OE.23.033927

[82] J. Lodewyck et al., Observation and Cancellation of a Perturbing dc Stark Shift in Strontium Optical Lattice Clocks, IEEE Transactions on Ultrasonics, Ferroelectrics, and Frequency Control, vol. 59, no. 3, 0885–3010 (2012)

[83] H. Schnatz et al., First phasecoherent measurement of visible radiation, Phys. Rev. Lett., 76 :18 (1996)

[84] Th. Udem, J. Reichert, R. Holzwarth, and T. W. Hänsch, Absolute optical frequency measurement of the Caesium D1-line with a mode-locked laser, Phys. Rev. Lett., 82 :3568 (1999)

[85] H. R. Telle et al., Kerr-lens, mode-locked lasers as transfer oscillators for optical frequency measurements, Appl. Phys. B 74, 1–6 (2002), DOI: 10.1007/s003400100735

[86] J. Stenger et al., Ultraprecise Measurement of Optical Frequency Ratios, Phys. Rev. Lett. 88 073601 (2002), DOI: 10.1103/PhysRevLett.88.073601

[87] S. A. King Absolute frequency measurement of the 2S1/2–2F7/2 electric octupole transition in a single ion of 171Yb+ with 10−15 fractional uncertainty, New Journal of Physics 14 013045 (13pp) (2012) doi:10.1088/1367-2630/14/1/013045

[88] G. P. Barwood et al., Trapped strontium ion optical clock, Proceedings Volume 10567, International Conference on Space Optics — ICSO 2006; 105672U (2017) https://doi.org/10.1117/12.2308177

[89] H. S. Margolis et al., Trapped Ion Optical Clocks at NPL, AIP Conference Proceedings 869, 92 (2006), doi: 10.1063/1.2400638

[90] I. R. Hill et al., A low maintenance Sr optical lattice clock, Journal of Physics: Conference Series 723 012019 (2016) doi:10.1088/1742-6596/723/1/012019

[91] S. B. Koller et al., Transportable Optical Lattice Clock with 7 × 10−17 Uncertainty, Phys. Rev. Let. 118, 073601 (2017)

[92] S. Origlia et al., A high-performance optical lattice clock based on bosonic atoms, arXiv:1803.03157v1 (2018)

[93] R. Le Targat et al., Experimental realization of an optical second with strontium lattice clocks, Nat. Comm. 4:2109 (2013), DOI: 10.1038/ncomms3109

[94] Phase-coherent comparison of two optical frequency standards over 146 km using a telecommunication fiber link, Applied Physics B 97: 541-551 (2009)

[95] T. Akatsuka et al., 30-km-long optical fiber link at 1397 nm for frequency comparison between distant strontium optical lattice clocks, Japanese Journal of Applied Physics 53, 032801 (2014), http://dx.doi.org/10.7567/JJAP.53.032801

[96] A. Yamaguchi et al., Direct Comparison of Distant Optical Lattice Clocks at the 1016 Uncertainty, The Japan Society of Applied Physics, Applied Physics Express 4 082203 (2011) DOI: 10.1143/APEX.4.082203

[97] M. Fujieda All-optical link for direct comparison of distant optical clocks, Optical Society of America (2011) OCIS codes: (120.3940) Metorology; (060.2360) Fiber optics links and subsystems; (120.4800) Optical standards and testing.

[98] F. Stefani al., Tackling the Limits of Optical Fiber Links, <hal-01090057> (2014)

[99] A. Bercy et al., TwoWay Optical Frequency Comparisons Over 100km Telecommunication Network Fibers, <hal01057013v1> (2014)

[100] O. Lopez et al., Frequency and time transfer for metrology and beyond using telecommunication network fibres, C. R. Physique 16 531–539 (2015), http://dx.doi.org/10.1016/j.crhy.2015.04.005

[101] C. Lisdat et al., A clock network for geodesy and fundamental science, Nature comm. 7:12443 (2016) DOI: 10.1038/ncomms12443

[102] O. Lopez et al., Cascaded multiplexed optical link on a telecommunication network for frequency dissemination, Optical Society of America (2010) (120.3930) Metrological instrumentation; (060.2360) Fiber optics links and subsystems; (140.0140) Lasers and laser optics; (120.5050) Phase measurement

[103] D. Luna et al., Three-Cornered Hat Method via GPS Common-View Comparisons, IEEE transaction on instrumentation and measurement, VOL. 66, NO. 8, (2017)

[104] G. J. Dick, Local oscillator induced instabilities in trapped ion frequency standards, in Proceedings of the Nineteenth Annual Precise Time and Time Interval (PTTI) Applications and Planning Meeting, Redondo Beach, CA, Dec 1987, pp. 133-147 (1987)

[105] P. G. Westergaard, Horloge à réseau optique au strontium: en quête de la performance ultime (PhD thesis) LNE-SYRTE, Observatoire de Paris-Meudon (2010)

[106] R. Le Targat Horloge à réseau optique au strontium: une deuxième génération d'horloges à atomes froids, (PHD Thesis) LNE-SYRTE, Observatoire de Paris-Meudon (2007)

[107] J. Gibbons et al., Achieving very long lifetimes in optical lattices with pulsed cooling, Phys. Rev. A 78, 043418 (2008)

[108] P. G. Westergaard, J. Lodewyck, and P. Lemonde *Minimizing the Dick Effect in an Optical Lattice Clock*, IEEE Transactions On Ultrasonics Ferroelectrics and Frequency Control, 57 (2010), pp. 623-628.

[109] J. Lodewyck, P. G. Westergaard, and P. Lemonde *Nondestructive measurement of the transition probability in a Sr optical lattice clock*, Phys. Rev. A, 79 (2009), p. 061401(R).

[110] B. R. Mollow, Stimulated Emission and Absorption near Resonance for Driven Systems, Phys. Rev. A Vol. 5, Num. 5 (1972)

[111] D. A. Steck, Quantum and Atom Optics, available online at http://steck.us/teaching (revision 0.12.0, 16 May 2017)

[112] M. B. Grey et al., Photodetector designs for low-noise, broadband, and high-power applications, Review of scientific instruments Volume 69, Number 11 (1998)

[113] P. Horowitz and W. Hill, The art of electronics, Cambridge University Press (1989)

[114] A. M. Fox, Quantum Optics: An Introduction (book), Oxford Master series in atomic, optical and laser physics (2006)

[115] A. Sørensen, L-M. Duan, J. I. Cirac and P. Zoller, Many-particle entanglement with Bose-Einstein condensates, Nature 409 63 (2001)

[116] G. Vitagliano et al., Spin squeezing and entanglement for an arbitrary spin, Phys. Rev. A 89, 032307 (2014)

[117] M. Kitagawa and M. Ueda, Squeezed spin states, Phys. Rev. A 47 5138 (1993)

[118] J. Hald et al., Spin Squeezed Atoms: A Macroscopic Entangled Ensemble Created by Light, Phys. Rev. Lett. VOLUME 83, NUMBER 7 (1999)

[119] Yan-Lei Zhang et al., Detuning-enhanced cavity spin squeezing, Phys. Rev. A 91, 033625 (2015)

[120] M. H. Schleier-Smith et al., Squeezing the collective spin of a dilute atomic ensemble by cavity feedback, Phys. Rev. A 81, 021804(R) (2010)

[121] Monika H. Schleier-Smith et al., States of an Ensemble of Two-Level Atoms with Reduced Quantum Uncertainty, Phys. Rev. Lett. 104, 073604 (2010)

[122] J. Appel et al., Mesoscopic atomic entanglement for precision measurements beyond the standard quantum limit, 10960–10965 PNAS

[123] Ian D. Leroux Orientation-Dependent Entanglement Lifetime in a Squeezed Atomic Clock, PRL 104, 250801 (2010)

[124] I. D. Lerou Implementation of Cavity Squeezing of a Collective Atomic Spin, Phys. Rev. Lett. 104, 073602 (2010)

[125] L K Thomsen, Continuous quantum nondemolition feedback and unconditional atomic spin squeezing, J. Phys. B: At. Mol. Opt. Phys. 35 (2002) 4937–4952

[126] A. Kuzmich, Atomic quantum non-demolition measurements and squeezing, Europhys. Lett., 42 (5), pp. 481-486 (1998)

[127] J. Ma, Quantum spin squeezing, Physics Reports 509 (2011) 89–165

[128] M. A. Norcia et al., Strong coupling on a forbidden transition in strontium and nondestructive atom counting, Phys. Rev. A 93, 023804 (2016)

[129] J. Hu Vacuum spin squeezing, arXiv:1703.02439v1

[130] R. J. Lewis-Swan et al., Robust spin squeezing via photon-mediated interactions on an optical clock transition, Phys. Rev. Lett. 121, 070403 (2018)

[131] E. S. Polzik et al., Entanglement and spin squeezing in a network of distant optical lattice clocks, Phys. Rev. A 93, 021404(R) (2016)

[132] L. I. R. Gi et al., Spin Squeezing in a Rydberg Lattice Clock, Phys. Rev. Lett. 112, 103601 (2014)

[133] Z. Chen et al., Cavity-aided nondemolition measurements for atom counting and spin squeezing, Phys. Rev. A 89, 043837 (2014)

[134] D. Meiser et al., Spin squeezing in optical lattice clocks via lattice-based QND measurements, New Journal of Physics 10 073014 (2008), doi:10.1088/1367-2630/10/7/073014

[135] R. H. Dicke, The effect of collisions upon the Doppler width of spectral lines, Phys. Rev. Let., 89 472 (1953)

[136] D. Leibfried et al., Quantum dynamics of single trapped ions, Rev. of Modern Physics, vol 75, (2003)

[137] D. J. Wineland et al., Laser cooling of atoms, Phys. Rev. A, volume 20, number 4 (1979)

[138] D. J. Wineland et al., Recoilless optical absorption and Doppler sidebands of a single trapped ion, Phys. Rev. A, vol 36 number 1 (1987)

[139] H. Frauenfelder, The Mossbauer effect, W. A; Benjamin, Inc. New York (1962)

[140] C. Aslangul, in Mécanique quantique 2 (book), ed. Deboeck supérieur (2018)

[141] C. Cohen-Tannoudji et al., in Mécanique quantique 2 (book), ed. EDP sciences/CNRS (2018)

[142] K. Beloy, Theory of the ac Stark Effect on the Atomic Hyperfine Structure and Applications to Microwave Atomic Clocks (PhD thesis) University of Nevada, Reno (2009)

[143] P. W. Langhoff et al., Aspects of time-dependent perturbation theory, Rev. of Modern Physics, vol. 44, num. 3 (1972)

[144] G. Vallet et al., A noise-immune cavity-assisted non-destructive detection for an optical lattice clock in the quantum regime, New J. Phys. 19, 083002 (2017)

## RÉSUMÉ

Ce tavail de thèse a été effectué au sein de laboratoire LNE-SYRTE de l'Observatoire de Paris et a porté sur l'opération et l'amélioration des performances d'une horloge à réseau optique au strontium. Une partie de l'activité a été dédiée à l'étude de deux effets sytematiques dégradant l'exactitude de l'horloge: l'hyperpolarisabilité et les collisions chaudes avec les gaz résiduels se trouvant dans la chambre à vide où sont piégés les atomes de strontium. Le traitement des collisions a requis la production d'un modèle théorique adapté au cas des horloges optiques. Une partie a consisté en l'opération de l'horloge lors de campagne de comparaisons à l'échelle européenne reposant sur un réseau continental de liens fibrés. Enfin, la plus large part du travail effectué a porté sur la réasilation d'un système de detection non destructive des atomes en cavité basé sur les aspects dispersifs de l'intéraction lumière-atome. La non destructivité classique, permettant une réduction de l'effet Dick limitant la stabilité de l'horloge, y à été réalisée et des résultats préliminaires ont prouvé la possibilité d'atteindre le régime quantique, permettant de reduire le bruit de projection quantique limitant également la stabilité de l'horloge.

## MOTS CLÉS

Horloge atomique, horloge à réseau otpique, métrologie temps-fréquence, stabilité et exactitude, mesure non desctructive, effet Dick, bruit de projection quantique, technologie quantique

## ABSTRACT

This thesis work has been carried out at the LNE-SYRTE laboratory hosted at the Observatoire de Paris. It consisted of the operation and the improvement of a strontium optical lattice clock. A part of the work has dedicated to the study of to systematic effects degrading the clock accuracy: hyperpolarizability and hot collisions with the residual background gas found in the vacuum chamber where the strontium atoms are trapped. The investigation of the collisions required the development of a model suitable to the optical lattice clocks case. A part consisted in the operation of the clock during European scale comparison campaigns, relying on an optical fiber links network. The larger part of this work was dedicated to the realization of non destructive system of detection of the atoms based on the dispersive properties of light-matter interaction. The classical non destructivity, allowing for a reduction of the Dick effect, limiting the clock stability, was achieved and preliminary results have proved the possibility of reaching the quantum non destructivity regime, which allows for the reduction of the quantum projection noise, as well limiting the clock stability.

## KEYWORDS

Atomic clocks, optical lattice clock, time and frequency metrology, stability and accuracy, non destructive measurement, Dick effect, quantum projection noise, quantum technology.